Particulate systems and thin-film based platforms- Development and characterization of fluorescent materials for sensing applications

DISSERTATION

zur Erlangung des akademischen Grades
doctor rerum naturalium
(Dr. rer. nat.)
im Fach Chemie

eingereicht an der
Mathematisch-Naturwissenschaftlichen Fakultät
der Humboldt-Universität zu Berlin

von
Dipl.-Chem. Mandy Hecht

Präsident der Humboldt-Universität zu Berlin:
Prof. Dr. Jan-Hendrik Olbertz

Dekan der Mathematisch-Naturwissenschaftlichen Fakultät:
Prof. Dr. Elmar Kulke

Gutachter/innen:

1. PD Dr. M.G. Weller
2. Prof. Dr. J. Kneipp

Tag der mündlichen Prüfung:
22.09.2015

I found myself again one morning when I opened the window and smelled the fresh daisies growing in my backyard. I ran outside and danced under the sunshine and nothing had felt that warm in a long time. The rays on my skin and the grass beneath my feet, nothing had been that normal for so long. I found myself in the novels I read and the music I played […] I found myself while walking along the beach and witnessing the sun setting down. It was beautiful and when the sun rose the next day, I found myself while trying to tie my curtains up. I made myself some hot tea and I thought to myself, "I'm going to be alright". Because I found myself while pacing down the open roads at midnight. And we laughed under the stars and I remember that the world is much bigger than I am and there is so much more out there than what we had. I found myself tracing back my footprints along the sand and listening to the waters rush along the creeks. I found the warmth of living and breathing after all the tragic. I found the person I was before I realized that bruises weren't just physical, they were internal, too. But I found that person again. I found the person who still believes that life is good.

Ming D. Liu

La lumière joue dans notre vie un rôle essential: elle intervient dans la plupart des nos activités. Les Grecs de l'Antiquité le savaient bien déjà, eux qui pour dire "mourir" disaient "perdre la lumière".

Light plays an essential role in our lives: it is an integral part of the majority of our activities. The ancient Greeks, who for "to die" said "to lose the light", were already well aware of this.

-Louis de Broglie, 1941

Content

Abbreviations

δ	Chemical shift
ε	Molar absorption coefficient
λ	Wavelength
τ_f	Fluorescence lifetime
Φ_f	Fluorescence quantum yield
AcOH	Acetic acid
APTES	3-(Aminopropyl) triethoxysilane
aq.	Aqueous
Au-NP	Gold nanoparticle
BE	Binding energy
$BF_3 \times OEt_2$	Boron trifluoride diethyl etherate
BODIPY	Boron dipyrromethene/4,4-difluoro-4-bora-3a,4a-diaza-s-indacene
br	Broad
BSA	Bovine serum albumin
CH_2Cl_2	Dichloromethane
CLSM	Confocal laser scanning microscopy
^{13}C-NMR	Carbon nuclear magnetic resonance
CP	Cellulose particle
CTAB	*N*-cetyltrimethylammonium bromide
CV	Cresyl violet
d	Doublet
DA	Diode array
DAD	Diode array detector/detection
DDQ	2,3-Dichloro-5,6-dicyano-*p*-benzoquinone
DEPT	Distortionless enhancement by polarization transfer
DIPEA	*N*,*N*-Diisopropylethylamine
DLS	Dynamic light scattering
DMF	Dimethylformamide
e.g.	*exampli gratia*
EPA	United states environmental protection agency
ESEM	Environmental scanning electron microscopy
ESI	Electrospray ionization
Et_2O	Diethyl ether
EtOAc	Ethyl acetate
EtOH	Ethanol
FEF	Fluorescence enhancement factor
FLIM	Fluorescence lifetime imaging microscopy
Hex	Hexane
^{1}H-NMR	Proton nuclear magnetic resonance
HMBC	Heteronuclear multiple bond coherence
HMQC	Heteronuclear multiple quantum coherence
HPLC	High performance liquid chromatography
HRMS	High resolution mass spectroscopy

HTM	Heavy or transition metal
Hz	Hertz
i.e.	*id est*
J	Coupling constant
LOD	Limit of detection
MA	γ-Methacryloxypropyl trimethoxysilane
MeCN	Acetonitrile
MeOH	Methanol
MHz	Megahertz
MS	Mass spectrometry
m/z	Mass to charge ratio
n.d.	Not determined
NB	Nile blue
NFC	Nanofibrillated cellulose
NFCP	Nanofibrillated cellulose particle
NMR	Nuclear magnetic resonance spectroscopy
NP	Nanoparticles
PBS	Phosphate-buffered saline buffer
PE	Petroleum ether
PEG	Polyethylene glycol
PET	Photoinduced electron transfer
PDI	Polydispersity index
pK_A	Acid dissociation constant
ppb	Parts per billion
ppm	Parts per million
q	Quartet
QD	Quantum dot
R6G	Rhodamine 6G
RT	Room temperature
s	Singlet
SiO_2	Silica
SNP	Nanoparticles functionalized with Sulforhodamine B
TEM	Transmission electron microscopy
TEOS	Tetraethyl orthosilicate
TFA	Trifluoroacetic acid
THF	Tetrahydrofuran
TLC	Thin layer chromatography
TSNP	Terpyridine–sulforhodamine-functionalized
UPLC	Ultrahigh performance liquid chromatography
UV/Vis	Ultraviolet-visible spectroscopy
WHO	World Health Organization
XPS	Photoelectron spectroscopy

Abstract

The combination of fluorescence and nanomaterials has developed into an emerging research area. Nanomaterials are at the leading edge of the rapidly developing field of nanotechnology and have attracted increasing interest for sensor research in recent years. The explosion of nanotechnology, leading to the development of materials with unique optical properties has opened up new horizons for fluorescence detection. Nonetheless until now the step from an organic sensory molecule to a final sensor format is a complex endeavor.

This thesis aimed at the preparation of particulate and thin-film based platforms for various analytes through combining the features of an appropriate host material with outstanding properties of dyes concomitant with sensitive fluorescence detection techniques.

In particular, pH sensitive fluorescent probes were sterically immobilized into a thin ion-permeable hydrogel membrane. The reversibly working dip-stick allows the assessment of the "turn-on" and "turn-off" process upon change in pH with the naked eye. Especially a probe working at high basic pH range was converted into a water-soluble analogue and was directly applied at the growth front of silica biomorphs to detect local pH changes.

But also particulate structures are suitable host materials. It is shown how the silica matrix of nanometer-sized nanoparticles lead to improved optical properties for electrostatically embedded oxazine dyes. The interactions of silica and fluorescent dyes within the pores of mesoporous particles in combination with the high pore loading capability were exploited to develop an actual sensor format based on signal amplification for the fast detection of the explosive TATP in the ppb range. In another approach the pores were equipped with polyethylene glycol chains and a sensitive hydrophobic dye was embedded. Within that special microenvironment it was possible to detect mercury ions in water with fluorescence enhancement which the probe alone could only accomplish in acetonitrile solution. Heavy metal ions were also successfully detected in a quencher displacement assay involving receptor-dye functionalized silica nanoparticles.

The impact of the unique surface properties of cellulose microparticles was shown by a fluorescent dye which allows an assessment of the surface functional groups and microenvironment through the reactivity and its changes in the optical properties.

The performance of the prepared materials were evaluated mostly by spectroscopic methods and if possible assessed in terms of sensitivity, selectivity and response time.

The newly developed and investigated materials based on fluorescent particulate and thin-films show the facile application of innovative sensor probes for potentially sensing devices.

Kurzzusammenfassung

Die Verbindung von hoch entwickelten Nanomaterialien mit fluoreszenzbasierten Technologien hat sich zu einem aufstrebenden Forschungsbereich entwickelt. Nanomaterialien sind die treibende Kraft im sich schnell entwickelnden Bereich der Nanotechnologie und mit zunehmendem Interesse Gegenstand der Sensorforschung der letzten Jahre. Die daraus entstandenen Materialien mit besonderen optischen Eigenschaften eröffnen neuartige Möglichkeiten im Bereich der fluoreszenzbasierten Detektion. Nichtsdestotrotz ist bis heute der Schritt von einem organischen Indikatormolekül zum real anwendbaren Sensorsystem ein komplexer Prozess.

Diese Arbeit zielte darauf ab, sensorische Materialien verschiedener chemischer Natur für diverse Analyten zu entwickeln, zu charakterisieren und zu etablieren. Dazu zählen sowohl partikuläre als auch Dünnfilm-basierte Systeme und Sensorplattformen, die durch die Verbindung geeigneter Materialien mit den besonderen Charakteristika ausgewählter Fluoreszenzfarbstoffe eine empfindliche und spezifische Detektion erlauben.

Hierbei wurden zunächst pH sensitive Fluoreszenzfarbstoffe auf Basis von Dipyrromethenen entwickelt und in dünnen, Ionen-durchlässigen Hydrogelmembranen immobilisiert. Ein daraus hergestellter reversibel arbeitender Teststreifen ermöglicht die einfache und schnelle Beurteilung von pH-Änderungen über fluoreszenzbasierte Prozesse mit dem bloßen Auge. Darüber hinaus wurde beispielhaft gezeigt, wie diese Farbstoffe auch in eine wasserlösliche Form überführt werden können. Damit konnten lokale pH-Änderungen im stark alkalischen Bereich an der Wachstumsfront von Silikat-Biomorphs erstmals mittels Fluoreszenzmikroskopie gezeigt und detektiert werden.

Auch partikuläre Systeme stellten sich als geeignete Trägermaterialien heraus. Es konnte gezeigt werden, wie die Silikat-Matrix von nanometer-großen Partikeln zu verbesserten optischen Eigenschaften für elektrostatisch eingebettete Oxazin-Farbstoffe führt. Zusätzlich wurden die Wechselwirkungen zwischen der Silikatoberfläche und Fluoreszenzfarbstoffen innerhalb der einzigartigen Porenstruktur mesoporöser MCM-41-Partikel untersucht und somit die Beladung der Poren mit fluoreszierenden Molekülen optimiert. Aufbauend auf dieser Untersuchung wurde ein effektives Sensorformat entwickelt. Mittels farbstoffbeladener Partikel konnte in einem Lateral-Flow-Assay über das Konzept der Signalverstärkung ein schneller Nachweis von explosivem TATP im ppb-Bereich etabliert werden.

Ein anderer Ansatz verfolgte das Ziel des sensitiven Nachweises von Quecksilberionen im wässrigen Medium durch Einbettung eines hydrophoben Sensorfarbstoffs innerhalb der partikulären Poren. Durch chemische Modifikation der Poren gelang es, eine geeignete

Mikroumgebung für das Sensormolekül zu schaffen und den bisher nur in Acetonitril arbeitenden Farbstoff zur Detektion von Quecksilberionen im ppb Bereich in Wasser zu etablieren.

In einem anderen System konnte die Oberfläche von Silikat-Nanopartikeln so mit Rezeptor und Farbstoff funktionalisiert werden, dass ein sensitiver und selektiver Nachweis von Schwermetallionen und Anionen über ein Quencher-Displacement-Assay mit einem partikulären System gelang.

Zusätzlich wurde die Besonderheit der einzigartigen Oberfläche von Zellulosemikropartikeln mithilfe eines neu entwickelten Fluoreszenzfarbstoffs untersucht. Dieser erlaubt durch seine Reaktivität zum einen die Beurteilung über erreichbare funktionelle Gruppen an der stark strukturierten Partikeloberfläche und lässt zum anderen Rückschlüsse über die Mikroumgebung des gebundenen Farbstoffs über die Änderung seiner optischen Eigenschaften in Abhängigkeit seiner chemischen Umgebung zu.

Die untersuchten Materialien und entwickelten Strategien zeigen, wie leicht innovative Moleküle für potentielle sensorische Systeme im wässrigen Medium auf Basis von fluoreszierenden Partikeln und dünnen Schichten geschaffen werden können. Das Verhalten der hergestellten Materialien wurde hauptsächlich über spektroskopische Methoden evaluiert und dabei, wenn möglich, die Parameter Sensitivität, Selektivität und Ansprechzeit beurteilt.

Publications

9. M. Hecht, T. Fischer, P. Dietrich, W. Kraus, A.B. Descalzo, W.E.S. Unger, K. Rurack, Fluorinated Boron-dipyrromethene (BODIPY) Dyes: Bright and Versatile Probes for Surface Analysis. *Chemistry Open* **2013**, *2*, 25-38, with an invited Cover Picture.

8. M. Hecht, E. Climent, M. Biyikal, F. Sancenón, R. Martínez-Máñez, K. Rurack, Gated Hybrid Delivery Systems—en route to Sensory Materials with Inherent Signal Amplification. *Coordination Chemistry Reviews* **2013**, *257*, 2589-2606.

7. E. Climent, D. Gröninger, M. Hecht, M.A. Walter, R. Martínez-Máñez, M.G. Weller, F. Sancenón, P. Amorós, K. Rurack, Selective, Sensitive, and Rapid Analysis with Lateral-Flow Assays Based on Antibody-Gated Dye-Delivery Systems: The Example of Triacetone Triperoxide. *Chemistry-A European Journal* **2013**, *19*, 4117-4122.

6. M. Hecht, W. Kraus, K. Rurack, A highly fluorescent pH sensing membrane for the alkaline pH range incorporating a BODIPY dye. *Analyst* **2013**, *138*, 325-332.

5. P. Calero, M. Hecht, R. Martínez-Máñez, F. Sancenón, J. Soto, J.L. Vivancos, K. Rurack, Silica Nanoparticles Functionalized with Cation Coordination Sites and Fluorophores for the Differential Sensing of Anions in a Quencher Displacement Assay (QDA). *Chemical Communications* **2011**, *47*, 10599-10601.

4. R. Martínez-Máñez, F. Sancenón, M. Hecht, M. Biykal, K. Rurack, Nanoscopic Optical Sensors Based on Functional Supramolecular Hybrid Materials. *Analytical and Bioanalytical Chemistry* **2011**, *399*, 55-74.

3. M. Biyikal, M. Hecht, R. Martínez-Máñez, K. Rurack, F. Sancenón, Supramolecular Hybrid Nanomaterials as Prospective Sensing Platforms. In: *Supramolecular Chemistry: From Molecules to Nanomaterials*, P.A. Gale, J.W. Steed (Eds.); J. Wiley & Sons: Chichester, Vol. 6, Section 10 Nanotechnology, **2011**, 3669-3697.

2. R. Martínez-Máñez , F. Sancenón, M. Biyikal, M. Hecht, K. Rurack, Mimicking Tricks from Nature with Sensory Organic-inorganic Hybrid Materials. *Journal of Materials Chemistry* **2011**, *21*, 12588-12604.

1. H.-J. Hamann, M. Hecht, A. Bunge, M. Gogol, J. Liebscher, Synthesis and Antimalarial Activity of new 1,2,4,5-Tetroxanes and novel Alkoxy-substituted 1,2,4,5-Tetroxanes Derived from Primary gem-Dihydroperoxides. *Tetrahedron Letters* **2011**, *52*, 107-111.

Berlin, 23.04.2015, _____

Mandy Hecht

Initial Remarks

The first chapter gives a general introduction about the relevance of the topic of fluorescent particulate systems and film-based platforms with regard to potential applications in chemical sensing. It points out the major aims of this thesis, which was prepared at the Federal Institute for Materials Research and Testing (BAM) under the supervision of PD Dr. Michael G. Weller (BAM 1.5 Protein Analysis) and Dr. Knut Rurack (BAM 1.9 Sensor Materials). Respective introductions to the topics and detailed descriptions of the obtained results are presented and discussed in the corresponding chapters.

1 General Introduction

In 1565 the Spanish physician and botanist Nicolas Monardes described in his *Historia Medicinal* (Sevilla, 1565) the peculiar blue color of an aqueous extract of the Mexican medicinal wood called *Lignum nephriticum*, used as a medical treatment for liver and kidney ailments.[1, 2] Throughout the centuries Kircher, Grimaldi, Boyle, Newton, Herschel and many other scientists and materialists were intrigued by this unusual phenomenon but it was finally not understood[3] -until George Gabriel Stokes, a physicist and professor of mathematics at Cambridge, first introduced the term "fluorescence" in his publication *On the Change of Refrangibility of Light* in 1852.[4] He demonstrated that the observed phenomenon was an emission of light following absorption of light. At the time the molecular structure of this earliest described fluorophore could be identified and the observed process finally explained. It is one of the tree's flavonoids, related to a group of non-fluorescent *C*- and *O*-*β*-glycosyl-α-hydroxydihydrochalcones (coatlines). Under mild alkaline conditions (pH~7.5) in water the fast, irreversible spontaneous oxidation of coatline B **1** occurred and yielded the pale-blue emitting matlaline **2**, a four-ring tetrahydromethanobenzofuro[2,3-*d*]oxacine (Figure 1).[5] The multiple color effects that attracted the attention of many investigators over centuries result from the combination of an intense absorption at λ = 429 nm and a very large emission yield in the blue spectral range (λ = 466 nm) of the reaction product **2**.

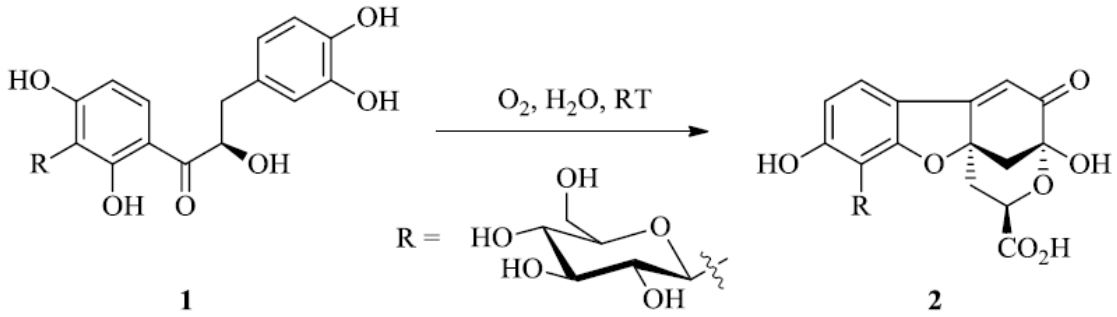

Figure 1 Reaction of coatline B 1 under mild basic conditions to the fluorescent derivate matlaline 2.

Based on these early observations absorption and fluorescence phenomena were exploited to establish powerful analytical tools which are essential in physical, biological and chemical sciences.[6] Furthermore absorption and fluorescence spectroscopy in conjunction with fluorescent dyes and labels allow fast detection times often with remarkable selectivity and especially very high sensitivity of fluorescence based methods. Excitation and emission are

separated processes which offer more possibilities to get detailed information about the molecule of interest, compared to absorption measurements alone.[7, 8]

With the recent explosion of nanotechnology new horizons for fluorescence based analytical methods have opened up. The combination of the prominent sensitivity and potential selectivity of fluorescent molecules, dyes and probes and the robustness of various host matrices like particles, scaffolds and films as investigated in the following chapters are attractive topics in contemporary research.[8] These supporting materials provide new possibilities for advanced analytical applications and accomplish the demand for sensitive analytical tools by offering an outstanding microenvironment for the fluorescent sensory probes. If one can control and tailor the properties of these new smart materials such as vary the size, composition and shape, in a predictable manner the needs of a specific application can be met.[9] One of the main challenges in this field however is to develop materials which can be prepared reproducibly and efficiently, possess lower detection limits and have fast response times, as well as exhibiting increased robustness and extended lifetimes compared to traditional fluorescent sensor molecules in solution.

1.1 Major objectives of this thesis

Based on current challenges in the development of smart materials this thesis had the following aims:

(i) The development and investigation of new sensitive and selective fluorescent molecules which are of interest for analytical applications

(ii) The incorporation and anchoring of fluorescent molecules to generate particulate and thin-film platforms to meet the need for improved nanomaterials

For aim (i), mainly 4,4-difluoro-4-bora-3a,4a-diaza-s-indacene (BODIPY) dyes were selected. These fluorescent dyes are potent and versatile probes because of their outstanding characteristics and sensing capabilities. The specific reasons for this will be discussed below. Aim (ii) was pursued in the frame of studying the influence of the material's microenvironment on the performance of the dyes for sensing of pH, heavy metal ions and anions in aqueous solution, as well as for the availability of functional surface groups.

2 Hydrogel matrix for pH sensing

In the first chapter the strategy of steric embedding of pH-sensitive hydrophobic boron dipyrromethene dyes into a polyurethane hydrogel matrix is presented resulting in pH-sensitive fluorescence sensor films, especially for the basic pH range, in which common pH glass electrodes can show alkaline errors. This concept was successfully transferred to a number of pH sensitive dyes additionally for the neutral and acidic range. The polymer matrix creates a special microenvironment comparable with an aqueous ethanolic solution, thus preserving the outstanding spectroscopic features of the fluorophores. Furthermore a water-soluble derivative is presented to extend the unique application capability of these new developed fluorescent compounds.

2.1 Introduction

The pH glass electrode is by far the most commonly used pH sensor. A major limitation of glass electrodes however is their rather poor performance at the extremes of the pH scale.[10] Regarding the strongly alkaline pH region, this is a significant disadvantage for applications for instance in the paper industry,[11] nuclear fuel reprocessing,[12, 13] waste and waste water treatment,[14-18] agriculture,[19] leather processing,[20, 21] metal mining and finishing[22, 23] or microbial production processes involving alkaliophiles.[24, 25] All of them requiring the monitoring and/or adjustment of alkaline pH. In more acidic solutions deviations from the linear range are also observed ("acid error"). That means the pH electrode exhibits a lower pH than the actual pH value which can be misleading regarding e.g. environmental and geological studies.[26] Although new reports on pH sensors are continually published, most of them deal with biotechnological applications and thus concern pH sensors for the physiological range.[27-31] Developments of pH sensors for extreme pH ranges are still rather rare.[32-36] Fluorescence based indicators offer several advantages over conventional electrochemical pH sensors, including sensitivity, proneness against alkaline errors, miniaturization, format adaptability and remote access. However, the development of optical sensors for the extremes of the pH scale of aqueous solutions remains challenging and their availability is still limited.

4,4-Difluoro-4-bora-3a,4a-diaza-s-indacene (BODIPY)[37] dyes are a potent and versatile platform for the construction of pH-sensitive fluorescent probes.[28, 38, 39] Moreover, BODIPYs have also proven to be suitable dyes for a number of other sensing applications,[30, 40-43] because of their outstanding characteristics such as excellent thermal and photochemical stability, relatively high molar absorption coefficients and high fluorescence quantum yields.[44, 45] In addition, the wide variety of synthetic pathways toward BODIPY dyes nowadays available renders the tailoring of desired spectroscopic responses and recognition chemistries facile. Nonetheless, it is still difficult to obtain BODIPY derivatives which show both good solubility and bright fluorescence in water. BODIPYs with suitable subunits are promising tools for the measurement of pH in both chemical and biological systems.[38]

Transforming this suitability into an actual sensor format requires the immobilization of the pH sensitive dyes in a thin ion-permeable membrane. The latter however has to avoid detrimental effects such as self-quenching between dye molecules at high concentrations, insufficient permeability or mobility of the analyte in question and leaching of the indicator, in the case that steric embedding is preferred to covalent attachment because it can dispense with time consuming pre-functionalization steps.

2.2 Results and discussion

2.2.1 Sensing in the basic pH range

*Synthesis and crystal structure of the pH sensitive BODIPY **5***

The BODIPY derivative **5** was synthesized in 45% yield by condensation of 4-hydroxybenzaldehyde with two equivalents of kryptopyrrole **4** using trifluoroacetic acid (TFA) as a catalyst, followed by oxidation with 2,3-dichloro-5,6-dicyano-*p*-benzoquinone (DDQ), deprotonation with triethylamine (NEt_3) and finally complex formation with boron trifluoride etherate ($BF_3 \times OEt_2$) at room temperature (RT) according to literature reports (Figure 2).[38, 46]

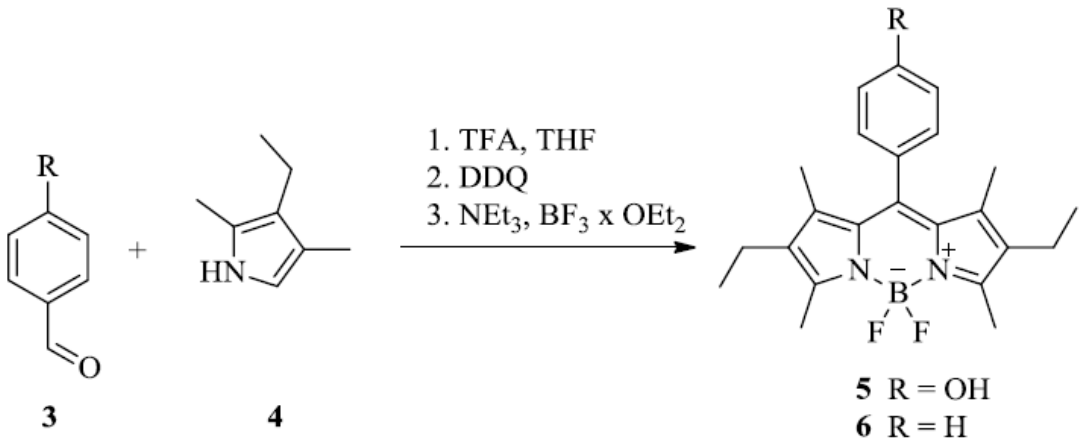

Figure 2 Synthesis of the pH sensitive BODIPY 5 and reference dye 6.

X-ray structure analysis of **5** revealed that the dye crystallizes in the monoclinic space group P21/n with one molecule in the asymmetric unit and four molecules in the unit cell. The three-dimensional structure of **5** is illustrated in Figure 3, together with the atomic labelling scheme.

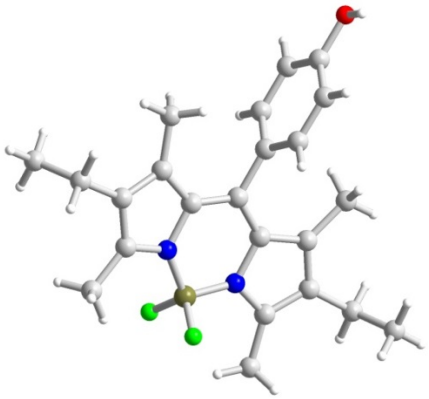

Figure 3 Crystal structure of 5 as derived from X-ray analysis.

The X-ray data show that the *meso*-phenyl ring is virtually perpendicular to the plane of the BODIPY core with a dihedral angle of 87.02(6)° and that the central six-membered ring of the core is almost coplanar with the adjacent five-membered rings with the average deviation from the mean plane being 0.0031(2) Å. The same accounts for the two pyrrole rings, the four methyl groups and the two ethylene carbons, with a maximum deviation of 0.081(2) Å from the least-squares mean plane for 18 atoms. These findings are in line with previous reports on highly internally twisted 1,7-alkyl-substituted BODIPYs.[47, 48]

Spectroscopic properties of ***5***

Table 1 shows the spectroscopic features of **5** investigated by absorption as well as steady-state and time-resolved fluorescence spectroscopy in various solvents with increasing polarity from hexane to water. The maxima of the absorption and fluorescence spectra are virtually independent of solvent polarity except for water in which a broadening of the absorption band is observed (Figure 4). This effect can be attributed to the moderate solubility of the hydrophobic dye in water, accompanied by the tendency for dimer formation, with microsolvation effects being possibly also involved (see also Chapter 3 and 5). The weak solvatochromism in organic solvents observed for **5** is advantageous because it reveals that the dye is insensitive to a change in an organic environment[49] and suggests that electrolyte effects should also not play a prominent role. Notably, in EtOH–H_2O **5** is found to be extremely brightly fluorescent in comparison to neat organic solvents. The molar absorption coefficient of 71 900 ± 630 M^{-1} cm^{-1} in acetonitrile is characteristically high. The fluorescence decay curves could be described by a single exponential fit ($\chi^2 < 1.2$) and the fluorescence decay times (τ_f) lie between 4.3 and 4.7 ns in organic solvents, and 5.6 ns in the ethanolic aqueous solution. In water, the fluorescence is distinctly quenched and the lifetime could only

be fitted to a non-exponential decay. In combination with the above mentioned spectral behavior in water, such a quenched fluorescence also supports dimer formation, the strength of the fluorescence of the dimer species being still a matter of debate.[50, 51] The complicated excited-state behavior of **5** in water disfavors a straightforward use of **5** as a pH indicator, because monomer–dimer equilibria tend to depend strongly on the electrolyte content, pH and other environmental features. In addition, the quenched fluorescence is unfavorable with regard to analytical performance.

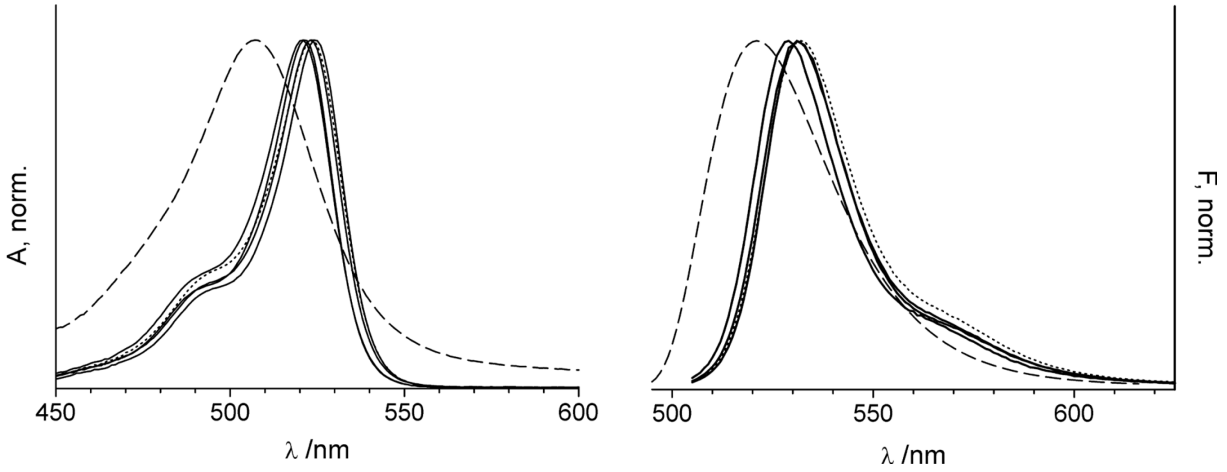

Figure 4 Normalized absorption and fluorescence spectra (λ_{exc} = 495 nm) of 5 in different solvents: Hex, Et_2O, THF (solid lines), EtOH–H_2O (dotted line), H_2O (dashed line).

Table 1 Selected spectroscopic data of 5 in various solvents at 298 K.

Solvent	λ_{abs} /nm	$\varepsilon_{\lambda abs}$ /M^{-1} cm^{-1}	λ_{em} /nm	Φ_f	τ_f /ns	k_r /10^8 s^{-1}	k_{nr} /10^8 s^{-1}
Hex	524	n.d.[a]	531	0.82	4.29	1.9	0.4
Et_2O	521	n.d.	529	0.91	4.72	1.9	0.2
THF	523	n.d.	531	0.92	4.57	2.0	0.2
MeCN	521	71900	531	0.83	4.72	1.8	0.4
H_2O/EtOH	523	n.d.	532	0.97	5.57	1.7	0.1
H_2O	523	n.d.	532	0.12[b]	2.67[c]	[d]	[d]

[a] Not determined. [b] Global fluorescence quantum yields of the species mixture in water when excited at 495 nm. [c] Longest lifetime component of multi-exponential fit, attributed to the monomeric form of **5**. [d] Not calculated because of species diversity. Further investigations are under way to shed more light on this behaviour.

pH-dependent absorption and fluorescence spectroscopy of ***5***

As mentioned above, the *meso*-phenol moiety of **5** is sensitive to the environmental pH and can be deprotonated to the phenolate anion in basic media. Because highly electron-rich *meso*-substituents commonly quench the fluorescence of the BODIPY core through an efficient electron transfer process,[46, 52] an increase in pH should gradually switch off the fluorescence of **5**. As depicted in Figure 5, an almost complete deprotonation of the phenolic OH group occurs above pH 13 indicated by the low fluorescence intensity. The effect of pH was assessed by altering the solution pH from 7 to 13 through successive addition of aq. KOH in ethanol–water 1:1 to avoid the formation of aggregates. The spectrophotometric and fluorometric pH titration spectra in Figure 5 reveal that the wavelength of the emission maximum remains unchanged, despite the strong signal decrease; the fluorescence quantum yield of $\mathbf{5}^-$ lies below 10^{-4}.

In addition, the absorption maximum was shifted to shorter wavelengths, in agreement with the influence that a change in the inductive effect of the meso-substituent exerts on the HOMO/LUMO of the BODIPY core when converting a phenol into a phenolate moiety. The protonation constant was determined to be pK_A 9.98 ± 0.02 by Boltzmann curve-fitting as a function of pH using the fluorescence intensity at 535 nm. The dynamic sensing range spans 3 pH units, 8.75–11.65. It has to be mentioned that for an accurate determination of the pK_A a correction by 0.2 according to ref.[53] is necessary to take into account the differences in proton activity coefficients and liquid junction potentials between the ethanol–water solvent mixture of the sample and the aqueous calibration solution.

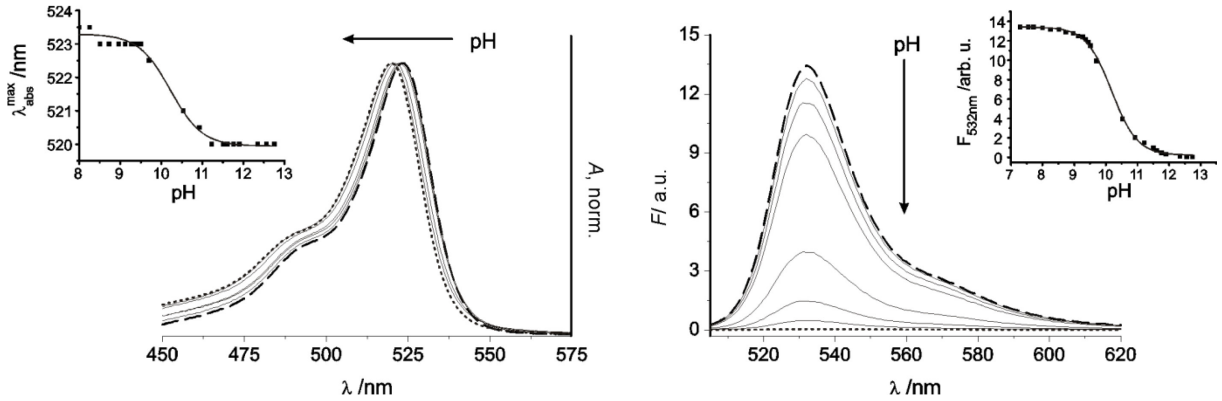

Figure 5 Dependence of the absorption and fluorescence of 5 on a change in pH from 7.3–12.8 upon addition of aq. KOH solutions (λ_{ex} = 495 nm, $c_5 = 1.39 \times 10^{-6}$ M, EtOH–H_2O); pH 7.3 (dashed line), pH 12.8 (dotted line); selected intermediate steps (solid lines). Insets: corresponding titration curves, shift of the absorption maximum (left) and the fluorescence intensity at the emission maximum (right) as a function of pH.

*Synthesis and properties of the sensory film containing **5***

The fluorescent thin film was prepared by simple dip coating of tailored 3D epoxy-functionalized polymer slides into the hydrogel–dye solution. After drying, the sensor was very robust and easy to apply. The thickness of the sensor layer was determined to be 9.3 ± 0.4 mm by ESEM through coating of similarly functionalized glass slides instead of polymer supports (Figure 6 and 7).

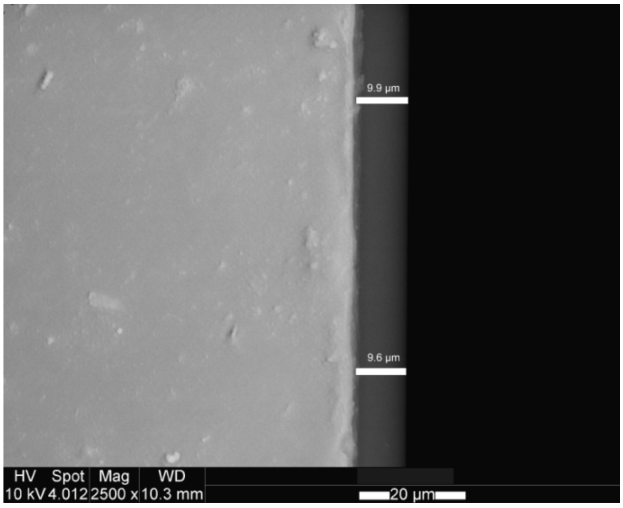

Figure 6 ESEM image of a hydrogel film on a glass support and determination of the layer thickness.

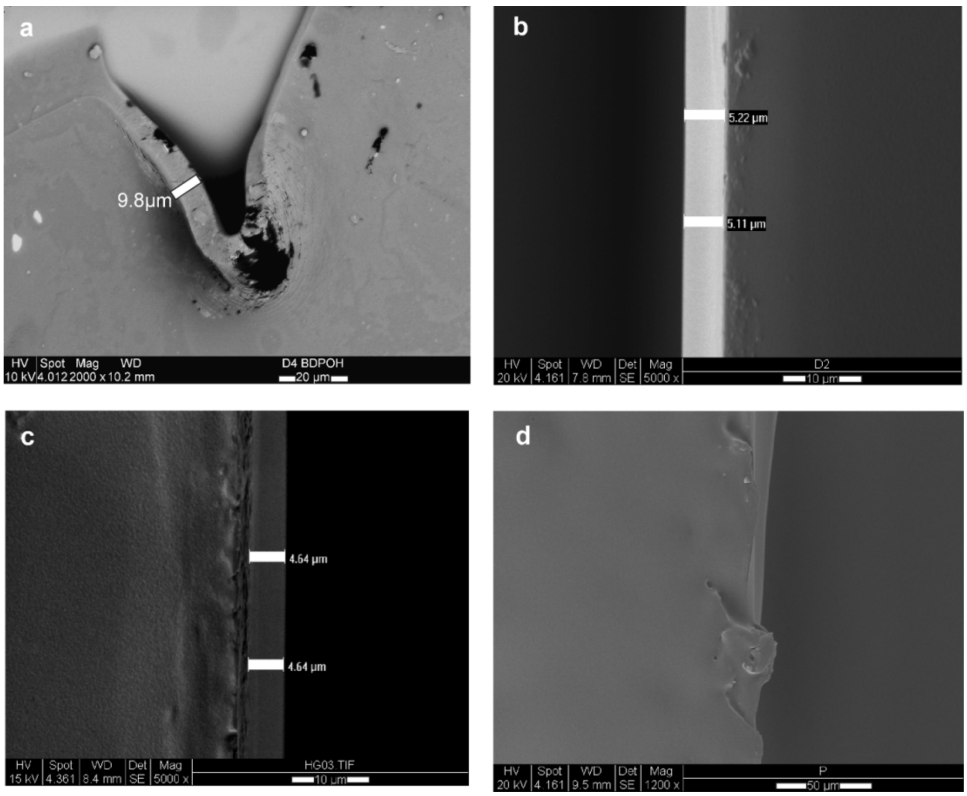

Figure 7 a) Detached polymer on glass support; variation of film thickness on glass support b) D2C1 c) D3C1; d) polymer D4 on polymer support. For sample code, see Table 2.

The replacement of the polymer support with glass was necessary due to the lack of contrast in the case of a hydrogel polymer on a polymer support (Figure 7d). An effective dye concentration of 0.81 mM in the dried hydrogel layer was calculated from the molar absorption coefficient and the thickness of the layer. A reduction of the film thickness down to 4 µm can be reproducibly realized by adjusting the initial amount of hydrogel (Figure 7b and c). As expected, the fluorescence signal decreases with the decrease in film thickness when the concentration of the dye is kept constant (Figure 8).

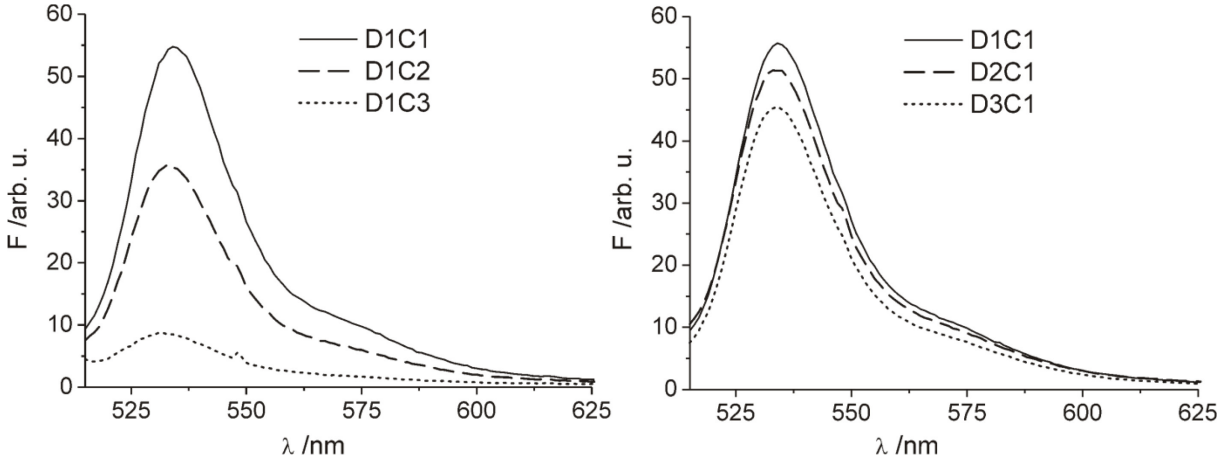

Figure 8 Variation of film thickness (left) and dye concentration (right), see Table 2.

Table 2 Reduction of the amount of polymer and dye concentration.

Sample	Amount of D4 /g	c_5 [a] /M	n_5 /mol (kg D4)$^{-1}$
D1C1	1.00	2.51×10^{-3}	2.00×10^{-6}
D1C2	1.00	1.26×10^{-3}	1.00×10^{-6}
D1C3	1.00	2.51×10^{-4}	2.00×10^{-7}
D2C1	0.75	2.51×10^{-3}	2.00×10^{-6}
D3C1	0.50	2.51×10^{-3}	2.00×10^{-6}

[a] Concentration of stock solution of **5**

In contrast to the applied 3D epoxy polymer substrate, plain and epoxysilane-functionalized glass surfaces showed no stable conjugation to the hydrogel. Films on these substrates were detached upon exposure to aqueous sample solutions (Figure 7a). Additional XPS investigations showed that the polymer support expresses a much higher number of C–O units at the surface than the glass slide, presumably influencing the adhesive forces between the support and the sensor layer (Table 3).

Table 3 Formal XPS elemental composition of used epoxy supports.

Element	Nexterion E (glass)	PolyAn 3D Epoxy (polymer)
Na	0.46	-
O	62.51	9.57
N	0.30	-
C	9.51	90.25
Si	23.42	0.26
Zn	0.79	-
B	2.96	-
Mg	1.55	-
CO-content	72.02	99.82

Regarding the spectroscopic behavior of **5** as shown in Figure 4 and Table 1, the absorption maximum of the sensor material is centered at 525 nm in water and the emission at 534 nm, comparable to that of **5** in an organic microenvironment or in EtOH–H_2O. In addition, the fluorescence lifetime of **5** amounts to 5.56 ns in the hydrogel film, similar to that of **5** in an ethanol–water mixture. Because the fluorescence decay was found to be mono-exponential, **5** seems to be distributed in a homogeneous environment in the film. The hydrogel matrix thus leads to a beneficial effect and preserves the exceptional features of **5** in its protonated state.

Performance of the sensor

The potential of the supported fluorescent polyurethane hydrogel matrix incorporating **5** for application purposes was assessed by monitoring the membrane's response toward various pH under different environmental settings. When the film-coated dipsticks are titrated with an aqueous KOH solution in pure water, absorption and fluorescence changes like those shown in Figure 9 are observed. As expected, the fluorescence intensity decreases as a function of pH, with shifts of the absorption and emission maxima being mainly absent, constituting another advantageous feature of the composite membrane. The pH titration curve of the sensor exhibits the typical sigmoidal shape and the pK_A was determined to be 11.44 ± 0.01. Presumably attributed to the interaction of the polyurethane matrix with the dye, the response of the sensor material lies at even more alkaline pH, rendering the material very suitable for this extreme pH range. In addition, a dynamic working range of 10.02–13.12 could be

established. Another important feature of the physical entrapment of the hydrophobic dye in the hydrogel matrix is that the shortcomings of aggregation and low solubility in aqueous environments can be nicely overcome. The absence of any fluorescence ascribable to **5** from a solution in which the sensor was incubated for 300 min showed that the film does not suffer from leaching of the dye due to swelling of the hydrogel. Regarding comparability of the fluorometrically obtained results with pH data recorded with the two digital pH meters employed, the sensor strips showed excellent agreement of all three devices yielding matching pH within ± 0.05 pH units.

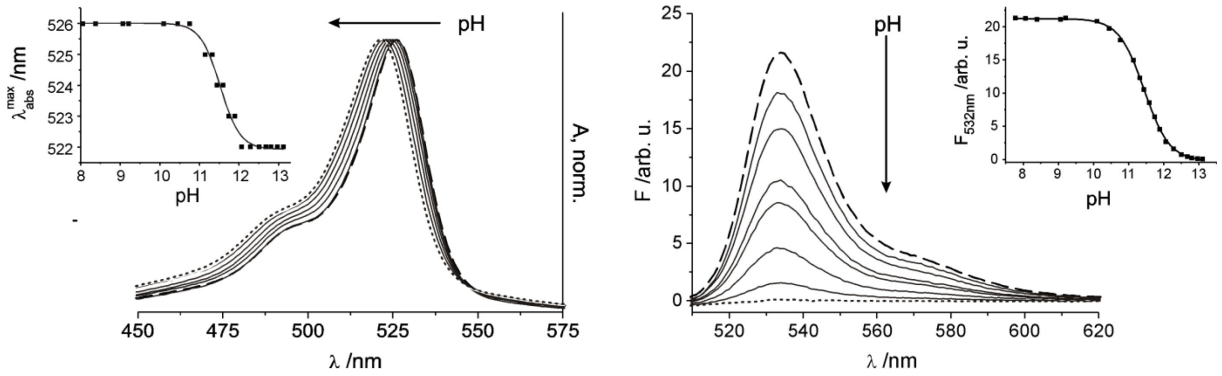

Figure 9 Dependence of the absorption and fluorescence spectra of the sensor film containing 5 in water on changes in pH (λ_{exc} = 495 nm). pH 8.2 (dashed line), pH 13.2 (dotted line), intermediate steps (solid lines). Insets show the corresponding titration curves when plotting the shift of the absorption maximum (left) and the fluorescence intensity at the emission maximum (right) as a function of pH.

Effect of anions and electrolyte background

It is known from the literature[52] that basic inorganic and organic anions can lead to a deprotonation of an organic dye that carries a potentially acidic group in organic solvents in which the anions are much less solvated than in water. Such behavior can potentially interfere with the desired pH indication reaction. Since the spectroscopic properties of **5** in the hydrogel matrix are more reminiscent of a (mixed) organic than a neat aqueous environment, the influence of potential interferents for neat and embedded **5** was studied. In organic solvents such as acetonitrile (Figure 10 and 11 left), **5** indeed suffers from deprotonation when basic anions such as fluoride, dihydrogen phosphate or benzoate are present at a 5-fold molar excess, discernible from the quenching of fluorescence.

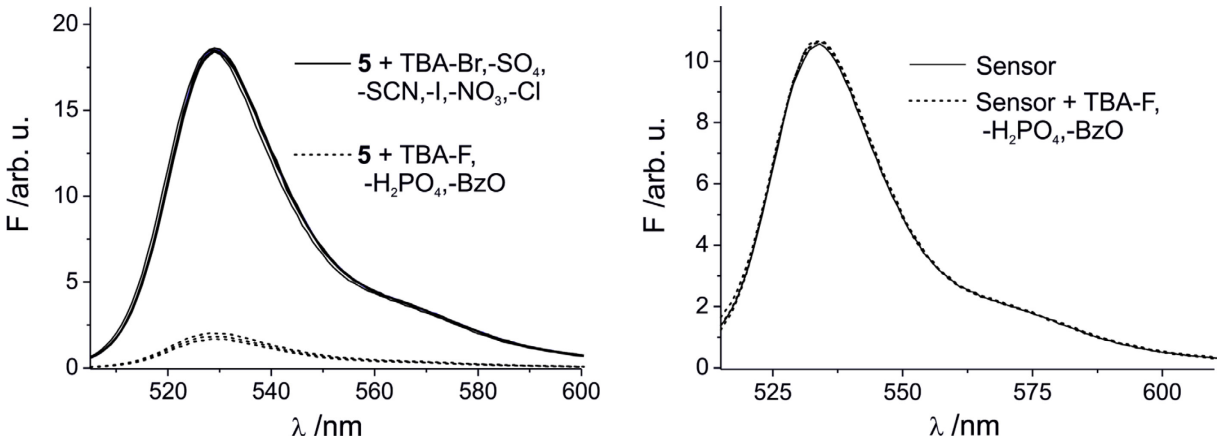

Figure 10 Fluorescence spectra of 5 in MeCN (left) upon addition of various anions and fluorescence spectra of the sensor film in water (right) upon addition of relevant anions $H_2PO_4^-$, F^- and BzO^- (c_{anion} = 7.5 × 10^{-6} M).

In contrast, already in EtOH–H_2O no remarkable changes in fluorescence intensity could be detected suggesting that the anions are well solvated (Figure 10 and 11 right and also 12).

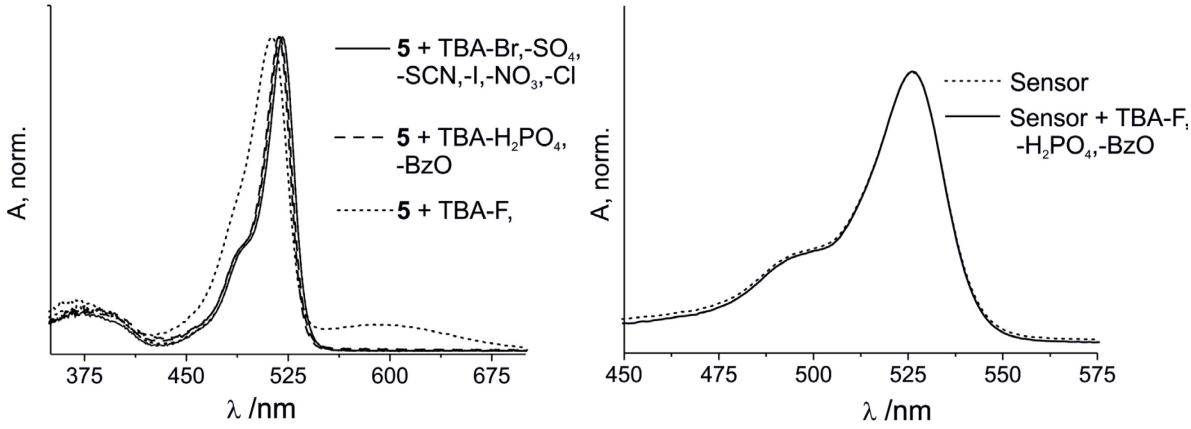

Figure 11 Absorption spectra of 5 in MeCN and of the sensor film in water upon addition of relevant anions (c_{anion} = 7.5 × 10^{-6} M)

Figure 12 Visible response of 5 to various anions under UV-light a) in EtOH–H_2O b) in MeCN.

When stepping to the sensory film and monitoring its fluorescence in water in the presence of the most potent interferents in organic solution, Figures 10 and 11 reveal that these species are spectroscopically silent under realistic sensing conditions, despite the different microenvironments in the hydrogel compared with water. Furthermore, it was demonstrated that the performance of the sensor film is unaffected by other ions using a simulated seawater composition of 3% (w/w) which corresponds to a saline concentration in the Atlantic.

Reversibility, surface water and sewage

To test the reversibility of the sensor film and to show the robustness against highly basic conditions the film was dipped alternately into an alkaline solution (pH = 12.14), which results in deprotonation of the dye associated with quenching of the fluorescence, and water of pH = 6.43, whereby the fluorescence intensity should return to its initial value at the end of each cycle (Figure 13). Switching between the fluorescent on/off states can thus be repeated without decomposition of the membrane or the embedded dye.

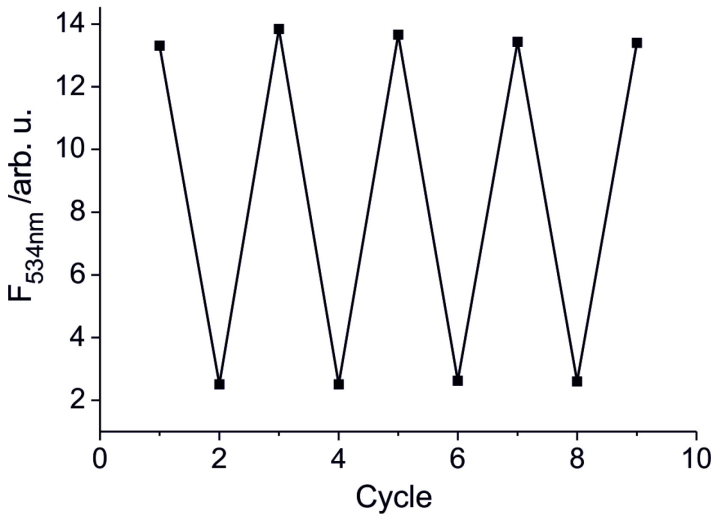

Figure 13 Reversibility of the fluorescence response of the sensor film upon successive deprotonation/protonation by dipping it into an alkaline solution of pH 12.14 and water of pH 6.43.

To evaluate the performance of the strips under realistic conditions and to assess the robustness and precision between batch preparations, three strips from individual batches were tested on three real samples, surface water from an inner city canal (sample 1) as well as influent (sample 2) and effluent (sample 3) water from a sewage treatment plant. All samples (2.5 ml) were spiked with 0.3 ml 0.1 M KOH. The reproducibility in the fluorescence readings between the strips was good with a relative uncertainty of ≤ 2.2% (Table 4), no matter if the pH of the samples was close to neutral or basic after spiking with 0.1 M KOH.

Table 4 Average fluorescence readings and corresponding pH values obtained for three different samples, samples were filtrated before measurement to remove suspended solids and fine sediments.

Spiking [a]	Sample 1 [b] $F_{532nm}/10^6$ cts	pH	Sample 2 [c] $F_{532nm}/10^6$ cts	pH	Sample 3 [d] $F_{532nm}/10^6$ cts	pH
no	4.97 ± 0.11	7.44	4.83 ± 0.11	7.93	4.76 ± 0.10	7.51
yes	2.89 ± 0.06	11.34	2.17 ± 0.04	11.56	2.79 ± 0.05	11.40

[a]All samples (2.5 ml) were spiked with 0.3 ml 0.1 M KOH. [b] Sample 1: surface water from Landwehrkanal, river kilometer 6.1 (Hallesches Tor), Berlin [c] Sample 2: influent water from sewage treatment plant "Teltowkanal Wassmannsdorf", Berlin. [d] Sample 3: effluent from same sewage treatment plant.

A representative selection of fluorescence spectra is shown in Figure 14. Since the initial pH of sample 2 was slightly higher than that of samples 1 and 3, the spiking with the same amount of alkaline solution led to a slightly stronger quenching in this case. For all cases, the optical data were again in good agreement (± 0.05 pH units) with the electrochemical data.

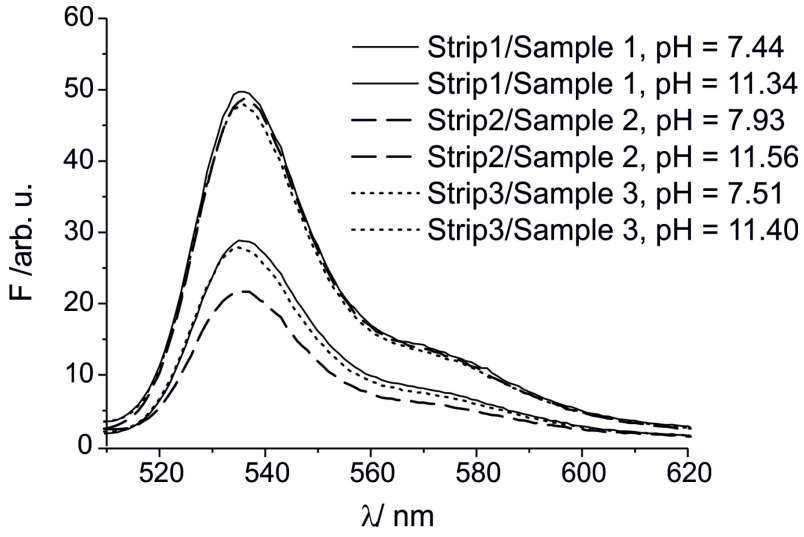

Figure 14 Representative fluorescence spectra of selected combination of test strips and samples; the determined pH is indicated.

Toward on-site application

Generally, assessment by the naked eye is considered the primary advantage of color-changing test strips over fluorescence-changing test strips. However, today with cell phones being almost ubiquitously prevalent and utmost of these devices being equipped with a digital camera, the present sensor matrix for a possible cell phone-based read-out was tested. For this purpose, half of a strip was coated with **5**-doped hydrogel and the other half with **6**-doped hydrogel for internal referencing (Figure 15). BODIPY **6** serves as a reference dye, possessing the same BODIPY core and the meso-phenyl ring as **5** yet lacking a pH-sensitive functional

group.[54] After dipping into solutions containing various KOH concentrations, the strip was photographed (with the camera's LED flash always firing). A defined area (10 × 10 mm) of both halves of the strip in each image was analyzed for their RGB values, which were then transformed to the CIE's XYZ scale. After averaging the latter values and plotting them versus pH, a calibration curve as that shown in Figure 16 was obtained.

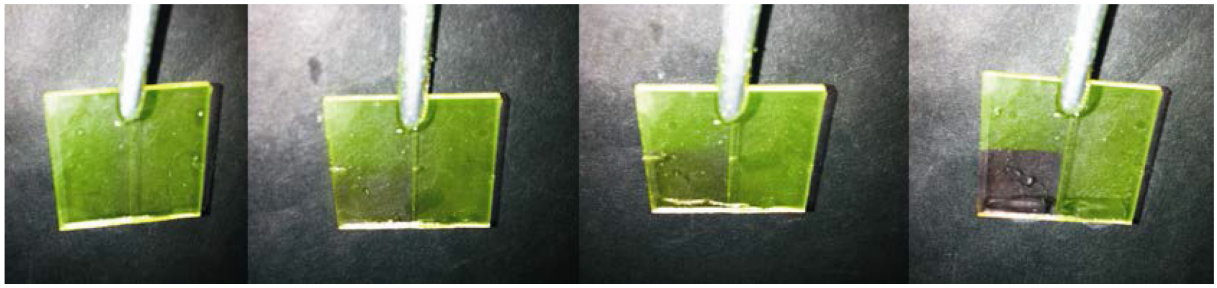

Figure 15 Visible response of the sensor to pH (left to right: pH = 9.0; 10.5; 11.2; 13.0).

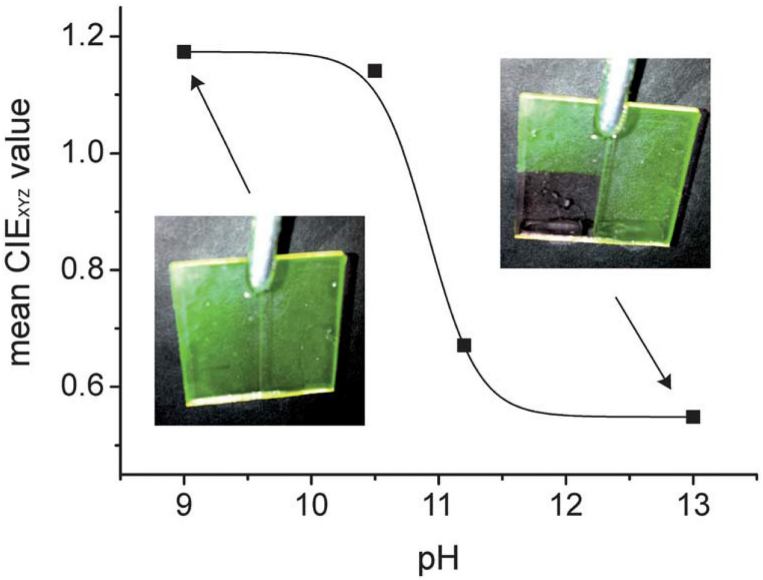

Figure 16 pH calibration curve obtained with half-5/half-6 coated test strips photographed with a cell phone camera after dipping into the respective KOH-containing solution.

The good agreement of the data obtained by this simple on-site procedure, requiring only a conventional cell phone (a mobile application allowing for direct data conversion and analysis in a smart phone is easily imaginable). The fluorimeter based data show the high potential such simple fluorescent sensors have in combination with rampant electronic communication devices.

2.2.2 Selected dyes for a broad-band pH-array

The choice of a fluorescent pH probe depends critically on the pH of the system under investigation. For broad-band pH indication, one can ideally choose a specific dye or several dyes which cover the pH range of interest. The classically used pH-indicator paper ranges from pH 1 to 14, but the color perception of the human eye is not very accurate and can differ from case to case. Furthermore the paper-based formats suffer from color bleaching after a certain time period. Concomitant with the lack of reversibility there is a high demand for reliable alternatives. Such a broad-band application in a simple kind of sensing device, which can be produced and readout by the method described in 2.2.1, could be achieved by tuning the pK_A values of the applied set of chromophores. Based on suitable BODIPY pH probes this can be achieved e.g., by the variation of the substitution pattern at the *meso*-phenyl-moiety of phenol- and aminophenyl hexaalkyl-substituted BODIPYs (Figures 17 and 18).

There are several literature reports dealing with pH sensitive BODIPYs.[38, 55, 56] But their pK_A values are mostly determined in aqueous-organic solutions due to their hydrophobic character and a prediction how they behave in the polyurethane hydrogel matrix is rather difficult. Furthermore, the pK_A values of hexaalkyl-substituted BODIPYs can differ from tetra- or di-alkylated ones. It should also be taken into account that the quantum yield of the fluorescent form should be preferably high compared to the non-fluorescent state to obtain an efficient on-off switching, so that in the ideal case the change in emission through fluorescence ‘turn-on’ or ‘turn-off’ processes could be even intense enough to make a visible read-out possible, concomitant with a suitable absorption and emission window.

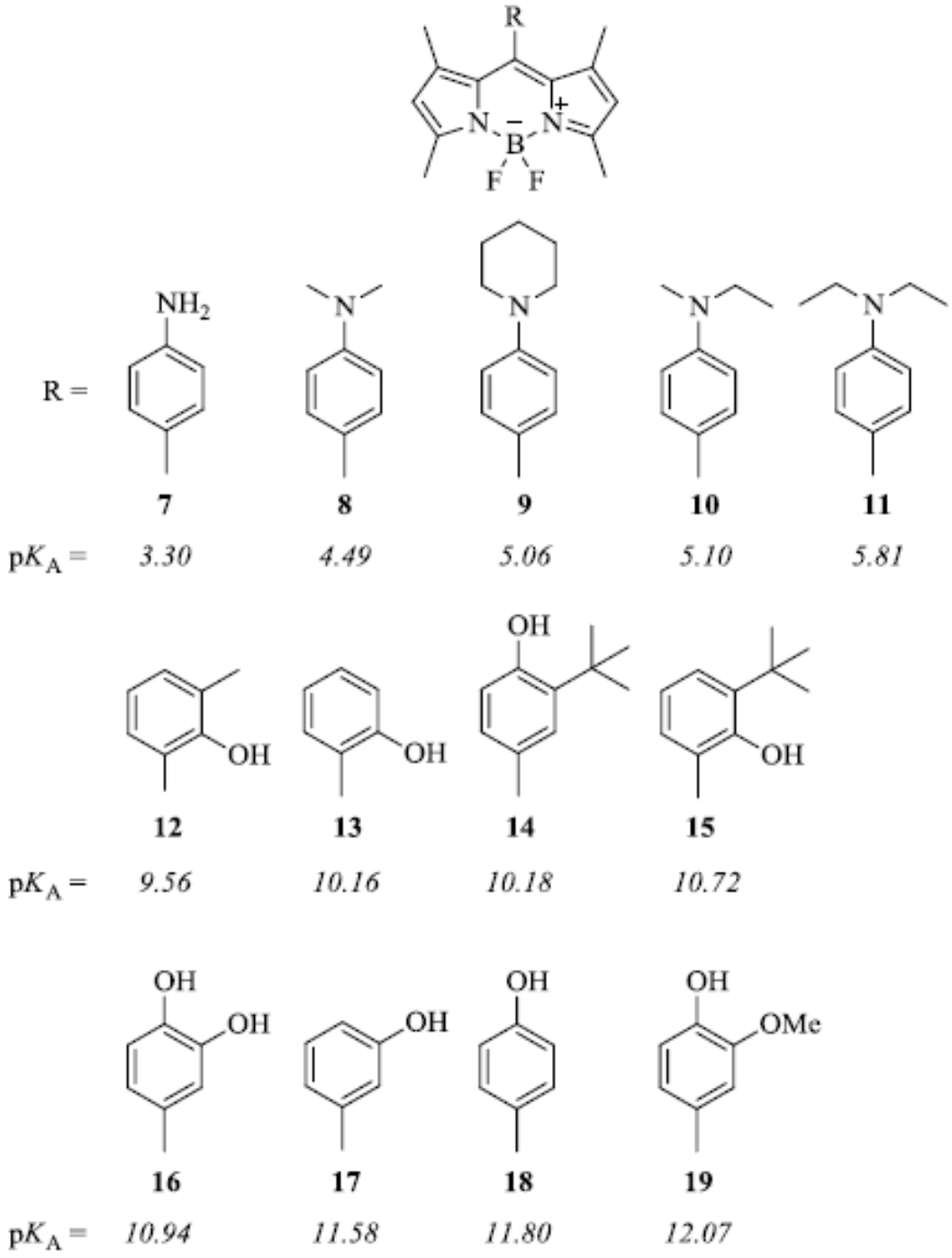

Figure 17 pK_A values of known pH sensitive BODIPY dyes in MeOH–H_2O.

Figure 17 lists some examples of published pH-sensitive BODIPYs and their corresponding pK_A -values in MeOH-H_2O and served as a starting point for choosing suitable compounds.[52, 55-57] Additional electron-withdrawing or -donating groups altering the electronic structure at the phenyl-moiety allow the tuning of the pK_A value.

*Synthesis of the pH sensitive BODIPYs **21a-e***

Several pH sensitive BODIPYs were synthesized by varying the nature of substituents located at the 8-position of the BODIPY core.

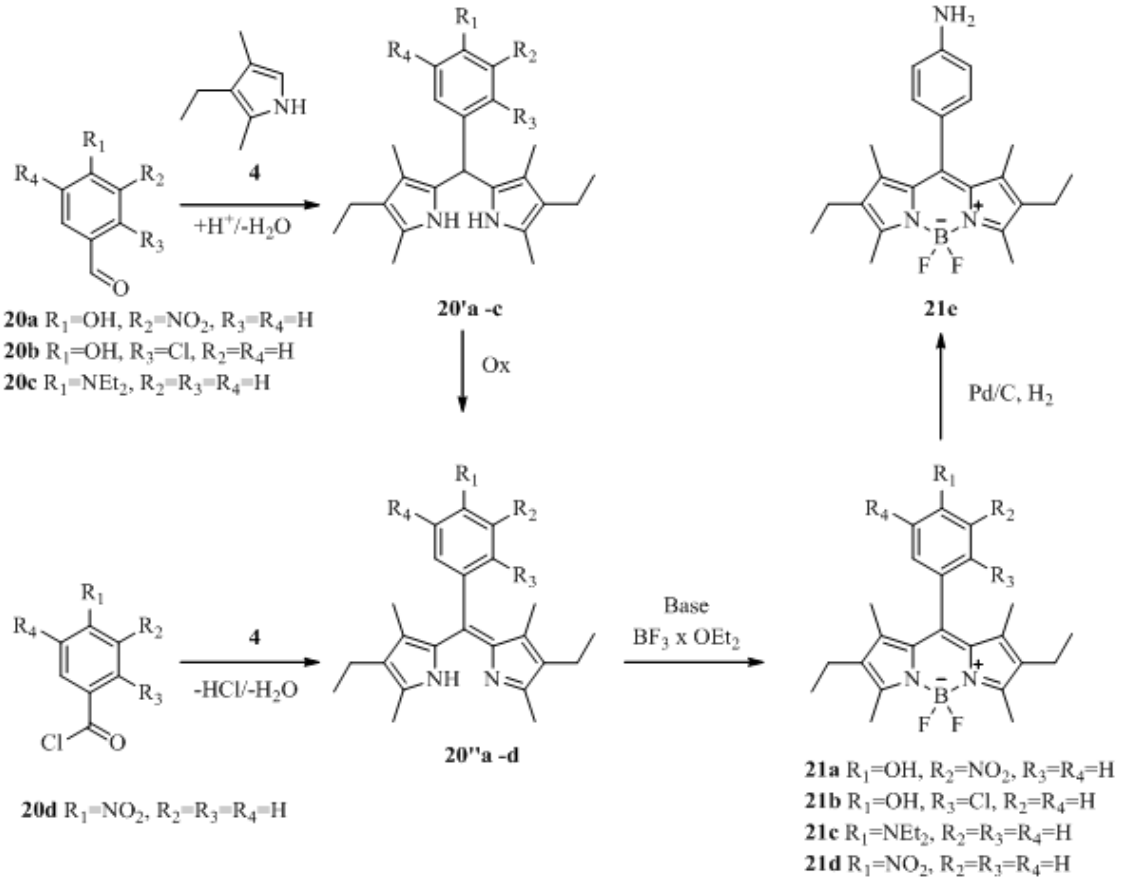

Figure 18 Synthesis and chemical structures of the investigated dyes 21a-21d.

Compounds **21a, 21b** and **21c** were synthesized in good yields by the as described condensation reaction of the corresponding aldehyde **20a-c** with two equivalents of kryptopyrrole **4** using TFA as a catalyst, followed by oxidation with tetrachlorobenzoquinone, deprotonation with base ($^{i}Pr_2NEt$ or NEt_3) and finally complexation with boron trifluoride etherate at RT (see also Chapter 2.2.1). 4-Nitrobenzoyl chloride **20d** was used as starting material for the synthesis of BODIPY **21d**, serving as precursor to generate **21e**. The condensation of 4-nitrobenzoyl chloride **20d** with kryptopyrrole **4** is straightforward and without an additional oxidation step. With this procedure, highly reactive intermediates causing side reactions will not be involved and nitro compound **21d** could be obtained without extensive purification steps. Finally the nitro substituent of **21d** was reduced to the desired amino group by catalytic hydrogenation (Figure 18) to yield **21e**.

The following compounds (kindly provided by co-workers) were additionally involved to fill up the missing pH ranges (Figure 19).

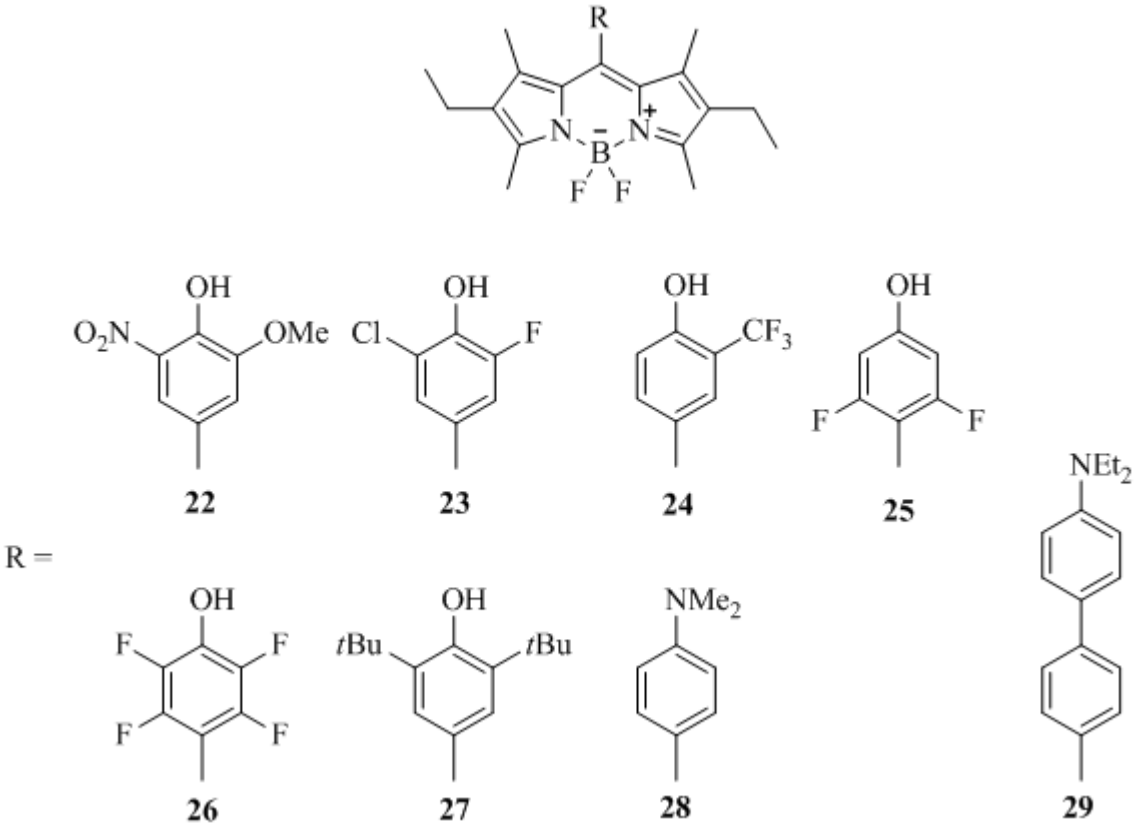

Figure 19 Additional pH-sensitive compounds kindly provided by co-workers.

The compounds **21-29** were characterized by absorption and fluorescence spectroscopy in mixed aqueous–organic media[58] as well as in the dip-stick format based on the detailed characterization of **5** in the previous section 2.2.1.

pH-dependent spectroscopic investigations in solution vs. hydrogel

Table 5 shows the spectroscopic features of the dyes **21-29** investigated by absorption as well as steady-state fluorescence spectroscopy in EtOH–H_2O and embedded in the polyurethane hydrogel matrix. For some compounds it was necessary to use dioxane stock solutions for preparing the dye doped hydrogels, due to a reduced solubility of the dye in CH_2Cl_2 or subsequent precipitation of the dye in the hydrogel solution.

Depending on the pH sensitive compound, aqueous solutions of KOH or $HClO_4$ were used for the fluorescence titration experiments. A deprotonation of the phenol group to the phenolate anion in basic media induces a fluorescence "turn-off" response through a photoinduced electron transfer-process (PET) for **21a**, **21b**, **22-27** as described for **5** (Chapter 2.2.1). On the other hand the protonation of the amino group bearing dyes **21c**, **21e**, **28**, **29** (almost

non-fluorescent in the non-protonated form) with aq. $HClO_4$ solutions leads to a significant enhancement of the fluorescence intensity. The protonation decreases the electron donating ability and thus leads to the inhibition of the quenching process resulting in the "switching-on" of the fluorescence, without spectral changes.

Table 5 Selected spectroscopic data of the investigated dyes 21-29 in EtOH–H_2O and D4 Hydrogel.

Medium	*EtOH–H_2O*			Φ_f	*D4*			
Compnd	λ_{abs} /nm	λ_{em} /nm	pK_A		λ_{abs} /nm	λ_{em} /nm	pK_A	ΔF
	NR_2/NR_2H^+				NR_2/NR_2H^+			
28	523/528	535/541	2.46 ± 0.01	0.74	526/529	536/541	0.90 ± 0.09*	1.83
21e	523/527	536/539	2.87 ± 0.01	0.76	525/529	536/540	2.11 ± 0.01	2.40
21c	523/528	535/544	4.46 ± 0.04	0.85	525/530	535/542	2.82 ± 0.02	2.60
29	–	–	– [a]	0.70	526/529	537/539	2.98 ± 0.03	2.53
	OH/ O^-				*OH/ O^-*			
26	540/538	553/548	5.13 ± 0.02	0.96	543/538	554/550	6.11 ± 0.01	5.45
22	529/526	542/540	6.09 ± 0.02	0.01	532/528	541/540	7.05 ± 0.03	6.30
21a	530/526	541/537	6.41 ± 0.02	0.004	532/528	540/536	7.41 ± 0.06	9.55
25	528/524	540/539	7.40 ± 0.01	0.85	531/527	541/540	8.43 ± 0.01	30.86
23	–	–	– [b]	0.98	534/536	540/538	8.94 ± 0.03	222.05
24	–	–	– [b]	0.89	532/527	539/535	9.96 ± 0.04	18.69
21b	5306/52	541/59	9.33 ± 0.02	0.96	533/528	541/540	10.58 ± 0.01	90.67
5	523/520	532/525	9.98 ± 0.02	0.90	526/522	536/533	11.44 ± 0.01	207.33
27	–	–	– [b]	0.93	531/529	542/537	12.83 ± 0.02	13.82

[a] forms aggregates in EtOH-H_2O mixtures, [b] not determined

Altering the substitution pattern at the *meso*-phenyl-moiety of the BODIPY has no remarkable effect on the absorption and emission maxima compared to **5**. The fluorescence quantum yield Φ_f of the nitro-group containing compounds **21a** and **A7** show lower values compared to the phenol bearing compounds due to the NO_2-group quenching effect. The ΔF value describes the difference of fluorescence intensity of the on- and off state which is much higher for the phenolic compounds.

By including all of the synthesized pH sensitive compounds nearly the complete pH range can be covered. The next step will be to include these data in a mobile application which allows the appropriate analysis after an image of a suitable sample was taken. Further experiments to extend the mobile application described in 2.2.1 are under investigation.

2.2.3 A water-soluble BODIPY analogue

Although the aforementioned polyurethane hydrogel is a suitable matrix to apply those traditional lipophilic and poorly water-soluble molecules in water (as described in Chapter 2.2.1 and 2.2.1), the conversion of the BODIPY scaffold into a hydrophilic analogue could serve as straightforward approach to overcome the limitation of the format of the supporting material. Reported synthetic strategies to create water-soluble BODIPYs typically involve additional synthetic steps to introduce e.g. oligo(ethylene glycol)[59-61], *N*,*N*-bis(2-hydroxyethyl) amine,[62] carbohydrates,[63] nucleotides,[64] or ionic hydrophilic groups such as carboxylic acid,[65, 66] sulfobetaines,[67] or ammonium groups[61, 68] at various positions of the BODIPY core. But depending on the coupling position the introduction of these groups is usually associated with changes in the optical properties due to altered electronic interaction within the BODIPY core.[69] Neutral water-soluble BODIPY dyes are advantageous over ionic species to avoid possible electronic interactions between the BODIPY dye and potential analytes or materials that carry a net charge such as many functionalized particles or cell compartments.[70]

Bearing these considerations in mind, a facile strategy to modify **5** to obtain compound **30** as an outstanding example for a water-soluble BODIPY pH probe without changing its optical properties was developed. The expedient strategy includes the introduction of oligo(polyethylenglycol) (PEG) moieties to the boron center via an ethynyl bond as shown in Figure 20.

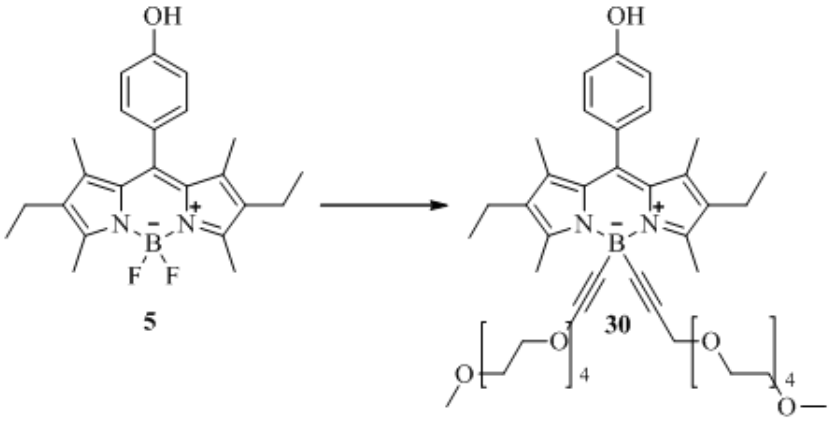

Figure 20 Introduction of PEG moieties to the BODIPY core to increase the water solubility.

The polyethylene glycol group can effectively enhance the interaction of BODIPYs with water and therefore significantly increase the water solubility of the dye because of the strong hydrophilic nature of the PEG residues.[71] Moreover, the induced steric hindrance by the PEG moieties could significantly reduce the formation of aggregates through π-π stacking

interactions between BODIPY cores in aqueous solution as described in section 2.2.1 and 3.2.1.[60]

*Synthesis of BODIPY **30***

The main strategy here was to replace the two fluorine atoms at the 4 and 4´position of the parent BODIPY **5**. Acetylide anions are good nucleophiles for the displacement of fluoride from the borondifluoride entity of the parent BODIPY dye. This could be realized with a previously synthesized propargyl-terminated tetra(ethylene glycol) methylether[72] via a Grignard reaction in THF at 60 °C according to Zhu *et al*.[60] With the applied reaction path no additional protection steps of the functional, pH sensitive group were necessary. Finally the corresponding boron-ethenyl-pegylated derivate **30** could be obtained in 60% yield as shown in Figure 21.

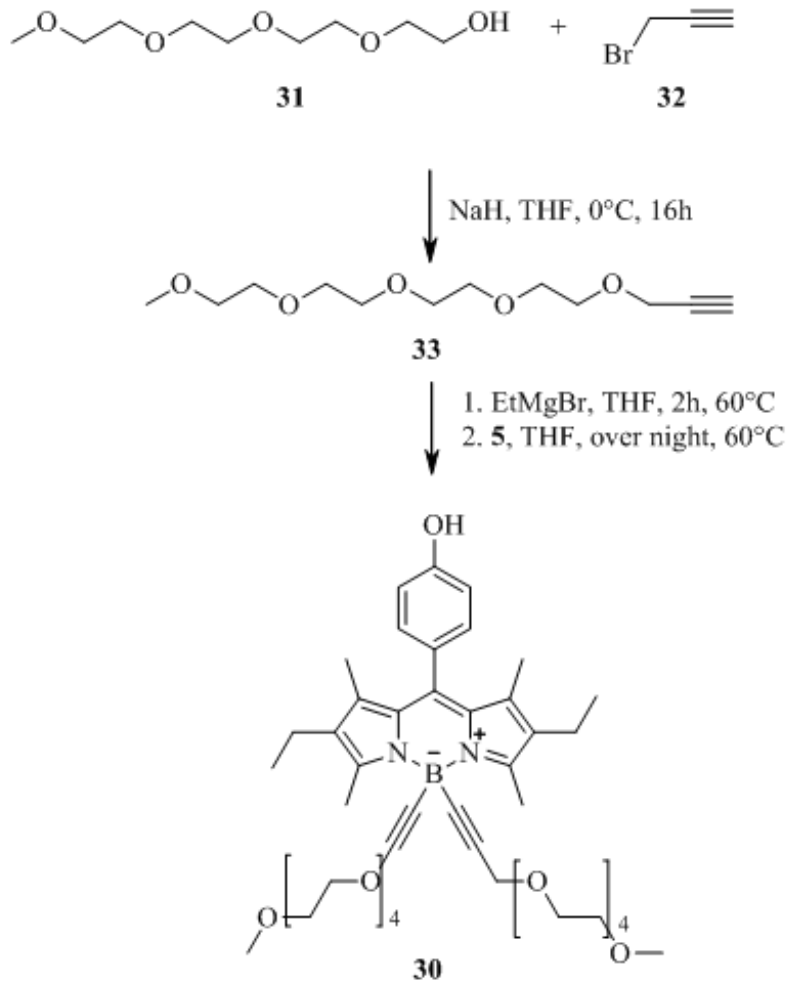

Figure 21 Synthetic route to the highly water-soluble BODIPY dye 30 bearing two tetra(ethylene glycol) methyl ether units at the 4,4'-position.

*Spectroscopic properties of **30***

The solubility of the obtained dye **30** could be significantly enhanced in water compared to **5** and it is also soluble in common solvents like MeCN (Figure 22, Table 6).

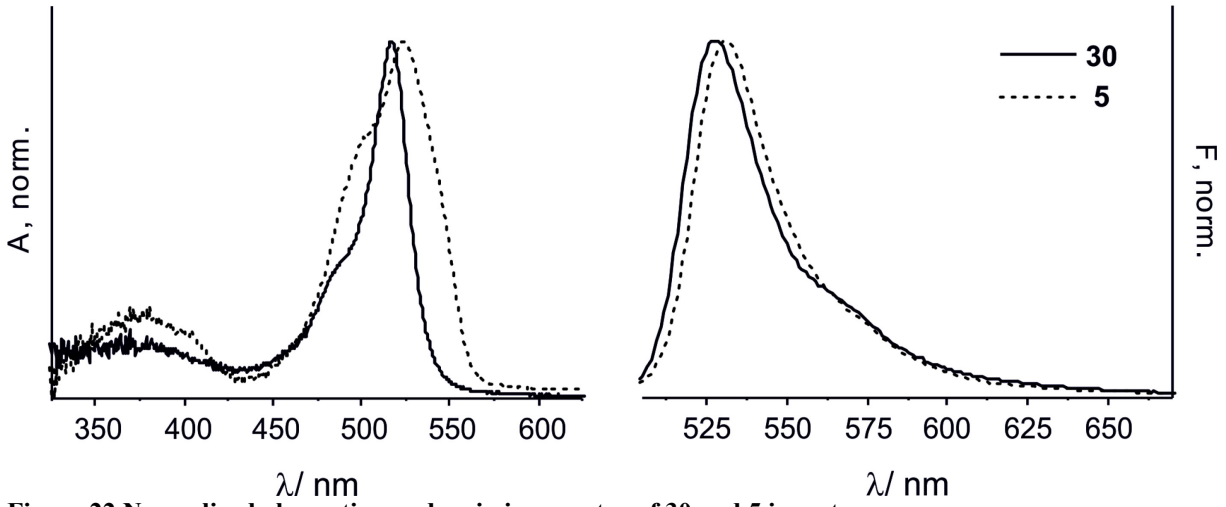

Figure 22 Normalized absorption and emission spectra of 30 and 5 in water.

Table 6 Spectroscopic data of 30 in selected solvents at 298K.

Compound	Solvent	λ_{abs} /nm	λ_{em} /nm	τ_f /ns
30	MeCN	517	526	n.d.
	H_2O/EtOH	518	527	4.72
	H_2O	517	527	3.42
5	MeCN	521	531	4.72
	H_2O/EtOH	523	532	5.57
	H_2O	523	532	2.67[a]

[a] Longest lifetime component of a multiexponential fit

The replacement of the fluorine atoms of **5** at the boron center of the BODIPY with propargyl-tetra(ethylene glycol)methylether subunits does not bring them in conjugation with the BODIPY core. The substitution causes only minor blue shifts of the absorption and emission maxima of **30** compared to the precursor **5**. These shifts may arise from decreased aggregation behavior of **30** in aqueous solution due to the bulky ethynyl substituents. In H_2O the absorption and fluorescence bands show no broadening due to aggregation compared to **5** in water which clearly revealed that the dye is well soluble in aqueous media. The fluorescence decay times of **30** in ethanolic aqueous solution and water show monoexponential decays and could be determined to be 4.72 ns and 3.42 ns, respectively.

These lifetimes correspond to the data of the parent dye **5** and lie between the values in ethanolic aqueous solution and water, where aggregation was observed ($^{a}\tau_{H2O}$ = 2.67 ns as longest lifetime of a multi-exponential fit).

*pH-dependent absorption and fluorescence spectroscopy of **30***

Similarly to **5**, BODIPY **30** is sensitive to the environmental pH and can be deprotonated in basic media (aq. KOH) as shown in Figure 23.

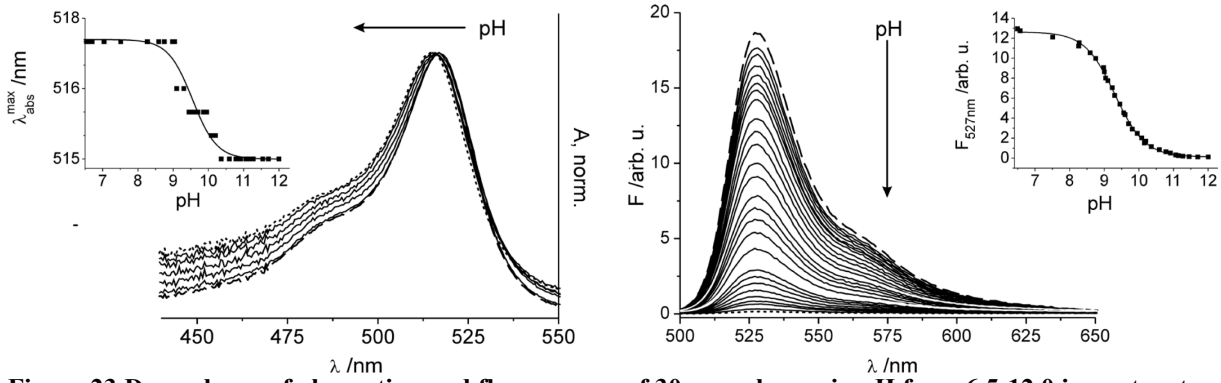

Figure 23 Dependence of absorption and fluorescence of 30 on a change in pH from 6.5-12.0 in neat water. Spectrum at pH 6.5 (dashed line), pH 12 (dotted line), intermediate steps (solid lines). Insets show the corresponding titration curves when plotting the shift of the absorption maximum (left) and the fluorescence intensity at the emission maximum right) as a function of pH.

The protonation constant of **30** was determined to be pK_A = 9.31 ± 0.01 in water by Boltzmann curve-fitting as a function of pH using the fluorescence intensity at 527 nm. Although the pK_A shifted 0.5 units compared to **5** the modification with two amphiphilic PEG moieties increases the solubility in water significantly while retaining the spectroscopic properties of the parent dye **5**.

*Application of **30** as pH indicator at the growth front of silica biomorphs*

Up to now there is no known water-soluble fluorescence dye for the highly basic pH range. Therefore the BODIPY dye **30** serves as suitable candidate to investigate basic pH changes in aqueous solution. In cooperation with the University of Konstanz, Kellermeier *et.al.* could show the versatility of the developed dye **30** through the growth process of "silica-carbonate biomorphs" (Figure 24 and 25). This material is an interesting model system to study the natural biomineralization processes which afford crystal frameworks of great diversity and utmost complexity of certain living forms like corals or seashells. [73, 74] Silica-biomorphs are complex crystal aggregates, which are formed through co-precipitation of barium carbonate in

silica-containing media using atmospheric CO_2 as a carbonate source at high pH values between 9.8 and 11.9.[75] That process finally yields biomimetic ultrastructures of uniform nanocrystals which occur especially at high pH values (Figure 24 and 25).

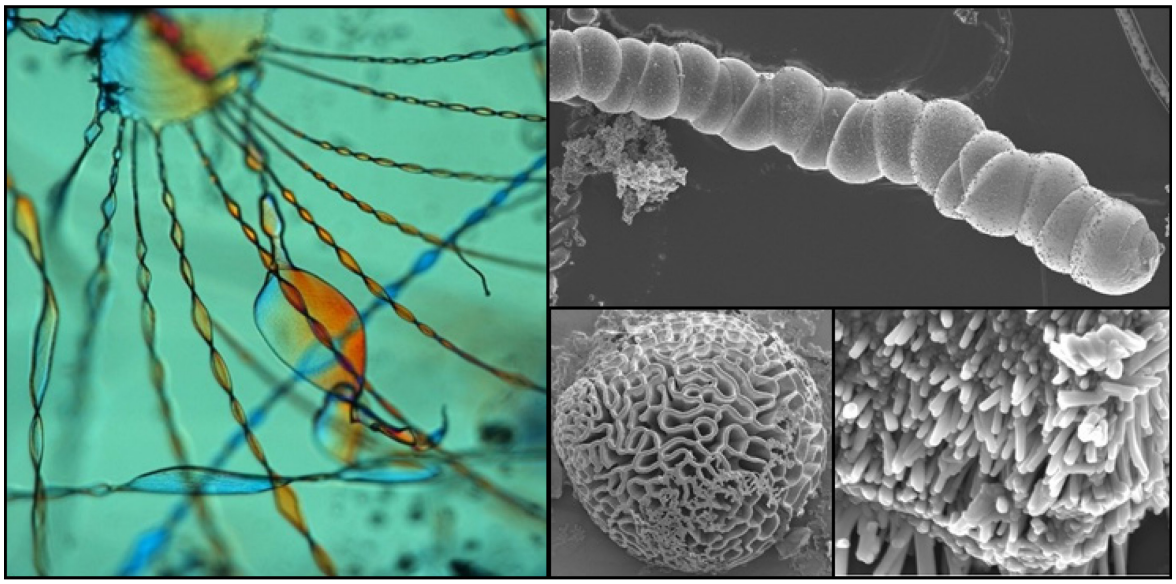

Figure 24 Morphologies obtained from synthesis of silica biomorphs, taken from ref[73].

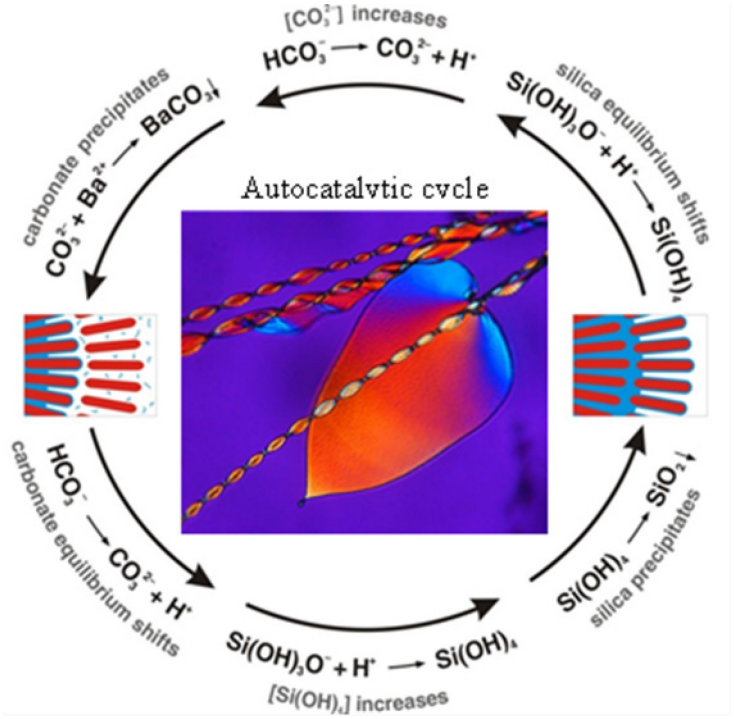

Figure 25 Co-precipitation of barium carbonate and silica through spontaneous self-assembly due to local pH variations taken from Kellermeier et al.

At the growth front of these nanocrystals a local pH gradient is expected. This can be proven by adding a solution of **30** during the growth process of the silica-carbonate biomorphs. The local decrease in pH upon carbonate growth in the aqueous bulk solution was shown by directly adding diluted dye solutions at the growth front visualizing the changes of the fluorescence intensity with a fluorescence microscope. As depicted in Figure 26 the bulk solution shows no fluorescence signal, indicating the non-fluorescent, deprotonated form of **30** at pH values around 11. At the growth front however the dye is highly fluorescent indicating a pH < 11.

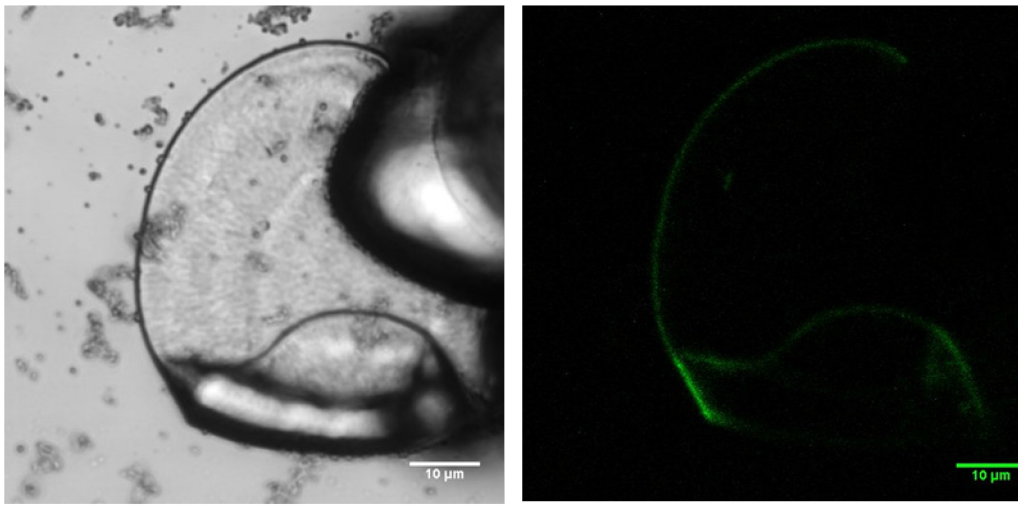

Figure 26 Visualization of the pH by compound 30 at the growth front of silica biomorphs by CLSM.

With that simple experiment the versatility of the water-soluble dye **30** could be illustrated. Additionally fluorescence lifetime imaging microscopy (FLIM) measurements would be helpful to discriminate if the change of the fluorescence intensity at the growth front solely arises from the change of pH or if this is a result of dye adsorption at the forming particle. For this setup monoexponential decay times will be expected for pH based signal changes and multiexponential decays for different states of adsorption as measured for BODIPY **5**.

2.3 Conclusion

First the development and characterization of a robust and reversible fluorescent pH sensing matrix coated onto a 3D epoxy polymer support for the alkaline pH range have been presented. The embedded pH indicator dye **5**, bearing a phenolic OH at the *para*-position of a *meso*-phenyl moiety attached to a BODIPY core, was synthesized through a simple one-pot synthesis procedure and shows high brightness independent of solvent polarity. The polymer material creates a microenvironment for the hydrophobic and poorly water-soluble dye which is comparable to an aqueous ethanolic solution, as shown by fluorescence lifetime measurements, rendering the composite matrix immune against detrimental effects of water on the optical properties of **5** such as dye aggregation and low solubility. The fluorescence intensity of the film in water also remains unaffected upon addition of various anions and a high electrolyte background. With this approach the application of a rather hydrophobic dye could be expanded to aqueous media and a dipstick sensor format for the alkaline region could be introduced where common pH electrodes show alkaline errors. Due to the gigantic change in brightness by more than four orders of magnitude, the response of the sensor material upon a change in pH is also visible to the naked eye and can be assessed conveniently by use of a cell phone camera.

Additionally the hydrogel concept could be extended to cover the majority of the pH range for a reversible broad-band pH indication. For this purpose a number of pH sensitive BODIPYs were synthesized with various amino- and phenol-substitution patterns at the 8-position of the BODIPY core and characterized by absorption and fluorescence spectroscopy regarding their suitability for an array arrangement.

To counteract the main drawback of poor aqueous solubility and to overcome the format limitation of the supporting material for the application of the presented BODIPY dyes a simple synthetic route was developed for transforming the parent pH-sensitive BODIPY into a highly water-soluble analogue. By tethering polyethylene glycol-chains at the boron center of the parent dye as water solubilization groups the conversion to a hydrophilic analogue without changing its spectroscopic properties could be achieved. For the first time the resulting compound was successfully applied to investigate pH variations at the growth front in biomineralization processes of barium-carbonate silica biomorphs.

3 Fluorescent Cellulose-Microparticles

The development of innovative nanomaterials with novel properties is a perpetual process in the area of material sciences and has attracted increasing interest for analytical applications in recent years. Especially micro- and nanoparticulate structures with their unique properties harbor tremendous potential and are at the leading edge of the rapidly developing field of nanotechnology. In the following chapter two interesting topics are combined: the unique porous structure and outstanding characteristics of encapsulated cellulose microparticles decorated with an amino-reactive BODIPY dye as fluorescent label to investigate the influence of the particles microenvironment on the photophysical properties of the dye. These results can be transferred to develop new particulate platforms for bioanalytical assays.

3.1 Introduction

With the increasing demand for biocompatible and sustainable natural materials, the popularity of cellulose based nanomaterials increased in the last few years.[76-78] Cellulose, first discovered and isolated by A. Payen in 1838,[79] is a polydisperse, linear homopolymer consisting of regio- and enantio-selective β-[1→4]-glycosidic linked *d*-glucose units as shown in Figure 27. It is the main structural component of plants and therefore the most abundant, renewable natural polymer in the biosphere. As a chemical raw material it is generally well-known and has been used in the form of fibers or derivatives[80, 81] for nearly 150 years for a wide spectrum of products and materials in daily life, e.g. as cellophane,[82] as food additive[83] and for wound treatment.[84]

The smallest native cellulose nanofibers are usually called "nanofibrillated cellulose".[85] Such fibers are obtained by cleavage of macroscopic cellulose fibers through mechanical shearing and high-pressure homogenization in combination with enzymatic hydrolysis. The products are nanocellulose hydrogels which can be further processed into powder by spray drying.[86] In contrast, acidic hydrolysis of native cellulose fibers commonly using sulphuric or hydrochloric acid results in rod-like, highly ordered, crystalline, and therefore less reactive, particles of nanocrystalline cellulose[87] or so called "cellulose nanowhiskers". For these particles, disordered or paracrystalline regions of the cellulose are preferentially hydrolyzed over crystalline regions, because the latter have a higher resistance to acid attack (Figure 27).[88-90] Their dimensions depend on the native cellulose source material, hydrolysis time and temperature.

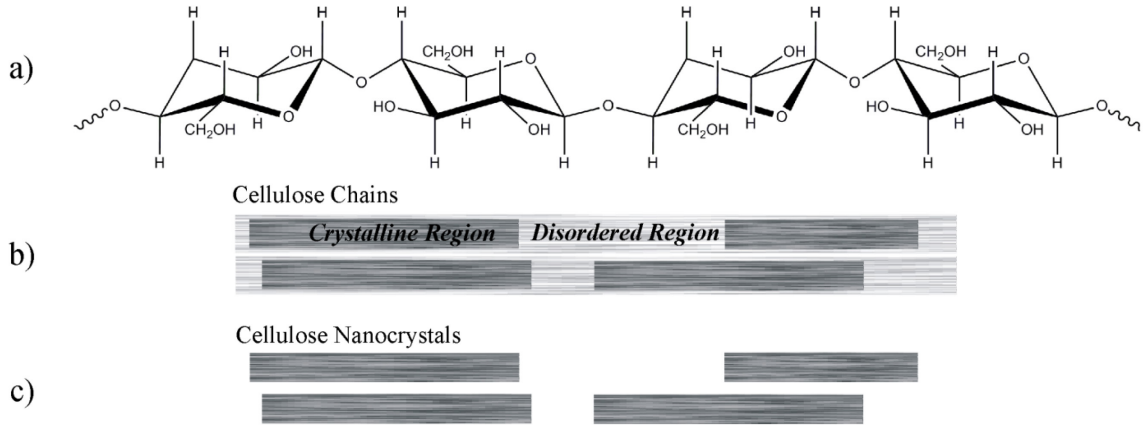

Figure 27 a) Molecular structure of cellulose repeating domains, b) cellulose microfibril with ordered (crystalline) and disordered (amorphous) regions, c) cellulose nanocrystals after acid hydrolysis.

To obtain micron-sized spherical porous nanofibrillated cellulose particles (NFCP) from microfibrillated cellulose (NFC) Martaniemi et al.[91] developed a simple method of spray-drying the NFC hydrogels.[92, 93] Compared to for instance mesoporous silica-based materials,

NFC particles have the unique advantage of bearing a variety of rather large pores and wrinkles within a matrix structure, which endows this natural material with a tremendous potential for bioanalytical applications. It is known that the efficiency of the immobilization of large biomolecules on particles and the quality of the final biochemically functionalized surface strongly depend on the functional group density and even more importantly, on the accessibility of the reactive groups on the surface.[94] The NFCPs unique porous structure offers a high specific surface associated with a high availability of binding sites. This may for instance lead to a reduction of fluorescence quenching effects of a potential fluorescent dye labelled biomolecule due to the minimization of possible steric hindrance in bioanalytical assays. Furthermore the influence of solvent molecules (e.g. in aqueous solution) on such a molecular label could be reduced due to the special microenvironment within the particles' pores.

Native NFCPs tend to swell in aqueous media due to their native hydroxyl groups on their outer and inner particle surface. This behavior consequently will be accompanied by a loss of their specific surface morphology. For a further application in aqueous media an encapsulation of these particles with a water-impermeable shell, retaining the native particle surface structure as well as offering relevant binding sites for biomolecules, e.g., amine groups, is thus crucial. Once encapsulated with a water-impermeable yet reactive shell, e.g., by using the well-known silane chemistry, it is important to assess the availability of the introduced reactive amine groups and to obtain information about the labelling density.

Although BODIPY dyes have up to now only been rarely used for the fluorescence labelling of surface species,[95, 96] the remarkable versatility of BODIPYs has sparked intense research on new modification strategies to be able to use BODIPYs with fine-tuned optical properties for such purposes as mentioned in chapter 2. During the past ten years, BODIPYs have received tremendous attention and are today widely used as biomolecule markers, fluorescent switches, chemosensors and laser dyes.[37, 38, 42, 44, 49, 97, 98] Moreover, several new strategies for their functionalization have recently been developed. For instance, a 3,5-dichloro-substituted BODIPY was first described by Dehaen and Boens.[56, 99] The halogenation of the BODIPY core is particularly interesting because the introduction of a halogen atom to the dipyrrin core facilitates further derivatization through nucleophilic aromatic substitution and palladium-catalyzed coupling reactions.[99, 100] Furthermore, the nature of the substituent strongly influences the photophysical properties of the BODIPY fluorophore. These features make the 3,5-dihalogen-substituted BODIPY systems very attractive, and their derivatives find already now many applications in the design of fluorescent probes.[100-103]

To assess the availability of the reactive amine groups and to obtain information about the labelling density on the particle surface after encapsulation, a coupling protocol was developed that relies on the active chloro groups in the 3,5-position of a fluorescent BODIPY label recently described.[95] The presented BODIPY **36** combines several advantages over previously reported compounds such as two amino-reactive chlorine moieties at the 3- and 5-position of the dipyrrin core that can undergo mono- or di-substitution reactions with nucleophiles under mild reaction conditions, an absorption band well within the excitation range of commercial fluorescence dyes, and a change in its absorption and fluorescence maxima as a consequence of chloro-substitution by amino groups, permitting to trace the successful labelling reaction.[104]

3.2 Results and Discussion

3.2.1 Synthesis and Characterization of the fluorescence label

*Synthesis of the amino-group reactive dye **36***

The most common approach to introduce functional groups at 3- and 5-positions of the BODIPY core involves the synthesis of appropriately substituted pyrroles, which in turn requires the often time-consuming synthesis of (photo)chemically rather labile pyrrole precursors. Recent synthetic developments in BODIPY chemistry thus focused on simpler methods such as the introduction of chloro substituents at the 3,5-positions and their subsequent nucleophilic substitution. The substitution reaction conditions can be adjusted in such a manner that either mono- or di-substitution occurs. Studies in solution showed that at RT only one chlorine atom is substituted. The reaction of both chlorine functionalities can be achieved under more drastic conditions, liked increased reaction temperature or addition of a base which is discussed in the following section. As shown in Figure 28, BODIPY **36** with two amino-reactive chlorine atoms could be obtained in a three-step synthesis, including chlorination prior to oxidation and complexation.[56, 104, 105] Separation of the intermediates from numerous side products after each step is advantageous over the common BODIPY one-step procedure.

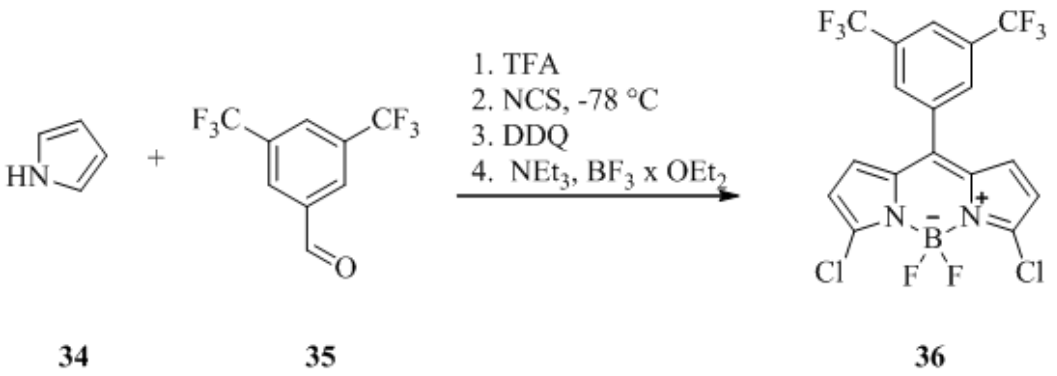

Figure 28 Synthesis of 36 via a 3-step route. Reagents and conditions: a) TFA; b) NCS, -78 °C; c) DDQ, NEt_3 followed by $BF_3 \times OEt_2$.

For comparative studies of the spectroscopic features of **36** the parent dyes **37** and **38** were also newly synthesized (Figure 29). The dyes **37** and **38** were obtained in 19 % and 45 % yield, respectively, by condensation of aldehyde **35** with 3-ethyl-2,4-dimethylpyrrole **4** (and 2,4-dimethylpyrrole **39**) in the presence of trifluoroacetic acid, followed by oxidation with p-chloranil, deprotonation with *N*,*N*-diisopropylethylamine (DIPEA) and complexation with $BF_3 \times OEt_2$. Use of the mild oxidation agent p-chloranil instead of the previously employed DDQ,[106-108] suppresses the formation of side products and leads to improved yields. Crystals suitable for X-ray structural analysis could be obtained from all compounds.

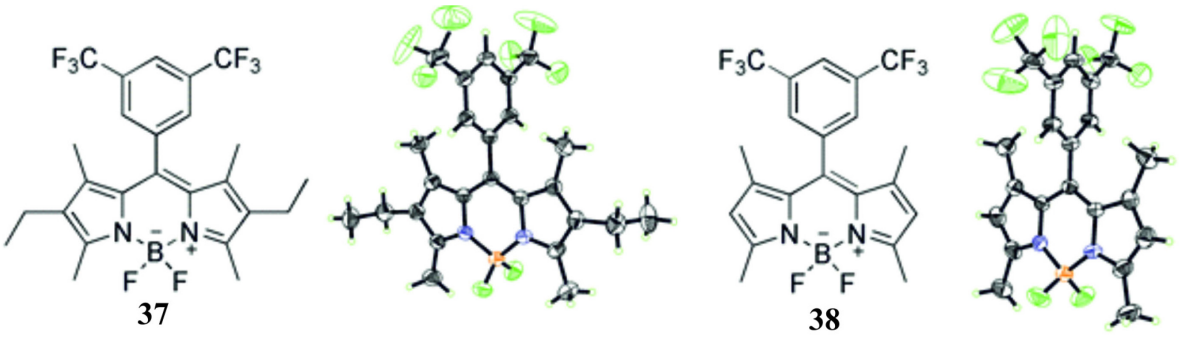

Figure 29 Chemical and crystal structure of parenting dyes 37 and 38.

*Optical spectroscopic properties of **36**, **37** and **38***

Table 7 and Figure 30 illustrate the spectroscopic features of **36** and the parent dyes **37** and **38**, investigated by absorption as well as steady-state and time-resolved fluorescence spectroscopy in various solvents with increasing polarity from hexane to methanol. For all dyes the maxima of the absorption and fluorescence spectra are essentially solvent independent, indicating the relatively small change in dipole moment between the ground and the excited state of these compounds.[109-112] BODIPYs **36**, **37**, **38** possess the characteristic spectroscopic features of BODIPYs including narrow absorption bands with an intense S_0–S_1

transition and a weak shoulder at the high-energy side due to the 0–1 vibrational transition, an emission band of mirror-image shape and mono-exponential fluorescence decay kinetics.[45, 109, 113, 114]

Table 7. Selected spectroscopic data of 36, 37, and 38 in various solvents at 298 K.

Compd	Solvent	λ_{abs} [nm]	λ_{em} [nm]	Φ_f	τ_f [ns]	$k_r \times 10^8$ [s^{-1}][d]	$k_{nr} \times 10^8$ [s^{-1}][d]
	Hex	521	536	0.12	0.70	1.7	12.6
	Bu_2O	521	536	0.16	0.98	1.9	8.6
	Tol	525	544	0.38	1.96	1.9	3.2
36	Et_2O	518	532	0.11	0.71	1.6	12.5
	THF	518	533	0.19	1.09	1.7	7.4
	MeCN	515[a]	530	0.19	1.25	1.5	6.5
	EtOH	518	534	0.14	0.88	1.6	9.8
	MeOH	516	532	0.14	0.93	1.5	9.3
	Hex	506	516	0.41	2.05	2.0	2.9
	Bu_2O	507	517	0.58	2.05	2.1	1.5
	Tol	510	521	0.88	3.59	2.5	0.3
38	Et_2O	505	514	0.47	2.41	1.9	1.8
	THF	506	517	0.68	3.08	2.2	1.0
	MeCN	503[b]	513	0.62	3.40	1.8	1.1
	EtOH	505	516	0.47	2.35	2.0	2.3
	MeOH	504	514	0.48	2.59	1.9	2.0
	Hex	531	544	0.59	4.13	1.4	1.0
	Bu_2O	531	543	0.66	4.54	1.5	0.8
	Tol	534	549	0.70	4.96	1.4	0.6
37	Et_2O	529	543	0.65	4.71	1.4	0.7
	THF	530	543	0.76	4.73	1.6	0.5
	MeCN	528[c]	541	0.72	5.29	1.4	0.5
	EtOH	530	545	0.66	4.41	1.5	0.8
	MeOH	529	543	0.65	4.85	1.3	0.7

[a] $\varepsilon_{\lambda abs}$ = 78230 ± 1550 M^{-1} cm^{-1}. [b] $\varepsilon_{\lambda abs}$ = 79470 ± 2040 M^{-1} cm^{-1}. [c] $\varepsilon_{\lambda abs}$ = 56500 ± 1080 M^{-1} cm^{-1}. [d] $k_r = \Phi_f \times \tau_f^{-1}$, $k_{nr} = (1 - \Phi_f) \times \tau_f^{-1}$. Measurement uncertainties: ± 0.01 × 108 s–1.

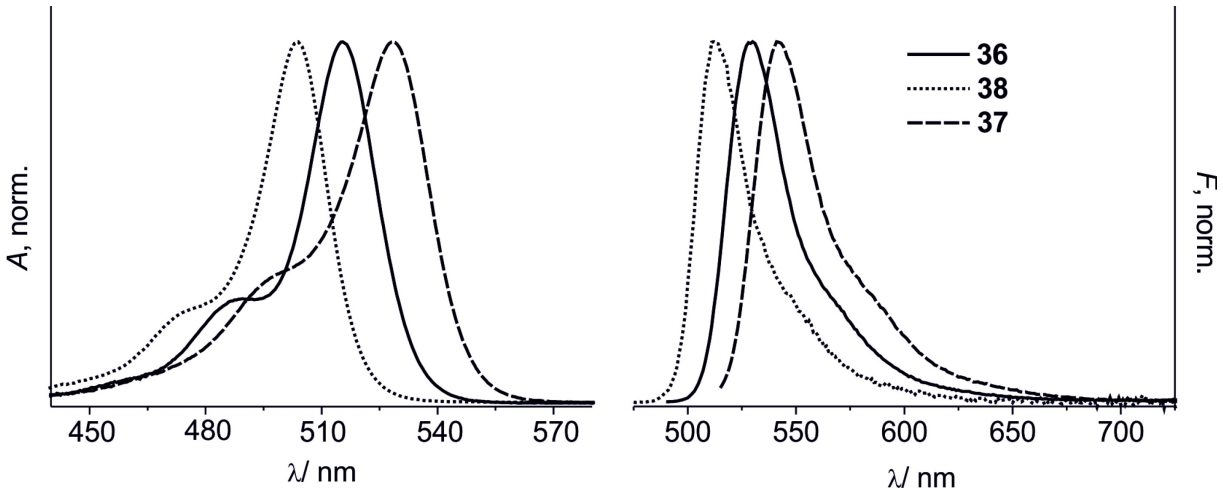

Figure 30 Normalized absorption and emission spectra of 36 (solid line), 37 (dashed line) and 38 (dotted line) in MeCN.

Electrostatic effects such as an enhanced dipole moment of the 1,3,5,7-tetramethyl compared with the 3,5-dimethyl and the 1,3,5,7-tetramethyl-2,6-diethyl BODIPY core lead to a more ionic nature of the 1,3,5,7-tetramethyl core and slightly blue-shifted absorption bands of **38** compared with **36** and **37**.[115] The fluorescence quantum yields (Φ_f) are strongly affected by the meso-substituent. Compared to the pentafluorophenyl substituted analogue with a Φ_f of virtually 1[95] in the case of **38** Φ_f varies around 0.6 in all solvents, a value that has also been found for the meso-phenyl analogue of **38**.[45] This can be explained by the stronger non-radiative decay due to the rotation of the trifluoromethyl groups and the strongly restricted rotation of the pentafluorophenyl moiety by the o-fluorine atoms in close neighborhood to the 1,7-methyl groups, as supported by the distinctly higher non-radiative decay rates (k_{nr}) of **38**. The crystal structures show almost orthogonal orientation of the phenyl substituent for all dyes bearing 1,7-methyl groups. In addition, also for the hexa-alkyl-substituted BODIPY core, an increased Φ_f is found when it is equipped with a pentafluorophenyl moiety (compare data of **37** in Table 7 and literature values of the meso-phenyl analogue,[45] which are very similar to those of **37**).[116]

For **36**, which does not possess the 1,7-alkyl substituents, the dihedral angle between the BODIPY core and the phenyl moiety amounts to only approximately 60° (estimated by single crystal structure analysis), indicating a partial conjugation of meso-substituent and BODIPY core and a higher rotational freedom. The first is supported by the bathochromic shift of the spectra compared with **38** and the latter by the lower fluorescence quantum yield of < 0.2, which is consistent with the higher k_{nr} value. Distinct bathochromic shifts were found for the absorption and emission maxima in toluene for all dyes which are caused by dispersive interactions between solvent and solute; toluene has a refractive index (n_D) close to 1.5, whereas all other solvents employed possess values of $1.3 < n_D < 1.4$.

*Reaction of **36** with amines in solution*

To assess to which extent the amino-group reactive model dye **36** will undergo a mono- or di-substitution reaction with amino groups on the cellulose particle surface and how the optical properties of the conjugated dye are influenced by the microenvironment of the particles' pores, control studies of **36** with various primary and secondary alkyl-amines were performed in solution prior to particle binding experiments (Figure 31).

It is known from related 3,5-dichloro-BODIPYs that the reaction conditions for a nucleophilic substitution of the chlorine atoms can be adjusted in such a manner that either mono- or di-substitution occurs.[102, 104] In addition, the mono- and di-substituted products can be distinguished by spectroscopic means, and both possess spectroscopic features still different from those of the unreacted di-chloro derivative.[117, 118] For this purpose **36** was incubated with the primary alkylamines 3-(aminopropyl) triethoxysilane **A** (APTES), which should be the prevalently reactive species on the particle surface, and with pentylamine **B** (PA) as a non-silylated analogue to investigate a possible influence of the silane groups.

Comparative studies were also performed by reacting **36** with secondary alkylamines diisopropylamine **C** (DiPrA) and diethylamine **D** (DEtA) to determine a possible influence of hydrogen-bonding interactions. The alkyl-amines served as both reactant and solvent. Furthermore the spectroscopic changes in the case of mono- and di-substitution of **36** in different microenvironments (organic and aqueous solution) were assessed.

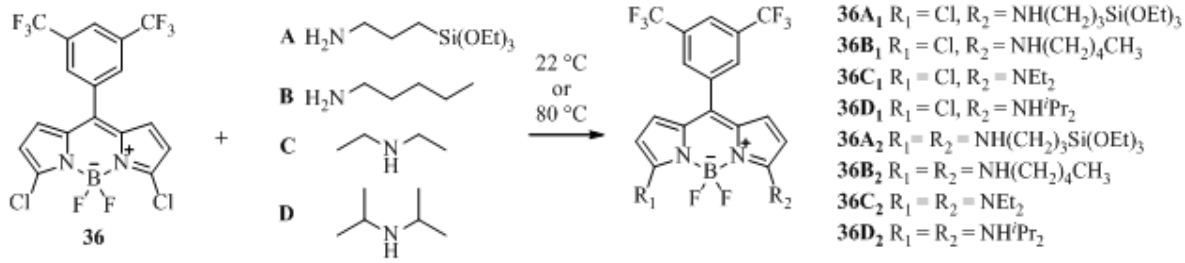

Figure 31 Reaction paths of 36 with primary and secondary alkylamines A-D at RT and 80 °C.

*Reaction of **36** with primary amines*

As shown in Figure 32 and Table 8, the reaction of **36** with the primary alkyl-amine APTES **A** at RT overnight leads to **36A$_1$** and results in a significant hypsochromic shift of the absorption band and a bathochromic shift and broadening of the emission band in MeCN (dotted line) compared to the native dye **36** in MeCN (solid line). In the absorption spectra a less intensive, second band appeared at λ_{abs} = 575 nm, which can be clearly attributed to the 3,5-di-aminated product **36A$_2$** of **36**, in accordance with the absorption maximum of the fully di-substituted product **36A$_2$** obtained at an elevated temperature of 80 °C (Table 8).

Incorporation of a second amino-alkyl moiety entails an additional red shift of 60 nm in λ_{abs} and 80 nm in λ_{em} relative to the dye **36** in MeCN (dashed line). Mono- and di-pentylamin conjugates **36B$_1$** and **36B$_2$** show very similar absorption and emission spectra as **36A$_1$** and **36A$_2$** in MeCN (not shown). This indicates that there is apparently no influence of the terminal silane groups of APTES **A** in organic solvents.

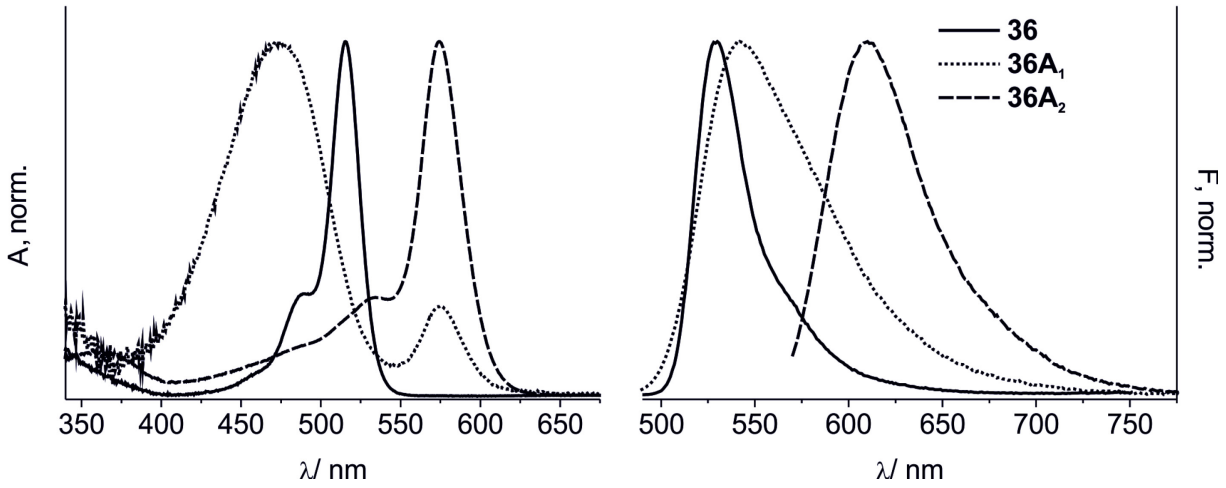

Figure 32 Normalized absorption and emission spectra of 36 (solid line), 36A$_1$ λ_{exc} = 470nm (dotted line) and 36A$_2$ λ_{exc} = 560nm (dashed line) in MeCN.

Table 8 Selected spectroscopic data of 36, 36A$_1$ and 36B$_1$ in various solvents at 298 K.

Sample	Solvent	λ_{abs} [nm] ^{RT}	λ_{abs} [nm] $^{80\,°C}$	λ_{em} [nm] ^{RT} λ_{exc}= 470nm	λ_{em} [nm] $^{80\,°C}$ λ_{exc}= 560nm
36	MeCN	515	-	530	-
36A$_1$	MeCN	474[a]	575	542	610
	EtOH:H_2O	479 [a]	578	545	618
	EG	480 [a]	580	546	617
	H_2O	497 [a]	588	547/641[b]	613
36B$_1$	MeCN	470 [a]	573	541	611
	EtOH:H_2O	475 [a]	578	544	619
	EG	478[a]	580	546	618
	H_2O	478 [a]	599	545	634[c]

[a] second absorption band indicates traces of the di-substituted product, [b] second emission band, [c] low fluorescence intensity.

Interestingly, in aqueous solution a broadening of the absorption band for mono- and di-substitution products **36A$_1$** and **36A$_2$** as well as **36B$_1$** and **36B$_2$** were observed compared to the corresponding MeCN solutions (Figure 33).

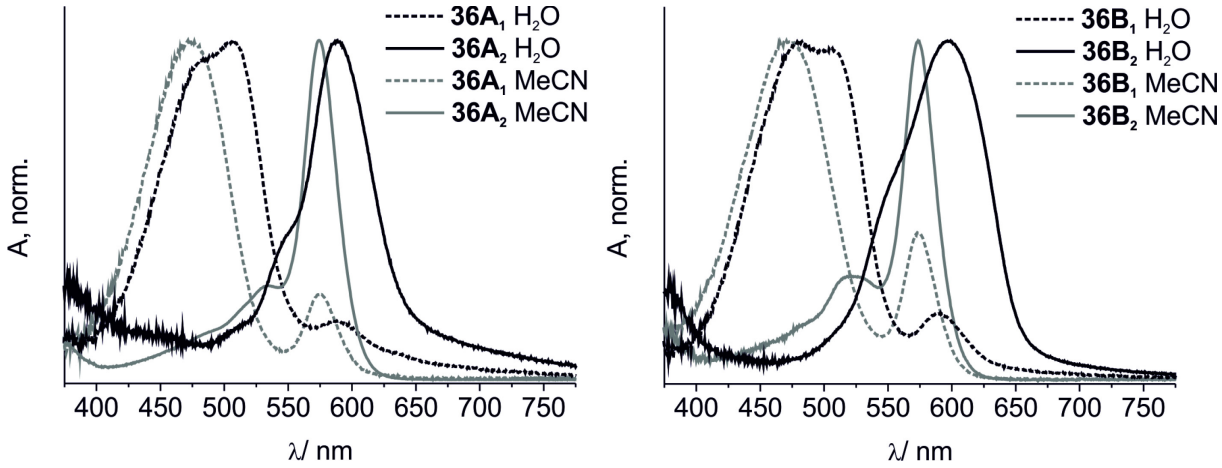

Figure 33 Normalized absorption spectra of $36A_1$ and $36A_2$ (left) and $36B_1$ and $36B_2$ (right) reaction products in water and MeCN, respectively.

Although the absorption and fluorescence maxima of mono- and di-substitution products **$36A_1$**, **$36A_2$** and **$36B_1$**, **$36B_2$** as non-silylated analogue are similar (Table 8), the emission intensity of the reaction products in aqueous solution differs from the MeCN solution (Figure 33).

With an excitation wavelength of 470 nm a remarkable fluorescence signal could be measured for **$36A_1$** in all investigated solvents. In contrast, **$36B_1$** shows a less intensive fluorescence band for the same optical density in aqueous solution. The enhanced fluorescence of **$36A_1$**and **$36A_2$** conjugates in water could be tentatively ascribed to the hydrophilic character of the presumably hydrolyzed ethoxy groups compared with the weak fluorescence of the hydrophobic **$36B_1$** and **$36B_2$**. Furthermore, a less intense second fluorescence band appeared at λ_{em} = 650 nm in aqueous solution for the mono-substituted products (Figure 33 and 34). The observed effects in water can be attributed to the moderate solubility of the hydrophobic reaction-products, accompanied by the tendency for non-fluorescent dimer formation, with micro-solvation effects being possibly also involved (see also chapter 2).

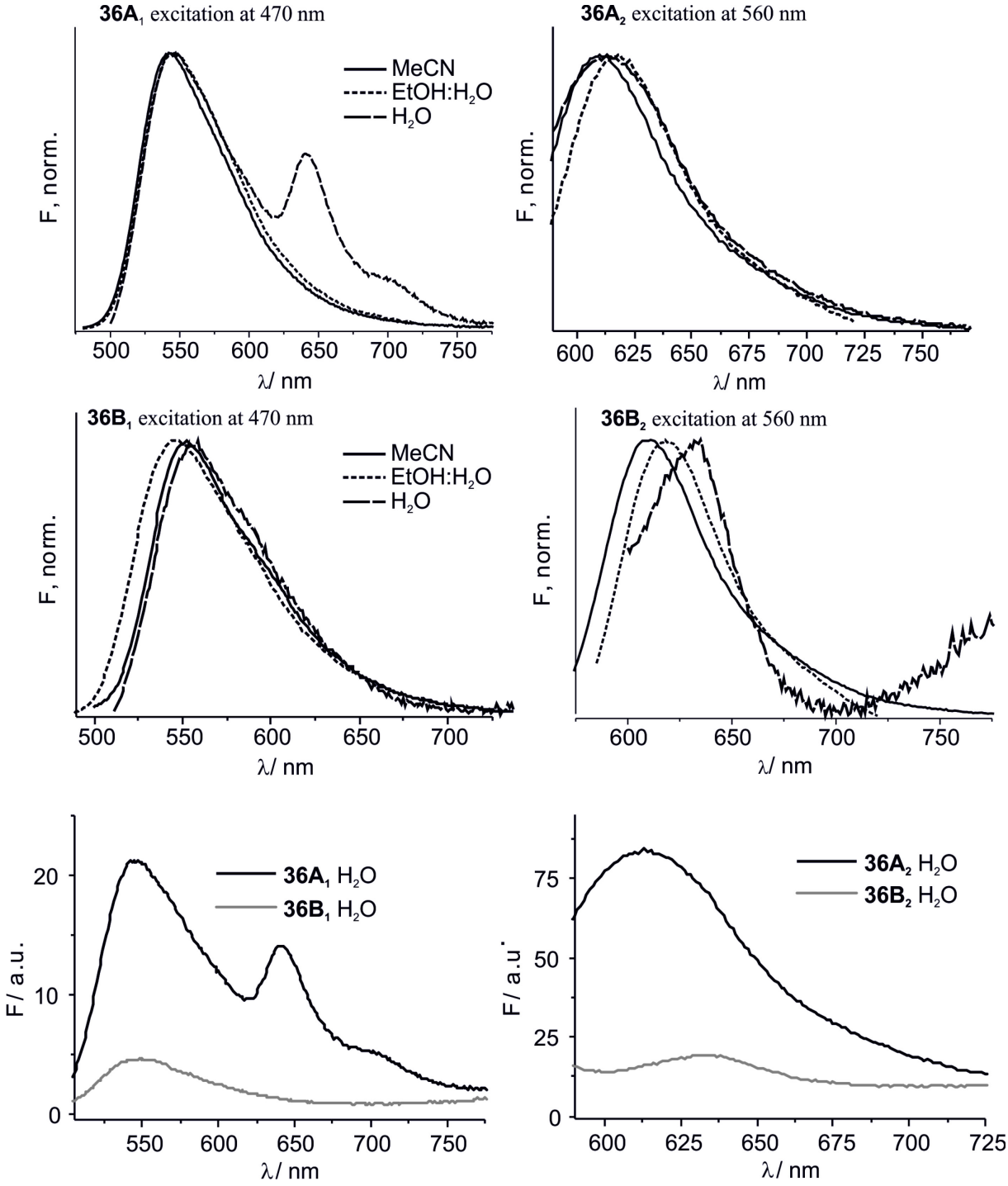

Figure 34 Top and middle: normalized fluorescence spectra of $36A_1$ and $36B_1$ (λ_{exc} = 470 nm) and $36A_2$ and $36B_2$ (λ_{exc} = 560 nm), bottom: Comparison of the fluorescence intensities of the species in water.

For the mono-substituted compounds **$36A_1$** and **$36B_1$** the emission of **$36A_1$** is distinctively brighter in water (cf. fluorescence spectra for matching optical densities in Figure 33) also suggests that the behavior in the excited state differs from that of **$36B_1$**. Presumably the more hydrophobic **$36B_1$** forms loose and disordered dimers which are known to be weakly or non-emissive.[50, 51]

Influence of dye concentration

To investigate the tendency to form dimers, oligomers or larger aggregates in aqueous solution the mono-aminated product of **36B$_1$** was used, because the onset of aggregation should be reached already at lower concentrations and to exclude any influence or possible condensation of the silane groups of **36A$_1$** conjugates at higher concentrations.

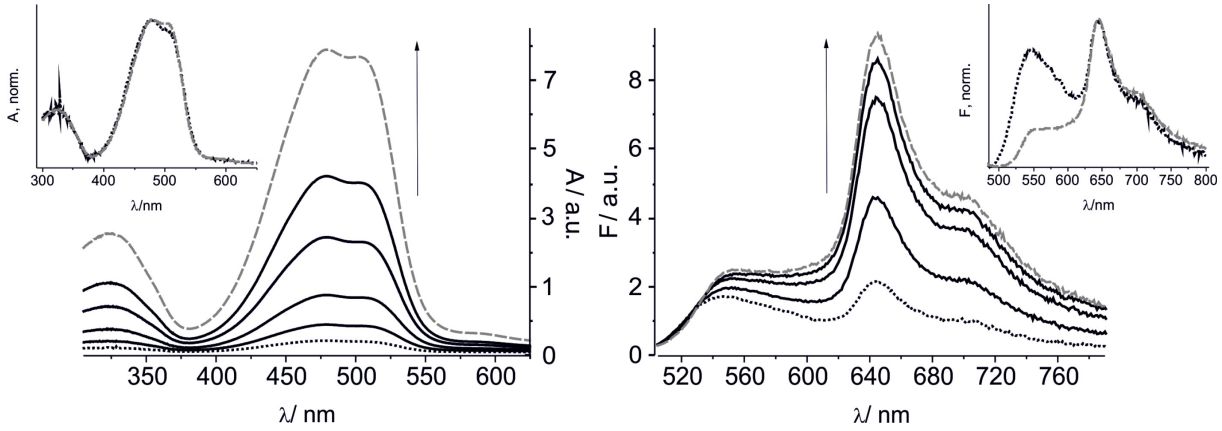

Figure 35 Absorption (left) and emission (λ_{exc} = 470 nm) of 36B$_1$ in aqueous solution at different concentrations (1.6 µM-dotted line, intermediate steps-solid lines, 24.4 µM-dashed-line). Insets show the corresponding normalized absorption and emission spectra at lowest and highest concentration, respectively.

The experiments have been performed with 1.6 µM to 24.4 µM solutions prepared from acetonitrile stock-solutions of **36B$_1$** (c = 4.1 mM) in water. A small percentage (0.04 - 0.60 %) of MeCN was thus present in the final sample solution, which corresponds to the small amount of MeCN stock solution that had to be employed to circumvent any dissolution errors by direct weighing into water.

Figure 35 shows that upon gradual increase of the dye concentration in aqueous solution, the shape and maxima of the absorption spectra did not change. Only the intensity of the shoulder at λ_{abs} = 515 nm increased slightly. The effect of an increase of dye concentration mainly occurs in emission. The structure of the emission band changed dramatically, the intensity of the emission band at ca. λ_{em} = 650 nm strongly increasing up to a dye concentration of 12.3 µM compared to the main band. A further increase in dye concentration did not change the band ratio significantly (Figure 36, $I_{560/650nm}$ vs. concentration). When recorded in the anomalous long-wavelength band, the excitation spectra (λ_{em} = 705 nm, λ_{exc} = 200-670 nm) and the absorption spectra show a good overlap. Compared with the strong absorbance of the di-substitution product in the 550-650 nm region the absence of such a dominant band in the fluorescence excitation spectra suggests that the red-shifted emission bands arises from excimers.[119]

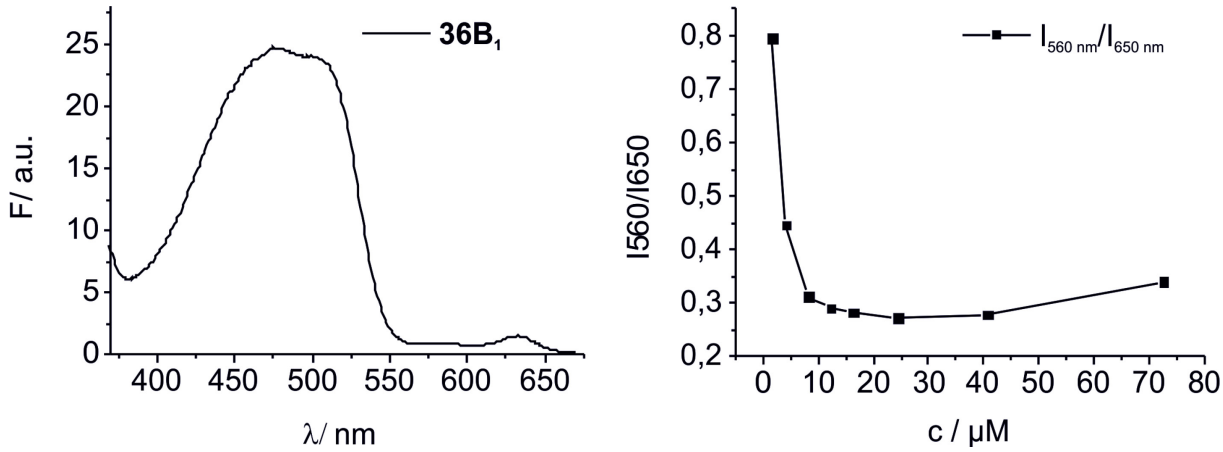

Figure 36 Excitation spectra of $36B_1$ (left) in H_2O and ratio of emission maxima at 560 and 650 nm (right).

*Reaction of **36** with secondary amines*

The reactions of primary amines with **36** resulted in secondary amine-dye conjugates possessing the NH-motif that is known to be an excellent partner in intra- and intermolecular hydrogen bonding interactions in solution. To investigate the influence of potential hydrogen bonding effects on the spectral properties of the dye-conjugates, the secondary alkylamines DEtA **C** and DiPrA **D** were incubated with **36** at RT and 80 °C, respectively. Under these conditions tertiary amine-dye conjugates should be obtained for which hydrogen bonding is aggravated because the nitrogen atom can only act as an H-bond acceptor, which is even sterically shielded in the case of DiPrA. In addition, it has to be kept in mind that the change from –NHR (with R = alkyl) to $–NEt_2$ and $–N^iPr_2$ is accompanied by a certain increase in electron donating strength of the amino substituent as reflected by the Hammett constant of theses amines.[120]

As can be deducted from Table 9, the absorption and emission maxima of mono-substituted $\mathbf{36C_1}$ and $\mathbf{36D_1}$ conjugates are comparable to those of the mono-substitution products of **36** with the primary amines APTES **A** ($\mathbf{36A_1}$) and PA **B** ($\mathbf{36B_1}$).

Table 9 Selected spectroscopic data of 36, 36C$_1$, 36D$_1$ in various solvents at 298 K.

Sample	Solvent	λ_{abs} [nm] ^{RT}	λ_{abs} [nm]$^{80\,°C}$	λ_{em} [nm] ^{RT} λ_{exc}= 470nm	λ_{em} [nm] $^{80\,°C}$ λ_{exc}= 560nm
36	MeCN	515	-	530	-
36C$_1$	MeCN	470[a]	543/581[b]	545[c]	637
	EtOH:H$_2$O	475[a]	535/582[b]	545[c]	649
	EG	478[a]	549/585[b]	556[c]	644
	H$_2$O	473[a]	549/595[b]	546	644
36D$_1$	MeCN	473[a]	573[d]	543	608[e]
	EtOH:H$_2$O	476[a]	576[d]	545	n.d.
	EG	478	577[d]	546	611[e]
	H$_2$O	494	586[d]	547	614[e]

[a] additional second absorption band indicates traces of the di-substituted product, [b] maximum of pronounced shoulder corresponding to *a*, [c] additional second emission band (di-substituted product), [d] almost complete destruction of the BODIPY structure, [e] weak emission (λ_{exc}= 560nm).

In MeCN and EtOH–H$_2$O, the absorption maxima are located at λ_{abs} = 470-475 nm and emission maxima are centered in the range of λ_{em} = 543-545 nm (λ_{exc} = 470nm). Notably in water **36C$_1$** is well dissolved, showing only a minor broadening of the absorption and emission band compared to the organic solvents with a less intense shoulder (Figure 37 and Figure 38). For **36D$_1$** in water the absorption maximum is slightly bathochromically shifted (λ_{abs} = 480nm) compared to MeCN due to the bulky, hydrophobic *i*-propyl-groups, showing a similar band structure like the primary amine-conjugates **36A$_1$** and **36B$_1$**.

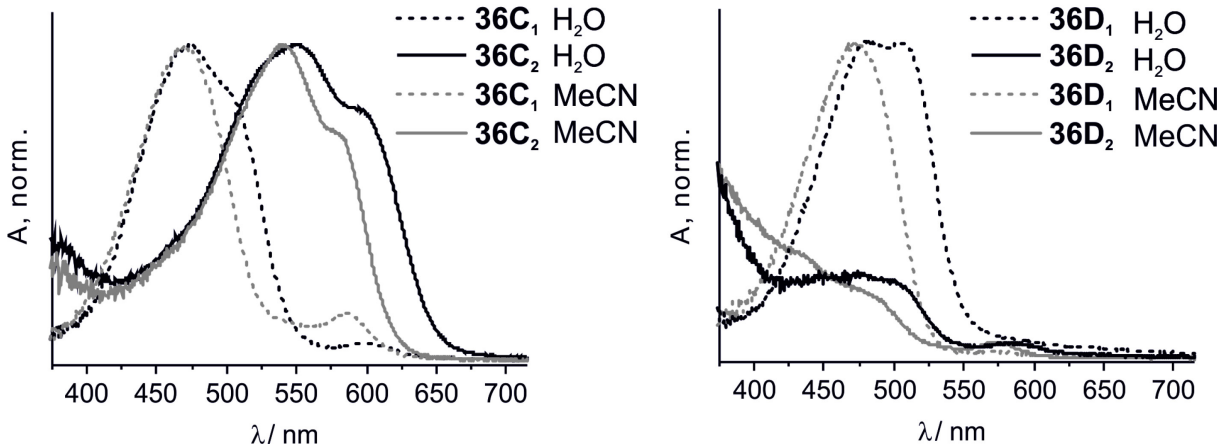

Figure 37 Normalized absorption spectra of 36C$_1$ and 36C$_2$ (left) and 36D$_1$ and 36D$_2$ (right) in water and MeCN, respectively.

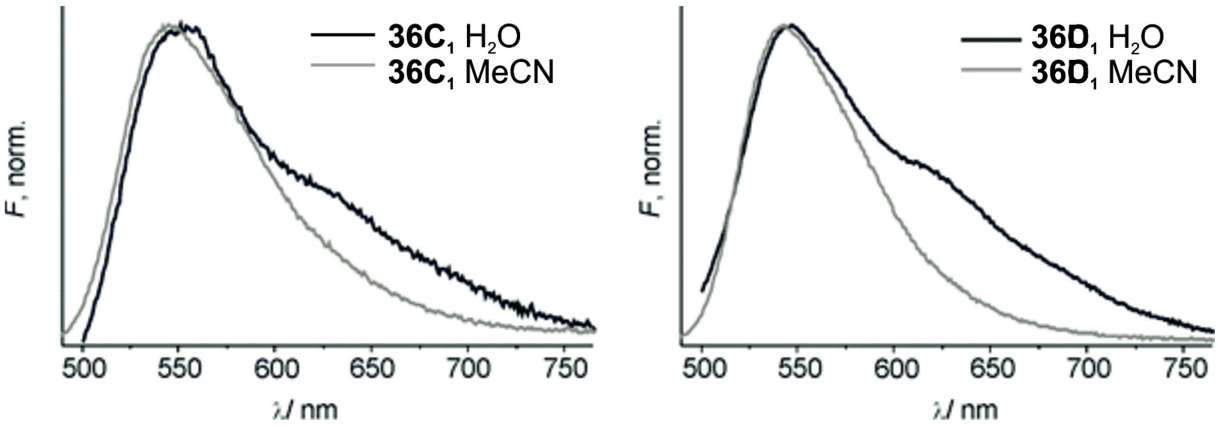

Figure 38 Normalized emission spectra of $36C_1$ (left) and $36D_1$ (right) in water and MeCN, respectively (λ_{exc} = 470 nm).

The shift of the emission band in water, showing a less pronounced shoulder, is minor compared to MeCN. For both, the reactions of **36** with the secondary amines **C** and **D** at RT, di-substitution occurs partly as indicated by weak absorption bands located at λ_{abs} = 530-650 nm, depending on the solvent used for the measurement (Figure 38).

The 3,5-aminated reaction products of **36** with **C** could be obtained at 80 °C (Figure 39). Interestingly, the di-substituted conjugate **$36C_2$** shows a very broad absorption band in the 450-650 nm region in all investigated solvents (Figure 37) which is in contrast to the narrow bands of **$36B_2$** and especially **$36A_2$** conjugates. With an excitation wavelength of 560 nm a bright fluorescence signal could be measured for **$36C_2$** in MeCN and EtOH–H_2O solution. In contrast **$36C_2$** shows no emission in water. With excitation at λ_{exc} = 600 nm no emission signal could be observed at all. The reaction of **36** with **D** did not result in an appreciable amount of **$36D_2$** conjugate (Figure 39). Only strongly reduced absorption bands in the region of **$36D_2$** were found which point to a decomposition of the BODIPY core upon reaction with the bulky amine under the harsher conditions employed.

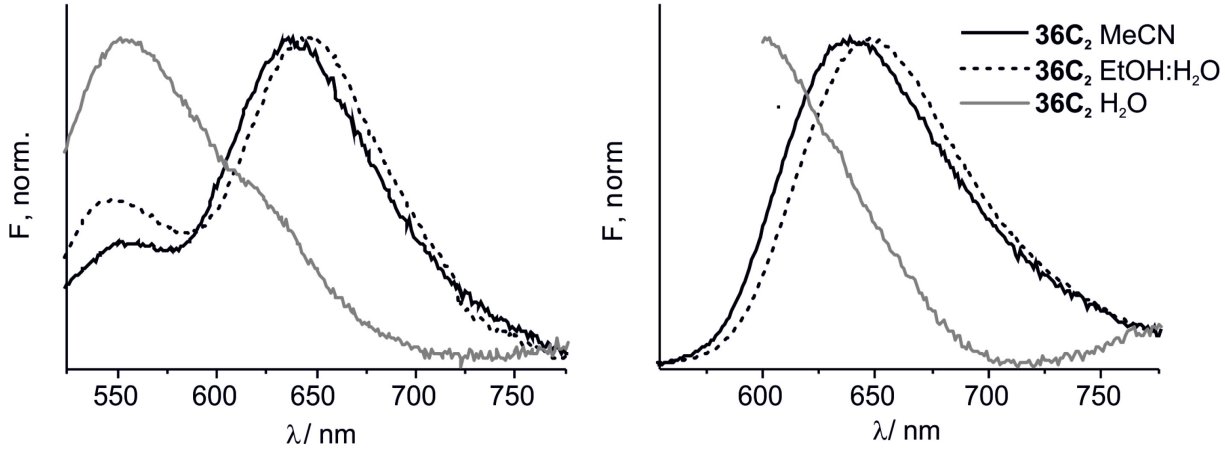

Figure 39 Normalized fluorescence spectra of $36C_2$ in various solvents, left: λ_{exc} = 470 nm, right: λ_{exc} = 560 nm.

For the correlation of the absorption maxima of all dye conjugates with common solvent parameters it is important to consider the solvent polarity as well as the solvent hydrogen-bonding donation ability which preferably could be described by Dimroth's $E_T(N)$-, $E_T(30)$[121]- or Catalan's SPP^N - scale.[122, 123] Regarding these scales the absorption maxima of the dye-conjugates show a typical behavior for organic dyes bearing alkylated (or partly alkylated) amino groups in the used solvents, i.e., the absorption shifts are neither entirely due to solvent polarity nor hydrogen bonding interactions. Correlations of the data with classical[122-124] or quantum mechanical solvent polarity models[125-128] as well as with hydrogen bond parameters[129, 130] are significantly worse.

The studies in solution have shown that at RT not only one chlorine atom is substituted by the appropriate amino compound but also the second chlorine atom reacts to some degree via nucleophilic substitution when the basic reaction partner serves as the solvent. At 80 °C, the substitution of both chlorine functionalities is accomplished. Heating at reflux or long reaction times of several days can be avoided in this way.[102]

Based on the extensive spectroscopic investigations of **36** and corresponding reaction-products with primary- and secondary amines presumably the examined properties could be transferred when **36** is covalently attached to surface-aminogroups on the NFCPs surface. The position of the absorption and emission bands could give information about the dyes microenvironment within the particle pores.

3.2.2 Particle encapsulation and swelling behavior

Because of native hydroxyl groups on their outer and inner surface, the NFCPs tend to swell in aqueous media and consequently lose their specific morphology. For a further application in aqueous media an encapsulation of these unique particles with a water-impermeable shell, retaining the native particle surface structure as well as offering relevant binding sites, is thus crucial. To satisfy both demands, common functional trialkoxysilanes $R\text{-}Si(OR')_3$ coupling agents which are widely used for the functionalization of silica-based systems, can principally be applied.[131, 132] The alkoxy groups OR' enable the silane to be anchored covalently to the hydroxyl group of the surface and the appropriate organic functionality of the silane, e.g. an amino group provides suitable anchors for further covalent chemical modification for specific bioanalytical applications.[133, 134] To prevent the swelling of the NFCPs during the encapsulation process and to minimize the build-up of three-dimensional siloxane networks to retain the native particle morphology, anhydrous organic solvents should be used.[135-137] The hydrolysis of the alkoxy groups of the silane lead to the formation of silanols through self-

condensation reactions. The silanol then reacts with the hydroxyl group of the cellulose fiber, forming stable covalent bonds.[138] Although the use of silane coupling agents is a very well-known practice for cellulose-based composites, to the best of our knowledge, the effect of silane modifications of NFC particles has previously never been investigated.

*Functionalization with 3-(aminopropyl) triethoxysilane **A***

In a first attempt, various amounts of APTES **A** were used for the particle encapsulation. With an increasing amount of **A** (**CPA1**-**CPA4**), the amount of amino-functionalities offered on the particle surface can be enhanced. After washing and drying of the particles, the functionalized particles were incubated for 30 min with water to investigate the swelling behavior after the silanization process. The aminosilane-modified NFCPs **CPA** showed a reduced tendency for swelling after the incubation with water compared to the native particles as depicted in Figure 40. But the size expansion of particle samples **CPA1**-**CPA4** is nearly the same (not shown due to similarity between the samples), despite the fact that the amount of **A** was increased from 6.45×10^{-4} to 2.18×10^{-3} mol (0.43–1.46 mol L^{-1}) in a solution of 100 mg particles per 1.5 mL toluene. Although the extent of swelling of the aminosilane-modified particles was reduced compared to the native particles, the silane network could not protect the particle surface sufficiently from water. This result may be caused by the hydrophilic character of the amino groups on the particle surface. The formation of hydrogen bonds between water molecules and amino groups possibly facilitate the permeation of water molecules through the loose silane network. Therefore the particles partly lost their specific surface porosity in water compared to the dried state.

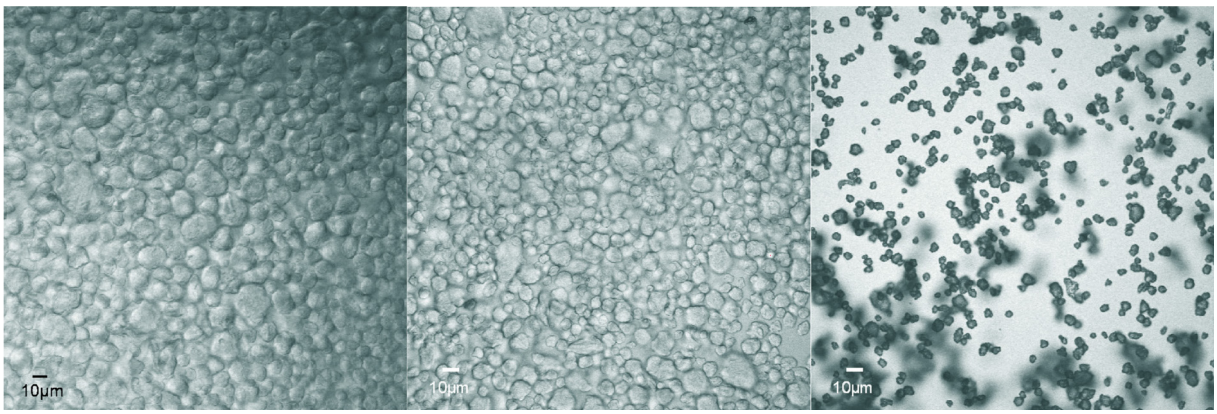

Figure 40 CLSM images of native NFCPs (left) and aminosilane-encapsulated particles CPA3 (middle) after incubation in water for 30min, dry NFCPs (right).

*Functionalization with γ- methacryloxypropyl trimethoxysilane **M***

According to previously reported findings a chemical modification with γ-methacryloxypropyl trimethoxysilane **M**,[139] a silane offering a more hydrophobic chain and thus potentially protecting the particle surface better from water, was attempted. The reaction of NFCPs with **M** in dry toluene led to stable particles bearing hydrophobic methacryloxypropyl moieties, presumably oriented toward the water–particle interface. The native fine-structured particle morphology could be retained even after the particle washing and drying procedure. ESEM images of the **M**-encapsulated particles (Figure 41) are similar in shape and size as the native NFCPs (see Cryo-ESEM[91]) - irregular, roughly spherical particles with diameters around 5 to 10 µm. The native, unfunctionalized NFCPs could not be measured with ESEM because of the reduced adhesion of the particles under the measuring conditions (vacuum).

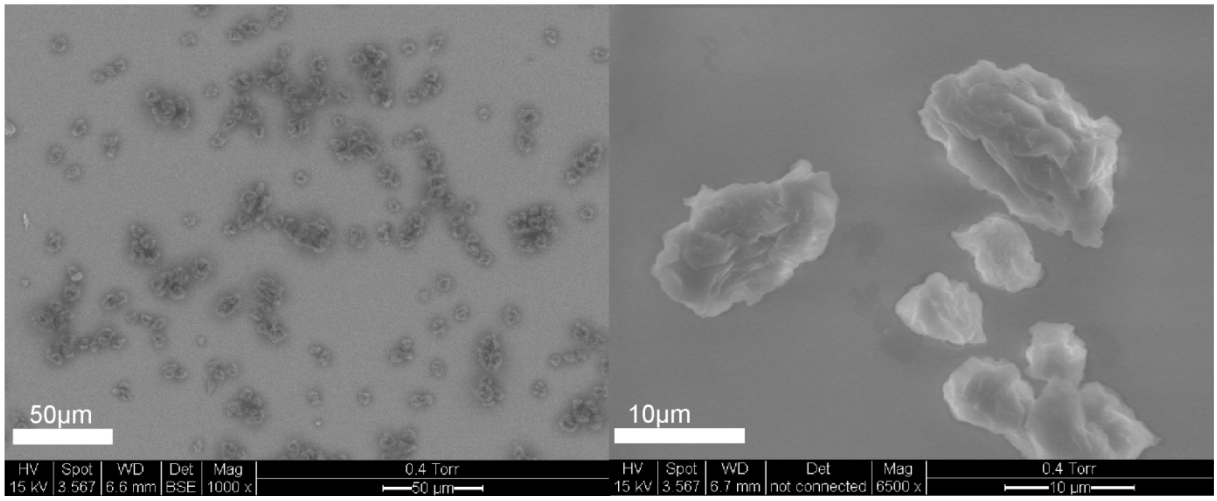

Figure 41 ESEM images of NFCPs treated with γ-methacryloxypropyl trimethoxysilane.

*Functionalization with **M** and **A***

To additionally include suitable functional groups, the initial amount of γ- methacryloxypropyl trimethoxysilane **M** was blended with 3-(aminopropyl)triethoxysilane **A** in different molar ratios.[140, 141] The amount of **A** used in the functionalization procedures was chosen in such a way that an appropriate amino-functionalization of the particle surface was reached and the hydrophobic methacrylate network still prevented the particles from swelling. As shown by confocal laser scanning microscopy (CLSM) most of the **AM** functionalized particles only slightly absorb water in comparison to the native, non-functionalized particles (Figure 40 and 42). In the case of a

high amount of **M** (particle fraction **CPAM4**), yielding more hydrophobic NP, the swelling is suppressed in general compared to particle species **CPAM1**-**CPAM3**. Having a closer look to the particle edges, the difference is especially obvious (Figure 42). A slight swelling indeed caused a less wrinkled appearance of the particles borders but compared with the virtually bubble-shaped, fully swollen native particles the porous network is largely retained in the **CPAM** samples (compared to Figure 40). Although the particles showed a minor swelling behavior in the different samples which could presumably be caused by the coating process itself, the favored wrinkled, porous particle morphology remained in all samples and the protection against water was significantly improved.

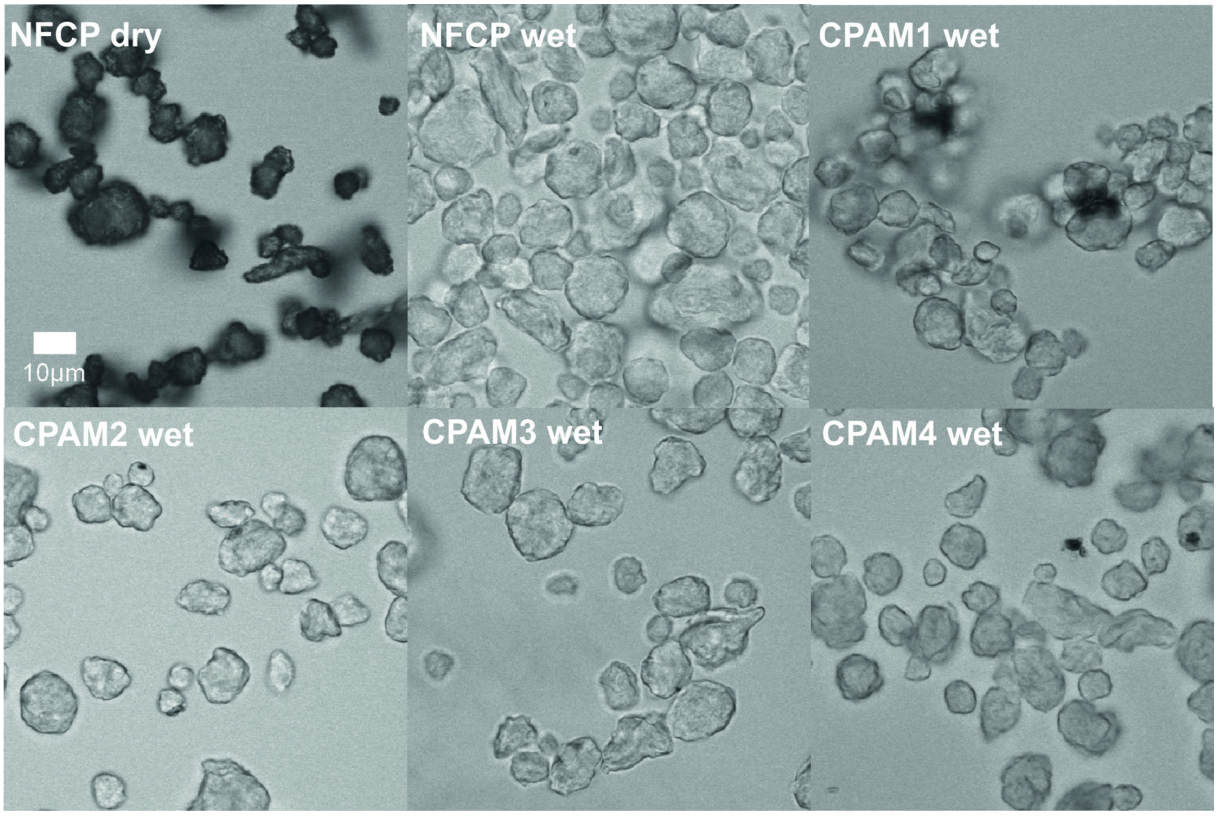

Figure 42 CLSM images of dry and wet, native NFCPs compared to MA functionalized NFCPs after 30 min in aqueous solution.

3.2.3 Labelling of encapsulated NFCPs with **36**

To get more information about the suitable amino-group density on the particle surface regarding further applications and to get more insight on the microenvironment within the particle pores and wrinkles after the encapsulation and functionalization process, the particles **CPAM1-CPAM4** were incubated for 24 h with the same concentrated ($c = 6.13 \times 10^{-3}$ M) solution of the amino-reactive model dye **36** in toluene while shaking in a thermomixer at RT (see also 3.2.1). The particles were washed until no fluorescence could be detected in the

washing solution and dried under vacuum. To investigate the spectroscopic features, the particles were suspended in water at a final particle concentration of 0.08 mg ml^{-1}.

One of the main questions was to assess in particular how the spectroscopic properties of the linked fluorophore will be affected by the microenvironment. In general dyes are very suitable reporter molecules to obtain more information on functional small molecules in confirmed media such as porous micro- or nanoparticles, because changes in the following features compared with the bulk media can determine their spectroscopic behavior.

(i) Adsorption of the dyes to the surface or surface functional groups usually leads to unspecific broadening of absorption and fluorescence bands, commonly accompanied by bathochromic shifts and fluorescence quenching.

(ii) Steric confinement or a reduction in mobility, for instance, because of intercalation into polymer strands or "pockets" can entail narrowed, often hypsochromically shifted spectra and an increased fluorescence.

(iii) An altered polarity of the solvent in the inner particle's interface, i.e., the functionalized pores compared with the solvent bulk can lead to mostly blue-shifted spectra and the concomitant, polarity-driven fluorescence intensity changes.

(iv) A locally high concentration of dyes in small inner voids can lead to a promotion of aggregation effects, entailing diverse absorption and fluorescence responses that depend on the dye employed and the type of aggregate the dye can form.

(v) Finally, if the dye is not prone to undergo aggregation in the solvent employed, a locally high concentration can also lead to excimer formation, i.e., unchanged absorption behavior but the appearance of a broad and red-shifted excimer band.

Keeping the spectroscopic properties of **36**-amino conjugates of the previous section 3.2.1 in mind, **36** seems to be a good candidate for these purposes. Accordingly, the encapsulated, fluorescence labelled cellulose particles (**CPAM'**) were characterized by absorption and fluorescence spectroscopy in aqueous solution as well as with CLSM to get additionally information about the distribution of the fluorescent label over the particle's inner and outer surface.

As shown in Figure 43, in aqueous solution (and also in EtOH–H_2O solution, Figure 44) with excitation at λ_{exc} = 470 nm particles **CPAM4'** (lowest amount of amino group density and therefor lowest amount of coupled dye) showed a distinct, bright emission band in the range typical for mono-amino-substituted **36** at around λ_{em} = 550 nm, revealing the dyes' existence primarily as conjugated molecules covalently attached through a single substitution site. For this NFCP species with the lowest amino group density, the typical absorption band

of the dye is least discernible compared with **CPAM1'- CPAM3'** in Figure 43, left, suggesting the corresponding lowest degree of secondary functionalization.

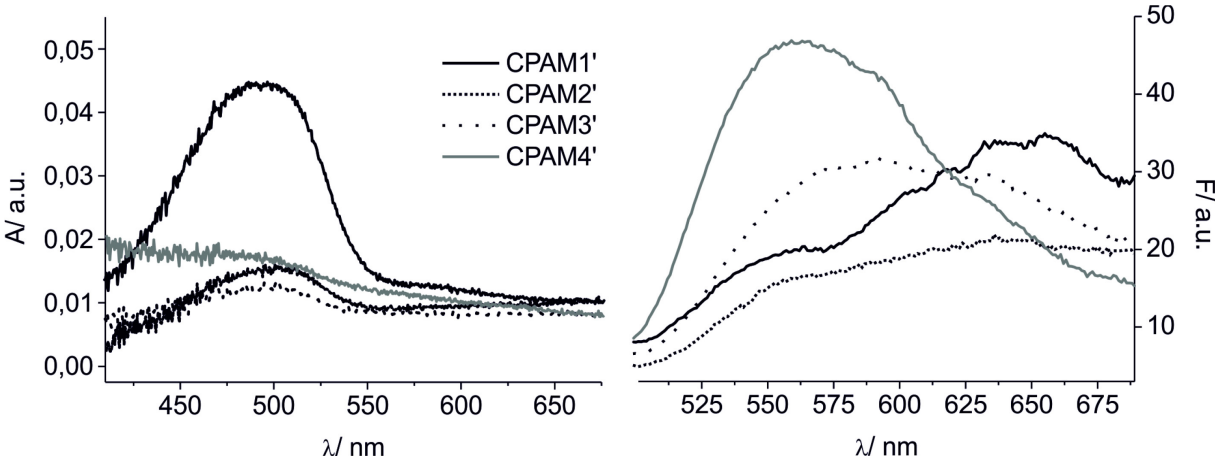

Figure 43 Absorption and emission spectra of 36 labelled cellulose particles CPAM1'-CPAM4' (c = 0.46 mg/ml in aqueous solution, λ_{exc} = 470nm).

Particles **CPAM1'** bearing the highest amino-group density on the particle surface and exhibiting the strongest **36** absorption (Figure 43, left), show a broad emission at λ_{em} = 650 nm and only a minor band at λ_{em} = 550 nm in water. In EtOH–H_2O particles **CPAM1'** show a comparable intensity for both bands (Figure 44). That means that there are more dye-monomers present because of the organic solvent.

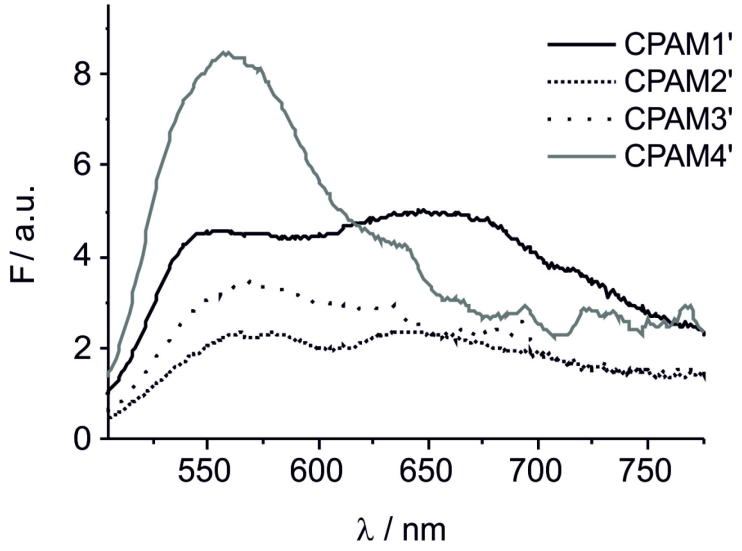

Figure 44 Fluorescence spectra of 36 labelled NFCPs CPAM1'-CPAM4' (c = 0.46 mg/ml in aqueous ethanolic solution, λ_{exc} = 470nm).

The emission spectra of samples **CPAM2'** and **CPAM3'** show very broad emission bands in water presumably due to the contribution of both types of emission bands. These particles represent intermediate stages between **CPAM1'** (highest amino group density) and **CPAM4'**

(lowest amino group density) with varying amounts of isolated and excimer- or dimer-forming dyes.

Although the absorption spectra for **CPAM1'** (highest amount of coupled dye) showed a minor shoulder, which could also hint at di-substituted species being present on the particle surface, control measurements with excitation at λ_{exc} = 560 nm directly in the main absorption band of the di-substituted species did not yield in any appreciable fluorescence signal for **CPAM1'** in the 600-700 nm range. Similar results were also obtained for **CPAM2'** and **CPAM3'**, that is, excitation at 560 nm did not give rise to any measurable fluorescence emission. This clearly excludes the possibility of di-substitution of **36** on the particle surface which might have been theoretically possible at higher concentration of amino-functions within the particle pores.

Table 10 Absorption- and global emission maxima of CPAM1'-CPAM4' in water.

Sample	λ_{abs} [nm]	λ_{em} [nm]
CPAM1'	495	650
CPAM2'	495	637
CPAM3'	495	593
CPAM4'	-[a]	550

[a] could not be determined due to low signal intensity

Confocal laser scanning microscopy

Images with the CLSM were recorded to investigate the spectroscopic features of the encapsulated NFCPs labelled with **36** in the dry state and in aqueous media. To enable an appropriate comparison of the particle species under the same instrument settings of the microscope, the respective particle fractions were blended as described.

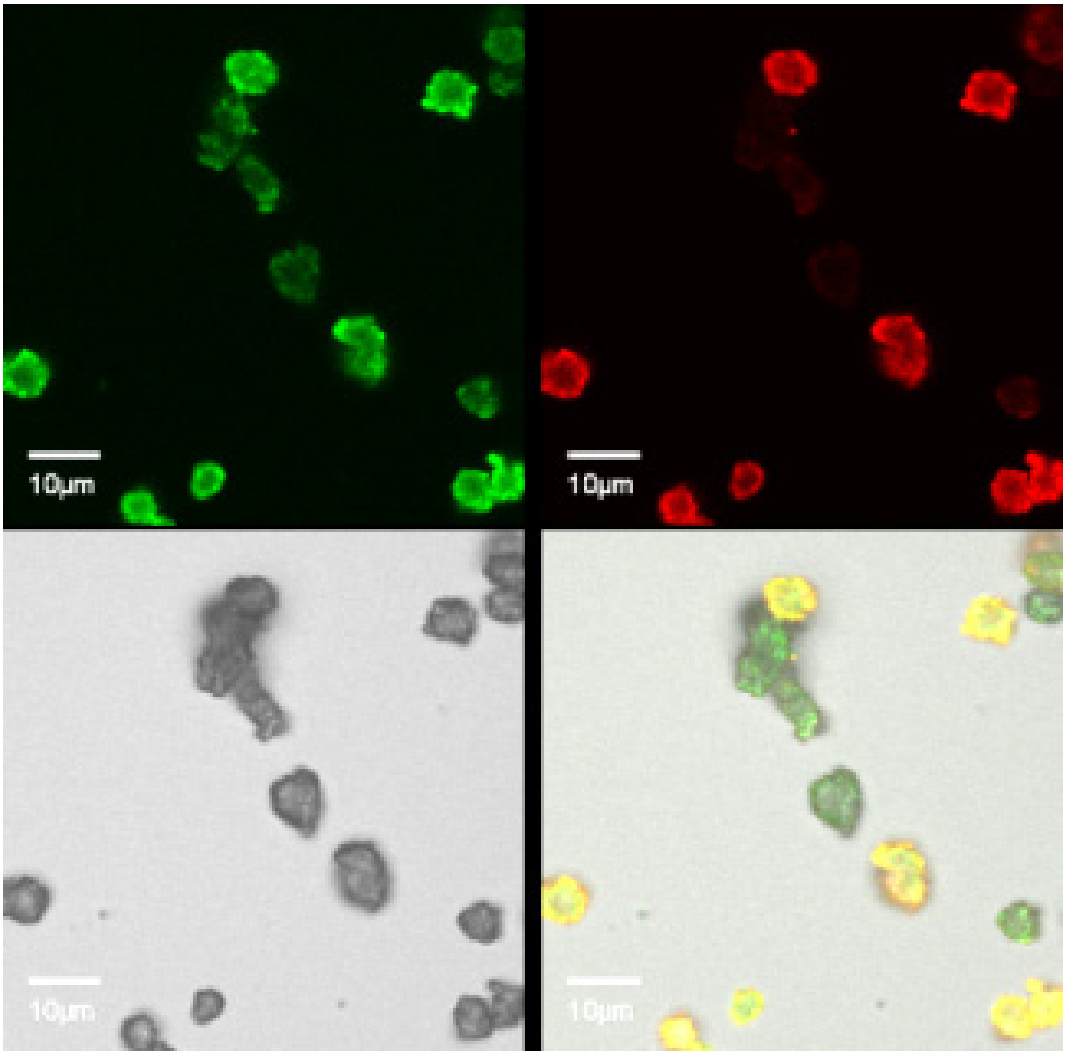

Figure 45 CLSM image of mixed, dry labelled CPAM1' and CPAM4' particles.

Figure 45 shows the mixture of dry particles **CPAM1'** (highest amount of coupled dye) and **CPAM4'** (lowest amount of coupled dye). In this state, the fluorescent amino-group label is distributed homogenously over the particle, indicating that the fluorescent dye is well distributed at the outer and inner particle surface, i.e., is only attached to the cellulose skeleton but does not occupy void pore space.

With an excitation wavelength of λ_{exc} =488 nm (λ_{emCh1} = 500-560 nm, λ_{emCh2} = 625-725 nm) both types of particles could be clearly distinguished by their emission behavior. Particles **CPAM4'** (lowest amount of coupled dye) shows a distinctly brighter fluorescence in the green channel 1 (λ_{exc} =488 nm, λ_{emCh1} = 500-560 nm), because of non-aggregated dye molecules bound to the particle surface, than in the red channel 2 (λ_{emCh2} = 625-725 nm). Particles **CPAM1'** (highest amount of coupled dye) exhibit comparatively bright fluorescence in both emission channels which is due to the presence of non-aggregated dye molecules and dimers/excimers. With the help of cross-images, the

particles can be clearly distinguished by their color code (green = **CPAM4'**, yellow-orange **CPAM1'**), corroborating the findings of the spectrometer-based experiments.

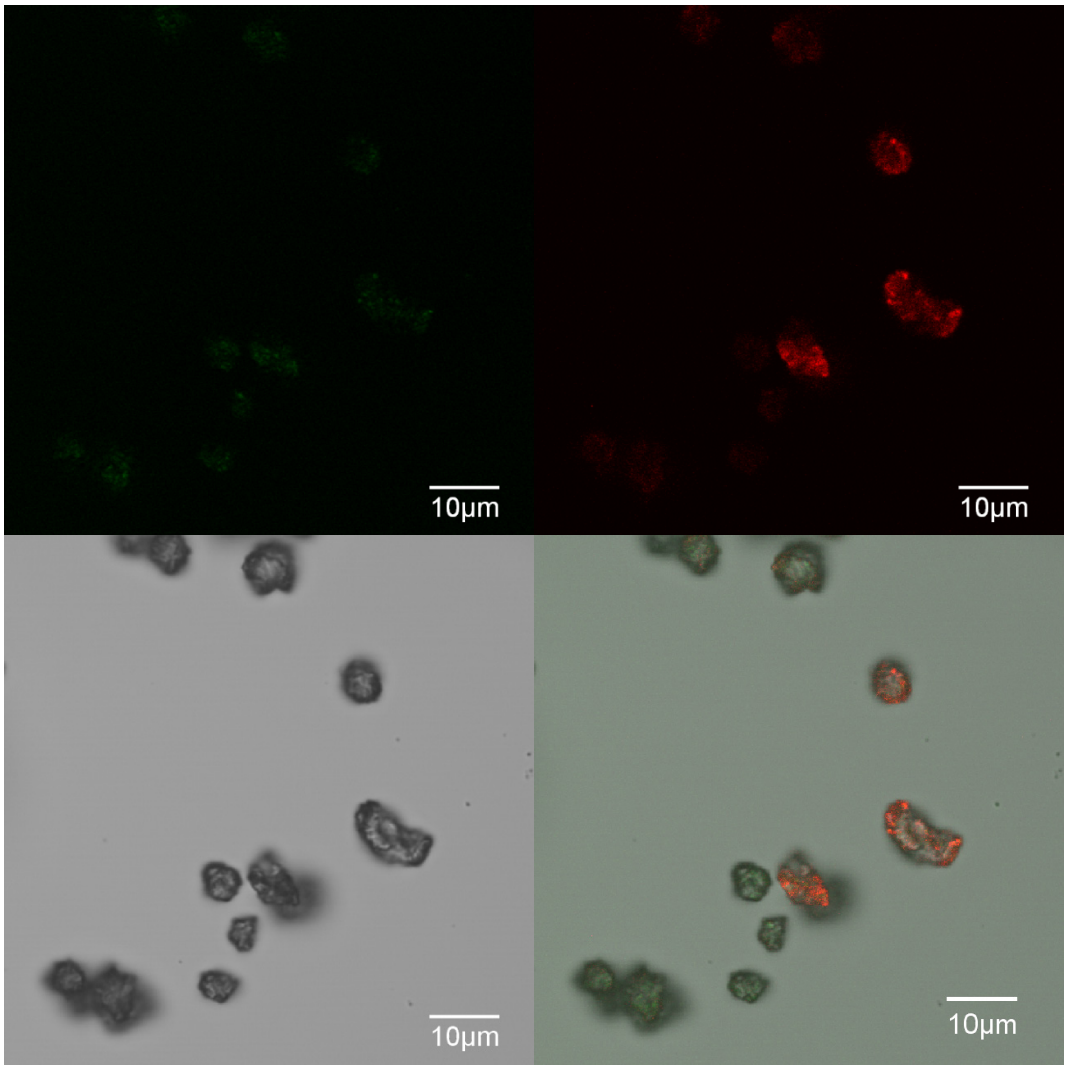

Figure 46. CLSM image of mixed, dry labelled CPAM1' and CPAM4' particles.

After incubation of the particle samples with water, the particles are slightly swollen and the fluorescence signals in both emission channels (λ_{exc} =488 nm, λ_{emCh1} = 500-560 nm, λ_{emCh2} = 625-725 nm) seem to be more located at the particles' outermost surface compared to the dry particles. The spectral shapes however remain the same.

After incubation with water particles **CPAM1'** (highest amount of coupled dye) show a bright fluorescence signal at λ_{emCh1} = 500-560 nm (λ_{exc} = 488 nm) due to the non-aggregated dye on the particle surface and within the particle pores as well as a pronounced signal in the red channel (λ_{exc} = 488 nm, λ_{emCh2} = 625-725 nm) due to dimers/excimers (Figure 47). Particles **CPAM4'** only emit in the green channel 1. Overlapping both images results in yellow-orange appearing particle boarders for **CPAM1'**.

Sets of a z-scan of particles **CPAM1'** and **CPAM4'** were recorded, to obtain images of planes at various depths within the samples. With this imaging mode the distribution of the dye at the outer- and inner particle surface can be depicted. Because of the particles' stray light no supporting data could be obtained. All particles were also excited at λ_{exc} = 545 nm to investigate the possible existence of 3,5-aminated **36** conjugates. But no remarkable emission could be detected which underlines the presence of excimer/dimers in aqueous solution.

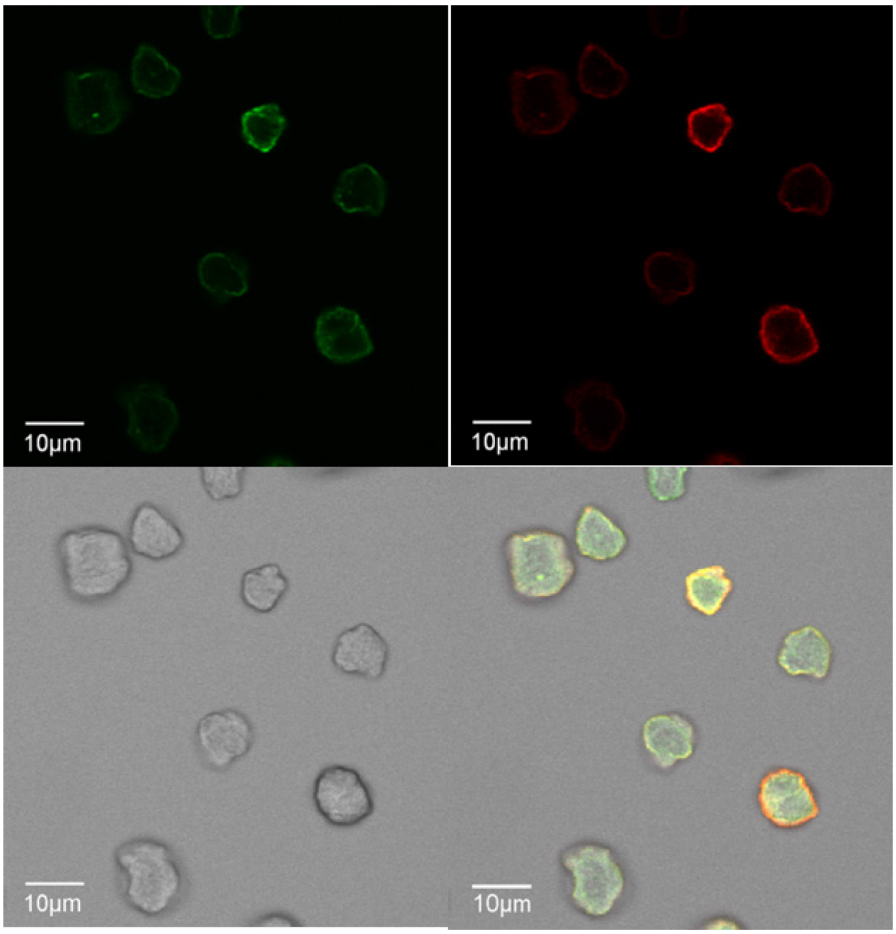

Figure 47 CLSM image of mixed labelled CPAM1' and CPAM4' particles after incubation with water.

To distinguish real fluorescence signals of the particles from scattered light and reflected laser light, unlabeled AM-coated particles as blank controls (**CPAM3**) were mixed with **CPAM3'** particles and incubated for 30 min in water. The CLSM images show strongly fluorescent particles (green) next to virtually non-fluorescent particles (Figure 48). Whereas the bright signals can be attributed to particles **CPAM3'**, the unlabeled particles appear only slightly green in channel 1 (λ_{exc} = 488 nm, λ_{emCh1} = 500-560 nm) because of the effect of light scattering at the particle surface. At longer wavelength (λ_{emCh2} = 625-725 nm) this effect is absent.

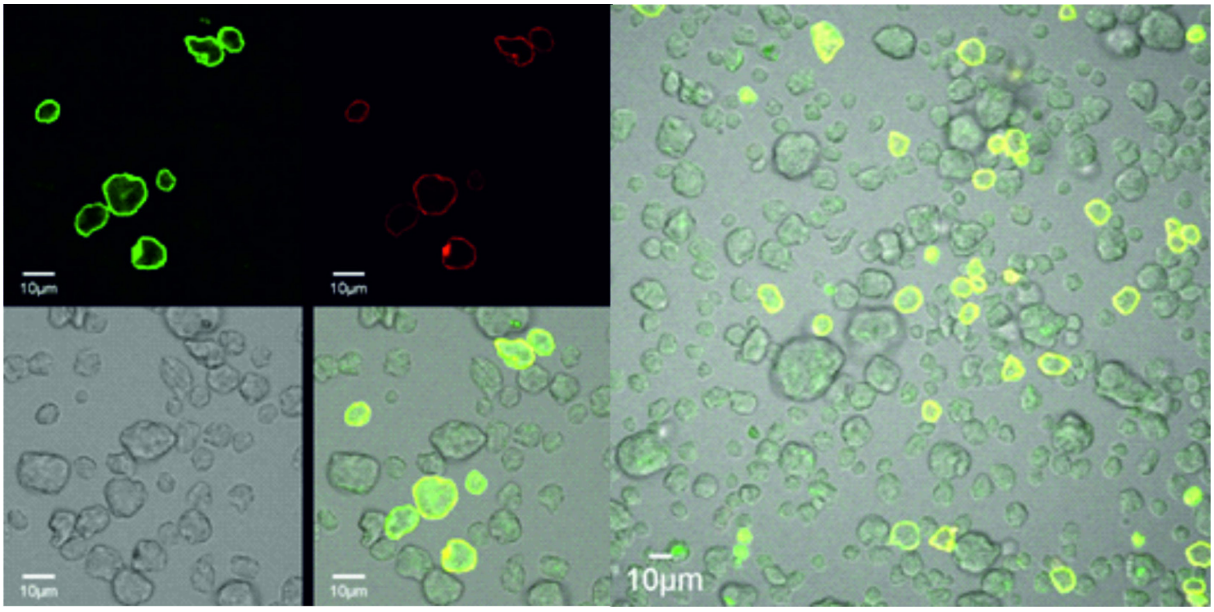

Figure 48 Blended particle samples CPAM3 and labelled CPAM3' after incubation with water at RT.

3.3 Conclusion

The work presented here describes a new approach for the encapsulation and functionalization of nanofibrillated cellulose particles (NFCPs) for the application as new supporting material in aqueous media. The particles offer a special microenvironment for rather hydrophobic label molecules within their pores and wrinkles, associated with a reduction of steric hindrance and higher availability of binding sites on the particle surface. The encapsulation with a water-impermeable silane-shell protects the particles from swelling and simultaneously offers reactive binding sites for further applications. Furthermore a family of bright BODIPY fluorophores with a high number of fluorine atoms (F-BODIPYs) has been developed and characterized spectroscopically. Especially the amino-reactive BODIPY **36** could be applied as fluorescent model compound for the characterization of the particle surface properties. **36** reacted via nucleophilic substitution with the amino-groups on the particle surface, corresponding to the observations of mono-aminated-dye reaction products in solution which induces a color shift depending on the substitution rate of the dye. The observed substitution of both chlorine functionalities of the amine-reactive dye, partly obtained at RT in solution, induces a bathochromic shift of the emission of the resulting conjugate, could not be observed during the labelling of the surface amino groups of the cellulose nanoparticles.

Nonetheless the cellulose matrix creates a microenvironment for the hydrophobic dye and detrimental effects of water on the optical properties of **36** such as dye aggregation and low solubility can be overcome by choosing the suitable amino-group density on the particle

surface. The particles' surface amino group density could be optimized with these experiments with regard to further bioanalytical applications.

4 MCM-41

The tremendous impact of the mesoporous silica network of MCM-41 particles is presented in the next chapter. First the loading and release capabilities of the material are optimized and the carrier system is loaded with a high amount of the indicator dye. If the appropriate detection chemistry is implemented, only the advent of an analyte molecule can trigger the delivery of the dye. The presented nanoscopic delivery system can release a larger number of indicator molecules than the number of analytes necessary to induce the release, which results in the phenomenon of amplified signaling. The remarkable versatility of this system is shown within an actually applicable sensing format - a fast strip-based-assay. The model analyte chosen was triacetone triperoxide (TATP), a small-molecule analyte that is difficult to target with supramolecular recognition chemistry because it lacks functional groups for classical non-covalent binding. In another approach it is shown how the mesoporous particles can serve as excellent host for water-insoluble sensor molecules for direct applications in aqueous solution keeping the natural sensing capabilities of the dye like in organic solvents. By adsorption of rather hydrophobic molecules within the particles' pore walls it is possible to sensitively detect for example heavy-metal ions directly in water even up to the ppb range. With this strategy the common problem of the applicability of sensitive hydrophobic sensor dyes within aqueous solutions can be simply extended by tailoring the molecules' microenvironment to finally obtain high impact functional materials.

4.1 Introduction

In the early 1990s the scientists of Mobil Oil Company discovered the first generation of periodic mesoporous silica materials (so-called M41S family) through the use of surfactants as organizing agents.[142-144] Unlike many non-porous materials, including hard (e.g. gold and iron oxide) and soft nanoparticles (e.g. dendrimers, proteins and polymer beads),[145] mesoporous silica materials are characterized by their chemical inertness, non-cytotoxicity character and homogeneous porosity associated with very large internal surface areas, still maintaining their highly porous nature after functionalization. Additionally prominent features of this class of material are its highly ordered pore system and well-defined pore radius distribution. In contrast to the microporous crystalline zeolites, however, the M41S materials have pore diameters from approximately 2 to 10 nm and therefore exceed those of the zeolite molecular sieves, which are commonly restricted to a pore size of around 1.5 nm. This allows the inorganic platform to house appreciable amounts of cargo without destabilization of the silica framework. The most common member of the M41S family is the hexagonally organized MCM-41 which probably is the most studied mesoporous silica material for applications e.g., in catalysis,[146, 147] filtration and separation,[148] gas adsorption and storage,[149] enzyme immobilization[150] and biomedical tissue regeneration.[151]

Especially for drug delivery applications[152, 153] and chemical/biochemical sensing[154-156] these highly porous, container-like structures are particularly exciting vehicles. When equipped with a chemically or physically addressable gating function at the openings of the voids, the release of the cargo can be controlled. Because many more molecules can be stored as cargo in the pores of the support than there are functional groups as anchoring sites for the gating entities attached to the outer surface (for efficient pore capping), the systems possess inherent features of signal amplification.[155] Another approach from the field of chemical signaling without gating mechanisms is based on guest-induced dye release strategies. The binding of the target molecule leads to the formation of a water-soluble fluorescent or colored product which is released into the solution.[157] Next-generation solids not only indicate a species, they contain also binding sites acting as scavengers. This approach is a very promising route to generate new and improved polyfunctional materials that allow monitoring of the progress of removal of e.g. toxicants without other external devices.[158]

To finally design a potent delivery or sensory system important prerequisites are the loading and/or release efficiencies of guest molecules into/from the mesoporous material. The most widely used loading process is the steric incorporation of organic compounds that involves immersing the porous particles into a solution of the desired guest molecule, e.g., a

fluorescent dye or drug. The abundance of silanol groups (Si-OH) on the surface of the MCM-41 particles makes them hydrophilic and thus dispersible in aqueous environments. If the interactions in the loading system are favorable, the guest molecules are forced to move from the solution into the pores and are trapped by the adsorption sites located there. After removal of the solvent by evaporation, the molecules will remain in the pores. The interactions between the cargo and the particle usually include hydrogen bonding (acting either as donors or acceptors) and electrostatic interactions.

For drug delivery several studies were published on the diffusion dependent processes like the loading and release efficiency of mesoporous materials with regard to the nature of the solvent, morphology of the inorganic support as well as the polarity and charge of the investigated guest molecule.[152, 153, 159, 160] The same factors are crucial for sensing and recognition applications with hybrid organic-inorganic materials loaded with fluorescent dyes. Furthermore, a fast response of these materials regarding their ability to release a high content of cargo is mandatory to allow the implementation in an actual sensor format, e.g., in a test-strip based assay.

For this purpose the loading and release efficiency of several fluorescent dyes with various electronic structures (cationic, anionic, neutral, and zwitterionic) in two different media (phosphate-buffered saline PBS, MeCN) were investigated. The mesoporous silica material MCM-41 was selected as inorganic scaffold based on previous studies to obtain an optimized, sensitive sensing protocol for a potential application in a test-strip based format.

4.2 Results and discussion

4.2.1 Loading and release studies of MCM-41

The sensitivity of the particulate system (regardless of the final sensing mechanism at the voids at this point) is mainly influenced through the loading-adsorption as well as release-desorption processes of the used dye. To gain insight into these processes in more detail and to obtain optimized materials for further applications, several commonly applied fluorescent dyes with different characteristics - ionic structures (anionic, cationic, inner salt, zwitterionic, neutral) and counter ions (“hard”/small, intermediate, “soft”/big) were chosen. For the loading process Rhodamine 101 chloride **40** (**Rh101-Cl**), Rhodamine 101 perchlorate **41** (**Rh101-ClO_4**) and Rhodamine B chloride **42** (**RhB-Cl**) were investigated as cationic dyes. Rhodamine 101 inner salt **43** (**Rh101**) and the BODIPY dye **5** (**Bo**) represent the class of zwitterionic dyes. Fluorescein 27 **44** (**Flu27**) has been selected as model dye, changing its

charge as a function of the pH[163, 164] and Sulforhodamine B sodium salt **45** (**SuRh-Na**) as anionic representative. The known chemical structures of the selected dyes are depicted in Figure 49. The molecular structure of fluorescein is characterized by a xanthene ring (for rhodamines substituted by two amino groups) and an *ortho*-carboxyphenyl at the 9-position carbon. The *ortho*-carboxyphenyl is roughly perpendicular to the xanthene skeleton.

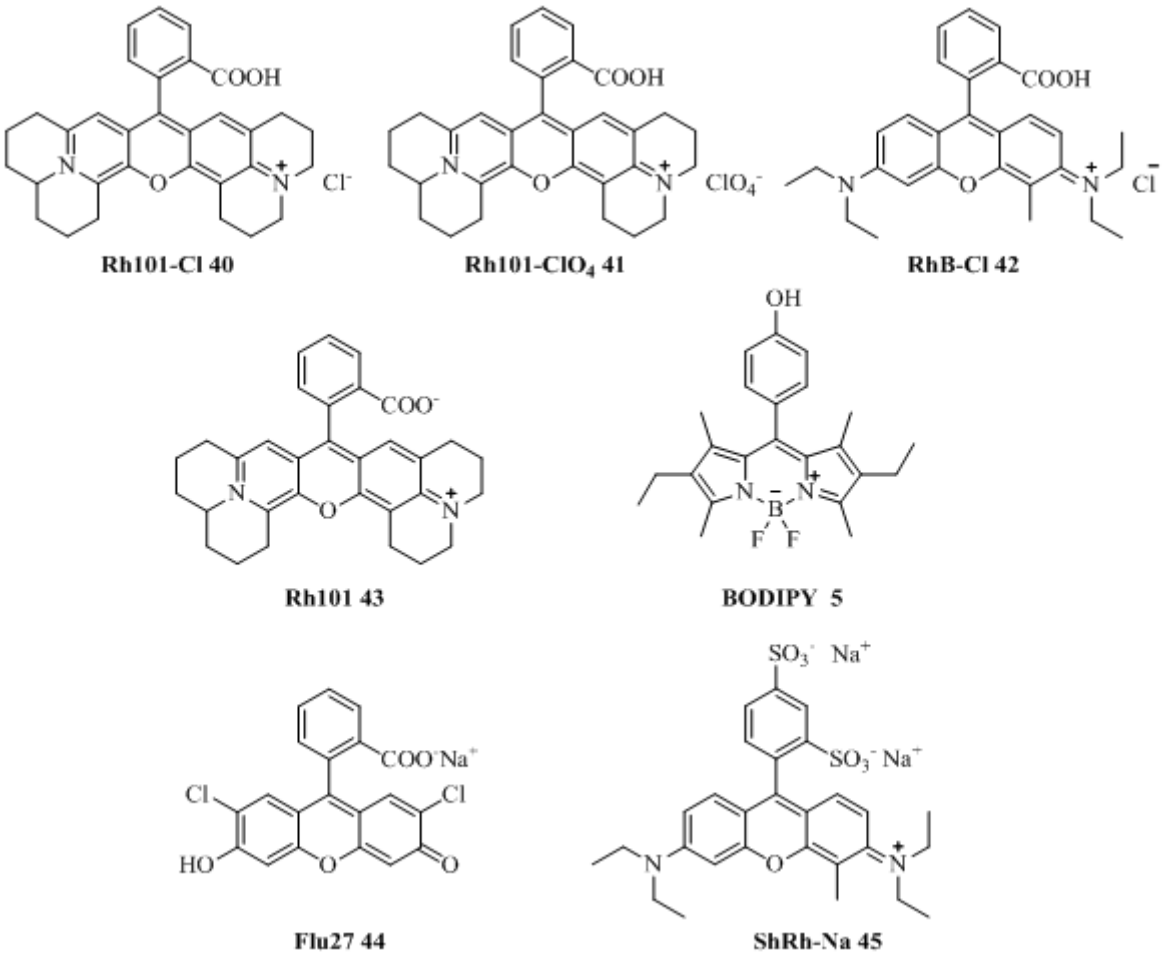

Figure 49 Chemical structures of selected dyes.

To study the loading process of the dyes into the mesoporous silica nanoparticles two different solvents were used. Acetonitrile was selected as an aprotic, organic polar solvent with a high dielectric constant whereas PBS buffer (pH 7.4) is the most common aqueous environment used in controlled release process-based experiments using loaded mesoporous materials. By suspending 10 mg of MCM-41 nanoparticles in acetonitrile or in PBS, containing the selected dyes in the range of 1.0 - 2.0 mmol L^{-1}, depending on the solubility in the appropriate solvent, 14 suspensions with a final concentration of 0.8 mmol dye g^{-1} solid could be obtained after stirring for 24 h at RT (for nomenclature see Table 11). After centrifugation and drying steps the residual solvent, which strongly adsorbs into the pore walls, could be removed.

Table 11. Nomenclature of the loaded solids.

Solvent	*Dyes*						
	Rh101-Cl **40**	***Rh101-ClO$_4$*** **41**	***RhB-Cl*** **42**	***Rh101*** **43**	***Flu27*** **44**	***ShRh-Na*** **45**	***Bo*** **5**
MeCN	**ARh101-Cl**	**ARh101-ClO$_4$**	**ARhB-Cl**	**ARh101**	**AFlu**	**AShRh-Na**	**ABo**
PBS	**BRh101-Cl**	**BRh101-ClO$_4$**	**BRhB-Cl**	**BRh101**	**BFlu**	**BShRh-Na**	**BBo**

The loading-adsorption as well release-desorption ability of the guest molecules is based on complex adsorption/desorption processes. Therefore the interactions between the molecules, the solvent and the surface of the material should be discussed.

(i) Compound-Solvent: The solvation process of the dye is mainly affected through dipole interactions and polarizability features of the solvent. The formation of compound-solvent complexes depends on the electronic structure of the dye and, if present, the counter ion generating ternary dye-solvent-counter- ion complexes. Those effects could stabilize the dissolution of the compound and reduces the adsorption ability of the dye within the material. On the other hand, a low solubility through repelling forces could improve the adsorption because of the favored affinity between the surface and the compound.

(ii) Compound-Compound: Hydrophobic interactions (π-π stacking) between the dye molecules can influence the loading and release process.

(iii) Compound-Surface material: A satisfactory degree of loading can only be achieved if the interactions of the compound and the material are sufficiently strong. However, too strong interactions are not favored because they would hinder a fast desorption process.

(iv) Surface material: The surface pH of the porous material could affect the dissolution of the compound that ionizes within a definite pH range. Furthermore the pore size and shape may have an influence on the mass transfer.[161]

Determination of molar absorption coefficients

To determine the amount of the organic content in the prepared solids as well as the release ability by spectrophotometric measurements the *Beer-Lambert* law[162, 163] can be used.

$$A = lg\frac{I_0}{I_1} = \varepsilon \cdot c \cdot d$$

A = Absorbance of the sample, optical density

I_0 = Intensity of light passing through the reference cell

I_1 = Intensity of light passing through the sample cell

ε = Molar absorption coefficient of the absorber

c = Concentration of the absorbing species

d = Path length

For this purpose first the molar absorption coefficients ε of the selected dyes were determined in MeCN and PBS buffer which were used in the loading processes (see experimental section for details). The values for λ_{max} and ε in $M^{-1}cm^{-1}$ for selected dyes are listed in Table 12.

Table 12. Molar absorption coefficients of selected dyes in $M^{-1}cm^{-1}$ in acetonitrile and PBS buffer at corresponding maximum wavelengths.

Sample	*Dye*	*Solvent*	*λ_{max} (nm)*	*ε ($M^{-1}cm^{-1}$)*
BRh101-Cl	**40**	PBS	576	86630
ARh101-Cl	**40**	MeCN	576	86330
BRh101-ClO_4	**41**	PBS	576	96890
ARh101-ClO_4	**41**	MeCN	572	96160
BRhB-Cl	**42**	PBS	555	97520
ARhB-Cl	**42**	MeCN	554	87120
BRh101	**43**	PBS	576	44570
ARh101	**43**	MeCN	576	12690
BBo	**5**	PBS	-[a]	-[a]
ABo	**5**	MeCN	507	69950
BFlu	**44**	PBS	503	92510
AFlu	**44**	MeCN	503	265
BSuRh-Na	**45**	PBS	564	95950
ASuRh-Na	**45**	MeCN	550	73320

[a] These values could not be determined due to the insolubility of the compound in the appropriate solvent.

Determination of the loading and release ability

With help of the *Beer-Lambert* law and the previously determined molar absorption coefficient ε it is possible to determine the concentration and amount of each dye in the appropriate solution before and after the loading process. With this procedure the finally loaded amount of each dye in the mesoporous material could be calculated. (Table 13)

Additionally, the appropriate amounts of the loaded dyes in the final materials were independently confirmed through elemental analysis of C, H, N and are in accordance to the data obtained by UV/vis measurements.

The delivery studies of the 14 prepared samples finally were carried out in PBS buffer at a pH of 7.4 with regard to prospective biochemical applications in environmental media where the presence of organic solvents would appear clearly as interfering factor. The amount of dye loaded into the pores of the mesoporous material determined their release ability. The final performance and sensitivity of the material was determined by the product of the loading and release ability. Table 13 shows the loaded and released amount of the appropriate dye in mmol g^{-1} SiO_2 and in % of the mesoporous material.

Table 13 Loaded and released amount of dye from MCM-41 particles.

	Solid	*mmol g^{-1} SiO_2 loaded by UV*	*mmol g^{-1} SiO_2 released by UV*	*% loaded* [a]	*% delivered PBS*	*% load × release*
cationic	**BRh101-Cl**	0.60	0.10	73	18	13
	ARh101-Cl	0.09	0.01	20	3	1
	BRh101-ClO_4	0.30	0.10	50	24	12
	ARh101-ClO_4	0.11	0.01	18	3	1
	BRhB-Cl	0.63	0.16	69	28	19
	ARhB-Cl	0.53	0.04	52	9	5
zwitter-ionic	**BRh101**	0.35	0.10	37	35	13
	ARh101	0.66	0.16	77	25	20
	BBo	-	-	-	-	0 [b]
	ABo	0.06	0.01	8	-	0

anionic	**BFlu**	0.10	0.04	12	45	5
	AFlu	0.12	0.02	15	17	3
	BSuRh-Na	0.08	0.07	11	73	8
	ASuRh-Na	0.68	0.44	90	61	55

[a] 100 % equals to the amount of the dye of the stock solution, [b]could not be assesed due to insolubility of **5** in PBS buffer, material was not loaded

The aforementioned interactions are complex and governed through the nature of the solvent (solvation ability), the dominating species in solution and on the surface of the MCM-41 material (silanol-, silanolate-, hydrogen-bonded silanol groups).[164] Especially the electronic structure and functional groups of the dye molecules play a fundamental role. In solution the investigated xanthen dyes can exist in the non-fluorescent lactone and fluorescent ionic forms (cationic and zwitterionic for rhodamines, mono- and dianionic for fluorescein).[165-167] The zwitterionic rhodamine form only exists in protic medium and is absent in aprotic solvents, whereas the lactone form can exist in both protic and aprotic solvents. The equilibrium between the lactone and zwitterion forms is complex and depends on the solvent polarity as well as on the hydrogen bond interaction.[168-171] In MeCN the loading capacities of **Rh101-Cl** and **Rh101-ClO$_4$** were moderate (20 % **ARh101-Cl** and 18 % **ARh101-ClO$_4$**). **RhB-Cl** showed a loading capacity of 52 %. These dyes exist in the form of HOOC-dye-NR^{2+} as ion pairs with poor solvated anions X^-, presumably restricting the interactions between NR^{2+} and silanol groups of the MCM-41 pore voids. The structure of **RhB-Cl** promotes the interactions with the pore walls compared to the bulky julolidyl groups of **Rh101-Cl** and **Rh101-ClO$_4$**. A final release of **RhB-Cl** could be restricted due to the strongly electrostatic bound molecules. In buffered aqueous solution the maximum loading capacity was reached with **Rh101-Cl**, **RhB-Cl** and **Rh101-ClO$_4$** (around 73 %, 69 %, 50 %, respectively). The anions are well solvated and the interactions between the cationic dye molecules and the pore walls are favored. Additionally the counter ion of rhodamine 101 (Cl^- or ClO_4^-) controlled the efficiency of the loading. Chloride anions are more solvated compared to the perchlorate[172] benefitting the interactions of the cationic dye with the silanol groups which finally lead to a higher loading amount of **Rh101-Cl** within the particle voids (50 % **BRh101-ClO$_4$** vs. 70 % **BRh101-Cl** and **BRhB-Cl**). The releasing ability from this system is moderate (20 - 30 %) and seems to be more influenced by the molecule structure as by the nature of anion (28 % **BRhB-Cl** vs. 70 % **BRh101-ClO$_4$** and **BRh101-Cl**, respectively).

The molar absorption coefficient ε of the zwitterionic dye **Rh101** has also been taken into account, indicating that the spiro-lacton equilibrium also plays a dominant role under the chosen conditions for this dye compared to the other rhodamines. In MeCN the non-fluorescent lactone form is dominating (low ε) and presumably easily enters the pores (loading of 77 %). In PBS around 50 % of the non-fluorescent spiro-lacton form is present.[173, 174] But moderate release was detected for both materials **ARh101** and **BRh101**. It is difficult to compare **Rh101** with the cationic dyes due to the unknown content of non-fluorescent spiro-lacton and fluorescent open zwitterionic form loaded in the appropriate solvent after finally releasing the dye from the MCM scaffolds. The lowest loading was obtained with the zwitterionic BODIPY **5** and anionic **Flu27**. Although **5** dissolved well in acetonitrile, presumably strong dye-solvent complexes hinder an appropriate adsorption of the dye on the material. Furthermore the electrostatic interactions are possibly too low due to the minor polarity compared to the other dyes. In aqueous solution **5** shows only poor solubility (see also chapter 2) and the appropriate data could not be determined. Fluorescein 27 exists as dianion with a minor amount of the monoanionic form at a pH of 7.4.[166, 167, 175] The interactions with the silanol groups are not favored and the repulsion forces hinder an appropriate loading yielding a very low loading release capability. The quantity of the loaded dye in the MCM-41 scaffolds is additionally influenced by the equilibrium between the adsorbed and dissolved dye. The solubility of the cationic dyes (**Rh101-Cl**, **Rh101-ClO_4** and **RhB-Cl**) in acetonitrile was determined to be higher than 2.0 mM, whereas for **Rh101** and **SuRh-Na** the respective values are 1.6 mM and 1.0 mM. The lower solubility of both dyes yielded in a higher loading efficiency. The preference for the polar microenvironment within the pores was higher compared to PBS.

Based on these results the following preference in the adsorption process at a pH of 7.4 in PBS buffer is obvious: positively charged dyes are distinctly adsorbed to a higher degree than the investigated zwitterionic or anionic dyes. The high solubility of the cationic dyes in acetonitrile reduces their adsorption capability whereas the adsorption of minor soluble anionic- and zwitterionic dyes is favored in acetonitrile solution. All in all, **Flu27** and **5** show only a low loading preference for both solvent systems.

As a general trend, the dyes loaded in PBS are distinctly easier delivered from the material than their counterparts prepared in acetonitrile. The maximum delivery of 73 % could be reached with **SuRh-Na**. Although a higher release could be observed for **BSuRh-Na** (73.1 % corresponds to 0.066 mmol dye g^{-1} SiO_2) the application of that material for controlled released protocols is limited because of the low amount of loaded dye (11.2 %) compared to

the **AShRh-Na** material (89.9 % loaded, 60.7 % release corresponding to 0.436 mmol dye g^{-1} SiO_2).

The reduced releasing ability of the **A**-materials (loading in MeCN) compared to the **B**-materials (loading in PBS) could be additionally explained by the solvation-adsorption equilibrium of the dyes in the appropriate solvent. The high solvation degree of the charged, hydrophilic dyes in aqueous buffered solution compared to the low solvation in acetonitrile increases the fast release of the dyes from the pores of the material significantly, concomitant with a fast mass transport. This trend can be summarized regarding at least the load-release ability:

A-materials: **Bo** < **Flu27** < **SuRh-Na** < **Rh101-ClO_4** < **Rh101-Cl=Rh101** < **RhB-Cl**

B-materials: **Bo** < **Rh101-ClO_4** < **Rh101-Cl** < **Flu27** < **RhB-Cl** < **Rh101** < **SuRh-Na**

To get more insight into the mechanism, kinetic release studies of the anionic dye **SuRh-Na** which showed the highest degree of release from the **A**-materials (**ASuRh-Na**) and the cationic dye **RhB-Cl** from sample **ARhB-Cl**, which showed a minor release, were investigated. (Figure 50)

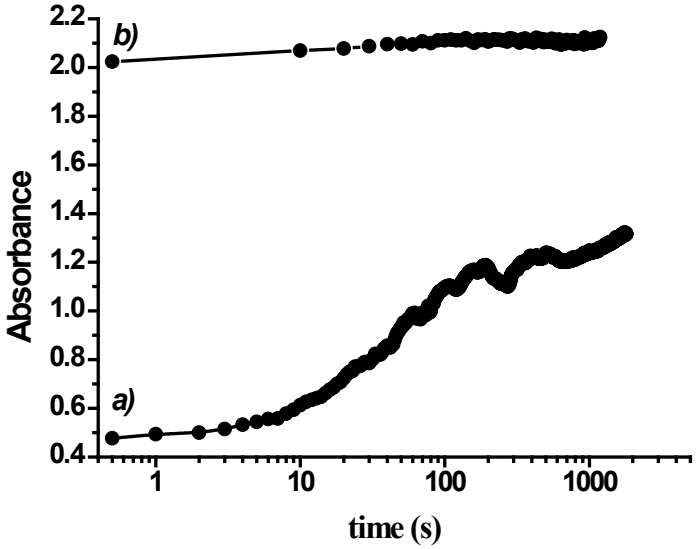

Figure 50 λ_{abs} of the respective dye at λ_{absmax} released from the solids a) ARhB-Cl and b) ASuRh-Na versus time.

The loading of the anionic dye **SuRh-Na** in acetonitrile yielded material **ASuRh-Na**. Presumably the main driving force here is the counter-ion effect. The solvation of Na^+ and Cl^- in acetonitrile is not preferred but the positively charged sodium could electrostatically interact with the silanol groups and therefore drag the dye in the pores.[176, 177] The fast release

of **SuRh-Na** is clearly related to the repulsion forces occurring between the anionic dye and the negatively charged silanolate on the pore walls.

Furthermore, it should be taken into account that van der Waals forces could also be present when guest molecules are present in mesoporous scaffoldings and have an important role in loading/delivery processes.[178] In fact, it has been demonstrated recently, that this local interactions (of van der Waals type) between the porous host and guest molecules modulates the macroscopic transport from the pores to the solution.[179] Stronger guest-matrix attractions (through van der Waals interactions) produced slower release kinetics and an increase in the amount of guest captured inside of the pores. The interactions between guest molecules and the inorganic scaffolding produces an accumulation of the former at the pore walls, which can be understood as a multilayer adsorption process and can result in a semipermeable layer that delays the release of the dye. This effect is also observed comparing electrostatic interactions between silica matrix and dyes. For instance, Ng et al. analyzed the loading and release of two fluorescent dyes (one anionic and the other cationic) from mesoporous silica spheres through confocal laser scanning microscopy.[180] Analysis of time-dependent release of both dyes showed different behavior: whereas concentration profiles of the anionic dye within the spheres showed a homogeneous distribution and the release followed a simple diffusion-driven process, the concentration of the cationic dye was not homogeneous. At this respect, these researchers observed a higher concentration of the cationic dye close to the surface of the spheres, compared to that in the core, and the release was controlled by diffusion after an initial process of rapid release.

Based on the result obtained by the loading and release studies, a high loading could be achieved with PBS for the cationic dyes (50-70 %), whereas acetonitrile should be used for anionic dyes (90 % for **SuRh-Na**). The loading efficiencies for zwitterionic- and neutral dyes are only moderate in both solvents. Regarding the release process in PBS, the best results could be obtained with anionic dyes (60-75 %) because the cationic representatives remained strongly adsorbed onto the pore walls due to favored electrostatic interactions. With respect to a high sensitivity and fast response the **ASuRh-Na** (**SuRh-Na** loaded with MeCN) is the optimized material showing a high dye content (0.68 mmol g^{-1} SiO_2, about 90 % dye loaded) and is additionally able to release about 61 % (0.44 mmol g^{-1} SiO_2) of the entrapped cargo.

4.2.2 Application of gated MCM-41 in a Lateral-Flow-Assay

Although the popularity of MCM-41 in drug delivery or related biomedical and pharmaceutical applications is well documented,[181] their breakthrough in the area of analytical

sciences is yet to come.[155] The potential of such systems for analytical purposes is nonetheless immediately clear. The key is thus to equip the particles with a selective gating mechanism that releases the cargo (e.g. a fluorescent dye) in a controlled manner and only the advent of the analyte molecule can trigger the delivery from the carrier system. This strategy possess inherent features of signal amplification because many more molecules can be stored as cargo in the pores of the support than there are functional groups as anchoring sites for the gating entities attached to the outer surface (for efficient pore capping).

An important feature when aiming to use the capped hybrid delivery systems in a test-strip assay is to obtain a highly selective and sensitive response while guaranteeing fast response times, that is, high delivery rates. Highly selective and sensitive immunological responses are best obtained with high-affinity antibodies. Such assays commonly rely on test strips that carry the (bio)chemical part of the detection system and which, after dipping the strip into the sample solution and evolution of the flow, develop a color that can be appreciated by eye. Few such assays are known for the determination of small-molecule analytes of environmental (e.g., atrazine),[182] diagnostic (e.g., morphine),[183] or terroristic (e.g., saxitoxin)[184] concern at trace (lower ppb) levels; those that are known commonly utilize antibody–gold nanoparticle (AuNP) conjugates or hapten–protein–AuNP conjugates, partly in combination with enhancer solutions. Alternatively, first reports on trace-level analysis by using quantum dot (QD) conjugates in strip-based assays and handheld fluorescence readers instead of AuNP-based assays have been reported recently.[185, 186] Inherent to both approaches are the facts that such assays are rapid, sensitive, specific, cheap, and easy to handle, clear advantages in routine applications by untrained personnel or in emergency cases. However, both AuNP- and QD-conjugate assays have a significant drawback, that is, they require protein conjugates to travel the active distance of the strip, which renders them prone to errors due to unspecific binding.

The model analyte chosen for the assay was triacetone triperoxide. TATP is the prototype of a small-molecule analyte that is difficult to target with supramolecular recognition chemistry because it lacks functional groups for classical non-covalent binding and is neither particularly polar nor apolar. TATP is also a high-priority analyte because of its popular use in improvised explosive devices for criminal and terrorist activities.[187, 188] However, although various methods for laboratory-based TATP detection in the liquid phase are available, selective and sensitive portable sensing systems are very scarce.[189-191]

Based on the loading and release studies presented in the previous chapter 4.2.1 finally a gated dye-delivery system could be developed and incorporated with a conventional test-strip-based lateral-flow assay. To implement the particles within an applicable sensing format the

next step was it to equip the MCM-41 with an addressable gating function at the openings of the voids.

General assay and setup in solution

As shown in Figure 51, the mesoporous material was loaded with the indicator dye **ShRh-Na** in MeCN to yield solid **S0** (as optimized system, described in the previous section 4.2.1). The external surface was subsequently functionalized with the suitable hapten III (solid **S1)** synthesized and investigated by project partners.[192] Finally a TATP-selective polyclonal antibody recently developed by co-workers [193-195] serves as a bulky stopper moiety, which was attached at the void openings and efficiently closes them (**S1-AB**).

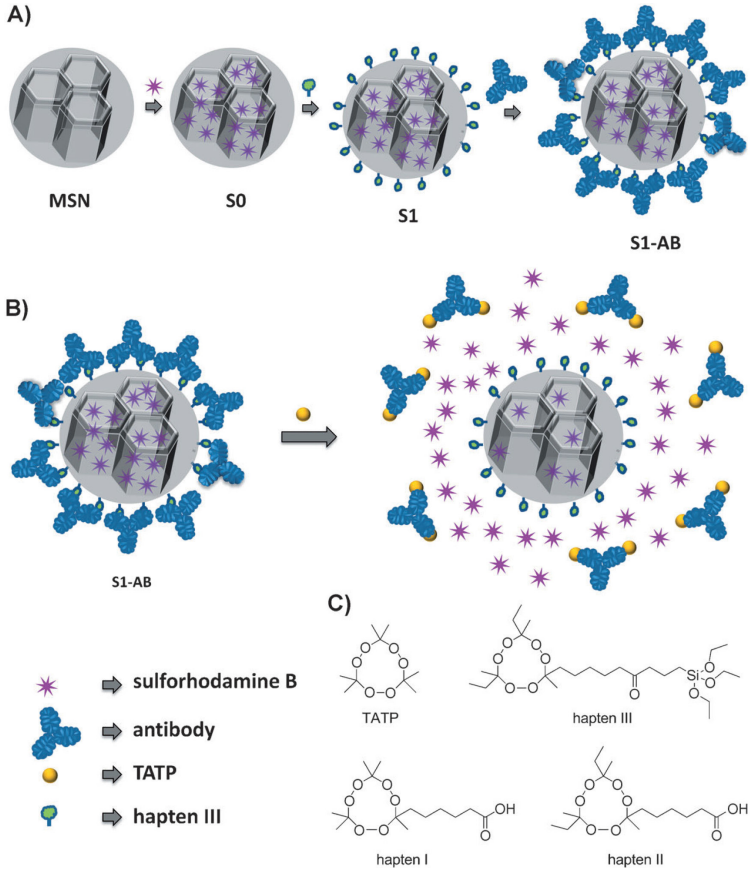

Figure 51 Schematic representation of the preparation of antibody-gated material S1-AB. a) Sensing scheme of the release. c) Chemical structures of TATP and the hapten derivatives I–III employed.

The tailored relay chemistry that connects stopper and support is thus based on non-covalent antibody–antigen interactions and (ideally) only TATP as stimulus should be able to successfully compete with the hapten for the antibody's binding sites, to dislocate the stoppers, to open the voids, and to release the entrapped indicator. The last can be monitored conveniently at excitation wavelengths between 500 and 570 nm and emission wavelengths between 550 and 650 nm, which cover prominent excitation sources and emission filter windows.

The response of **S1-AB** in the presence of various amounts of TATP was first studied in suspension.[192] The presence of TATP induced a fast opening of the pores with subsequent release of the entrapped dye, whereas virtually no release was observed in the absence of TATP. The maximum delivery of **ShRh-Na** from **S1-AB** in the presence of TATP (5 ppm) amounted to 25% of the initial content of dye in **S1-AB**. Regarding the limit of detection of the assay, TATP could be detected at concentrations as low as 12.5 ppb. The selectivity of the capped material was studied by monitoring the uncapping process in the presence of other species as well.

Lateral-flow based assay

Encouraged by these results in solution the **S1-AB** material was integrated with a lateral-flow assay for the straightforward on-site detection of TATP. As can be deduced from Figure 52, the strip contains an interaction and a detection zone. Only the first zone A contains the (bio)chemistry—**S1-AB** (Figure 52a)—that is necessary to generate the response and the second zone B is an arbitrary area at the solvent front in which a signal is collected (Figure 52 c).

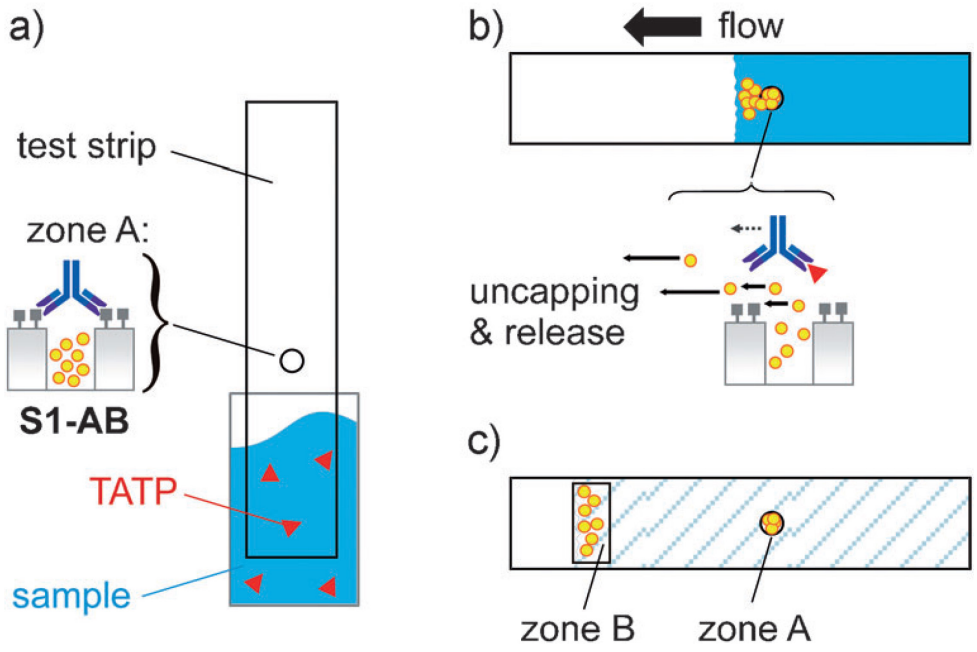

Figure 52. Principle of operation of the lateral-flow assay: a) S1-AB is deposited at zone A b) after dipping, the presence of the analyte leads to (partial) uncapping of the pores and release of the dye, which is transported at the solvent front; c) after development and drying, zone B contains the amount of dye that corresponds to the amount of analyte in solution and zone A the residual, unreleased dye.

When TATP is present in the sample, uncapping takes place when the solvent front reaches zone A because of competition between TATP and the grafted hapten for the binding sites of the antibody, thus leading to formation of the more stable TATP–antibody complex, and the

liberated dye is transported at the solvent front due to the flow conditions (Figure 52 b). Because the MCM-41 is large enough it will not be transported by an aqueous flow in the strip membrane. Therefore capped and uncapped **S1-AB** both are still retained at the spot of deposition (Figure 52 c, zone A). Depending on the amount of TATP in the sample, the flow transports a certain amount of released dye away from zone A and a fluorescence signal can be detected at the solvent front in zone B. A high-flow nitrocellulose membrane was selected as the support. Strips 0.5 × 2.5 cm in size were prepared and **S1-AB** (0.5 μL) was deposited from suspensions of the sensing material (2 mg mL^{-1}) on zone A with a micropipette. The strips were then dipped into buffered solutions containing various amounts of TATP. After 90 s of development, the test strips were dried and the fluorescence was measured with a flow assay reader at 625 nm (λ_{exc} = 520 nm). When strips were developed from solutions containing TATP in a concentration down to 15 ppb, distinct fluorescence signals could be detected in zone B due to the selective uncapping of the pores in the presence of TATP and subsequent **SuRh-Na** release. In the absence of TATP, no signal was found in zone B. Dye released showed a linear dependence on TATP concentration in the 10–50 ppb range.

The drying step is essential because varying amounts of residual liquid on the strip influence the fluorescence of the dye. This step is also the time-limiting step, that is, when using a hair dryer (in cold air blow mode), the assay can be completed in approximately 2 min (90 s development plus 30 s drying), and when letting the strip dry at room temperature under normal atmosphere, approximately 8 min are required to obtain a stable signal. When the PBS sample solution did not contain TATP, a negligible fluorescence signal was recorded in zone B (Figure 53a). However, when a similar experiment was performed, for example, with a solution containing TATP (0.5 ppm), a clear signal was found in zone B (Figure 53b). This is the first report of a flow assay based on massive indicator release from a nanoscopic chemical container device.

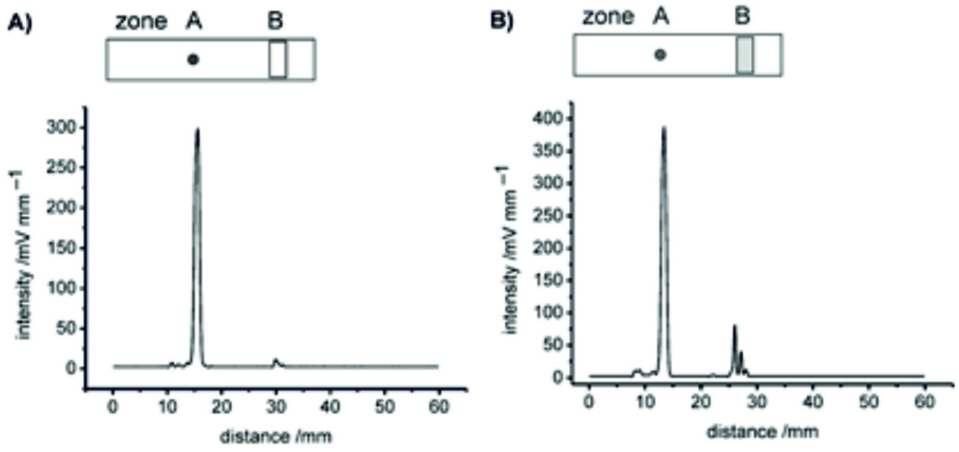

Figure 53 Signal obtained with the fluorescence reader (λ_{exc} = 520 nm, λ_{em} = 625 nm) in zones A and B after dye release and development of the flow assay in a) the absence and b) the presence of 0.5 ppm TATP in PBS buffer (pH 7.4); grey shades on the sketched strips resemble signal intensity.

The amount of dye released for each concentration was calculated through the ratio between the area of zone A and the total area of the test strip (Figure 54). A limit of detection of 15 ppb of TATP was determined by using this simple procedure.

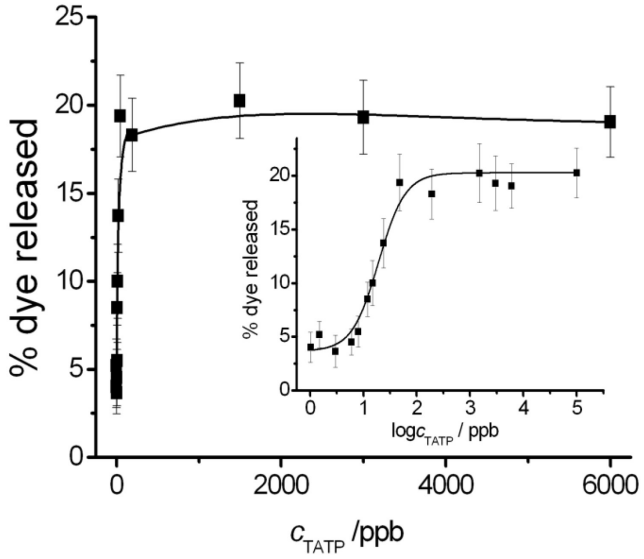

Figure 54 Sulforhodamine B release from test strips containing S1-AB at zone A in the presence of different amounts of TATP. The amount of release dye was determined through fluorescence at λ_{em} = 620 nm (λ_{exc} = 520 nm).

Performance of the strips under realistic conditions

Finally, the strips were tested under realistic conditions and were able to detect TATP in tap water (pH 7.4) as well as influent (pH 7.9) and effluent (pH 7.5) water of a sewage treatment plant at lower ppb concentrations, when for instance PBS 10X solution (0.1 mL) was added to the sample (0.9 mL) prior to dipping of the strip (Figure 55).

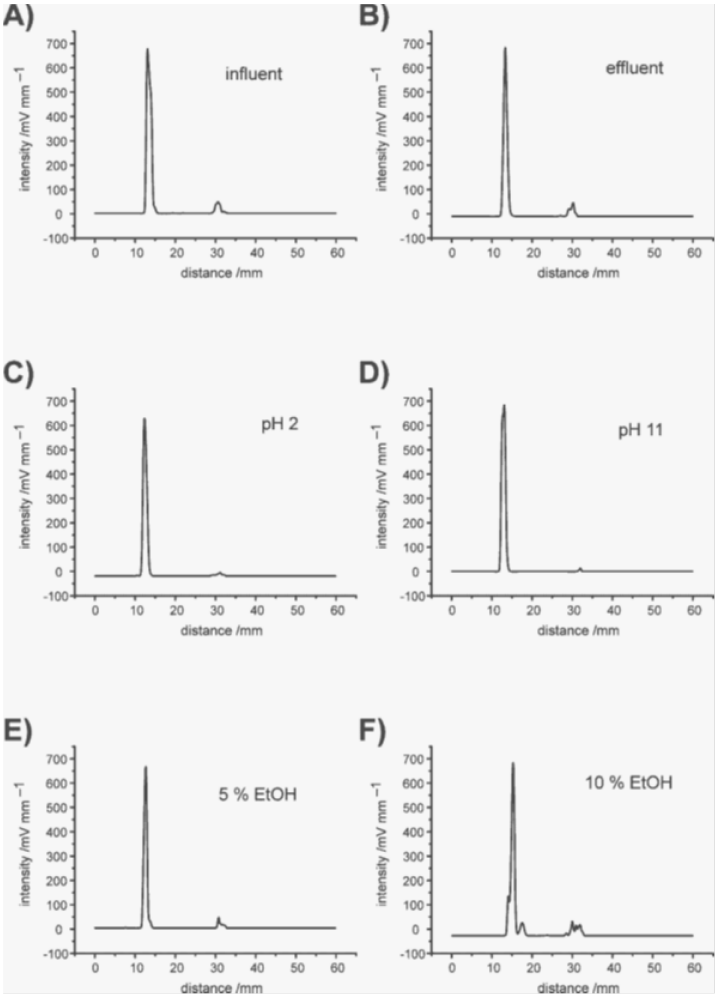

Figure 55. Performance evaluation of the strips with a) influent and b) effluent water of sewage treatment plant "Teltowkanal Wassmannsdorf", Berlin, c) and d) two selected pH as well as e) and f) two selected ethanol contents, 5 ppm TATP used in all the samples.

Regarding pH tolerance, the system was tested in the pH range 1–12 and TATP-induced delivery was observed at any pH value. However, below pH 4 and above pH 8.5, the delivery rates were reduced, presumably because at acidic pH, TATP starts to decompose[196 197]and at alkaline pH, the structure of the silica scaffold might be altered.[197] In addition, testing the assay on samples with ethanol s of 1–10% v/v revealed that enhanced release is observed only above 5%, most likely due to accelerated dissociation of the caps. Evidently, the strip-based assay is robust enough to accomplish the task of reliably determining the presence of TATP in scenarios to locate IED "bomb factories". This assay protocol finally allows small-molecule sensing at the ppb level in an easy-to-operate manner and an overall assay time of 2–10 min, which is considerably fast for a biochemical test.

4.2.3 Application of MCM-41 as host for a mercury sensitive BODIPY

The development of new or improved sensing methods for the sensitive and selective determination of mercury, applicable in a wide range of different sites and environments is of topical interest. Mercury is well known as one of the most toxic environmental metals,[198, 199] generated by many industrial sources such as gold production, coal mining and it can be found in electrical equipment.[200] Mercury ions are not biodegradable and can be accumulated in the environment which results in contaminated food and water.[201] It causes disorders of the central nervous system and leads to various cognitive and motor disorders due to accumulation processes like the Minamata disease.[202, 203] Therefore, the World Health Organization (WHO) and the United States Environmental Protection Agency (EPA) have strictly defined concentration limits in drinking water to 2 ppb.[204] The most common methods to detect mercury ions include atomic absorption spectroscopy and inductively coupled plasma mass spectrometry.[205, 206] But these are instrumentally expensive methods and often require extensive sample preparation. Spectroscopic techniques using chromo- or fluorogenic sensors[207] on the other hand allow the monitoring of non-fluorescent species like heavy or transition metal (HTM) ions with the advantageous features of optical spectroscopy also directly at site. In particular, the active part in optical sensors is often an indicator dye that responds to the analyte by a change in color or fluorescence. Considerable effort has thus been devoted to the development of fluoro- and chromogenic indicator dyes for Hg^{2+}.[157, 208, 209] But many of these molecules bear drawbacks in terms of actual applicability (lack of water solubility, cross-sensitivity toward other metal ions, matrix interferences). It has to be mentioned that fluorescent "turn-on" sensors are more desirable than "turn-off" sensors in terms of increased sensitivity and selectivity compared to "turn-off" related systems. However, the development of fluorescent "turn-on" sensors remains challenging because many HTM ions are intrinsic fluorescent quenchers.[210-214]

Besides the growing impact of sophisticatedly designed mesoporous silica materials on sensing application during the last decades,[9, 215, 216] a more straightforward attempt for mercury sensing through fluorescence enhancement in the lower ppb range was developed in this thesis. This approach is based on the understanding gained in the loading/release studies of the various dyes and MCM-41 as discussed in Chapter 4.2.1 and extended by the fact that the walls of silica scaffolds can be easily tuned for instance in polarity by covalent silane chemistry.[152, 217] The control of the adsorption capabilities within the pores of the mesoporous material by functionalization with various silane coatings will thus be exploited, offering a tailored microenvironment to harbor fluorescent molecules. In addition, a water-insoluble aza-

crown receptor bearing BODIPY was newly developed and loaded into MCM-41 materials using the mesoporous particles as suitable host material. This arrangement allows the application of the rather hydrophobic dye as sensitive mercury sensor in aqueous solution.

*Synthesis of sensor molecule **47***

The new BODIPY derivative **47** was synthesized in 29% yield by condensation of 4-(N-AT$_4$15C5)benzaldehyde **46** with two equivalents of kryptopyrrole **4** using TFA as a catalyst, followed by oxidation with DDQ, deprotonation with DIPEA and finally complexation with boron trifluoride at room temperature (Figure 56).[218]

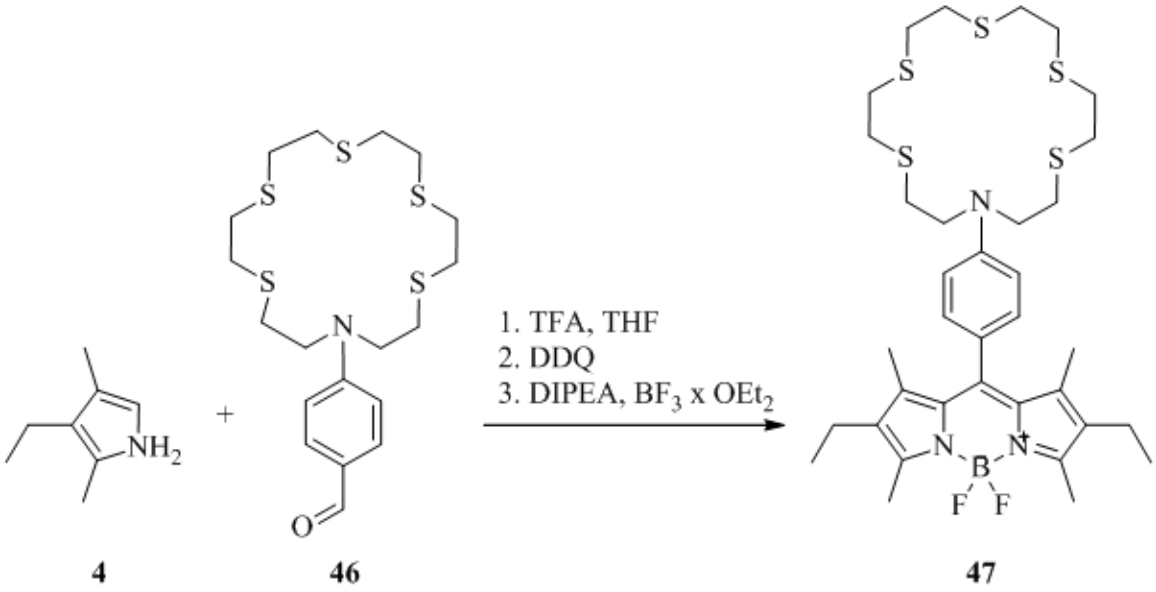

Figure 56 Synthesis of the mercury sensitive BODIPY 47 via the One-Step procedure.

*Spectroscopic properties of **47** in solution*

As shown in Figure 57 and Table 14 the main feature of **47** is its solvent dependent behavior accompanied with its outstanding sensing capabilities. In acetonitrile the fluorescence is strongly quenched and a dual emission is observed with an additional, red-shifted, broad charge transfer band next to the well-known BODIPY-localized emission band at 725 nm (locally excited state).[45]

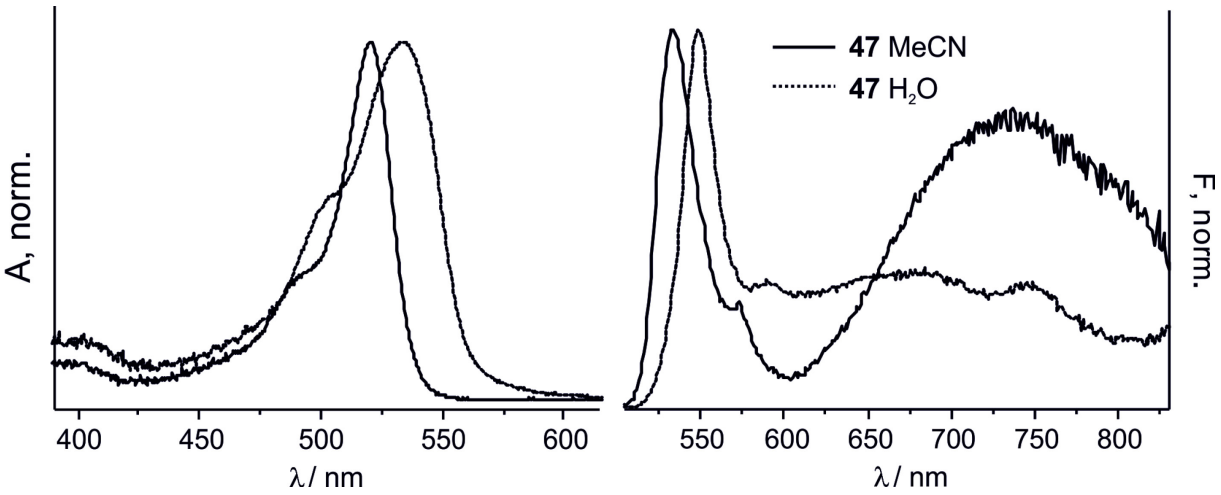

Figure 57 Normalized absorption and emission spectra of 47 in acetonitrile (solid line) and in water (dotted line), λ_{exc} = 490 nm.

In aqueous solution BODIPY **47** tends to form aggregates due to its hydrophobic character inducing a broadening of the absorption band and a shifting of the absorption and fluorescence maxima as discussed in general for this class of dyes in Chapter 2. The reaction of **47** with the thiophilic ions Hg^{2+} and Ag^{+} in solution, leads to complex formation. Whereas the binding leads to a large increase in fluorescence intensity, the changes in absorption are minor. The detailed photophysical behavior of an analogous compound in solution has been discussed in detail elsewhere. [45, 219]

Table 14 Spectroscopic data of 47 and 47-Hg^{2+} in water and acetonitril at room temperature.

Sample	λ_{abs} [nm]	λ_{em} [nm]
47 in H_2O	533	548
47 in H_2O + Hg^{2+}	526	538
47 in MeCN	521	534
47 in MeCN + Hg^{2+}	525	537

*Functionalization of MCM-41 and loading with **47***

Based on the observed properties of **47** in solution (Figure 57 and Table 14) the pores of the MCM-41 particles were first modified with various functional groups (amino, cyano or polyethylene glycol groups) via well-known silane chemistry to generate a suitable microenvironment for the hydrophobic dye **47**. In a second step the **47** was embedded within

the functionalized voids via non-covalent interactions. The functionalities of the anchored silane could potentially simulate a suitably polar microenvironment (similar to that in MeCN solution) for the dye within the particle pores, exploiting its outstanding sensing capabilities toward Hg^{2+} in this medium. After washing and drying the loaded particles could be applied in aqueous solution with reduced aggregation effects compared to the neat dye in water. Additionally non-functionalized MCMs bearing native hydroxyl groups were investigated for comparative purpose, too.

*Comparison of the functionalized and **47**-loaded MCM-41particles*

The position and form of the absorption and emission band of **47** could indicate if the dye forms aggregates, as shown in solution. The different functionalized MCM-41 particles were thus investigated in water with focus on the spectroscopic behavior of **47** within the particle pores giving information about the microenvironment of the dye.

The emission maximum of **47**-loaded, native MCM-41 particles (**MCM-OH**) in aqueous solution is centered at λ_{em} = 535 nm and thus the dye's microenvironment seems to be more similar to that in MeCN solution (Figure 57 and Table 15). But a slight broadening of the absorption band of **MCM-OH** particles comparable to the λ_{abs} of **47** in aqueous solution could be observed which could be an indication for possible dye aggregation under these conditions.

The aminated particles **MCM-NH_2** were obtained by the reaction of the particles' surface silanol groups with APTES **A** in solution. The functionalization with the aminosilane **A** has a twofold function: The hydrophobic BODIPY-core could presumably be embedded within the alkyl-chains of silane **A** maintaining the polar microenvironment with the NH_2-groups. Under the same loading conditions and dye concentration as for material **MCM-OH**, the absorption and emission maxima are more like that of the neat dye **47** in aqueous solution**. 47** seems to be aggregated within the particle pores or additionally adsorbed at the outer particle surface. Furthermore a diffuse offset appears in the fluorescence spectra at longer wavelengths which apparently did not change during the complexation with the metal-ions which is discussed later. To further simulate an appropriate polar microenvironment for **47** within the particle pores and to exploit its desired sensing capabilities finally cyano and poly(ethylene glycol) bearing silanes (**E** and **F**) were introduced on the particle surface and within the pores, too.

Additionally the concentration of **47** during the loading process was reduced to the half for **MCM-PEG** particles to avoid the observed dye aggregation effects. As depicted in Figure 58 and Table 15 the shapes and positions of the emission band of both materials are very similar to that of **47** in MeCN centered at λ_{em} = 536-537 nm. The main difference is the absence of

the broad long-wavelength shifted emission typical for **47** in MeCN (not shown for reasons of clarity).

Table 15 Spectroscopic data of 47 in solution and within the functionalized MCM-41 particles at room temperature, λ_{exc} = 490 nm.

Sample	Solvent	λ_{abs} [nm]	λ_{em} [nm]
47	MeCN	521	534
47	H_2O	533	548
MCM-OH	H_2O	525	535
MCM-NH$_2$	H_2O	528	544
MCM-CN	H_2O	525	537
MCM-PEG	H_2O	525	536

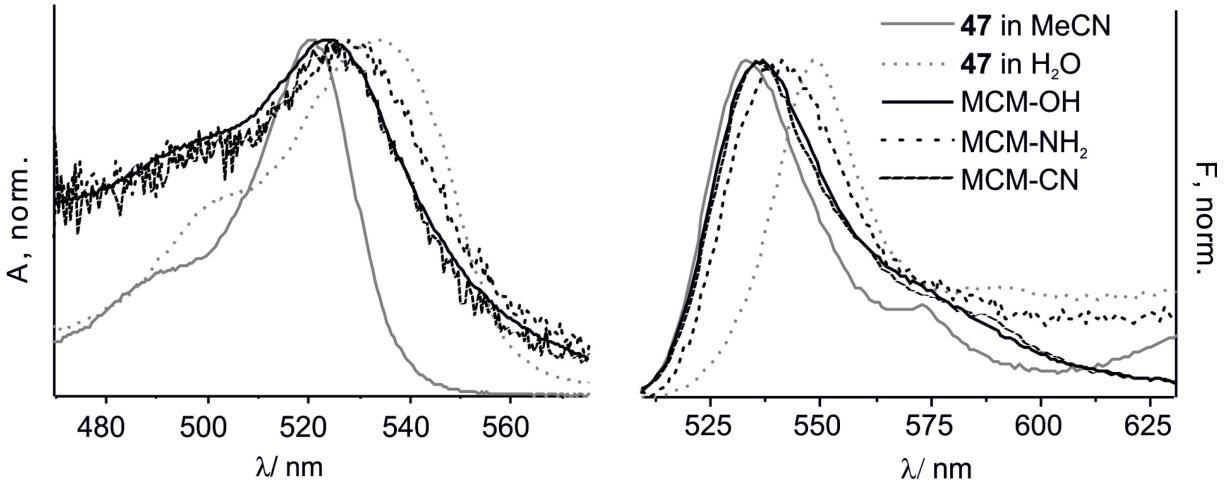

Figure 58 Normalized absorption and emission spectra of 47 (solid and dotted grey line) and the 47 loaded surface functionalized MCM-41 particles (solid, dotted and dashed black line), λ_{exc} = 490 nm.

Leaching test

Due to the fact that the **47**-Hg^{2+}-complex is water-soluble,[45, 219] the possibility of dye leaching out of the particle pores was investigated, too. For this purpose three particle samples of **MCM-NH$_2$** particles were incubated with 8 ppb, 800 ppb and 80 ppm Hg^{2+}, stirred for 10 min, centrifuged and the fluorescence intensity of the supernatant was measured. Applying the same particle concentration for all samples, the supernatant stays nearly colorless up to a concentration of 800 ppb Hg^{2+}. According to the expected increase of the fluorescence signal due to the mercury amount the slits of the spectrometer were adjusted properly. At a

concentration of 80 ppm the **47**-Hg^{2+} complex leached out of the pores and induced a drastic enhancement of fluorescence intensity in the supernatant. At concentrations in the desired lower ppb range no leaching could be observed. That means the measured fluorescence enhancement should solely be induced by the embedded **47**-Hg^{2+} complex within the particle pores.

Mercury sensing capabilities

The influence of the different microenvironments of **47** within the functionalized particle pores is remarkable regarding its sensing capabilities toward mercury ions. The addition of small amounts of Hg^{2+} in the lower ppb range, respectively leads to an increase of the fluorescence signal for all particle samples. Particle samples **MCM-OH**, **MCM-NH_2** and **MCM-CN** only show relatively small fluorescence enhancement factors (FEF) within the lower ppb range of Hg^{2+}.

Table 16 Fluorescence enhancement factor of the investigated materials after addition of 8 ppb Hg^{2+}.

Sample	[Hg^{2+}] ppb	I/I0
MCM-OH	8	1.15
MCM-NH_2	8	1.30
MCM-CN	8	1.37
MCM-PEG	8	2.06

Presumably the aggregation of **47** within the particle pores significantly hindered the Hg^{2+}-complexation ability of the dye concomitant with a low fluorescence signal enhancement. The effect of a low enhancement factor in the lower ppb range could also be observed for **47** in aqueous solution, when a comparably concentrated dye solution (stock solution of **47** in MeCN to ensure complete dissolution) was titrated with Hg^{2+} (Figure 59). At a high mercury concentration of 9.5 ppm only a factor of 41.7 was reached. This result underlined the aggregation hindered sensing performance of the investigated particle samples.

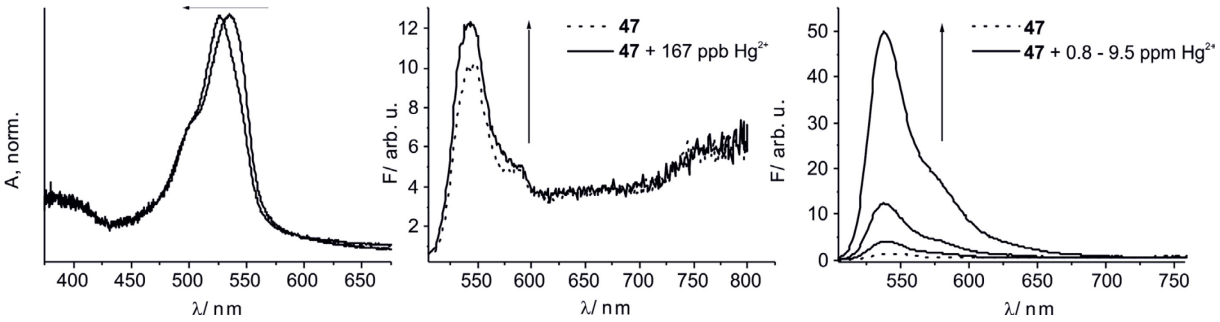

Figure 59 a) Normalized absorption spectra and b) Fluorescence spectra of 47 in water (λ_{exc} = 490 nm) during addition of various amounts of Hg^{2+}.

In contrast only **MCM-PEG** particles show increased sensing capabilities even in the lower ppb range Figure 60). At a mercury concentration of 0.8 ppb a FEF of 1.6 could be reached and the material seems to be a suitable candidate for mercury sensing in aqueous solution.

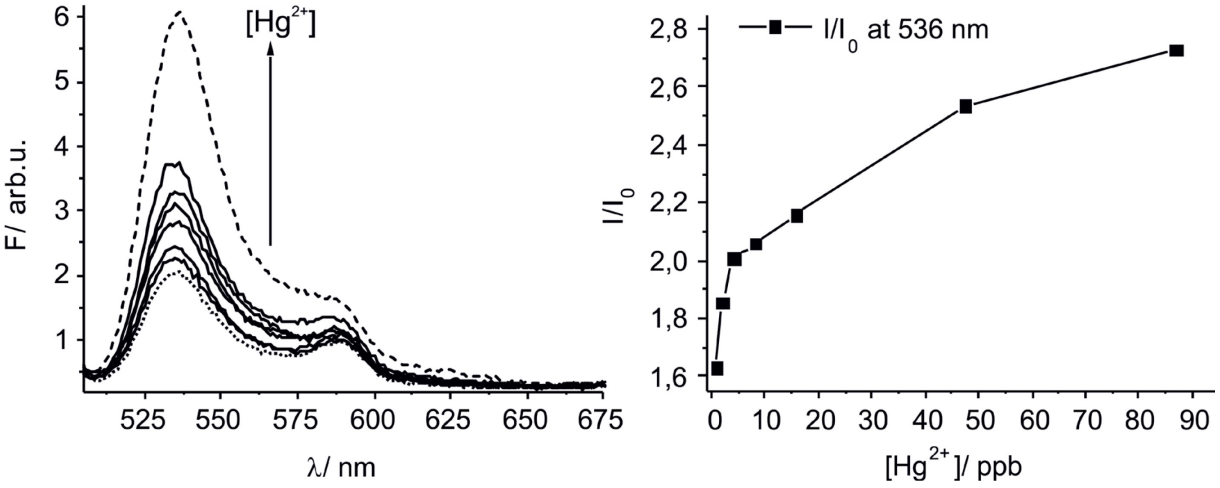

Figure 60 Left: Dependence of the fluorescence of 47 loaded MCM-PEG particles on change in mercury concentration from 0.8-86 ppb upon addition of aq. $Hg(ClO_4)_2$ solution (λ_{exc} = 490 nm), right: the plot of the FEF as a function of [Hg^{2+}].

Fluorescence lifetimes

To additionally get more insight in the photophysical behavior of **47** the fluorescence lifetimes of the dye and dye-M^+-complexes within the MCM-41 were determined. In water **47** show multi-exponential decay times (compare Chapter 2.2.1 compound **5**). **47**-loaded **MCM-OH** particles show a bi-exponential decay in aqueous solution. In agreement with the chelation-enhanced fluorescence, the fluorescence decay-times of the **47**-M^+-complexes increase drastically. The fluorescence lifetimes allow a distinct discrimination of the analytes (Table 17). Mono-exponential decay kinetics were only found for the Hg-complex, whereas for the Ag-complex the decays are bi-exponential. The fluorescence lifetimes of **47**-M^+ complexes within the particles' pores are in accordance with results of the neat dye obtained

in acetonitrile but with the difference that the system can be applied in pure water. As shown by Rurack *et al*. for an analogue compound a fluorescence enhancement effect (but less pronounced compared to Hg^{2+} and Ag^{+}) and a bi-exponential decay was only observed for Cu^{2+}, among all the other heavy and transition metal ions (Cu^{2+}, Ni^{2+}, Co^{2+}, Zn^{2+}, Cd^{2+}, Pb^{2+}).[219] This renders the high versatility of the particle based system for analytical purposes.

Table 17 Fluorescence lifetimes of 47 and MCM-OH particles in aqueous solution at 298K.

	τ_{f1} / ns, rel a	τ_{f2} / ns, rel a	τ_{f3} / ns, rel a
47 in H_2O	0.01, 94 %	0.116, 4.1%	3.89, 1.1%
MCM-OH H_2O	-	0.126, 75%	1.95, 25%
MCM-OH H_2O + Hg^{2+}	-	-	4.89, 100 %
MCM-OH H_2O + Ag^{+}	-	0.281, 54 %	2.73, 46%

Note: due to similarity of fluorescence lifetimes distributions of the other particle samples were not investigated yet

These results demonstrate that a sensitive and selective detection of the widely known fluorescence quencher Hg^{2+} can be achieved by generating a PEGylated surface as suitable microenvironment for the hydrophobic BODIPY dye **47** within functionalized MCM-41 particle pores. With the combination of the newly synthesized dye **47** and the high surface area of the mesoporous particle system a FEF of 1.6 could be achieved for 0.8 ppb Hg^{2+} in aqueous solution. In ongoing studies of co-workers the initially observed aggregation effects of the dye, were avoided by grafting propyl chains on the outer particle surface prior to carrying out the functionalization of the voids. Furthermore, the amount of loaded dye could be reduced to finally successfully improve this system for a mercury sensing in the upper ppb range in aqueous solution.

4.3 Conclusion

In summary, first the loading and release efficiency of mesoporous silica particles were optimized, investigating several fluorescent dyes with different electronic structures. The highest loading could be achieved with cationic dyes, due to the electronic interactions with the negatively charged particle surface, whereas a high release of the fluorescent dye molecules from the particle voids could be reached through electrostatic repulsion with the anionic structured dyes. The best candidate which showed a high loading as well as release ability was sulforhodamine B.

Based on these optimizations antibody-gated MCM-41 were designed that were loaded with sulforhodamine B and that can be used for the determination of the peroxide-based explosive TATP with a lateral-flow fluorescence reader, allowing detection limits in the lower ppb range. The mechanism of the detection relies on a displacement of the antibody from the surface of the hybrid material because of highly affine antibody–TATP interactions and the subsequent rapid release of a much larger number of entrapped dye molecules from the pores than antibodies are displaced. The high selectivity of the antibody is retained in the gated material, thus allowing for a remarkable discrimination against H_2O_2. System design and optimization led to straightforward integration into a lateral-flow assay without further treatment or conditioning of the test strips while guaranteeing fast overall assay times of < 10 min. Moreover, besides showing a remarkable robustness, the inherent architecture of the assay relies on a single-step immunochemical reaction. It can dispense with secondary (labelled) antibodies and enables ratiometric signal assessment in the presence of the analyte by simple comparison of the fluorescence signals in two zones. Because of the modularity of the approach, the concept is easily generalizable and applicable for many small-molecule analytes.

In the third part of the chapter the ability of the particle pores to serve as carrier platform for a newly synthesized mercury sensitive BODIPY dye **47** have been presented. The functionalization of the MCM-41 pores with poly(ethylene glycol) moieties generates an appropriate microenvironment for the hydrophobic dye without the need of a covalent linkage. The main feature of the dye bearing a thioaza-crown to show enhanced fluorescence signals by the presence of lower ppb amounts of mercury ions in acetonitrile could be transferred with this particulate system to aqueous solution. With this arrangement dye aggregation effects could be prevented and the step to an actual sensor format for application in aqueous solution could be accomplished.

5 Silica Nanoparticles

Dye-doped silica nanoparticles containing embedded or anchored dyes offer superior optical properties and open up new horizons for fluorescence detection. They are increasingly used, e.g., as fluorescent labels and probes for bioanalysis and medical diagnostics,[220, 221] compared to other nanomaterials like quantum dots that suffer from potential toxicity and brightness.[222] The silica matrix protects the dye molecules from the outer environment (chemical protection, reduction of quenching by molecular oxygen), increases photostability, provides enhanced signals because a nanoparticle hosting multiple dye molecules and often allows for better modularity in equipping such objects with different reactive groups. The enormous interest in synthetic nanoparticles for a variety of applications has led to the development of improved synthetic methods in order to evaluate their potential impact for analytical applications. The high versatility of silica nanoparticles as host for fluorescent dyes and the impact of the silica-network on the incorporated dyes are presented in the last chapter. Finally a silica nanoparticle based smart material for the sensitive, fluorometric recognition of anions and cations is presented.

5.1 Introduction

Since the pioneering report by Stöber and co-workers in 1968 producing virtually monodisperse spherical silica nanoparticles (SiO_2NP) in a defined size range between 0.05 µm to 2 µm,[223] the synthesis, characterization and application of these materials has extensively been exploited.[224, 225] There are principally two methods to synthesize monodisperse spherical SiO_2NP: Stöber's sol-gel and the reverse microemulsion method. In the case of reverse microemulsion method, established by Arriagada and Osseo-Asare[226] in the 1990s, the nanoparticles are synthesized inside surfactant-stabilized water droplets (micelles) which are dispersed in a non-polar solvent. The aforementioned Stöber method relies on the sol-gel chemistry of silicon alkoxides. Ammonium hydroxide is used as catalyst in water-ethanol solutions to control the hydrolysis and condensation rates of alkoxysilanes.[227] As depicted in Figure 61 first the alkoxysilane is hydrolyzed by water catalyzed by ammonia followed by condensation of the silicic acids to form polysilicic acid with Si-O-Si bonds, finally resulting in a three-dimensional network of spherical silica covered with hydroxyl groups. However, every small change in the experimental conditions (temperature, solvent, concentration, nature of the catalyst, stirring rate, molar compositions of the compounds) affects the final particle size in a considerable manner.[228]

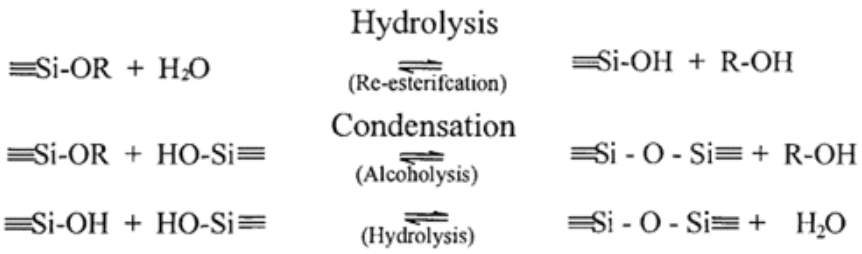

Figure 61 Reactions of the Stöber process.

The Stöber method was thus extensively investigated by several groups to determine the effects of the various reagents on size, reaction kinetics, monodispersity and sphericity of the particles and a wide range of particle sizes of SiO_2NP were thus realized. To improve the monodispersity and size control the seeded regrowth method was introduced. The less controllable nucleation step where small seed particles are formed was separated from the regrowing under well-defined conditions.[229, 230] Nonetheless the main limitation of the Stöber process still remains in preparation of smaller particles in the lower nanometer range. The smallest particles that can be prepared have a size around 15-20 nm and a very high polydispersity (typically >20%).[230] That limitation could be overcome with the use of the

basic amino acids arginine or lysine in a heterogeneous solvent system in which cyclohexane is used to decrease the hydrolysis rate of tetraethyl orthosilicate (TEOS). [231]

These essential achievements in silica particle synthesis and the widespread use of fluorescence in bioanalytical sciences furthermore led to the development of various kinds of fluorescent SiO_2NP for imaging and sensor applications.[232, 233] The silica matrix is an excellent host material to protect the dye molecules from the outer environment (chemical protection, reduction of quenching by molecular oxygen) and additionally could increase the photostability and provide enhanced signals.[234, 235] The silica material offers a biocompatible and easy to functionalize surface and therefore opens up new horizons for fluorescence based sensor systems. VanBlaaderen and co-workers first reported on the covalent incorporating of organic fluorophores into Stöber's colloidal silica by coupling them to reactive organosilicates.[229, 236] Throughout this work, the particle sizes reported remained in the hundreds of nanometers to microns range, but they are generally too large to be effective probes for biological applications. Comprehensive syntheses have since been performed to obtain dye doped SiO_2NP.[237, 238] Modifications using non-ionic surfactants to improve monodispersity and sphericity in the lower size ranges have also been extensively studied.[239-241] A main drawback of this approach is that the coupling of fluorescent dyes with appropriate silanes requires additional functionalization steps and the influence of these conjugates in the final particle synthesis is hard to predict. The incorporation of fluorescent molecules via electrostatic interactions is more straightforward because the dye is simply added during the particle synthesis. But the lack of covalent attachment of the fluorophore to the silica matrix means that the dye molecules can leach out of the particles over time, potentially decreasing the brightness per-particle which in turn might increase background signals and exposes the dyes to their environment.

Another important point is the question of dopant aggregation in sol-gel cages which has already emerged in 1984, in the very first report of molecular sol-gel entrapment describing the photophysical behavior of Rhodamine 6G (R6G) confined in a SiO_2 matrix. The encapsulation of dye molecules into the inner porosity of a sol-gel matrix affords a good molecular dispersion in the solid phase to prevent self-quenching effects due to aggregation of dye molecules. Whereas it was originally assumed that caging of a single molecule was taking place, it was later established that a high concentration (in the order of several mmol g^{-1}) in doped sol-gel materials aggregation was actually occurring. Typically at a dopant concentration > 10^{-3} M molecular aggregation starts as shown for example by fluorescence studies of silica-entrapped rhodamines (rhodamines tend to form non-fluorescent aggregates in the adsorbed state). [242, 243]

Although there are various reports on the preparation of quasi monodisperse and dye doped silica nanoparticles, the reproduction of those systems is quite difficult and there is still a lack in reliable protocols especially in the range below 100 nm. The incorporation of fluorescent dyes through electrostatic embedding or covalent attachment for advanced application purposes is an ongoing process. The spectroscopic properties of quasi monodisperse dye doped SiO_2NP in the lower size range were thus investigated and compared regarding the behavior of the encapsulated dyes within the silica microenvironment. Besides optical properties, various aspects such as particle size tuning, the behavior of the dyes, which show improved spectroscopic compared to the free dye and deposition of particles on flat surfaces will be discussed. Additionally the application of SiO_2NP functionalized with fluorophores and receptors for the selective and sensitive recognition of anions which play fundamental roles in chemical and biological processes[244, 245] are presented. [189, 190]

5.2 Results and Discussion

5.2.1 Synthesis and Characterization of SiO_2NP

Stöber method

There are myriads of publications dealing with the synthesis of quasi monodisperse SiO_2NP based on the aforementioned Stöber method. Due to the sensitive reaction composition first of all several reported formulas were examined and adapted to find a reproducible procedure. They basically have in common that ethanol, water, ammonia hydroxide and TEOS are used in different molar compositions. Depending on the reaction conditions (temperature, stirring rate) and adding procedure, theoretically different particle sizes could be obtained. Ethanol serves as co-solvent for the water-insoluble silane and ammonium hydroxide catalyzes the hydrolysis and condensation reactions and furthermore deprotonates the surface silanol groups. The resulting silanolate groups on the particles' surface lead to a stable dispersion due to electrostatic repulsion between the particles. Next to the stability monodisperse particle systems have consistent physical properties compared to polydisperse ones which is crucial for reliable protocols. Following several literature reports mostly polydisperse or bimodal SiO_2NPs were obtained (Table 18).[246-250] These experiments are not discussed in detail here due to their unsatisfactory results. Although the exact reaction conditions were followed only one reliable procedure afforded monodisperse SiO_2NPs with ~300 nm in size which are shown in Figure 62. DLS analysis was used to obtain the diameters and polydispersity of

these particles with a particle size analyzer. As listed in Table 18, it has to be mentioned that the particle sizes obtained by TEM measurements are reduced compared to DLS measurements, because in the latter the method yields the hydrodynamic radius of the particles.

Table 18 Investigated SiO_2NP synthesis routes from literature.

Sample	$Ø_{DLS}$ [nm]	TEM	Literature
Chen 60 °C	94.38 ± 7.38	Polydisperse	Chen et. al.[247]
Chen 50 °C	78.02 ± 9.61	Polydisperse	
Chen 45 °C	76.42 ± 2.68	Polydisperse	
Chen 40 °C	150.60 ± 6.13	Polydisperse	
Chen 31 °C	201.90 ± 13.80	Polydisperse	
Chen 25 °C	235.00 ± 4.55	Polydisperse	
Razo1-4	100.05 ± 10.07	Polydisperse	Razo et. al.[246]
StöberSil60	73.64 ± 9.37	Polydisperse	Thomassen et. al.[248]
StöberSil140	209.20 ± 4.23	Polydisperse	
StöberSil335	305.20 ± 2.17	monodisperse	

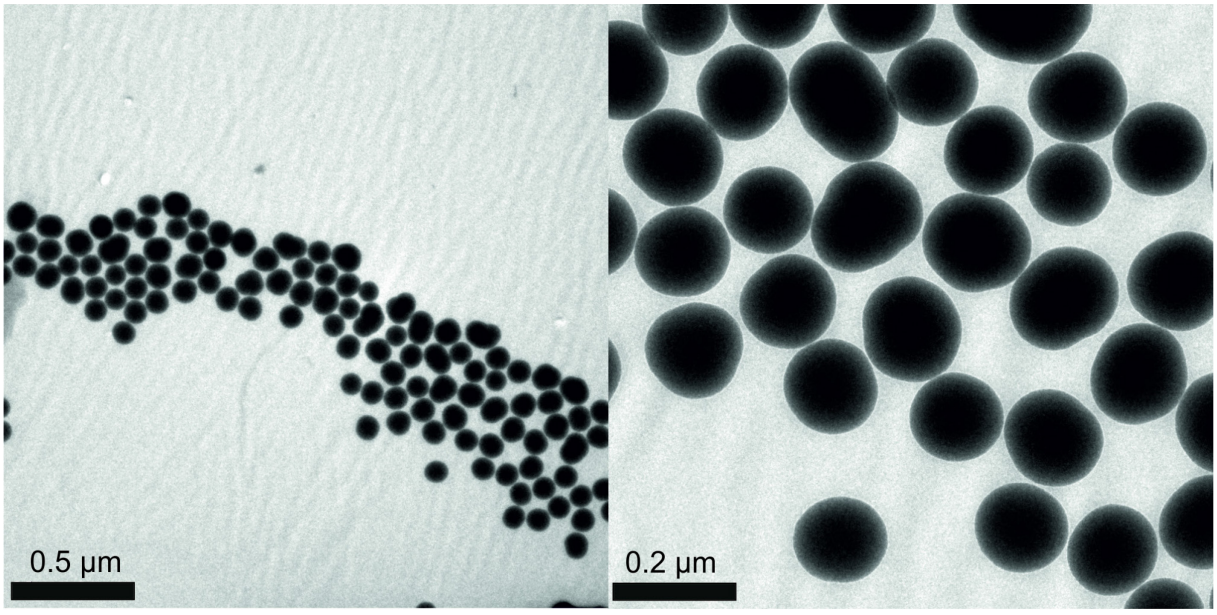

Figure 62 TEM image of 300nm silica particles.

Clearly, these images demonstrate that the silica particles of sample **StöberSil335** are nanometer-sized and highly monodisperse. The average particle sizes are listed in Table 18. But these results also show that the influence of the different synthesis parameters on the final

particle size (and monodispersity) is very complex and a size-controlled synthesis is apparently not reproducible from lab to lab.

Amino-acid catalyzed method

An important breakthrough in the synthesis of monodisperse SiO_2NP in the size range below 100 nm which could not be obtained by the common Stöber method could be reached by Yokoi et al. and was further elaborated by Thomassen et al.[248, 251, 252] Particles in this size range are very important for further bioanalytical applications to prevent unwanted endocytotic uptake.[253, 254]

Two particle samples (**Lys26** and **Lys36**) were obtained by drop wise adding various amounts of TEOS to a stirred aqueous ethanolic solution at 60 °C containing L-lysine as the basic catalyst. The hydrolyzed TEOS is delivered slowly using a top layer of hexane. The two sols were aged for 72 h and dialyzed against water to remove remaining reactants. It has to be pointed out that a cleaning by common known washing and centrifugation steps was not successful due to the irreversible formation of particle aggregates which can be prevented by using dialysis. TEM images of synthesized SiO_2NP according to this procedure are shown in Figure 63.

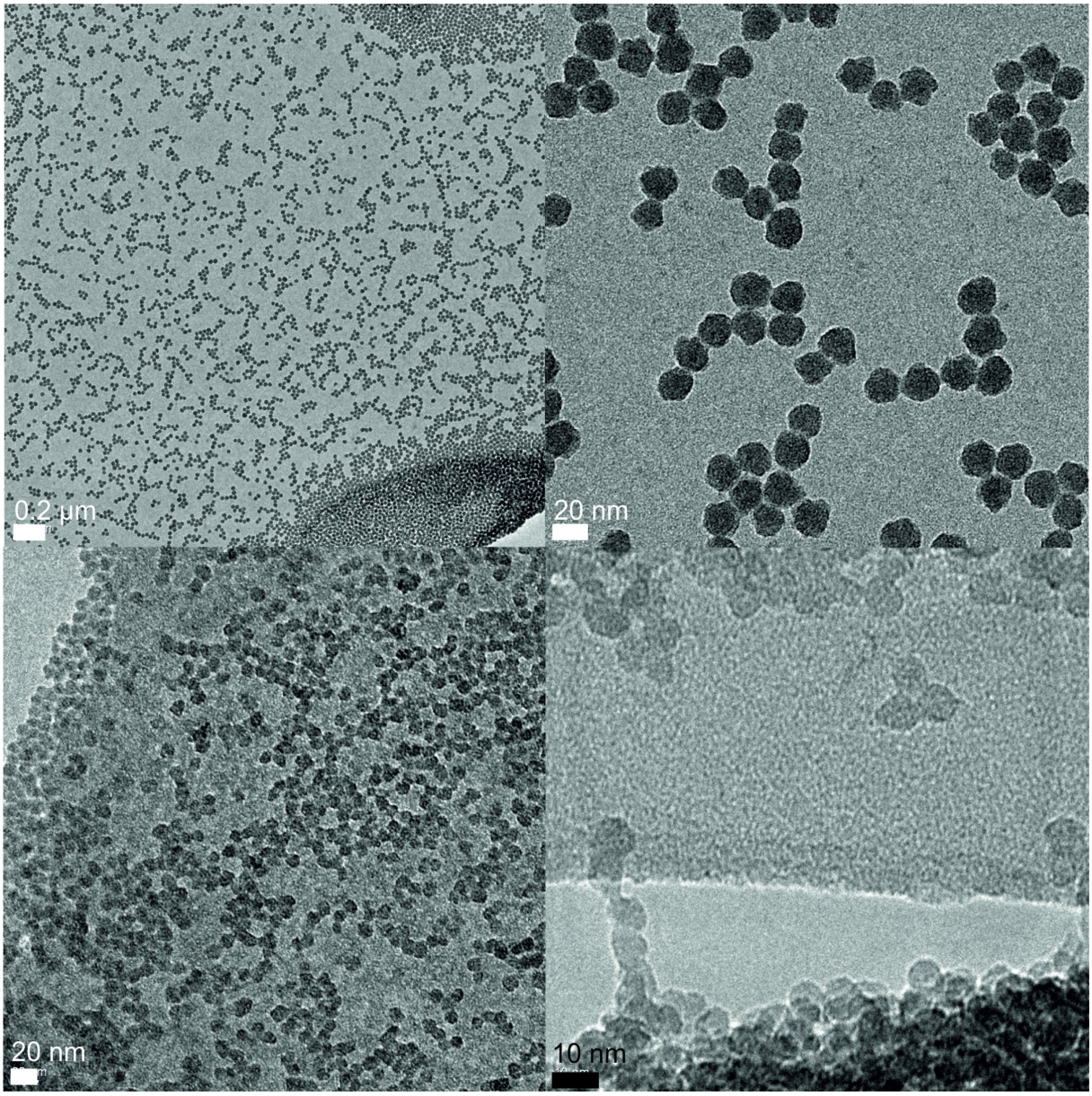

Figure 63 TEM images of SiO_2NP obtained by L-lysine catalyzed synthesis route.

The images demonstrate nanometer-sized and monodisperse SiO_2NPs obtained following that procedure. The average particle sizes shown by TEM and DLS measurements are listened in Table 19.

Table 19 Average particle diameter obtained by TEM and DLS measurements.

Sample	$Ø_{av}$ (TEM) [nm]	$Ø_{av}$ (DLS) [nm]
Lys26	8.31 ± 1.47	9.34 ± 0.09
Lys36	22.87 ± 1.87	32.95 ± 0.49

The particles of sample **Lys26** have a size around 8 nm. They are spherical but with a rough surface more seed-shaped. Obviously the amount of silane is not sufficient to form a smoother surface structure. With a 5-fold higher molar amount of TEOS particle sample **Lys36** was obtained with a particle size of 23 nm. The impact of L-lysine one the one hand is the

aforementioned role as catalyst for the hydrolysis of TEOS. On the other hand it influences the size of the silica spheres more generally compared to the Stöber method, because the lysine molecules cover the particles in the growth process through the electrostatic interaction (hydrogen bonding) of their protonated amino groups with the anionic silicate groups. The pK_A values of the α-COOH, α-NH_3^+, and α-$(CH_2)_4NH_3^+$ in L-lysine are determined to be 2.18, 8.90, and 10.28, respectively, and the isoelectric point of L-lysine is 9.74, i.e., about 92% of α-$(CH_2)_4NH_2$ and 33% of α-NH_2 would be protonated under the synthesis conditions (pH 9.2).[251, 255] The main benefit is the possibility to obtain monodisperse, small SiO_2NP with this procedure, besides the drawback of a relatively long reaction time of 72 h.

Utilizing this approach as a starting point, Hartlen *et al.*[231] reported on the facile preparation of highly monodisperse silica particles ranging from 15 nm to 200 nm using a regrowth approach and L-arginine instead of L-lysine as basic catalyst in aqueous media. The so called *silica seeds* were synthesized by adding TEOS to an L-lysine containing aqueous-ethanolic solution with a cyclohexane top-layer and after only 20 h and clean-up via dialysis, highly monodisperse 25 nm sized SiO_2NP were obtained (H_1-$H_{1''}$). SiO_2NP of this size could be reproducibly synthesized in several trials as shown in Figure 64 and Table 20.

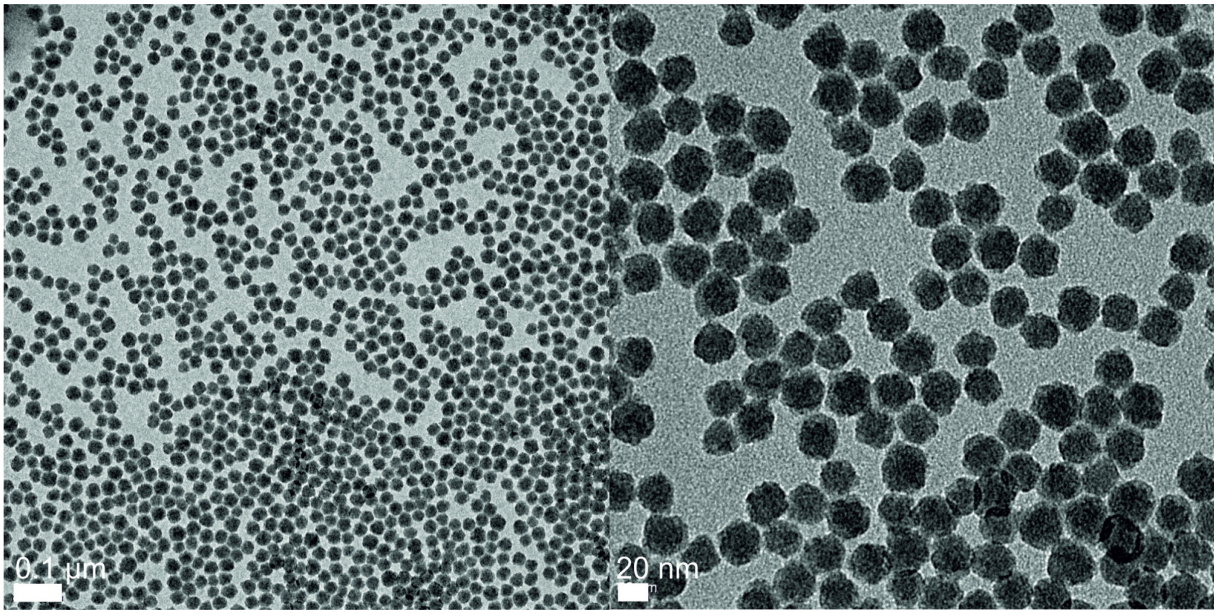

Figure 64 Seed particles obtained by L-arginine catalyzed synthesis route.

Table 20 Average particle diameter obtained by TEM and DLS measurements.

Sample	$Ø_{av}$ (TEM) [nm]	$Ø_{av}$ (DLS) [nm]
H_1	25.17 ± 2.28	29.64 ± 8.81
$H_{1'}$	n.d.	28.24 ± 6.40
$H_{1''}$	n.d.	26.12 ± 8.51

Compared to the method of Yokoi *et al*. TEOS is added in one portion which excludes any variations during the addition procedure. Additionally the reaction time only amounts to 20 h. Because of the good reproducibility of the particle size this procedure can be further used as reliable protocol. Another advantage is the option to increase the particle size directly to 45 nm through a single regrowth step where the as-prepared seed solution is directly taken from the reaction solution without further cleaning steps. The concentration of L-arginine is sufficient to grow a silica layer on the seed particles through simple addition of TEOS. The final volume ratio of total TEOS to cyclohexane remained at 1:1. After 30 h at 60 °C and dialysis to remove remaining reactants, particles with an average size of 45 nm as shown in Figure 65 were obtained.

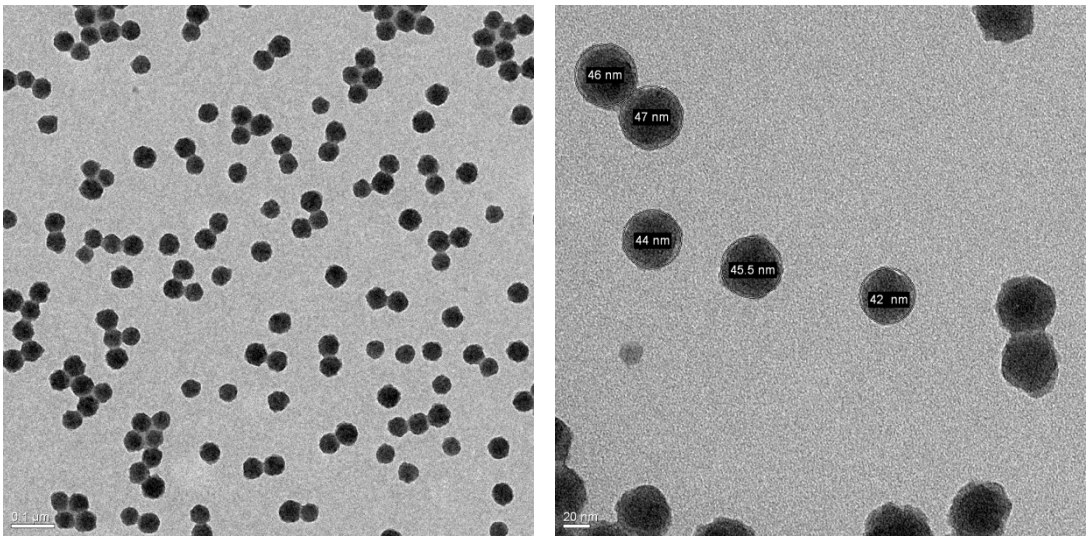

Figure 65 SiO_2NP 1. Regrowth from silica seeds.

Variation of the reaction conditions

The question raised weather it is possible to tune the reaction conditions in such a manner that with straightforward methods further useful particle sizes could be reached (enhanced reactivity and greater ability to penetrate tissues and cell membranes).[256, 257] Based on the described seed procedure, first of all the influence of the reaction temperature on the seed particle formation was investigated while keeping the molar composition of the reactants constant. The obtained SiO_2NP are shown in Figure 66 and Table 21.

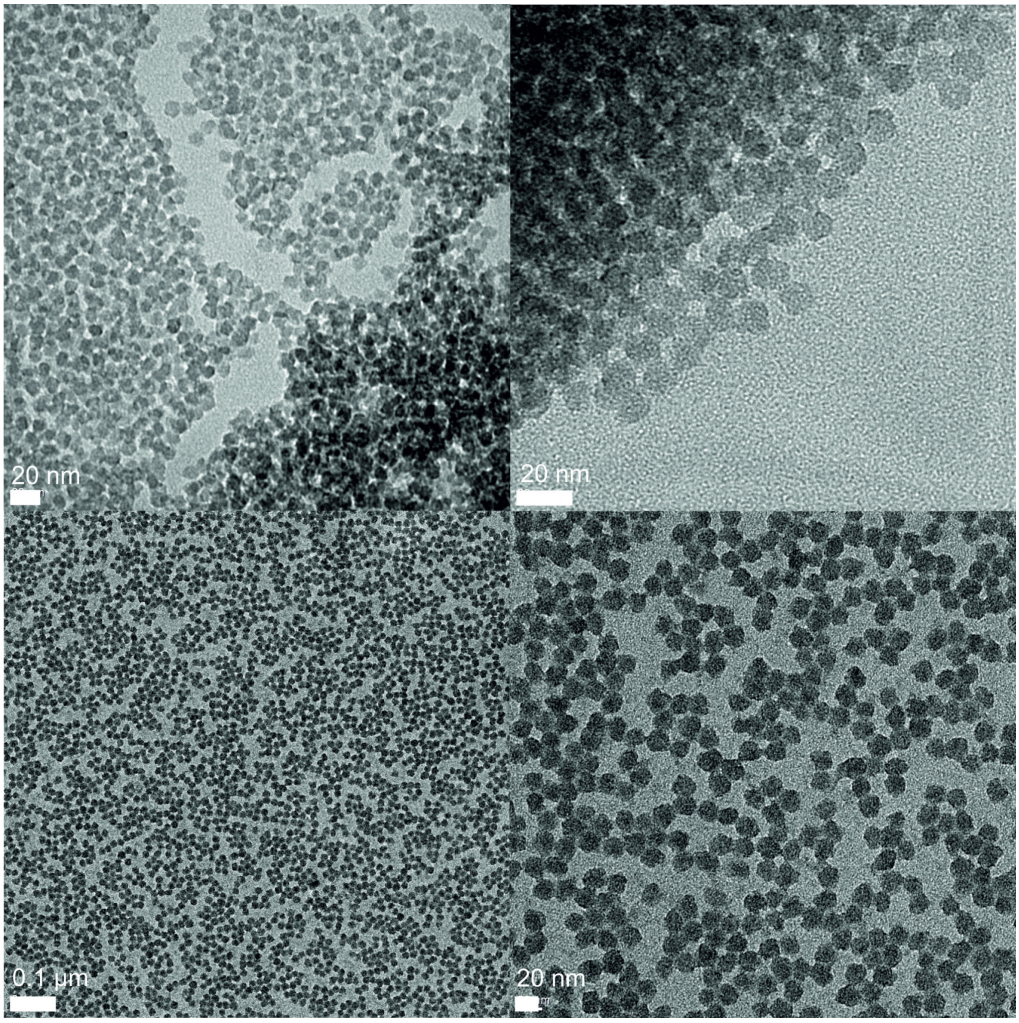

Figure 66 TEM imagesof SiO_2NPs, top: 40 °C reaction temperature, bottom: 50 °C.

Compared to a reaction temperature of 60 °C the particle size is reduced up to ~ 14 nm using 40 °C and up to ~17 nm for 50 °C. At a reaction temperature of 22 °C only a bulky amorphous material could be obtained and no particles were formed (not shown).

Table 21 Average particle size obtained by TEM and DLS measurements.

Sample	$Ø_{av}$ (TEM) [nm]	$Ø_{av}$ (DLS) [nm]
$\mathbf{H_{40\ °C}}$	11.01 ± 2.45	n.d.
$\mathbf{H_{50\ °C}}$	13.90 ± 2.11	n.d.

This means that the reduction of the reaction temperature leads to smaller particle sizes, yet that temperatures below 40 °C are not convenient to induce seed formation. In the second approach the influence of the added amount of TEOS was investigated keeping the molar composition of the other compounds constant at a reaction temperature of 60 °C. Based on the procedure to obtain silica seeds (samples $\mathbf{H_2}$-$\mathbf{H_3}$) the amount of added TEOS was increased up to 1.75 molar equivalents and for the first regrowth stage up to 2.00 molar equivalents as shown in Table 22.

Table 22 Average seed particel sizes obtained by TEM and DLS measurements.

Sample	$Ø_{av}$ (TEM) [nm]	$Ø_{av}$ (DLS) [nm]	n_{TEOS} [eq.]
H_2	n.d.	28.43 ± 7.76	1.25
H_3	26.11 ± 3.25	29.71 ± 6.90	1.50
H_4	35.72 ± 2.09	37.19 ± 8.45	1.75

By increasing the molar amount of TEOS (+75%) in the initial silica seed synthesis the final particle diameter is increased around 10 nm. But the observation was made that new silica seeds are formed under the chosen conditions. (Figure 67). 25%-50% molar excess of TEOS did not have any significant influence on the particle size (not shown).

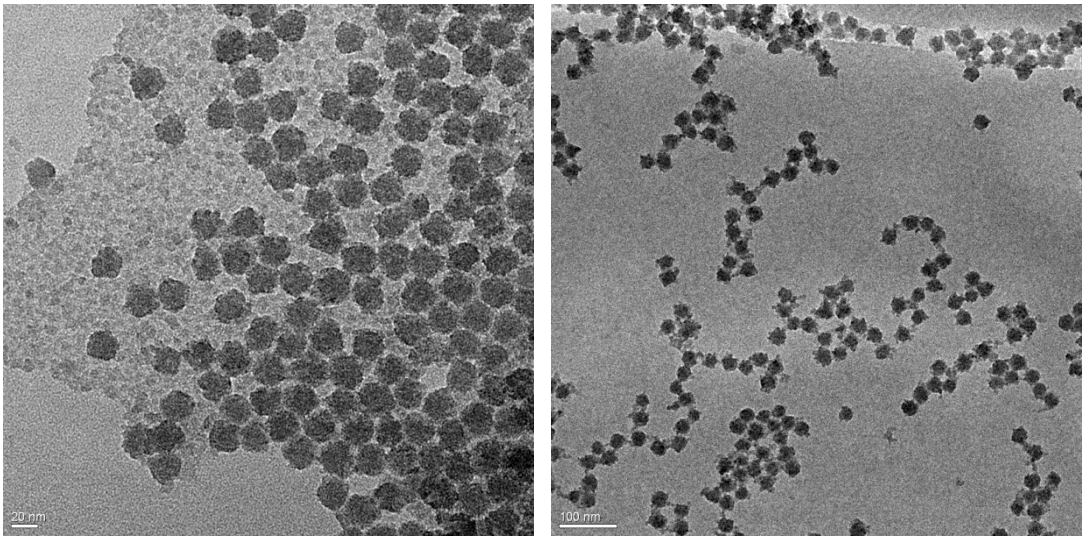

Figure 67 TEM image of samples H_3 (left) and H_4 (right).

5.2.2 Synthesis of dye doped silica nanoparticles

One of the main tasks of recent research in the area of nanobiotechnology is the development of highly photostable multifunctional nanocomposites for fluorescence-based detection in bioimaging and biolabeling. These materials with submicron-sized dimensions are starting to replace ttraditional types of organic dyes as fluorescent markers especially for optical imaging applications. Dye-doped silica nanoparticles containing embedded dyes offer superior optical properties and open up new horizons for fluorescence detection.[258-260]

Based on the previously outlined synthesis of SiO_2NPs, the question arose if it is possible to directly incorporate fluorescent dyes while keeping the particle size and monodispersity constant. For this purpose long-wavelength emitting oxazine dyes Nile Blue **48** (NB) and Cresyl Violet **49** (CV) were chosen which facilitate the potential bioanalytical application

attributed to the decrease in possible interferences from biological material at these wavelengths (Figure 68).[261, 262]

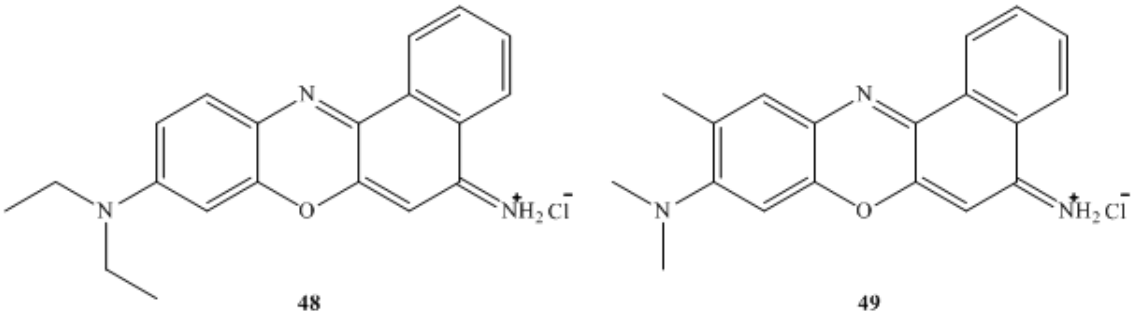

Figure 68 Chemical structures of Nile Blue 48 (NB) and Cresyl Violet 49 (CV).

By the simple addition of an aqueous solution of the respective dye (**48** or **49**) to the particle reaction mixture, the appropriate fluorophore was embedded through electrostatic attractions between the charged organic dye and the negatively charged silica network (see also Chapter 4.2.1). After dialysis against water, the supernatant showed no fluorescence signal, indicating that there is no dye-leaching and the dye molecules are entrapped within the particle matrix. Thus the covalent attachment of the dyes to an appropriate silane precursor was not necessary.

With this procedure 20 nm monodisperse SiO_2NPs were synthesized via the as-described amino acid-catalyzed method with initial dye concentrations between 13 µM – 1.3 mM (**NB_1-NB_3 20nm**). 45 nm core-shell SiO_2NPs were synthesized with a dye-doped silica shell and 25 nm silica core (**NB_1-NB_3 45nm**) and 300 nm monodisperse SiO_2NPs (**NB_1-NB_3 300nm**) were synthesized via the ammonium hydroxide-catalyzed Stöber method (Chapter 5.2.1).

Table 23 Reproducible dye-doped SiO_2NP obtained by the ammonium- and amino-acid catalyzed Stöber method.

Sample	DLS	TEM
NB 20nm	18 ± 2 nm	17 nm
NB 45 nm	50 ± 10 nm	47 nm
NB 300 nm	294 ± 30 nm	310 nm

Spectroscopic characterization of dye-doped SiO_2NPs

Figure 69 and Table 24 show the spectroscopic features of the dyes and the resulting dye-doped silica nanoparticles investigated by absorption as well as steady-state and time-resolved

fluorescence spectroscopy. The spectral features of the synthesized SiO_2NPs were compared to the neat dyes in aqueous and ethanolic solution (Figure 69). The absorption maxima of **48** in water and EtOH are located at ca. λ_{abs} = 625 nm. In EtOH a shoulder appears at 500 nm which is absent in water. Due to low dye concentration and additional scattering effects of the silica particle matrix, the absorption spectra of the particles were not exploitable and are not shown. The emission maxima of **48** in water is located at λ_{em} = 668 nm and shifted to shorter wavelength in ethanolic solution (λ_{em} = 650 nm). The silica matrix generates a microenvironment comparable to an ethanolic solution indicated by the emission maximum of the particles of λ_{em} = 648 nm.

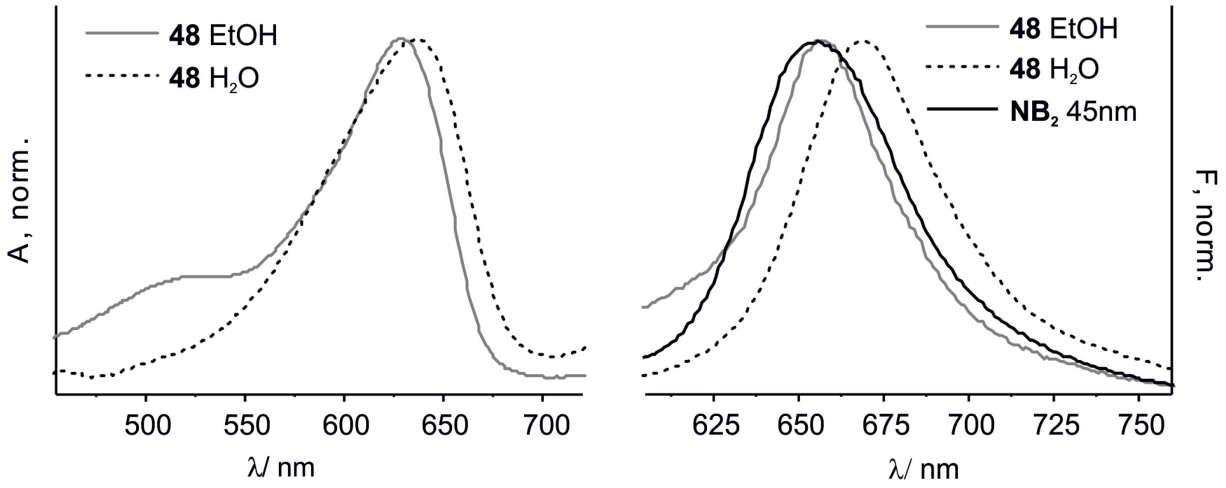

Figure 69 Normalized absorption and fluorescence spectra (λ_{exc} = 575 nm) of NB in H_2O and EtOH and NB-doped 45 nm sized core-shell SiO_2NPs in H_2O.

Figure 70 shows the emission spectra of **48** doped SiO_2NPs of various sizes obtained at λ_{exc} = 575 nm. At the highest dye concentration of 1.3 mM in the final reaction mixture quenching effects occur for the 45 nm and 300 nm sized particles. This could not be observed for the smallest 26 nm - sized particles. Spectra of **49** doped particles are not shown and discussed in detail due to similarity.

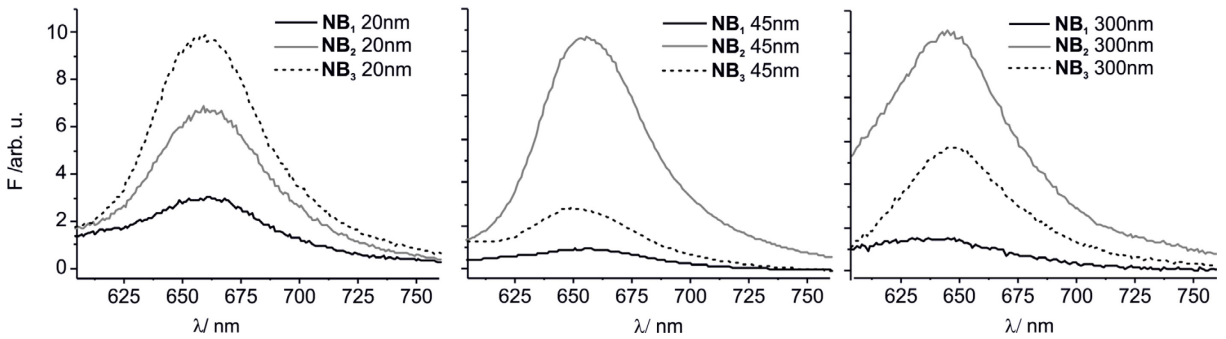

Figure 70 Nile blue 48 doped SiO_2NPs (26 nm, 45 nm, 300 nm) in water, NB_1 = 1.3 × 10^{-3} M, NB_2 = 1.3 × 10^{-4} M, NB_3 = 1.3 × 10^{-5} M.

The steric embedding of the dyes leads to increased fluorescence intensities of the incorporated fluorophores in water and ethanol. The fluorescence lifetimes of the 300 nm particles revealed that **NB_2** (0.13 mM) and **NB_3** (13 µM) show stronger fluorescence compared to the free dye in ethanolic solution. **NB_1** (1.3 mM) with the highest doping leads to the lowest fluorescence intensity due to the formation of non-emissive dimers or aggregates (only slow component observed in the decays, see below).

Table 24 Determination of fluorescence lifetimes of dye-doped SiO_2NPs and the free dye in solution.

	τ_f	
	Nile Blue **48**	Cresyl Violet **49**
EtOH	1.59 ± 0.23 ns	3.33 ± 0.37 ns
Water	317 ± 65 ps	2.33 ± 0.27 ns
Particle	1.84 ± 0.30 ns[a]	2.46 ± 0.24 ns

[a] Bimodal fluorescence lifetime distributions are found for particles **NB_2** and **NB_3** (minor component 0.55 ± 0.08 ns).

With a decrease of the doping degree, the relative amount of long-lived **48** species, that has a lifetime comparable to the free dye in polar organic solvents, increased.

The electrostatic embedding of the oxazine dyes **48** and **49** into SiO_2NP by a simple protocol improved the fluorescence and stability features of the dyes in aqueous media compared to the free dye in solution, especially for the weaker fluorescent and stronger Stokes-shifted **48** compared to **49**.

Deposition of SiO_2NPS on glass surfaces

It has already be shown, that 25 nm sized SiO_2NPs could be deposited on glass surfaces in homogeneous and stable monolayer to enhance the surface area and improve signal to noise ratios for microarray based bioanalytical applications.[263-266] We thus investigated the formation and stability of single monolayers of commercial available 2 µm sized SiO_2NPs.

Aqueous particle suspensions ranging from 0.60-25.00 mg ml^{-1} were directly placed on the glass surface of microscopy slides, bearing an appropriate mask. After evaporation of the solvent and drying overnight at 100 °C in a vacuum oven, the obtained particle layers were stable against washing and functionalization steps. With optimized amounts of 5.00 mg ml^{-1} (100 µg) stable bilayers could be generated. Monolayers were produced by placing 2.50 mg ml^{-1} (50 µg) particle suspension on the glass as shown in Figure 71 a and b. After the

successful attachment of reactive amino groups with APTES **A** (Figure 71 c) the enhanced sensing performance could possibly be evaluated, e.g. according to the protocol for flat surfaces of Ref. 95 with the amino-reactive fluorescent BODIPY **36** (Chapter 3.2.1).

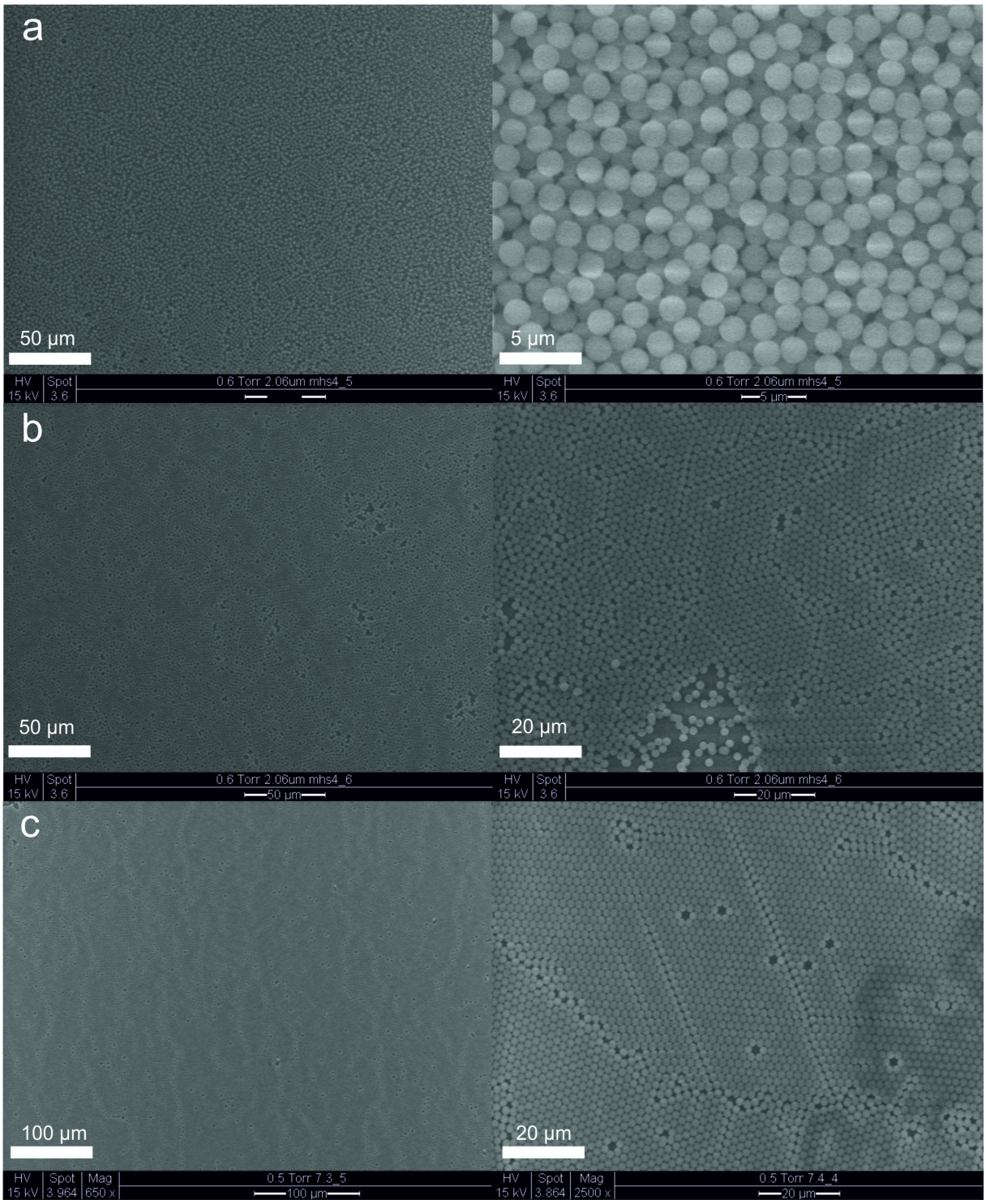

Figure 71 2 µm SiO_2NPs on glass, a) Bilayer, b) Monolayer, c) APTES functionalized Monolayer.

5.2.3 Application of functionalized SiO_2NPs for ion sensing

Using silica nanoparticles as supporting material for sensing applications has received tremendous interest during the past years. [267, 268] Among different inorganic supports silica nanoparticles have been extensively used for hybrid sensing materials due to their straightforward preparation and surface functionalization and high stability in aqueous suspensions.[62, 269] The independent functionalization of inorganic surfaces with receptor and fluorophore units is an appealing approach that overcomes the synthetic problems usually immanent to the classical ‘‘binding site–signaling subunit’’ architecture.[270] Moreover, signal amplification and cooperative binding effects associated with the independent anchoring of receptors and fluorophores in close proximity to each other and to the surface of the support are noticeable features of this strategy, allowing for instance intercommunication between both subunits without the need for a direct covalent link between them. Employing silica nanoparticles functionalized with fluorophores and suitable coordination sites, this approach has recently been used for the selective recognition of metal cations.[271, 272] In contrast, hybrid nanoparticles for the optical recognition of anions are much less explored.[273, 274] Due to the fundamental roles that anions play in chemical and biological processes the development of chromo- and fluorogenic chemosensors especially for anions is an ongoing process.[244, 245] The spectroscopic properties of functionalized silica nanoparticles with cation coordination sites (terpyridine) and fluorophores (sulforhodamine B) in the differential sensing of anions were investigated which was developed by Calero *et al*.[275] The attached fluorophore (F) and receptor (R) do not bind to the analyte but to a mediator. A quenching metal ion (Q), which is at the same time a good binder for the target anion, then served as the mediator, i.e., as the displaceable species, arriving at a quencher displacement assay (QDA, Figure 72). First the R units of the highly fluorescent receptor- and fluorophore-functionalized nanoparticles are loaded with Q, switching off the hybrid’s fluorescence. Second, addition of the target analyte, which shows a higher affinity for Q than R does, displaces Q from R, leading to revival of the fluorescence. In a third step, regeneration of the material is simply accomplished by reloading Q onto the sulforhodamine B functionalized NPs. The terpyridine units as R for the quencher metal ions Q and sulforhodamine B as signaling units F were independently anchored onto the surface of the silica nanoparticles.

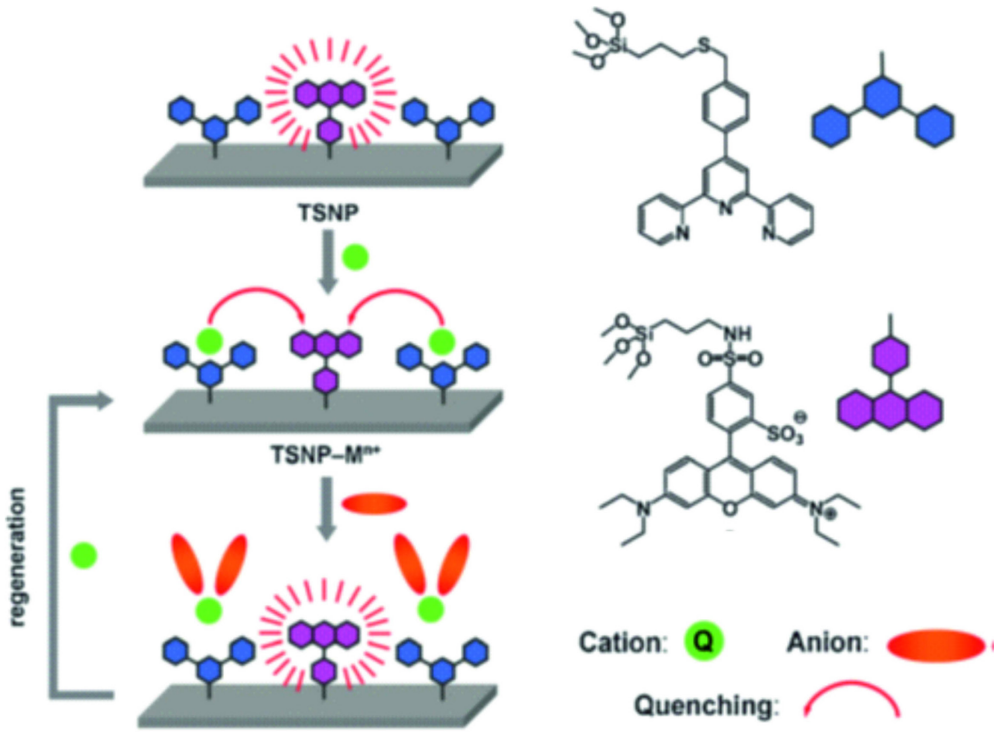

Figure 72 Design concept of the quencher displacement assay involving terpyridine-sulforhodamine-functionalized silica nanoparticles and metal ion quenchers.

Spectroscopic characterization of the functionalized particles

The terpyridine–sulforhodamine-functionalized nanoparticles (TSNP) and nanoparticles functionalized only with **SuRh-Na** (SNPs) as reference show a homogenous particle size of 20 ± 2 nm (Figure 73). The emission of the sulforhodamine fluorophore was retained after the grafting of the signaling units onto the surface of the nanoparticles. Excitation of acetonitrile suspensions of TSNPs at 575 nm gave rise to an emission band at 580–660 nm, similar to that obtained for sulforhodamine B chloride in acetonitrile (Figure 73). Fluorescence lifetime measurements revealed that the decay times of the dye in the TSNPs (τ_f = 2.21 ns; and SNPs τ_f = 2.21 ns) is virtually identical to that of the isolated molecule in solution (τ_f = 2.24 ns) which stresses the fact that the single dye molecules do not interact with each other when attached to the surface and that grafting has also no influence on the fluorophore's properties.

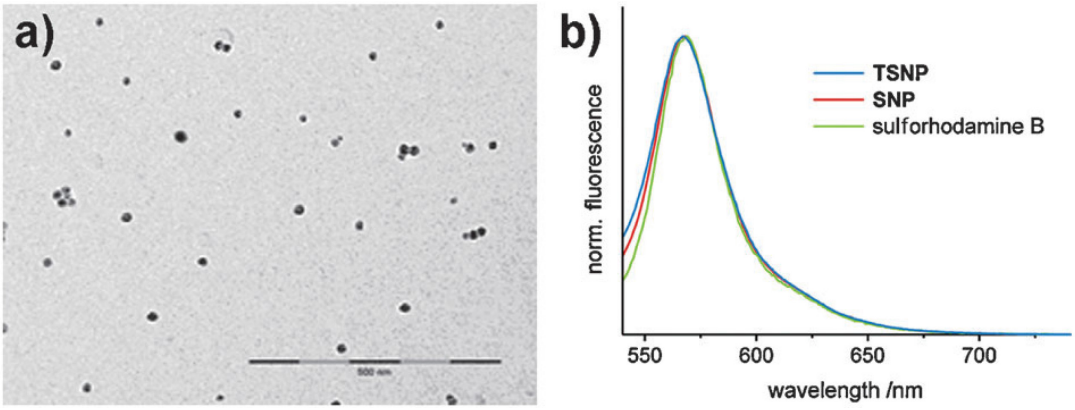

Figure 73 TEM image of TSNPs (left), fluorescence spectra of TSNP and SNP suspended and SuRh-Na dissolved in MeCN (right).

Effect of various heavy- and transition metal ions in MeCN

Suspensions of TSNP (2.5 mg in 20 mL) were titrated with Fe^{3+}, Hg^{2+}, Cu^{2+}, Ni^{2+} and Pb^{2+} (as perchlorate salts). It would be expected that the rather non-selective ligand, terpyridine binds all these metal ions. In all cases, a quenching of 94–99% of the rhodamine emission was observed. The quenching of the dye's fluorescence involves an energy or electron transfer or enhanced spin–orbit coupling because of the heavy atom effect.[276] At saturation quenching, the major lifetime components in the complexed hybrids amount to 20–45 ps for TSNP–Fe^{3+}, TSNP–Hg^{2+}, TSNP–Pb^{2+} and TSNP–Cu^{2+} and 0.11 ns for TSNP–Ni^{2+}. In contrast to metal ions bound directly at a fluorophore, for which paramagnetic ions such as Cu^{2+} usually show static quenching, i.e., a non-emissive complex, and heavy metal ions like Hg^{2+} a complex with a reduced lifetime, here, due to the separation of R and F, all metal ions lead to a reduction of the lifetime of F, stressing the fact that a distance-dependent process is active. The critical role of the terpyridine receptor was demonstrated in parallel studies using the model SNPs that are only functionalized with F but do not contain R. The addition of metal ions to acetonitrile suspensions of SNPs induced negligible changes in the emission of the dye, indicating that the presence of the R units in TSNP is critical for the quenching mechanism. Only when coordinated to terpyridine are the metal ions in a spatial proximity with the fluorophore that is close enough to induce quenching.

Effect of anions

The corresponding TSNP–Q hybrid materials (Q = Cu^{2+}, Fe^{3+}, Hg^{2+}, Ni^{2+} and Pb^{2+}) were tested as sensing systems for anions. The anion could compete with the terpyridine units for the metal ion and displace the latter from the R units which results in a fluorescence enhancement. This enhancement should be a direct consequence of a sensitive balance between the binding strength of the metal ion with terpyridine and the affinity of the cation for the added anion. To test the ability of the TSNP–Q ensembles for differential recognition of small monovalent anions, acetonitrile solutions of TSNP–Q chemosensors were prepared by adding 1.0 eq. (with respect to the molar amount of R units on the particles) of the corresponding metal ion to quench the emission of sulforhodamine. Then, 0.1–10.0 eq. of the respective anions $H_2PO_4^-$, HSO_4^-, F^-, Cl^-, Br^-, I^- and NO_3^- were added to the TSNP–Q suspensions. Except in one case (see below), no uniquely selective fluorescence changes were found. As a general trend the addition of $H_2PO_4^-$ and F^- induced a remarkable fluorescence enhancement, addition of Cl^-, Br^- and HSO_4^- induced a moderate increase of the emission whereas the addition of I^- and NO_3^- induced only poor fluorescence change.

Fluorescence lifetime studies of the ternary systems revealed that upon addition of anions, the lifetime features of the TSNP–M^{n+} ensembles are gradually turned into the features of TSNP, i.e., the major 2.2 ns component of the sulforhodamine is recovered, meaning that the metal ions are actual displaced from the terpyridine units. Whereas the TSNP–Q systems, with Q = Cu^{2+}, Fe^{3+}, Hg^{2+} or Ni^{2+}, show a differential but no selective response in the presence of small inorganic anions, TSNP–Pb^{2+} behaves different, i.e., only the addition of $H_2PO_4^-$ restores the sulforhodamine fluorescence whereas the other anions remain relatively silent (Figure 74).

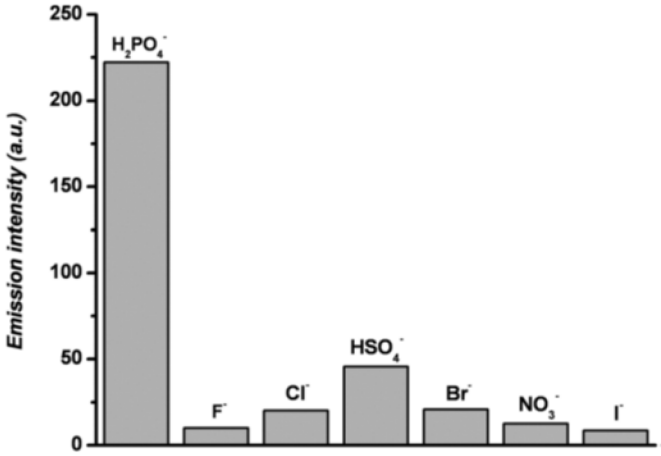

Figure 74 Emission intensity of TSNP-Pb^{2+} in MeCN in the presence of 5.0 eq. (1.0 mmol) of the respective anions.

Using this procedure, concentrations as low as 5 ppm of $H_2PO_4^-$ can be detected. A final control experiment revealed that the addition of anions to acetonitrile suspensions of TSNPs (in the absence of Q) or SNPs did not result in changes of the dye's fluorescence, pointing out the importance of the quenching metal ion as the mediator in this sensing application. A further benefit of the system is obvious. Once an analytical reaction has been performed and Q displaced, regeneration is easily accomplished by addition of an appropriate metal salt.

5.3 Conclusion

In summary, reliable protocols were examined for the reproducible synthesis of 20 nm, 25 nm, 45 nm and 300 nm silica nanoparticles by variation of the reaction conditions. These particles were doped with long-wavelength emitting oxazine dyes Nile blue and Cresyl violet by electrostatic embedding of the positively charged fluorophores within the negatively charged silica network. The simple protocol improved the fluorescence and stability features of the dyes in aqueous media compared to the need dyes in solution.

Furthermore 2 µm sized commercial SiO_2NPs were used to generate stable mono and bilayers on glass surfaces. After an additional functionalization step further and more complex bioanalytical applications with the microarray technology are feasible. The active surface of the substrate was enhanced and unified with the arrangement of the particles which essentially ensure more sensitive and comparable applications within the microarray field.

Finally the surface of SiO_2NPs was decorated with terpyridine binding sites and sulforhodamine B signaling units for the differential fluorometric recognition of anions. The final response of the TSNP–Q system to a particular anion is a balance between the binding strength of the metal ion with the terpyridine and the affinity of the cation for the added anion. This allows differential recognition of small inorganic anions in a quencher displacement assay. Furthermore, the regeneration of the system is possible in a straightforward manner. The facile and independent functionalization of silica surfaces with various chemical entities and the possible use of a number of different coordination units and metal ions make this approach highly appealing for the search for new chemosensors for anions

6 Outlook

The strategies presented in the thesis describe new approaches to step from organic molecules to smart materials for applicable sensory formats. The prominent features of particulate and thin-film based materials were exploited and combined with the outstanding properties of selected fluorescent dyes.

Following up on the presented strategies, further studies are conceivable. At first the robust and reversible fluorescent pH sensing membrane could be investigated concerning long-term stability and performance tests under high-electrolyte background and biological as well as chemical contaminants. The expansion to a multiple sensor molecules-bearing dip-stick in one membrane or an arrangement of membrane spots possible in a self-referenced manner for the whole pH range is under investigation. For the read-out of this multi-pH format by e.g. the presented cell phone camera based approach -more complex mobile apps must be programmed.

The versatility of particulate systems was demonstrated with various examples. A next step for the nanofibrillated microparticles would be to functionalize them with fluorescent biomolecules and investigate if the special surface structure can lead to a the reduction of known fluorescence quenching effects due to the minimization of possible steric hindrance compared to a known system e.g. on polymer particles of the same size dimension in a bioanalytical assay. Furthermore these particles could serve as "*green*" and non-toxic alternatives for potent analytical applications.

The tremendous impact of mesoporous particles combined with the high sensitivity of sensory BODIPY molecules can be extended by improving the described system through grafting of suitable chemical entities on the particle surface and within in the voids to generate an appropriate microenvironment for e.g. other sensory molecules or combinations thereof.

Furthermore, the developed sensory particles can be deposited on glass surfaces in homogeneous and stable monolayers as presented to improve existing microarray based bioanalytical applications allowing excellent signal-to-noise ratios due to the enhanced surface area compared to conventional set ups. The application of the developed particles in microfluidic systems or embedding of advanced particles in appropriate sensor formats will be a promising step into the direction of smart sensor-technology.

7 Materials and methods

7.1 Materials and instruments

All reagents were obtained from commercial suppliers and were used without further purification if not stated otherwise. Deionized water was sourced from a Milli-Q Synthesis A10 system equipped with a Quantum EX Ultrapure Organex cartridge (Millipore, Billerica, Massachusetts, USA) or from a Seralpur PRO 90 CN system equipped with a Supur DCF 0.2 µm filter (Seral, Ransbach-Baumbach, Germany). All solvents employed for the spectroscopic measurements were of UV spectroscopic grade (Aldrich). All air- and moisture-sensitive reactions were carried out under argon atmosphere in oven-dried glassware.

Spray-dried NFC microparticles (UPM-Kymmene Corporation, Helsinki, Finland) were used as received. The particles were prepared by spray-drying UPM Fibril Cellulose hydrogel dispersion at low concentration. The nanofibrillated cellulose was in native form, obtained from bleached birch pulp by mechanical treatment.

Schott Nexterion Slide E and PolyAn 3D-Epoxy Slides were used as solid supports for the dye-doped hydrogel and were cut into 10 mm strips which fit into commercially available PMMA cells. The hydrogel HydroMed D4 (ether-based hydrophilic urethane, water content 50%) was received from AdvanSource Biomaterials Corporation, Wilmington, MA.

Sheets of nitrocellulose membrane High Flow Plus HF13502 from Millipore were cut into 0.5 × 2.5 cm strips with a paper cutting machine. Fluorescence measurements on strips were recorded with an ESE-Quant FL and a universal strip holder from Qiagen.

Thin layer chromatography (TLC) was performed on Merck Silica Gel 60 F254 TLC plates with a fluorescent indicator for 254 nm excitation. Compounds were visualized under UV light at 254 nm. Column chromatography was carried out with Merck Silica gel 60 (0.040-0.063 mm) using the eluents specified.

Nuclear magnetic resonance spectroscopy (NMR) spectra were recorded on a Bruker AV 400 or on a Bruker AVANCE III 500 MHz at 27 °C using residual protonated solvent signals as internal standard (^{1}H: δ[$CDCl_3$] = 7.26 ppm and ^{13}C: δ[$CDCl_3$] = 77.16 ppm). Assignments are based on chemical shifts and/or DEPT spectra (Ar is used as abbreviation for assigning aromatic moieties).

High resolution mass spectrometry (HR-MS) was performed with a Thermo Scientific Exactive Orbitrap in the positive ion mode using the Thermo Xcalibur operating and data acquisition software or on a Waters LCT Premier XE. Ultrahigh-performance liquid chromatography mass spectrometry (UPLC-MS) was performed with a Waters Acquity

UPLC equipped with a Waters LCT Premier XE mass detector for high-resolution MS (HR-MS, ESI-ionization) and with Waters Alliance systems (consisting of a Waters Separations Module 2695, a Waters Diode Array detector 996 and a Waters Mass Detector ZQ 2000) equipped with a Acquity BEH C18 (2.1 × 50 mm) column.

Ultraviolet-visible (UV/Vis) absorption spectra were recorded on an Analytik Jena Specord 210 Plus spectrophotometer. Steadystate fluorescence measurements were carried out on a Horiba Jobin–Yvon FluoroMax-4P spectrofluorometer and a Spectronics Instrument 8100 spectrofluorometer, using standard 10 mm path length quartz cuvettes or PMMA cells. Fluorescence lifetimes were determined with a unique customized laser impulse fluorometer with picosecond time resolution described elsewhere. [109, 277] The fluorescence lifetime profiles were analyzed using the Horiba Scientific software package DAS 6.

Environmental scanning electron microscope (ESEM) measurements were performed with a XL 30 ESEM from FEI. All samples were coated with Aurum (Scancoat Six Sputter Coater from Edwards) by sputter coating for 90 s with a deposition rat e of 15 nm min^{-1}.

Confocal laser scanning microscope (CLSM) images were recorded on a Olympus FluoView™ FV1000 (Olympus GmbH, Hamburg, Germany) with a multiline argon ion laser (30 mW) as excitation source (excitation wavelength of 488 nm), which was reflected by a dichroic mirror (DM351/488/543) and focused onto the sample through an Olympus objective UPLSAPO 40X (numerical aperture N.A. 0.90). A 4-fold digital zoom was applied for virtual magnification of the particles resulting in an image size of ca. 80 µm × 80 µm. The fluorescence emission was recollected by the same objective and focused into the photomultipliers. Detection channels were set to modified FITC channel 1 (variable band pass filter position 500 nm (495), filter range 40 nm) and modified Cy 3 channel 2 (variable band pass filter position 625 nm (637), filter range 100 nm). The two emission channels were shown separately and as an overlay of the two emission channels together with the transmission channel. All fluorescence measurements were performed at room temperature.

Dynamic light scattering (DLS) measurements were performed on a Zetasizer Nano ZS (Malvern Instruments Ltd., Worcestershire, UK.) with a 633 nm He-Ne-laser. All values shown in this work are the average of six measurements of aqueous particle solutions (100-500 kcps).

Transmission electron microscopy (TEM) was conducted on a FEI Tecnai G2 20 S-TWIN instrument (FEI Company, Oregon, USA) operating at 200 kV equipped with a GATAN (Warrendale, PA, USA) Multi-Scan CCD camera model 794P. One drop of the colloidal emulsion was placed on the sample grid, and the solvent was allowed to evaporate. The

average size and standard deviation were determined from TEM images by averaging diameters of more than 100 particles.

pH values were monitored with a digital pH meter (pH lab 827, Metrohm GmbH) equipped with a glass electrode (Biotrode). For comparison, pH measurements were also performed with a second digital pH meter (WTW pH 537), equipped with a glass electrode InLab 423 (Mettler Toledo). Calibration of the instruments was performed with standard aqueous solutions of pH 4.00, 7.00 and 9.00 from Metrohm GmbH. The measurement uncertainties of the pH electrodes amount to $\leq \pm$ 0.03 pH.

X-ray photoelectron spectroscopy (XPS) measurements were carried out with an AXIS Ultra DLD photoelectron spectrometer manufactured by Kratos Analytical (Manchester, UK). XPS spectra were recorded using monochromated Al Kα excitation at pass energies of 80 eV for survey and 20 eV for high-resolution core-level spectra. Additionally the charge neutralization system was applied. The electron emission angle was 0° and the source-to-analyzer angle was 60°. The binding energy scale of the instrument was calibrated following a Kratos Analytical procedure which uses ISO 15472 binding energy (BE) data. [278, 279] The binding energy scale was corrected for static charging by using BE = 285.0 eV for the aliphatic C 1s component.[280] High resolution C 1s core level spectra were analyzed using the CasaXPS peak fit program (Casa Software Ltd., Teignmouth). In curve fitting of C 1s spectra, full widths at half maximum were constrained to be equal resulting in values ranging from 1.2–1.4 eV. A Gaussian/Lorentzian product function peak shape model (G/L = 30) was used in combination with a Shirley background.

Structures were drawn with ChemSketch 10.02 (Advanced Chemistry Development, Toronto, Canada). Diagrams and graphs were prepared with Origin 8G (OriginLab Corporation, Northampton, Massachusetts, USA). Crystal structure ORTEP plots were generated with ORTEP-III (Oak Ridge National Laboratory, Tennessee, USA) by Werner Kraus (BAM Federal Institute for Materials Research and Testing, Berlin, Germany). Citation management was done with Endnote X7 (Thomson Reuters, New York, New York, USA).

7.2 General procedures

Fabrication of the membrane-coated pH strips

The dye-doped hydrogels were prepared from 1.0 g HydroMed D4 dissolved in a mixture of 10.8 g EtOH and 1.2 g H_2O. Starting from a stock solution of the appropriate dye in CH_2Cl_2 (c = 2.51 mM), an adequate volume of the stock solution was added to the viscous hydrogel

solution to achieve a final dye concentration of 2 mmol g^{-1} of polymer.[281] The mixture was vigorously stirred at RT for 1 h. The polymer strips were dip-coated into the hydrogel solution and air-dried for 3 h prior to use. To reduce the film thickness or to obtain reduced dye concentrations in the film, hydrogels were prepared as described but with the compositions listed in Chapter 2.

Determination of molar absorption coefficients and fluorescence quantum yields

The molar absorption coefficients ε (λ_{ex}) were determined from three separately weighed and dissolved stock solutions in a repeat determination of each sample (N = 6 independent measurements). The dilution was chosen in such a way that the absorbance of the sample solutions equaled 0.5. The fluorescence quantum yields Φ_f were determined relative to dye **6**, **49**, **52**, **R6G**.[45, 54, 116] The fluorescence spectra presented here were spectrally corrected. The rate constants for radiative (k_r) and non-radiative (k_{nr}) deactivation were calculated using the standard expressions below (measurement uncertainties amount to ± 0.01 × 10^8 s^{-1}):

$$k_r = \Phi_f \times \tau_f^{-1}$$

$$k_{nr} = \left(1 - \Phi_f\right) \times \tau_f^{-1}$$

*Modification of NFCPs with 3-(aminopropyl)triethoxysilane **A***

10 mg NFCPs were suspended in 500 µL toluene under argon and heated to 100 °C. The appropriate amount of 3-(aminopropyl)triethoxysilane **A** and additional toluene to reach a final reaction volume of 1.5 mL, according to Table 25, were added to the NFCP suspension and gently shaken in a thermomixer for 3.5 h. After centrifugation and removal of the supernatant, the particles were washed three times with toluene and dried in a vacuum concentrator at 100 °C overnight.

Table 25 Modification of NFCPs with A.

Sample	V_{APTES}/ µL	V_{Tol}/ µL	n_{APTES}/mol	c_{APTES}/mol L^{-1}
CPA1	151.0	1349.0	6.45×10^{-4}	0.43
CPA2	255.0	1245.0	1.09×10^{-3}	0.73
CPA3	408.0	1.092	1.74×10^{-3}	1.16
CPA4	511.0	0.989	2.18×10^{-3}	1.46

*Modification of NFCPs with γ- methacryloxypropyl trimethoxysilane **M** and **A***

100 mg NFCPs were suspended in 10 mL toluene in a headspace bottle under argon and heated to 100 °C. (Trimethoxysilyl)propyl methacrylate **M** and the appropriate amount of 3-(aminopropyl)triethoxysilane **A** according to Table 26, previously dissolved in 1 mL hot toluene, were added to the stirred NFCP suspension through a syringe and the reaction was allowed to proceed for 6 h at 100 °C. After centrifugation and removal of the supernatant, the particles were washed three times with 10 mL acetone and dried in a vacuum concentrator at 100 °C overnight.

Table 26 Molar composition of A and M for the particle encapsulation.

Sample	n_{MA}/mol	$V_{MA}/\mu L$	n_{APTES}/mol	$V_{APTES}/\mu L$
CPAM1	1.05×10^{-3}	250.0	1.05×10^{-3}	246.0
CPAM2	2.00×10^{-3}	474.0	1.05×10^{-4}	24.6
CPAM3	2.09×10^{-3}	497.0	1.05×10^{-5}	2.46
CPAM4	2.10×10^{-3}	499.0	1.05×10^{-6}	0.5
CPM	2.10×10^{-3}	499.0	-	0.0

*Reaction of modified of **CPAM**s with **36***

20 mg of **CPAM1**- **CPAM4** and **CPM** were suspended in 1 mL toluene, respectively. 300 µL of a **36** stock solution in toluene ($c = 6.13 \times 10^{-3}$ mol L^{-1}, 1.84×10^{-6} mol) were added. After gently shaking at RT overnight in a thermomixer, the particles were centrifuged and washed 3 times with toluene and acetone, respectively. The slightly orange colored particles were dried in a vacuum concentrator at 30 °C overnight.

*Reaction of **36** with amines **A, B, C, D***

1 mL of the corresponding amine (**A**, **B**, **C**, **D**) was added to a small amount of **36**. The sample was divided into 2 × 500 µL fractions and the reactions were carried out at RT and 80 °C in a thermomixer overnight, respectively. Spectroscopic measurements were carried out directly after the reaction without any purification in water, acetonitrile and EtOH/H_2O 1:1.

Sample preparation for spectroscopic characterization of cellulose particle samples

Absorption and fluorescence measurements were carried out using particle stock solutions of 10 mg mL^{-1} in water. 20 µL of the respective particle stock solution was added to 2.5 mL H_2O (or EtOH–H_2O) in a PMMA cuvette to obtain a final particle concentration of 0.08 mg mL^{-1}. For the CLSM measurements a small amount of dried particles was placed on a microscope cover slip. To investigate the swelling behavior of the particles approximately 100 µL H_2O were added, mixed with the particles and measured after 30 min incubation at RT.

Buffer solutions

Phosphate-buffered saline (PBS 10x; 70 mmol dm^{-3} Na_2HPO_4, 10 mmol dm^{-3} NaH_2PO_4, 145 mmol dm^{-3} NaCl, pH 7.4) was used for controlled guest molecule loading processes and release experiments.

Synthesis of MCM-41 nanoparticles

N-cetyltrimethylammonium bromide (CTAB, 1.00 g, 2.74 mmol) was dissolved in deionized water (480 mL). Then, NaOH (3.5 mL, 2.00 mol L^{-1}) in deionized water was added to the CTAB solution, followed by adjusting the solution temperature to 80 ºC. TEOS (5.00 mL, 25.70 mmol) was subsequently added drop wise to the surfactant solution. The mixture was stirred for 2 h yielding a white precipitate. Finally, the solid product was centrifuged, washed with deionized water and ethanol, and dried at 60 ºC (MCM-41 as-synthesized). To prepare the final porous material (MCM-41), the as-synthesized solid was calcined at 550 ºC using an oxidant atmosphere for 5 h in order to remove the template phase.

*Loading of dyes **40-45** into MCM-41*

MeCN and PBS solutions of selected dyes were freshly prepared under ultrasonication with a final dye concentrations of 2.00 mmol L^{-1}. Acetonitrile solutions of **Rh101 43** and **SuRh-Na 45** were prepared with a final dye concentration of 1.60 mmol L^{-1} and 1 mmol L^{-1}, respectively due to reduced solubility in acetonitrile. For each loading process 10 mg of mesoporous MCM-41 nanoparticles were added to 3.75 mL of the respective

as-prepared dye containing MeCN or PBS solution to obtain a final concentration of 0.8 mmol dye g^{-1} solid. The suspensions were stirred for 24 h at room temperature. The particle suspensions were centrifuged for 10 min at 6000 rpm, the colored supernatant were almost completely removed and the particles were dried using a vacuum dryer at 40 ºC for 12 h, yielding dry, colored solids.

Dye release experiments

1 mg of each solid was suspended in 2 ml PBS buffer (pH 7.4), under gently shaking using a vortex mixer for 15 sec. After centrifugation (10 min, 6000 rpm) the colored supernatant was removed and directly analyzed by UV/Vis.

Kinetic release of MCM-41

Release kinetics were performed mixing 0.3 mg of the appropriate MCM-41 material in 3 mL of PBS in an ultraviolet cuvette. The dye release behavior was monitored by measuring the absorption values (at 564 nm for **SuRh-Na 45** and at 555 nm for **RhB-Cl 42**) versus time.

Quantification of the loaded and released amount of dye

The amount of loaded and released dye within the PBS solutions was investigated by UV/Vis measurements applying the *Lambert-Beer* equation, using the maximum of absorbance (A_{max}) of the selected dyes with the corresponding molar absorption coefficient of each dye in PBS. Additionally elemental analysis was carried out to confirm the dye contents obtained through UV/Vis measurements. From elemental analysis of C, H, N the amount of each dye in mmol per gram of solid (mmol g^{-1} solid) in the final solid was calculated using the following equation,

$$a_A = \frac{\Delta M_i x\%1000}{nPM_i} \qquad \left(\frac{mmol}{g\ solid} \right)$$

where $\Delta Wi\%$ (i = C, N, S) are the weight percentages of carbon or nitrogen. M_i is the corresponding atomic weight and n is the number of the corresponding atom type in one molecule.

Functionalization of MCM-41 with various silanes[282]

2.13 mmol of the appropriate silane 3-(aminopropyl)triethoxysilane **A**, 3-(triethoxysilyl)propionitrile **E** or 2-[methoxy(polyethyleneoxy)propyl]trimethoxysilane **F** was added to 100 mg MCM-41 particles suspended in 20 mL of toluene under argon and heated to 95 °C for 4 h. The resulting functionalized material (**MCM-NH$_2$**, **MCM-CN**, **MCM-PEG**) was centrifuged for 10 min at 6000 rpm, the supernatant was removed and the particles were washed twice with ethanol and acetone by centrifugation-redispersion cycles. The particles were finally dried at 70 °C for 12 h.

*Loading of **47** into MCM-41*

5.56 mg of **47** were dissolved in 8.0 mL MeCN (stock solution $c_1 = 0.96\times 10^{-4}$ mol L^{-1}) under ultrasonication. Dye solution of $c_2 = 4.81 \times 10^{-5}$ mol L^{-1} (1:20) was also prepared. For each loading process 10 mg of microporous MCM-41 nanoparticles were added to 3.75 mL of the freshly prepared dye solution. The suspensions were stirred for 24 h at room temperature. The particles were centrifuged for 10 min at 6000 rpm. The colored supernatant was almost completely removed. The resulting particles were washed 5 times with water and finally dried using a vacuum dryer at 40 ºC for 12 h, yielding dry, orange colored solids.

Titration studies of functionalized and loaded MCM-41

Particle stock solutions of 4.0 mg mL^{-1} were prepared by suspending 2.0 mg of the respective material in 500 µL H_2O under ultrasonication for 10 s. 20 µL of the freshly prepared particle stock solution were added to 2.5 mL water to obtain a final particle concentration of 32 µg mL^{-1}. For every step of the titration small amounts of aq. $Hg(ClO_4)_2$ or $AgClO_4$ (0.01 mM-0.1 M) were added under stirring.

Leaching studies functionalized and loaded MCM-41

To investigate upon which metal-ion concentration the dye-metal complex will leach out of the particle pores in solution, 3 particle samples (32 µg mL^{-1}) were incubated with 8, 800 and 80.000 ppb Hg^{2+} or Ag^{+} under stirring for 5 min, respectively. The suspensions were centrifuged and the emission of the retaining solution was measured.

Test-Strip based assay

Strips of 0.5 × 2.5 cm of nitrocellulose membranes were prepared and 0.5 µL of **S1-AB** was dispended on zone A from suspensions of the sensing material (2 mg mL^{-1}) with a micropipette. The strips were then dipped into the PBS-buffered sample solutions without or with varying concentrations of TATP and let to develop for 90 s. After the test the strips were dried (30 s with hair dryer in cold air blow mode or 8 min at normal room temperature), the fluorescence was measured using a flow assay reader at 625 nm (λ_{exc} = 520 nm). The amount of dye released for each concentration was calculated through the ratio between the fluorescence of zone B and the entire strip.

For the tests of real water samples spiked with different amounts of TATP were run by measuring off 900 µL of spiked sample, adding 100 µL of a PBS 10X solution and running the normal lateral flow assay protocol. Addition of the buffer allows the suppression of matrix effects and the determination of TATP down to 75 ppb.

The assessment of the interference of pH was tested as follows. Acidic and basic solutions were adjusted to the respective pH with either 0.25 M aqueous HCl solution or 0.1M aqueous KOH solution. Subsequently, 10 µL of TATP stock solution were added to 990 µL of the as-prepared pH solutions and gently shaken for 15 min under ambient temperature. These solutions were used in the assay in the same way as the real water samples. For the tolerance tests toward ethanol, solutions containing 1–10 % ethanol were prepared in a similar manner and subjected to the assay also in the same way.

Synthesis of SiO_2NPs according to Chen et al.[247]

8 ml EtOH, 4.85 ml H_2O and 3.6 ml NH_4OH were heated to the appropriate temperature under stirring in a 20 ml vial. A solution of 31 ml TEOS in 8 ml EtOH were added in one portion. After 5h the particles were dialyzed against water for 48 h.

*Synthesis of SiO_2NPs (**StöberSil**) according Thomassen et al.*[248]

TEOS was added drop wise to the aqueous ethanolic solution containing ammonium hydroxide while stirring at 400 rpm. The sols were aged for 24 h at room temperature.

*Synthesis of SiO_2NPs seeds **H_1-H_1'',*[231]

9.1 mg L-arginine (52.0 µmol, 0.02 eq.) was dissolved in 6.9 ml water (0.38 mmol, 155.5 eq.) while thoroughly mixing the solution in a 20 mL vial. Then 0.45 ml cyclohexane (4.17 mmol, 1.7 eq.) was added to the water-arginine solution and the reaction was heated to 60 °C in a water bath under stirring at 300 rpm. Once the reactants have warmed up, 0.55 ml TEOS (2.5 mmol, 1.0 eq.) were added and after 20 h the particles were dialyzed against water.

Influence of the reaction temperature

To investigate the influence of the reaction temperature in the synthesis of SiO_2 seeds, the reactions were carried out at 22 °C (**$H_{20°C}$**), 40 °C (**$H_{40°C}$**)or 50 °C (**$H_{20\,°C}$**), respectively.

*Influence of the added amount of silane in the seed synthesis **H_2-H_4***

The seed synthesis was modified by increasing the amount of silane as shown in Table 27.

Table 27 Variation of the amount of silane in the seed synthesis.

Sample	$V_{TEOS} \times 10^{-3}$ [L]	n_{TEOS} [mol]	n_{TEOS} [eq.]
H_2	0.688	3.10	1.25
H_3	0.825	3.72	1.50
H_4	0.963	4.34	1.75

First shell trough seeded-regrowth method[231]

1 mL of the as-prepared seed-solution was directly taken after synthesis and diluted with 3.6 ml water. 0.5 mL cyclohexane and 0.352 mL TEOS were added. The reaction was allowed to proceed for 30 h while maintaining the stirring at 300 rpm and constant temperature of 60 °C.

Influence of the added amount of silane (1.regrowth)

The procedure was modified by increasing the amount of silane in the regrowth step as shown in Table 28.

Table 28 Variation of the amount of silane in the 1. regrowth step.

Sample	$V_{TEOS} \times 10^{-3}$ [L]	n_{TEOS} [mol]	n_{TEOS} [eq.]
H_{11}	0.440	1.98	1.25
H_{12}	0.528	2.38	1.50
H_{13}	0.616	2.77	1.75
H_{14}	0.704	3.17	2.00

Dialysis of Nile blue and Cresyl violet-doped SiO_2NPs

After the reactions the particle suspensions were dialyzed against 5 L of water with VISKING dialysis tubes type 20/31. The dialysate was refreshed five times with a minimum time interval of 2 h. The total dialysis time was 24 h.

Fluorescence studies with TSNP in the presence of metal cations and anions

Functionalized silica nanoparticles TSNP and SNP were used as received. 2.5 mg TSNP nanoparticles were suspended in 20 mL MeCN and then sonicated for 5 min in order to obtain a homogeneous suspension. Acetonitrile solutions of the metal cations (1.0×10^{-2} mol L^{-3}) and anions (2.0×10^{-2} mol L^{-3}) were prepared. The emission intensity of TSNP nanoparticles at 581 nm (λ_{ex} = 550 nm) was first measured in the presence of increasing quantities of metal cations (Fe^{3+}, Hg^{2+}, Cu^{2+}, Ni^{2+} and Pb^{2+}). A complete quenching was observed upon addition of 1.0 eq. of metal cation (with respect to the content of the terpyridine unit). Then, 20 µL (2.0×10^{-4} mmol) of the acetonitrile solutions of metal cations were added to 3 mL of the TSNP suspension (containing 1.9×10^{-4} mmol of the terpyridine unit). To this suspension, increasing quantities of the corresponding anions were added and the emission intensity at 581 nm were measured (λ_{ex} = 550 nm).

7.3 Synthetic procedures

General procedure 1(GP1)[283]

The corresponding aldehyde (4.0 mmol, 1.0 eq.) and kryptopyrrole **4** (8.0 mmol, 2.0 eq.) were dissolved in dry THF (120 ml) under argon. A few drops of trifluoroacetic acid were added

and the solution was stirred at room temperature overnight in the dark until total consumption of the aldehyde (monitored by TLC). DDQ (908.0 mg, 4.0 mmol, 1.0 eq.) dissolved in 30 ml THF was added and the mixture was stirred for additional 4h. Subsequently, 24.0 ml Et_3N (17.3 mmol, 43.0 eq.) and 24 ml $BF_3 \times OEt_2$ (20.0 mmol, 59.0 eq.) were added drop wise at 0 °C. After stirring overnight, the solvent was removed under reduced pressure. The dark residue was dissolved in 100 ml CH_2Cl_2 and washed with water (3 × 100 ml). After extraction of the aqueous phase with CH_2Cl_2 (3 × 100 ml), the combined organic solutions were dried over Na_2SO_4 and concentrated under reduced pressure. The crude product was purified by silica-gel flash column chromatography as specified.

8-(4-hydroxyphenyl)-1,3,5,7-tetramethyl-2,6-diethyl-4,4-difluoro-4-bora-3a,4a-diaza-*s*-indacene 5. **5** was synthesized according to *GP1*. The crude product was purified by column chromatography on silica using CH_2Cl_2 as eluent to give compound **5** as shiny, reddish-orange crystals (713 mg, 45%).

^{1}H-NMR (300 MHz, $CDCl_3$) [ppm]: δ = 0.98 (t, 6H, *J* = 7.6 Hz, 2 × CH_2-C<u>H</u>$_3$), 1.35 (s, 6H, 2 × C-C<u>H</u>$_3$), 2.30 (q, 4H, *J* = 7.6 Hz, 2 × C<u>H</u>$_2$-CH_3), 2.53 (s, 6H, 2 × N-C-C<u>H</u>$_3$), 6.94 (m, 2H, 2 × C<u>H</u>$_{ar}$), 7.12 (m, 2H, 2 × C<u>H</u>$_{ar}$).

^{13}C-NMR (75 MHz, $CDCl_3$) [ppm]: δ = 12.0 (CH_3), 12.6 (CH_3), 14.8 (CH_3), 17.2 (CH_2), 116.1 (CH_{ar}), 128.1 (C_q), 129.9 (CH_{ar}), 131.3 (C_q), 132.0 (C_q), 138.6 (C_q), 140.3 (C_q), 153.7 (C_q), 156.3 (C_q).

HR-MS (ESI+): m/z calculated for $C_{23}H_{27k}BF_2N_2O$ $[M+H]^+$: 396.2185, found: 396.2248.

General procedure 2 (GP2)

The corresponding aldehyde (4.0 mmol, 1.0 eq.) and pyrrole **4** or **39** (8.0 mmol, 2.0 eq.) were dissolved in dry CH_2Cl_2 (70 ml) under argon. A few drops of trifluoroacetic acid were added and the solution was stirred at room temperature in the dark until total consumption of the aldehyde (monitored by TLC). Tetrachloro-*p*-benzoquinone (983.5 mg, 4.0 mmol, 1.0 eq.) was added and the mixture was stirred for additional 5 min. The reaction mixture was then treated with 5.0 ml *N*,*N*-diisopropylethylamine (28.0 mmol, 7.0 eq.) and 5.5 ml $BF_3 \times OEt_2$ (44.0 mmol, 11.0 eq.). After stirring for another 15 min, the dark solution was washed with water (3 × 50 ml). After extraction of the aqueous phase with CH_2Cl_2 (3 × 50 ml), the combined organic solutions were dried over Na_2SO_4 and concentrated under reduced pressure. The crude product was purified by silica-gel flash column chromatography as specified.

8-(3,5-bis(trifluoromethyl)phenyl)-1,3,5,7-tetramethyl-2,6-diethyl-4,4-difluoro-4-bora-3a,4a-diaza-*s*-indacene 37. **37** was synthesized according to *GP2*. The crude product was purified by column chromatography on silica using toluene as eluent to give compound **37** as orange-red shining crystals (929 mg, 45 %).

^{1}H-NMR (500 MHz, $CDCl_3$) [ppm] δ = 0.99 (t, 6H, *J* = 7.6 Hz, 2 × CH_2-C$\underline{H}_3$), 1.22 (s, 6H, 2 × C$\underline{H}_3$), 2.31 (q, 4H, *J* = 7.6 Hz, 2 × C$\underline{H}_2$-CH_3), 2.54 (s, 6H, 2 × -C$\underline{H}_3$), 7.84 (s, 2H, 2 × C$\underline{H}_{ar}$), 8.03 (s, 1H, C$\underline{H}_{ar}$).

^{13}C-NMR (126 MHz, $CDCl_3$) [ppm]: δ = 12.2 (CH_3), 12.8 (CH_3), 14.7 (CH_3), 17.2 (CH_2), 119.9 (C_q), 122.0 (C_q), 122.7 (CH_{ar}), 124.2 (C_q), 126.4 (C_q), 129.5 (CH_{ar}), 130.4 (C_q), 132.4 (C_q), 132.7 (C_q), 133.0 (C_q), 133.2 (C_q), 133.9 (C_q), 135.5 (C_q), 137.5 (C_q), 138.3 (C_q), 155.6 (C_q).

HR-MS (ESI+): m/z calculated for $C_{25}H_{26}BF_8N_2$ $[M+H]^+$ 517.2055, found 517.2046.

8-(3,5-bis(trifluoromethyl)phenyl)-1,3,5,7-tetramethyl-4,4-difluoro-4-bora-3a,4a-diaza-*s*-indacene 38. **38** was synthesized according to *GP2*. The crude product was purified by column chromatography on silica using PE/CH_2Cl_2 7:3 as eluent to give compound **38** as orange crystals (350 mg, 19 %).

^{1}H-NMR (500 MHz, $CDCl_3$) [ppm]: δ =1.36 (s, 6H, 2 × C$\underline{H}_3$), 2.60 (s, 6H, 2 × C$\underline{H}_3$), 6.07 (s, 2H, 2 × C$\underline{H}$), 7.84 (s, 2H, 2 × C$\underline{H}_{ar}$), 8.04 (s, 1H, C$\underline{H}_{ar}$).

^{13}C-NMR (126 MHz, $CDCl_3$) [ppm]: δ = 14.8 (CH_3), 14.9 (CH_3), 119.8 (C_q), 122.0 (C_q), 122.3 (CH), 122.9 (CH_{ar}), 124.1 (C_q), 126.3 (C_q), 129.3 (CH_{ar}), 131.1 (C_q), 132.6 (C_q), 132.9 (C_q), 133.1 (C_q), 133.4 (C_q), 137.0 (C_q), 137.5 (C_q), 142.4 (C_q), 157.3 (C_q).

HR-MS (ESI+): m/z calculated for $C_{21}H_{18}BF_8N_2$ $[M+H]^+$: 461.1429, found: 461.1422.

8-(4-nitrophenyl)-1,3,5,7-tetramethyl-2,6-diethyl-4,4-difluoro-4-bora-3a,4a-diaza-*s*-indacene 21d.[284] 1.0 g 4-Nitrobenzoyl chloride **20d** (5.4 mmol, 1.0 eq.) and 1.23 g 3-ethyl-2,4-dimethylpyrrole **4** (10.0 mmol, 2.0 eq.) were dissolved in 100 ml CH_2Cl_2. After stirring at room temperature for additional 4 days, 4.6 ml Et_3N (32.4 mmol, 6.0 eq.) and 5.4 ml $BF_3 \times OEt_2$ (43.2 mmol, 8 eq.) were added. After stirring overnight, the dark solution was washed with water (3 × 75 ml). After extraction of the aqueous phase with CH_2Cl_2 (3 × 75 ml), the combined organic solutions were dried over Na_2SO_4 and concentrated under reduced pressure. The crude product was purified by column chromatography on silica using PE/CH_2Cl_2 1:1 as eluent to give compound **21d** as red crystals (689 mg, 30%).

^{1}H-NMR (500 MHz, $CDCl_3$) [ppm]: δ = 0.97 (t, 6H, *J* = 7.6 Hz, 2 × CH_2-C$\underline{H}_3$), 1.25 (s, 6H,

2 × C-C$\underline{H}_3$), 2.29 (q, 4H, *J* = 7.5 Hz, 2 × C$\underline{H}_2$-CH$_3$), 2.53 (s, 6H, 2 × N-C-C$\underline{H}_3$), 8.21 (dd, 2H, *J* = 8.8 Hz, 1.7 Hz, 2 × C$\underline{H}_{ar}$), 8.28 (dd, 2H, *J* = 8.8 Hz, 1.9 Hz, 2 × C$\underline{H}_{ar}$).

HR-MS (ESI+): m/z calculated for $C_{23}H_{27}BF_2N_3O_2$ $[M+H]^+$: 426.2164, found: 426.2164.

8-(4-aminophenyl)-1,3,5,7-tetramethyl-2,6-diethyl-4,4-difluoro-4-bora-3a,4a-diaza-*s*-indacene 21e.[284] 378 mg **21d** (0.98 mmol, 1.0 eq.) and 90 mg 10% Pd/C (99.0 µmol, 0.1 eq.) were dissolved in 40ml CH_2Cl_2/MeOH 1:1 (v/v). The solution was saturated with hydrogen gas and stirred for 16 h. The Pd/C was removed by filtration and the solvent was evaporated to give compound **21e** as shiny orange crystals (348 mg, 99%).

^{1}H-NMR (500 MHz, $CDCl_3$) [ppm]: δ = 0.98 (t, 6H, *J* = 7.6 Hz, 2 × CH$_2$-C$\underline{H}_3$), 1.39 (s, 6H, 2 × C-C$\underline{H}_3$), 2.30 (q, 4H, *J* = 7.6 Hz, 2 × C$\underline{H}_2$-CH$_3$), 2.52 (s, 6H, 2 × N-C-C$\underline{H}_3$), 6.77 (m, 2H, 2 × C$\underline{H}_{ar}$), 7.00 (m, 2H, 2 × C$\underline{H}_{ar}$).

HR-MS (ESI+): m/z calculated for $C_{23}H_{27}BF_3N_2$ $[M+H]^+$: 396.2423, found: 396.2389.

General procedure 3 (GP3)

The corresponding aldehyde **20a**, **20b** or **20c** (1.5 mmol, 1.0 eq.) and 3-ethyl-2.4-dimethylpyrrole **4** (3.3 mmol, 2.0 eq.) were dissolved in dry toluene (150ml) under argon. A few drops of trifluoroacetic acid were added and the solution was stirred at room temperature overnight. DDQ (350 mg, 1.5 mmol, 1.0 eq.) in 50ml toluene was added and the mixture was stirred for additional 4h. The reaction mixture was treated with 9.0 ml Et_3N (17.3 mmol, 43.0 eq.) and 9 ml $BF_3 \times OEt_2$ (20.0 mmol, 59.0 eq.). After stirring overnight, the solvent was removed under reduced pressure. The dark residue was dissolved in 70ml CH_2Cl_2 and washed once with 5 % (m/v) $NaHCO_3$ and twice with water (100 ml). After extraction of the aqueous phase with CH_2Cl_2 (3 × 100 ml), the combined organic solutions were dried over Na_2SO_4 and concentrated under reduced pressure. The crude product was purified by silica-gel flash column chromatography as specified.

8-(4-hydroxy-3-nitrophenyl)-1,3,5,7-tetramethyl-2,6-diethyl-4,4-difluoro-4-bora-3a,4a-diaza-*s*-indacene 21a. The crude product was purified by column chromatography on silica using PE/CH_2Cl_2 3:1 as eluent to give compound **21a** as orange solid (129 mg, 15%).

^{1}H-NMR (300 MHz, $CDCl_3$) [ppm]: δ = 1.01 (t, 6H, *J* = 7.6 Hz, 2 × CH$_2$-C$\underline{H}_3$), 1.38 (s, 6H, 2 × C-C$\underline{H}_3$), 2.33 (q, 4H, *J* = 7.6 Hz, 2 × C$\underline{H}_2$-CH$_3$), 2.56 (s, 6H, 2 × N-C-C$\underline{H}_3$), 7.54 (m, 2H, 2 × C$\underline{H}_{ar}$), 8.11 (d, 1H, *J* = 2.1 Hz, C$\underline{H}_{ar}$).

HR-MS (ESI-): m/z calculated for $C_{23}H_{25}BF_2N_3O_3$ $[M-H]^+$: 440.1957, found 440.1956.

8-(2-chloro-4-hydroxyphenyl)-1,3,5,7-tetramethyl-2,6-diethyl-4,4-difluoro-4-bora-3a,4a-diaza-*s*-indacene 21b. The crude product was purified by column chromatography on silica using PE/CH_2Cl_2 4:1 as eluent to give compound **21b** as purple solid (129 mg, 20%).
^{1}H-NMR (300 MHz, $CDCl_3$) [ppm]: δ = 0.99 (t, 6H, *J* = 7.6 Hz, 2 × CH_2-C$\underline{H}_3$), 1.39 (s, 6H, 2 × C-C$\underline{H}_3$), 2.31 (q, 4H, *J* = 7.6 Hz, 2 × C$\underline{H}_2$-CH_3), 2.53 (s, 6H, 2 × N-C-C$\underline{H}_3$), 6.86 (dd, 1H, *J* = 2.4, 8.4 Hz, C$\underline{H}_{ar}$), 6.99 (d, 1H, *J* = 2.4 Hz, C$\underline{H}_{ar}$), 7.10 (d, 1H, *J* = 8.4 Hz, C$\underline{H}_{ar}$).
HR-MS (ESI+): m/z calculated for $C_{23}H_{27}BF_2N_2O$ $[M+H]^+$: 431.1873, found 431.1873.

8-(4-diethylaminophenyl)-1,3,5,7-tetramethyl-2,6-diethyl-4,4-difluoro-4-bora-3a,4a-diaza-*s*-indacene 21c. The crude product was purified by column chromatography on silica using PE/CH_2Cl_2 7:3 as eluent to give compound **21c** as red solid (250 mg, 18%).
^{1}H-NMR (400 MHz, $CDCl_3$) [ppm]: δ = 0.99 (t, 6H, *J* = 7.6 Hz, 2 × CH_2-C$\underline{H}_3$), 1.21 (t, 6H, *J* = 7.0 Hz, 2 × N-CH_2-C$\underline{H}_3$), 1.42 (s, 6H, 2 × C-C$\underline{H}_3$), 2.30 (q, 4H, *J* = 7.6 Hz, 2 × C$\underline{H}_2$-CH_3), 2.52 (s, 6H, 2 × N-C-C$\underline{H}_3$), 3.41 (q, J = 6.1 Hz, 12.8 Hz, 4H, 2 × N-C$\underline{H}_2$-CH_3), 6.74 (m, 2H, 2 × C$\underline{H}_{ar}$), 7.03 (m, 2H, 2 × C$\underline{H}_{ar}$).
HR-MS (ESI+): m/z calculated for $C_{27}H_{37}BF_2N_3$ $[M+H]^+$: 452.3049, found 452.3009.

1,3,5,7-tetramethyl-2,6-diethyl-8-{4-(1,4,7,10-tetrathia-13-aza-cyclopentadec-13-yl)-phenyl-4- difluoro-4-bora-3a,4a-diaza-*s*-indacene 47.[219] **47** was synthesized according to *GP2*. 118.0 mg Aldehyd-A415T5 (0.379 mmol, 1 eq.) and 103.0 mg 4-ethyl-3,5-dimethylpyrrole **4** (0.834 mmol, 2.2 eq.) yielded shiny, orange crystals of **47** (70 mg, 29%).
^{1}H-NMR (400 MHz, $CDCl_3$) [ppm]: δ = 0.99 (t, 6H, *J* = 7.6 Hz, 2 × CH_2-C$\underline{H}_3$), 1.36 (s, 6H, 2 × C-C$\underline{H}_3$), 2.30 (q, 4H, *J* = 7.5 Hz, 2 × C$\underline{H}_2$-CH_3), 2.52 (s, 6H, 2 × N-C-C$\underline{H}_3$), 2.86 (m, 16H, 4 × C$\underline{H}_2$-S-C$\underline{H}_2$), 3.67 (m, 4H, 2 × N-C$\underline{H}_2$), 6.91 (d, 4H, *J* = 8.7 Hz, 4 × C$\underline{H}_{ar}$), 7.14 (d, 4H, *J* = 8.8 Hz, 4 × C$\underline{H}_{ar}$).
HR-MS (ESI+): m/z calculated for $C_{33}H_{47}BF_2N_3S_4$ $[M+H]^+$: 662.2714, found: 662.2721.

Synthesis of 8-(3,5-bis(trifluoromethyl)phenyl)-3,5-dichloro-4,4-difluoro-4-bora-3a,4a-diaza-*s*-indacene 36. Pyrrole (50.0 ml, 720 mmol, 25.0 eq.) and 3,5-bis(trifluoromethyl)benzaldehyde (6.97 g, 28.8 mmol, 1.0 eq.) were added to a dry round-bottomed flask and degassed with a stream of argon for 10 min. TFA (222 µl, 2.88 mmol, 0.1 eq.) was added and the solution was stirred under argon at room temperature for 30 min. After quenching with 50 ml of 0.1 M NaOH ethyl acetate (50 ml) was added. The organic

phase was washed with water and dried over Na_2SO_4, after extraction with ethyl acetate the solvent was removed under vacuum to afford brown oil. The excess of pyrrole was removed through bulb-to-bulb distillation (80 °C, 0.1 × 10^{-3} bar).

After purification by silica-gel flash column chromatography (1:1 v/v CH_2Cl_2/PE), 8.0 g of the brown solid was dissolved in 300 ml of dry tetrahydrofuran. The solution was purged with argon and cooled to –78 °C. To the cooled solution, a suspension of 8.20 g of *N*-chlorosuccinimide (61.4 mmol, 2.0 eq.) dissolved in 50 ml of THF was added. The reaction mixture was stirred at –78 °C for 2 h and placed in the freezer overnight at –20 °C. After stirring at room temperature for additional 5 h, 150 ml of water were added. After extraction with CH_2Cl_2, the organic layer was dried over Na_2SO_4, the solvent was removed under reduced pressure and the residue was chromatographed on silica gel (1:2 v/v CH_2Cl_2/PE).

4.7 g (0.011 mol, 1.0 eq.) of the intermediate were dissolved in 200 ml CH_2Cl_2 and 2.5 g DDQ (0.011 mol, 1.0 eq.) dissolved in 70 ml CH_2Cl_2 were added. After stirring for 1 h, 20 ml TEA (0.144 mmol, 13.0 eq.) and 20 ml BF3 × OEt_2 (0.160 mmol, 20.0 eq.) were added slowly under vigorously stirring. After stirring overnight, the solvent was removed under reduced pressure. The dark brown residue was dissolved in 100 ml CH_2Cl_2 and washed once with 5 % (m/v) $NaHCO_3$ and twice with water. After extraction of the aqueous phase for three times with CH_2Cl_2, the combined organic solutions were dried over Na_2SO_4 and concentrated under reduced pressure. The crude product was purified by silica-gel flash column chromatography using CH_2Cl_2/PE 4:6 as eluent. Red crystals of **36** were obtained as dark-red crystals (882 mg, 6% over all steps).

^{1}H-NMR (500 MHz, $CDCl_3$) [ppm]: δ = 6.51 (d, 2H, *J* = 4.4 Hz, 2 × C<u>H</u>), 6.72 (d, 2H, *J* = 4.4 Hz, 2 × C<u>H</u>), 7.98 (s, 2H, 2 × C<u>H</u>$_{ar}$), 8.11 (s, 1H, C<u>H</u>$_{ar}$).

HR-MS (ESI+): m/z calculated for $C_{17}H_8BF_8N_2Cl_2$ $[M+H]^+$: 473.0030, found: 473.0076.

2,5,8,11,14-pentaoxaheptadec-16-yne 33.[72] To a solution of 1.60 g NaH (60% dispersion in mineral oil, 40.0 mmol, 0.7 eq.) in 400 ml THF, 8.16 g tetra(ethylene glycol) monomethyl ether **31** (40.0 mmol, 0.7 eq.) was added slowly, while cooling in an ice bath. After 30 min 8.92 g propargyl bromide **32** (80% in toluene, 60.0 mmol, 1.0 eq.) was added to the suspension. After stirring overnight at room temperature, the solvent was removed under reduced pressure. The brown oil was taken up in 100 ml diethyl ether. The organic phase was washed with 100 ml water, dried over Na_2SO_4, filtered and concentrated. The crude product was purified by column chromatography on silica using CH_2Cl_2 as eluent to give compound **33** as yellow-brown oil (7.39 g, 75%).

^{1}H-NMR (400MHz, $CDCl_3$) [ppm]: δ = 2.41 (t, 1H, *J* = 2.4 Hz, C<u>H</u>), 3.36 (s, 3H, C<u>H</u>$_3$), 3.52 (m, 2H, C<u>H</u>$_2$), 3.65 (m, 14H, C<u>H</u>$_2$), 4.19 (d, 2H, *J* = 2.4 Hz, C<u>H</u>$_2$-C).
HR-MS (ESI+): m/z calculated for $C_{12}H_{22}O_5Na$ $[M+Na]^+$: 269.1359 , found 269.1350.

8-(4-hydroxyphenyl)-1,3,5,7-tetramethyl-2,6-diethyl-4,4-bis(3,6,9,12-tetraoxaheptadec-16-ynyl)-4-bora-3a,4a-diaza-*s*-indacene 30.[60] To a solution of 2.10 g **33** (8.0 mmol, 10.0 eq.) in 20 ml anhydrous THF, 9.50 ml ethylmagnesium bromide (9.5 mmol, 1.0 M solution in THF, 12.0 eq.) was added. The reaction was heated at 60 °C overnight. After cooling down to room temperature, a solution of 317.0 mg (0.8 mmol, 1.0 eq.) **5** in 15 ml anhydrous THF was added. The resulting mixture was stirred at 60 °C for additional 5 h until complete consumption of the starting material. Subsequently the solution was concentrated under reduced pressure to remove parts of the THF. Then 100 mL CH_2Cl_2 was added and the organic phase was washed with 100 ml brine. After extraction of the aqueous phase for three times with CH_2Cl_2, the combined organic solutions were dried over Na_2SO_4 and concentrated under reduced pressure. The crude product was purified by column chromatography on silica using EA : MeOH as eluent to give compound **30** as purple-brown oil (0.407 g, 60%).
HR-MS (ESI+): m/z calculated for $C_{47}H_{69}BN_2O_{11}Na$ $[M+Na]^+$: 870.4923, found 870.4908.
^{1}H-NMR (400MHz, $CDCl_3$) [ppm]: δ = 0.97 (t, 6H, *J* = 7.5 Hz, 2 × CH_2-C<u>H</u>$_3$), 1.32 (s, 6H, 2 × C-C<u>H</u>$_3$), 2.30 (q, 4H, *J* =7.5 Hz, 2 × C<u>H</u>$_2$-CH_3), 2.67 (s, 6H, 2 × N-C-C<u>H</u>$_3$), 3.37 (s, 6H, 2 × C<u>H</u>$_3$), 3.54 (m, 4H, 2 × C<u>H</u>$_2$), 3.64 (m, 28H, 2 × C<u>H</u>$_2$), 4.18 (d, *J* = 2.4 Hz, 4H, 2 × C<u>H</u>$_2$-C), 6.92 (d, 2H, *J* = 8.6, 2 × C<u>H</u>$_{ar}$), 7.06 (d, 2H, *J* = 8.6, 2 × C<u>H</u>$_{ar}$).

8-(phenyl)-1,3,5,7-tetramethyl-2,6-diethyl-4,4-difluoro-4-bora-3a,4a-diaza-*s*-indacene 6
Compound 6 was synthesized according reference [285] 336 µl benzoyl chloride (1.98 mmol, 1.0 eq.) and 3-ethyl-2,4-dimethylpyrrole **4** (4.06 mmol, 2.0 eq.) were dissolved in dry CH_2Cl_2 (10 mL) under argon and refluxed until total consumption of the aldehyde (monitored by TLC). 1.5 ml Et_3N (10.8 mmol, 5.0 eq.) were added and the mixture was stirred for additional 5 min. The reaction mixture was then treated with 1.5 ml $BF_3 \times OEt_2$ (11.9 mmol, 6.0 eq.). After stirring overnight, the dark solution was washed with water (3 × 50 ml). After extraction of the aqueous phase with CH_2Cl_2 (3 × 50 ml), the combined organic solutions were dried over Na_2SO_4 and concentrated under reduced pressure. The crude product was purified by column chromatography on silica using toluene as eluent to give compound **6** as bright reddish crystals (441 mg, 29%).

^{1}H-NMR (500 MHz, $CDCl_3$) [ppm]: δ = 0.98 (t, 6H, *J* = 7.6 Hz, 2 × CH_2-C<u>H</u>$_3$), 1.27 (s, 6H, 2 × C-C<u>H</u>$_3$), 2.29 (q, 4H, *J* = 7.6 Hz, 2 × C<u>H</u>$_2$-CH_3), 2.53 (s, 6H, 2 × N-C-C<u>H</u>$_3$), 7.27-7.29 (m, 2H, 2 × C<u>H</u>$_{ar}$), 7.46-7.48 (m, 3H, 3 × C<u>H</u>$_{ar}$).

HR-MS (ESI+): m/z calculated for $C_{23}H_{28}BF_2N_2$ $[M+H]^+$: 381.2314, found: 381.2267.

Bis-(3,5-(3,5-bis(trifluoromethyl)phenyl)vinyl)-8-(3,5-bis(trifluoromethyl)phenyl)-1,7-dimethyl-2,6-diethyl-4,4-difluoro-4-bora-3a,4a-diaza-*s*-indacene 54. 0.103 g (0.2 mmol, 1.0 eq.) of **37** and 74 µl of 3,5-bis(trifluoromethyl)benzaldehyde (0.46 mmol, 2.3 eq.) were dissolved in 10 ml CH_2Cl_2 and 10 mL dimethylformamide (DMF). After the addition of 150 µl glacial acetic acid (2.6 mmol, 13.0 eq.) and 180 µl piperidine (3.1 mmol, 15.5 eq.), the reaction mixture was refluxed for 26 h with a small amount of 4-Å molecular sieves. The solvents were evaporated under reduced pressure and the blue solid was directly chromatographed on silica (3:7 v/v CH_2Cl_2/PE) to obtain cyan needles of **54** (41.0 mg, 21 %).

^{1}H-NMR (500 MHz, $CDCl_3$) [ppm]: δ = 1.21 (t, 6H, *J* = 7.6 Hz, 2 × CH_2-C<u>H</u>$_3$), 1.31 (s, 6H, 2 × C<u>H</u>$_3$), 2.64 (q, 4H, *J* = 7.5 Hz, 2 × C<u>H</u>$_2$-CH_3), 7.35 (d, 2H, *J* = 16.8 Hz, CH=CH), 7.84 (s, 2H, 2 × C<u>H</u>$_{ar}$), 7.85 (d, 2H, *J* = 16.7 Hz, CH=CH), 7.91 (s, 2H, 2 × C<u>H</u>$_{ar}$), 7.99 (s, 4H, 4 × C<u>H</u>$_{ar}$), 8.10 (s, 1H, C<u>H</u>$_{ar}$).

HR-MS (ESI-): m/z calculated for $C_{43}H2_8BF_{20}N_2$ $[M-H]^+$: 963.2026, found: 963.2028.

8-(4-fluorophenyl)-1,3,5,7-tetramethyl-2,6-diethyl-4,4-difluoro-4-bora-3a,4a-diaza-*s*-indacene 48. 48 was synthesized according to *GP1*. The crude product was purified by column chromatography on silica using toluene/CH_2Cl_2 9:1 as eluent to give compound **48** as purple solid (183 mg; 13 %).

^{1}H-NMR (300 MHz, $CDCl_3$) [ppm]: δ = 1.0 (t, 6H, *J* = 7.6 Hz, 2 × CH_2-C<u>H</u>$_3$), 1.33 (s, 6H, 2 × C-C<u>H</u>$_3$), 2.30 (q, 4H, *J* = 7.6 Hz, 2 × C<u>H</u>$_2$-CH_3), 2.54 (s, 6H, 2 × N-C-C<u>H</u>$_3$), 7.14-7.32 (m, 4H, 4 × C<u>H</u>$_{ar}$).

^{13}C-NMR (75 MHz, $CDCl_3$) [ppm]: δ = 11.8 (CH_3), 12.5 (CH_3), 14.6 (CH_3), 17.0 (CH_2), 116.1 (CH_{ar}), 116.4 (CH_{ar}), 130.1 (CH_{ar}),130.2 (CH_{ar}), 130.9 (CH_q), 131.6 (CH_q), 131.7 (CH_q), 133.0 (CH_q), 154.0 (C_q), 161.4 (C_q), 164.7 (C_q).

HR-MS (ESI+): m/z calculated for $C_{23}H_{27}BF_3N_2$ $[M+H]^+$: 398.2256, found: 398.2204.

8-(4-hydroxyphenyl)-1,3,5,7-tetramethyl-2,6-diethyl-dipyrromethene 49 25.0 ml Pyrrole (360 mmol, 25.0 eq.) and 4-hydroxybenzaldehyde **3** (1.76 g, 14.4 mmol, 1.0 eq.) were added to a dry round-bottomed flask and degassed with a stream of argon for 10 min. TFA (111 µL, 1.4 mmol, 0.10 eq.) was added and the solution was stirred under argon at room temperature for 30 min. After quenching with 25 mL of 0.1 M NaOH ethyl acetate (15 mL) was added.

The organic phase was washed with water and dried over Na_2SO_4. After extraction with ethyl acetate the solvent was removed under vacuum to afford a brown oil. The excess of pyrrole was removed trough bulb-to-bulb distillation (80 °C, 0.1 × 10^{-3} bar). Recrystallization with $CHCl_3$/PE afforded compound **49** as slight brown solid (500 mg, 15 %). **^{1}H-NMR** (500 MHz, $CDCl_3$) [ppm]: δ = 5.33 (s, 1H, C<u>H</u>), 5.83 (m, 2H, 2 × C<u>H</u>), 6.08 (dd, 2H, *J* = 2.8 Hz, 5.9 Hz, 2 × C<u>H</u>), 6.61 (dd, 2H, *J* = 2.6 Hz, 4.2 Hz, 2 × C<u>H</u>), 6.67 (d, 2H, *J* = 8.6 Hz, 2 × C<u>H</u>$_{ar}$), 6.99 (d, 2H, *J* = 8.5 Hz, 2 × C<u>H</u>$_{ar}$), 7.86 (s_{br}, 2H, 2 × NH).

^{13}C-NMR (500 MHz, $CDCl_3$) [ppm]: δ = 43.1 (CH), 107.1 (CH), 108.4 (CH), 115.4 (CH), 117.2 (CH), 129.6 (CH), 132.9 (C_q), 134.4 (C_q), 154.5 (C_q).

HR-MS: n.d.

8-(4-acetamidophenyl)-1,3,5,7-tetramethyl-2,6-diethyl- dipyrromethene 50[286] 457 mg Acetaminobenzaldehyde (2.8 mmol, 1.0 eq.) and 756 µl 3-ethyl-2,4-dimethylpyrrole (5.6 mmol, 2.0 eq.) were dissolved in 125 ml CH_2Cl_2. TFA (0.02 ml) was added and the mixture was left at room temperature for 16 h. 640 mg DDQ (2.8 mmol, 1.0 eq.) was added. After 1h the mixture was washed with water (100 ml), dried over Na_2SO_4 and concentrated under reduced pressure. The crude product was purified by column chromatography on silica using CH_2Cl_2/MeOH 9:1 as eluent to give compound **50** as red solid (450 mg, 42%).

^{1}H-NMR (500 MHz, $CDCl_3$) [ppm]: δ = 0.98 (t, 6H, *J* = 7.6 Hz, 2 × CH_2-C<u>H</u>$_3$), 1.25 (s, 3H, C(O)C<u>H</u>$_3$), 1.40 (s, 6H, 2 × C-C<u>H</u>$_3$), 2.30 (q, 4H, *J* = 7.6 Hz, 2 × C<u>H</u>$_2$-CH_3), 2.52 (s, 6H, 2 × N-C-C<u>H</u>$_3$), 3.84 (s_{br}, 1H, NH), 6.77 (d, 2H, *J* = 8.1 Hz, 2 × C<u>H</u>$_{ar}$), 7.00 (d, 2H, *J* = 8.1 Hz, 2 × C<u>H</u>$_{ar}$).

HR-MS (ESI+): m/z calculated for $C_{25}H_{31}BF_2N_3O$ $[M+H]^+$: 438.2528, found: 438.2707.

8-(4-benzoic-methylester)-1,3,5,7-tetramethyl-4,4-difluoro-4-bora-3a,4a-diaza-*s*-indacene 51. The crude product was purified by column chromatography on silica using Hexane/CH_2Cl_2 1:1 as eluent to give compound **51** as red powder (321 mg, 21%).

^{1}H-NMR (500 MHz, $CDCl_3$) [ppm]: δ = 1.28 (s, 6H, 2 × N-C-C<u>H</u>$_3$), 2.48 (s, 6H, 2 × C-C<u>H</u>$_3$), 3.90 (s, 3H, COOC<u>H</u>$_3$), 5.91 (s, 2H, 2 × C<u>H</u>), 7.33 (d, 2H, *J* = 8.3 Hz, 2 × C<u>H</u>$_{ar}$), 8.11 (d, 2H, *J* = 8.4 Hz, 2 × C<u>H</u>$_{ar}$).

HR-MS (ESI+): m/z calculated for $C_{21}H_{22}BF_2N_2O_2$ $[M+H]^+$: 383.1742, found: 383.1785.

8-(4-benzoic-acid)-1,3,5,7-tetramethyl-4,4-difluoro-4-bora-3a,4a-diaza-*s*-indacene 52.

To an anhydrous THF solution (3 ml) of the red solid obtained at the previous step (161mg, 0.42 mmol, 1.0 eq.) an aqueous solution (3 ml) of lithium hydroxide (132 mg, 5.5 mmol, 13

eq.) was added. The reaction mixture was stirred at 40 °C until complete consumption of **51** (20h). The reaction mixture was acidified until pH=2-3 is reached by adding a 10% (v/v) aqueous solution of hydrochloric acid. The crude mixture is extracted 5 times with ethyl acetate and once with chloroform. The combined organic phases are dried over Na_2SO_4, filtered, and evaporated to dryness in vacuo. The crude product was purified by column chromatography on silica using CH_2Cl_2/MeOH 95:5 as eluent to give compound **52** as red-brown powder (153 mg, 99%).

^{1}H-NMR (500 MHz, $CDCl_3$) [ppm]: δ = 1.34 (s, 6H, 2 × N-C-C$\underline{H}_3$), 2.53 (s, 6H, 2 × C-C$\underline{H}_3$), 5.93 (s, 2H, 2 × C$\underline{H}$), 7.42 (d, 2H, *J* = 8.2 Hz, 2 × C$\underline{H}_{ar}$), 8.21 (d, 2H, *J* = 8.2 Hz, 2 × C$\underline{H}_{ar}$), 10.54 (s, 1H, COO$\underline{H}$).

UPLC-MS: n. d.

8-(4-nitrophenyl)-1,3,5,7-tetramethyl-4,4-difluoro-4-bora-3a,4a-diaza-*s*-indacene 53. The crude product was purified by column chromatography on silica using CH_2Cl_2 1:1 as eluent to give compound **53** as red crystals (147 mg, 7%).

^{1}H-NMR (500 MHz, $CDCl_3$) [ppm]: δ = 1.36 (s, 6H, 2 × N-C-C$\underline{H}_3$), 2.56 (s, 6H, 2 × C-C$\underline{H}_3$), 6.01 (s, 2H, 2 × C$\underline{H}$), 7.53 (d, 2H, *J* = 8.7 Hz, 2 × C$\underline{H}_{ar}$), 8.38 (d, 2H, *J* = 8.7 Hz, 2 × C$\underline{H}_{ar}$).

^{13}C-NMR (126 MHz, $CDCl_3$) [ppm]: δ = 8.8 (CH_3), 14.8 (CH_3), 122.0 (CH), 124.5 (CH_{ar}), 129.8 (CH_{ar}), 130.8 (C_q), 138.5 (C_q), 142.1 (C_q), 142.7 (C_q), 148.5 (C_q), 156.8 (C_q) .

HR-MS (ESI+): m/z calculated for $C_{19}H_{19}BF_2N_3O_2$ $[M+H]^+$: 370.1538, found: 370.1523.

Literature cited

1. M. Muyskens, *J. Chem. Educ.*, 2006, 83, 765-768.

2. A. U. Acuna, *J. Chem. Educ.*, 2007, 84, 231-231.

3. J. R. Partington, *Ann. Sci.*, 1955, 11, 1-26.

4. G. G. Stokes, *Philos. Trans. R. Soc. London*, 1852, 142, 463-562.

5. A. Ulises Acuna, F. Amat-Guerri, P. Morcillo, M. Liras and B. Rodriguez, *Org. Lett.*, 2009, 11, 3020-3023.

6. Bernard Valeur and J.-C. Brochon, in *Springer Series on Fluorescence*, ed. O. Wolfbeis, 2001, vol. 1.

7. O. Wolfbeis, in *Fiber Optic Chemical Sensors and Biosensors*, CRC Press, Boca Raton, 1991.

8. S. Zhu, T. Fischer, W. Wan, A. B. Descalzo and K. Rurack, in *Luminescence Applied in Sensor Science*, eds. L. Prodi, M. Montalti and N. Zaccheroni, 2011, vol. 300, pp. 51-91.

9. R. Martinez-Manez, F. Sancenon, M. Hecht, M. Biyikal and K. Rurack, *Anal. Bioanal. Chem.*, 2011, 399, 55-74.

10. A. A. Belyustin, *J. Solid State Electrochem.*, 2011, 15, 47-65.

11. J. N. Moorthy, T. Shevchenko, A. Magon and C. Bohne, *J. Photochem. Photobiol. A-Chem.*, 1998, 113, 189-195.

12. H. Tomiyasu and Y. Asano, *Prog. Nucl. Energy*, 1998, 32, 421-427.

13. S. I. Stepanov, A. V. Boyarintsev, M. V. Vazhenkov, B. F. Myasoedov, E. O. Nazarov, A. M. Safiulina, I. G. Tananaev, H. V. So, A. M. Chekmarev and A. Y. Civadze, *Russ. J. Gen. Chem.*, 2011, 81, 1949-1959.

14. T. Astrup, R. Jakobsen, T. H. Christensen, J. B. Hansen and O. Hjelmar, *Waste Manage. Res.*, 2006, 24, 491-502.

15. W. M. Mayes, L. C. Batty, P. L. Younger, A. P. Jarvis, M. Koiv, C. Vohla and U. Mander, *Sci. Total Environ.*, 2009, 407, 3944-3957.

16. P. B. Dhamole, R. R. Nair, S. F. D'Souza and S. S. Lele, *Appl. Biochem. Biotechnol.*, 2008, 151, 433-440.

17. P. Sharma, H. Kaur, M. Sharma and V. Sahore, *Environ. Monit. Assess.*, 2011, 183, 151-195.

18. W. M. Mayes, P. L. Younger and J. Aumonier, *Environ. Sci. Technol.*, 2006, 40, 1237-1243.

19. V. O. Biederbeck, C. A. Campbell, H. Ukrainetz, D. Curtin and O. T. Bouman, *Can. J. Soil Sci.*, 1996, 76, 7-14.

20. Q. Huang, Y. Peng, X. Li, H. F. Wang and Y. Z. Zhang, *Curr. Microbiol.*, 2003, 46, 169-173.

21. A. Dayanandan, J. Kanagaraj, L. Sounderraj, R. Govindaraju and G. S. Rajkumar, *J. Clean Prod.*, 2003, 11, 533-536.

22. C. Swaminathan, P. Pyke and R. F. Johnston, *Miner. Eng.*, 1993, 6, 1-16.

23. M. Graefe, G. Power and C. Klauber, *Hydrometallurgy*, 2011, 108, 60-79.

24. K. Horikoshi, *Fems Microbiol. Rev.*, 1996, 18, 259-270.

25. T. A. Krulwich, *Mol. Microbiol.*, 1995, 15, 403-410.

26. D. K. Nordstrom, C. N. Alpers, C. J. Ptacek and D. W. Blowes, *Environ. Sci. Technol.*, 2000, 34, 254-258.

27. A. S. Kocincova, S. Nagl, S. Arain, C. Krause, S. M. Borisov, M. Arnold and O. S. Wolfbeis, *Biotechnol. Bioeng.*, 2008, 100, 430-438.

28. N. Boens, W. W. Qin, M. Baruah, W. M. De Borggraeve, A. Filarowski, N. Smisdom, M. Ameloot, L. Crovetto, E. M. Talavera and J. M. Alvarez-Pez, *Chem.-Eur. J.*, 2011, 17, 10924-10934.

29. J. Y. Han and K. Burgess, *Chem. Rev.*, 2010, 110, 2709-2728.

30. Y. T. Chen, H. L. Wang, L. Wan, Y. Z. Bian and J. Z. Jiang, *J. Org. Chem.*, 2011, 76, 3774-3781.

31. S. M. Borisov and O. S. Wolfbeis, *Chem. Rev.*, 2008, 108, 423-461.

32. A. Safavi and H. Abdollahi, *Anal. Chim. Acta*, 1998, 367, 167-173.

33. A. Safavi and M. Bagheri, *Sens. Actuator B-Chem.*, 2003, 90, 143-150.

34. T. Werner and O. S. Wolfbeis, *Fresenius J. Anal. Chem.*, 1993, 346, 564-568.

35. H. W. Xu and O. A. Sadik, *Analyst*, 2000, 125, 1783-1786.

36. T. A. Canada, D. B. Beach and Z. L. Xue, *Anal. Chem.*, 2005, 77, 2842-2851.

37. A. Treibs and F. H. Kreuzer, *Liebigs Ann. Chem.*, 1968, 718, 208-214.

38. N. Boens, V. Leen and W. Dehaen, *Chem. Soc. Rev.*, 2012, 41, 1130-1172.

39. T. Bura, P. Retailleau, G. Ulrich and R. Ziessel, *J. Org. Chem.*, 2011, 76, 1109-1117.

40. A. Coskun and E. U. Akkaya, *J. Am. Chem. Soc.*, 2006, 128, 14474-14475.

41. H. Sunahara, Y. Urano, H. Kojima and T. Nagano, *J. Am. Chem. Soc.*, 2007, 129, 5597-5604.

42. H. Kobayashi, M. Ogawa, R. Alford, P. L. Choyke and Y. Urano, *Chem. Rev.*, 2010, 110, 2620-2640.

43. H. Y. Lee, D. R. Bae, J. C. Park, H. Song, W. S. Han and J. H. Jung, *Angew. Chem. Int. Ed.*, 2009, 48, 1239-1243.

44. G. Ulrich, R. Ziessel and A. Harriman, *Angew. Chem. Int. Ed.*, 2008, 47, 1184-1201.

45. M. Kollmannsberger, K. Rurack, U. Resch-Genger and J. Daub, *J. Phys. Chem. A*, 1998, 102, 10211-10220.

46. C. Dumas-Verdes, F. Miomandre, E. Lepicier, O. Galangau, T. T. Vu, G. Clavier, R. Meallet-Renault and P. Audebert, *Eur. J. Org. Chem.*, 2010, 13, 2525-2535.

47. Y. Kubota, J. Uehara, K. Funabiki, M. Ebihara and M. Matsui, *Tetrahedron Lett.*, 2010, 51, 6195-6198.

48. I. Pochorovski, B. Breiten, W. B. Schweizer and F. Diederich, *Chem.-Eur. J.*, 2010, 16, 12590-12602.

49. A. Loudet and K. Burgess, *Chem. Rev.*, 2007, 107, 4891-4932.

50. D. Tleugabulova, Z. Zhang and J. D. Brennan, *J. Phys. Chem. B*, 2002, 106, 13133-13138.

51. F. Bergstrom, I. Mikhalyov, P. Hagglof, R. Wortmann, T. Ny and L. B. A. Johansson, *J. Am. Chem. Soc.*, 2002, 124, 196-204.

52. J. G. Wang, Y. J. Hou, C. Li, B. W. Zhang and X. S. Wang, *Sens. Actuator B-Chem.*, 2011, 157, 586-593.

53. M. Maus and K. Rurack, *New J. Chem.*, 2000, 24, 677-686.

54. H. Rohr, C. Trieflinger, K. Rurack and J. Daub, *Chem.-Eur. J.*, 2006, 12, 689-700.

55. S. Hoogendoorn, A. E. M. Blom, L. I. Willems, G. A. van der Marel and H. S. Overkleeft, *Org. Lett.* , 2011, 13, 5656-5659.

56. M. Baruah, W. W. Qin, N. Basaric, W. M. De Borggraeve and N. Boens, *J. Org. Chem.*, 2005, 70, 4152-4157.

57. B. C. Guo, X. J. Peng, A. J. Cui, Y. K. Wu, M. Z. Tian, L. Z. Zhang, X. Q. Chen and Y. L. Gao, *Dyes Pigment.*, 2007, 73, 206-210.

58. W. W. Qin, M. Baruah, A. Stefan, M. Van der Ameraer and N. Boens, *ChemPhysChem*, 2005, 6, 2343-2351.

59. S. Atilgan, T. Ozdemir and E. U. Akkaya, *Org. Lett.*, 2008, 10, 4065-4067.

60. S. L. Zhu, J. T. Zhang, G. Vegesna, F. T. Luo, S. A. Green and H. Y. Liu, *Org. Lett.*, 2011, 13, 438-441.

61. A. Romieu, C. Massif, S. Rihn, G. Ulrich, R. Ziessel and P.-Y. Renard, *New J. Chem.*, 2013, 37, 1016-1027.

62. L. J. Jiao, J. L. Li, S. Z. Zhang, C. Wei, E. H. Hao and M. G. H. Vicente, *New J. Chem.*, 2009, 33, 1888-1893.

63. V. H. Yen, L. Micouin, C. Ronet, G. Gachelin and M. Bonin, *ChemBioChem*, 2003, 4, 27-33.

64. K. Giessler, H. Griesser, D. Goehringer, T. Sabirov and C. Richert, *Eur. J. Org. Chem.*, 2010, 19, 3611-3620.

65. O. Dilek and S. L. Bane, *Bioorg. Med. Chem. Lett.*, 2009, 19, 6911-6913.

66. S. C. Dodani, Q. W. He and C. J. Chang, *J. Am. Chem. Soc.*, 2009, 131, 18020-18021.

67. S.-L. Niu, G. Ulrich, P. Retailleau, J. Harrowfield and R. Ziessel, *Tetrahedron Lett.*, 2009, 50, 3840-3844.

68. S. L. Niu, G. Ulrich, R. Ziessel, A. Kiss, P. Y. Renard and A. Romieu, *Org. Lett.*, 2009, 11, 2049-2052.

69. T. Bura and R. Ziessel, *Org. Lett.* , 2011, 13, 3072-3075.

70. A. M. Courtis, S. A. Santos, Y. Guan, J. A. Hendricks, B. Ghosh, D. M. Szantai-Kis, S. A. Reis, J. V. Shah and R. Mazitschek, *Bioconjugate Chem.*, 2014, 25, 1043-1051.

71. S. Atilgan, Z. Ekmekci, A. L. Dogan, D. Guc and E. U. Akkaya, *Chem. Commun.*, 2006, 42, 4398-4400.

72. E. Jahnke, J. Weiss, S. Neuhaus, T. N. Hoheisel and H. Frauenrath, *Chem.-Eur. J.*, 2009, 15, 388-404.

73. M. Kellermeier, H. Colfen and J. M. Garcia-Ruiz, *Eur. J. Inorg. Chem.*, 2012, 32, 5123-5144.

74. J. Eiblmeier, M. Kellermeier, D. Rengstl, J. Manuel Garcia-Ruiz and W. Kunz, *CrystEngComm*, 2013, 15, 43-53.

75. J. Eiblmeier, S. Dankesreiter, A. Pfitzner, G. Schmalz, W. Kunz and M. Kellermeier, *Cryst. Growth Des.*, 2014, 14, 6177-6188.

76. S. Kalia, A. Dufresne, B. M. Cherian, B. S. Kaith, L. Averous, J. Njuguna and E. Nassiopoulos, *Int. J. Polymer Sci.*, 2011, 2011, 1-35.

77. M. A. Hubbe, O. J. Rojas, L. A.Lucia and M. Sain, *BioResources*, 2008, 3, 929-980.

78. S. J. Eichhorn, A. Dufresne, M. Aranguren, N. E. Marcovich, J. R. Capadona, S. J. Rowan, C. Weder, W. Thielemans, M. Roman, S. Renneckar, W. Gindl, S. Veigel, J. Keckes, H. Yano, K. Abe, M. Nogi, A. N. Nakagaito, A. Mangalam, J. Simonsen, A. S. Benight, A. Bismarck, L. A. Berglund and T. Peijs, *J. Mater. Sci.*, 2010, 45, 1-33.

79. A. Payen, *C. R. Hebd. Seances Acad. Sci.*, 1838, 7, 1052-1056.

80. D. Klemm, B. Heublein, H. P. Fink and A. Bohn, *Angew. Chem. Int. Ed.*, 2005, 44, 3358-3393.

81. D. Klemm, D. Schumann, F. Kramer, N. Hessler, M. Hornung, H.-P. Schmauder and S. Marsch, in *Polysaccharides* ed. D. Klemm, 2006, vol. 205, pp. 49-96.

82. S. Paunonen, *BioResources*, 2013, 8, 3098-3121.

83. H. Barreteau, C. Delattre and P. Michaud, *Food. Technol. Biotech.*, 2006, 44, 323-333.

84. W. Czaja, A. Krystynowicz, S. Bielecki and R. M. Brown, *Biomaterials*, 2006, 27, 145-151.

85. I. Siro and D. Plackett, *Cellulose*, 2010, 17, 459-494.

86. C. Chang and L. Zhang, *Carbohyd. Polym.*, 2011, 84, 40-53.

87. Y. Habibi, L. A. Lucia and O. J. Rojas, *Chem. Rev.*, 2010, 110, 3479-3500.

88. J. Araki, M. Wada, S. Kuga and T. Okano, *Colloid. Surface A*, 1998, 142, 75-82.

89. R. R. Lahiji, X. Xu, R. Reifenberger, A. Raman, A. Rudie and R. J. Moon, *Langmuir*, 2010, 26, 4480-4488.

90. D. Bondeson, A. Mathew and K. Oksman, *Cellulose*, 2006, 13, 171-180.

91. H. Mertaniemi, A. Laukkanen, J.-E. Teirfolk, O. Ikkala and R. H. A. Ras, *RSC Adv.*, 2012, 2, 2882-2886.

92. R. Kolakovic, T. Laaksonen, L. Peltonen, A. Laukkanen and J. Hirvonen, *Int. J. Pharm.*, 2012, 430, 47-55.

93. R. Kolakovic, L. Peltonen, T. Laaksonen, K. Putkisto, A. Laukkanen and J. Hirvonen, *AAPS PharmSciTech*, 2011, 12, 1366-1373.

94. D. I. Rożkiewicz, B. J. Ravoo and D. N. Reinhoudt, *The Supramolecular Chemistry of Organic-Inorganic Hybrid Materials*, Wiley Hoboken, 2010

95. M. Hecht, T. Fischer, P. Dietrich, W. Kraus, A. B. Descalzo, W. E. S. Unger and K. Rurack, *ChemistryOpen*, 2013, 2, 25-38.

96. Y. Xing and E. Borguet, *Langmuir*, 2007, 23, 684-688.

97. S. Suzuki, M. Kozaki, K. Nozaki and K. Okada, *J. Photochem. Photobiol. C-Photochem. Rev.*, 2011, 12, 269-292.

98. R. Ziessel, G. Ulrich and A. Harriman, *New J. Chem.*, 2007, 31, 496-501.

99. T. Rohand, W. Qin, N. Boens and W. Dehaen, *Eur. J. Org. Chem.*, 2006, 20, 4658-4663.

100. L. Li, B. Nguyen and K. Burgess, *Bioorg. Med. Chem. Lett.*, 2008, 18, 3112-3116.

101. D. W. Domaille, L. Zeng and C. J. Chang, *J. Am. Chem. Soc.*, 2010, 132, 1194-1195.

102. Y. A. Volkova, B. Brizet, P. D. Harvey, A. D. Averin, C. Goze and F. Denat, *Eur. J. Org. Chem.*, 2013, 2013, 4270-4279.

103. I. Moczar, P. Huszthy, Z. Maidics, M. Kadar and K. Toth, *Tetrahedron*, 2009, 65, 8250-8258.

104. T. Rohand, M. Baruah, W. W. Qin, N. Boens and W. Dehaen, *Chem. Commun.*, 2006, 3, 266-268.

105. B. J. Littler, M. A. Miller, C. H. Hung, R. W. Wagner, D. F. O'Shea, P. D. Boyle and J. S. Lindsey, *J. Org. Chem.*, 1999, 64, 1391-1396.

106. K. Rurack, A. B. Descalzo, T. Fischer and T. Behnke, *Difluoroboradiazaindacen-Farbstoffe*, DE102009028982, 2011.

107. K. Rurack, A. B. Descalzo, T. Fischer and T. Behnke, *Difluoroboradiazaindacen-Farbstoffe*, EP2302002, 2011.

108. K. Rurack, A. B. Descalzo, T. Fischer and T. Behnke, *Difluoroboradiazaindacene Dyes*, US20110054187, 2011.

109. Z. Shen, H. Rohr, K. Rurack, H. Uno, M. Spieles, B. Schulz, G. Reck and N. Ono, *Chem.-Eur. J.*, 2004, 10, 4853-4871.

110. Y.-H. Yu, A. B. Descalzo, Z. Shen, H. Roehr, Q. Liu, Y.-W. Wang, M. Spieles, Y.-Z. Li, K. Rurack and X.-Z. You, *Chem. Asian J.*, 2006, 1, 176-187.

111. Y. Chen, L. Wan, D. Zhang, Y. Bian and J. Jiang, *Photochem. Photobiol. Sci.*, 2011, 10, 1030-1038.

112. S. Mula, A. K. Ray, M. Banerjee, T. Chaudhuri, K. Dasgupta and S. Chattopadhyay, *J. Org. Chem.*, 2008, 73, 2146-2154.

113. F. Lopez Arbeloa, J. Banuelos Prieto, V. Martinez Martinez, T. Arbeloa Lopez and I. Lopez Arbeloa, *ChemPhysChem*, 2004, 5, 1762-1771.

114. A. Filarowski, M. Kluba, K. Cieslik-Boczula, A. Koll, A. Kochel, L. Pandey, W. M. De Borggraeve, M. Van der Auweraer, J. Catalan and N. Boens, *Photochem. Photobiol. Sci.*, 2010, 9, 996-1008.

115. K. Rurack, P. Saalfrank and J. Daub, unpublished results.

116. C. Trieflinger, H. Rohr, K. Rurack and J. Daub, *Angew. Chem. Int. Ed.*, 2005, 44, 6943-6947.

117. W. Qin, V. Leen, T. Rohand, W. Dehaen, P. Dedecker, M. Van der Auweraer, K. Robeyns, L. Van Meervelt, D. Beljonne, B. Van Averbeke, J. N. Clifford, K. Driesen, K. Binnemans and N. Boens, *J.Phys. Chem. A*, 2009, 113, 439-447.

118. W. Qin, V. Leen, W. Dehaen, J. Cui, C. Xu, X. Tang, W. Liu, T. Rohand, D. Beljonne, B. Van Averbeke, J. N. Clifford, K. Driesen, K. Binnemans, M. Van der Auweraer and N. Boens, *J. Phys. Chem. C*, 2009, 113, 11731-11740.

119. D. W. Cho, M. Fujitsuka, K. H. Choi, M. J. Park, U. C. Yoon and T. Majima, *J. Phys. Chem. B*, 2006, 110, 4576-4582.

120. C. Hansch, A. Leo and R. W. Taft, *Chem. Rev.*, 1991, 91, 165-195.

121. K. Dimroth, F. Bohlmann, C. Reichard and T. Siepmann, *Liebigs Ann. Chem.*, 1963, 661, 721-896.

122. E. Lippert, *Z. Naturforsch.*, 1955, 10a, 541-545.

123. E. Lippert, *Z. Elektrochem.*, 1957, 61, 962.

124. N. Mataga, Y. Kaifu and M. Koizumi, *Bull. Chem. Soc. Jpn.*, 1956, 29, 465-470.

125. E. G. McRae, *J. Phys. Chem.* , 1957, 61, 562-572.

126. N. G. Bakhshiev, *Opt. Spectrosc.* , 1961, 10, 279-283.

127. N. G. Bakhshiev, *Opt. Spectrosc.* , 1962, 13, 24-28.

128. L. Bilot and A. Kawski, *Z. Naturforsch.*, 1962, 17a.

129. R. W. Taft and M. J. Kamlet, *J. Am. Chem. Soc.*, 1976, 98, 2886-2894.

130. M. J. Kamlet and R. W. Taft, *J. Am. Chem. Soc.*, 1976, 98, 377-383.

131. Y. J. Xie, C. A. S. Hill, Z. F. Xiao, H. Militz and C. Mai, *Compos. Part A-Appl. Sci. Manuf.*, 2010, 41, 806-819.

132. K. Missoum, M. N. Belgacem and J. Bras, *Materials*, 2013, 6, 1745-1766.

133. M. C. B. Salon, M. Abdelmouleh, S. Boufi, M. N. Belgacem and A. Gandini, *J. Colloid Interface Sci.*, 2005, 289, 249-261.

134. C. Gebald, J. A. Wurzbacher, P. Tingaut, T. Zimmermann and A. Steinfeld, *Environ. Sci. Technol.*, 2011, 45, 9101-9108.

135. J. Lu, P. Askeland and L. T. Drzal, *Polymer*, 2008, 49, 1285-1296.

136. M. Abdelmouleh, S. Boufi, A. ben Salah, M. N. Belgacem and A. Gandini, *Langmuir*, 2002, 18, 3203-3208.

137. M. Abdelmouleh, S. Boufi, M. N. Belgacem, A. P. Duarte, A. Ben Salah and A. Gandini, *Int. J. Adhes. Adhes.*, 2004, 24, 43-54.

138. A. A. El Hadad, D. Carbonell, V. Barranco, A. Jimenez-Morales, B. Casal and J. Carlos Galvan, *Colloid Polym. Sci.*, 2011, 289, 1875-1883.

139. J. Yang, C. R. Han, J. F. Duan, M. G. Ma, X. M. Zhang, F. Xu, R. C. Sun and X. M. Xie, *J. Mater. Chem.*, 2012, 22, 22467-22480.

140. P. Innocenzi, G. Brusatin, S. Licoccia, M. L. Di Vona, F. Babonneau and B. Alonso, *Chem. Mater.*, 2003, 15, 4790-4797.

141. S. Gross and K. Mueller, *J. Sol-Gel Sci. Technol.*, 2011, 60, 283-298.

142. J. S. Beck, J. C. Vartuli, W. J. Roth, M. E. Leonowicz, C. T. Kresge, K. D. Schmitt, C. T. W. Chu, D. H. Olson, E. W. Sheppard, S. B. McCullen, J. B. Higgins and J. L. Schlenker, *J. Am. Chem. Soc.*, 1992, 114, 10834-10843.

143. C. T. Kresge, M. E. Leonowicz, W. J. Roth, J. C. Vartuli and J. S. Beck, *Nature*, 1992, 359, 710-712.

144. J. Y. Ying, C. P. Mehnert and M. S. Wong, *Angew. Chem. Int. Ed.*, 1999, 38, 56-77.

145. D. Mishra, J. R. Hubenak and A. B. Mathur, *Journal of Biomedical Materials Research Part A*, 2013, 101, 3646-3660.

146. A. Corma, *Chem. Rev.*, 1997, 97, 2373-2419.

147. D. E. De Vos, M. Dams, B. F. Sels and P. A. Jacobs, *Chem. Rev.*, 2002, 102, 3615-3640.

148. A. Walcarius and L. Mercier, *J. Mater. Chem.*, 2010, 20, 4478-4511.

149. M. Kruk and M. Jaroniec, *Chem. Mater.*, 2001, 13, 3169-3183.

150. J. F. Diaz and K. J. Balkus, *J. Mol. Catal. B Enzym.*, 1996, 2, 115-126.

151. M. Vallet-Regi, M. Colilla and I. Izquierdo-Barba, *J. Biomed. Mater. Res. A*, 2008, 4, 1-15.

152. M. Vallet-Regi, A. Ramila, R. P. del Real and J. Perez-Pariente, *Chem. Mater.*, 2001, 13, 308-311.

153. M. Vallet-Regi, F. Balas and D. Arcos, *Angew. Chem. Int. Ed.*, 2007, 46, 7548-7558.

154. I. I. Slowing, B. G. Trewyn, S. Giri and V. S. Y. Lin, *Adv. Funct. Mater*, 2007, 17, 1225-1236.

155. M. Hecht, E. Climent, M. Biyikal, F. Sancenon, R. Martinez-Manez and K. Rurack, *Coord. Chem. Rev.*, 2013, 257, 2589-2606.

156. A. B. Descalzo, R. Martinez-Manez, R. Sancenon, K. Hoffmann and K. Rurack, *Angew. Chem. Int. Ed.*, 2006, 45, 5924-5948.

157. J. V. Ros-Lis, M. D. Marcos, R. Martinez-Manez, K. Rurack and J. Soto, *Angew. Chem. Int. Ed.*, 2005, 44, 4405-4407.

158. J. V. Ros-Lis, R. Casasus, M. Comes, C. Coll, M. D. Marcos, R. Martinez-Manez, F. Sancenon, J. Soto, P. Amoros, J. El Haskouri, N. Garro and K. Rurack, *Chem.-Eur. J.*, 2008, 14, 8267-8278.

159. J. Andersson, J. Rosenholm, S. Areva and M. Linden, *Chem. Mater.*, 2004, 16, 4160-4167.

160. M. Manzano and M. Vallet-Regi, *J. Mater. Chem.*, 2010, 20, 5593-5604.

161. L. F. V. Ferreira, M. J. Lemos, M. J. Reis and A. M. B. do Rego, *Langmuir*, 2000, 16, 5673-5680.

162. R. W. Bonsnes and H. H. Taussky, *J. Biol. Chem.*, 1945, 158, 581-591.

163. D. F. Swinehart, *J. Chem. Educ.*, 1962, 39, 333-335.

164. X. S. Zhao, G. Q. Lu, A. K. Whittaker, G. J. Millar and H. Y. Zhu, *J. Phys. Chem. B*, 1997, 101, 6525-6531.

165. E. Martin, A. Pardo, M. S. Guijarro and J. I. Fernandez-Alonso, *J. Mol. Struc,*, 1986, 142, 197.

166. N. Klonis and W. H. Sawyer, *J. Fluoresc.*, 1996, 6, 147-157.

167. N. Klonis, A. H. A. Clayton, E. W. Voss and W. H. Sawyer, *Photochem. Photobiol.*, 1998, 67, 500-510.

168. R. W. Ramette and E. B. Sandell, *J. Am. Chem. Soc.*, 1956, 78, 4872–4878.

169. D. A. Hinckley and P. G. Seybold, *Spectrochim. Acta A*, 1988, 88, 1053–1059.

170. D. A. Hinckley, P. G. Seybold and D. P. Borris, *Spectrochim. Acta A*, 1986, 42.

171. K. K. Rohatgi-Mukherjee and I. Lopez-Arbeloa, *J. Photochem. Photobiol. A*, 1991, 58, 277–288.

172. P. A. Bergstroem, J. Lindgren and O. Kristiansson, *J. Phys. Chem.*, 1991, 95, 8575–8580.

173. I. L. Arbeloa and K. K. Rohatgi-Mukherjee, *Chem. Phys. Lett.*, 1986, 128, 474-479.

174. C. J. Collison, M. J. O'Donnell and J. L. Alexander, *J. Phys. Chem. C*, 2008, 112, 15144–15150.

175. F.Hofmeister, *Arch. Exp. Pathol. Pharmacol.* , 1888, 24, 247-260.

176. W. J. McKinney and A. I. Popov, *J. Phys. Chem.*, 1970, 74, 535-541.

177. J. F. Coetzee and W. R. Sharpe, *J. Solution Chem.*, 1972, 1, 77-91.

178. A. B. Descalzo, K. Rurack, H. Weisshoff, R. Martinez-Manez, M. D. Marcos, P. Amoros, K. Hoffmann and J. Soto, *J. Am. Chem. Soc.*, 2005, 127, 184-200.

179. T. Ukmar, U. Maver, O. Planinsek, A. Pintar, V. Kaucic, A. Godec and M. Gaberscek, *J. Mater. Chem.*, 2012, 22, 1112-1120.

180. J. B. S. Ng, P. Kamali-Zare, H. Brismar and L. Bergstrom, *Langmuir*, 2008, 24, 11096-11102.

181. A. S. Hoffman, *J. Controlled Release*, 2008, 132, 153-163.

182. J. Kaur, K. V. Singh, R. Boro, K. R. Thampi, M. Raje, G. C. Varshney and C. R. Suri, *Environ. Sci. Technol.*, 2007, 41, 5028-5036.

183. S. Gandhi, N. Caplash, P. Sharma and C. R. Suri, *Biosens. Bioelectron.*, 2009, 25, 502-505.

184. A. Komano, H. Maruko, H. Sekiguchi and Y. Seto, *Forensic Toxicol.*, 2011, 29, 38-43.

185. Z. Zou, D. Du, J. Wang, J. N. Smith, C. Timchalk, Y. Li and Y. Lin, *Anal. Chem.*, 2010, 82, 5125-5133.

186. Y. Bai, C. Tian, X. Wei, Y. Wang, D. Wang and X. Shi, *RSC Adv.*, 2012, 2, 1778-1781.

187. Report of the European Security Research Advisory Board ESRAB—Meeting the Challenge: the European Security Research Agenda, Office for Official Publications

of the European Communities, Luxembourg., http://ec.europa.eu/enterprise/policies/security/files/esrab_report_en.pdf, , 2006.

188. NCTC 2010 Report on Terrorism, National Counterterrorism Center, Washington DC, 2011, http://www.nctc.gov/witsbanner/docs/2010_report_on_terrorism.pdf (see, for example, Chart 10: Wounded Victims Grouped by Weapon Type).

189. R. M. Burks and D. S. Hage, *Anal. Bioanal. Chem.*, 2009, 395, 301-313.

190. S. Girotti, E. Ferri, E. Maiolini, L. Bolelli, M. D'Elia, D. Coppe and F. S. Romolo, *Anal. Bioanal. Chem.*, 2011, 400, 313-320.

191. R. Schulte-Ladbeck, P. Kolla and U. Karst, *Analyst*, 2002, 127, 1152-1154.

192. E. Climent, D. Groeninger, M. Hecht, M. A. Walter, R. Martinez-Manez, M. G. Weller, F. Sancenon, P. Amoros and K. Rurack, *Chem.-Eur. J.*, 2013, 19, 4117-4122.

193. M. A. Walter, U. Panne and M. G. Weller, *Biosensors*, 2011, 1, 93-106.

194. M. A. Walter, D. Pfeifer, W. Kraus, F. Emmerling, R. J. Schneider, U. Panne and M. G. Weller, *Langmuir*, 2010, 26, 15418-15423.

195. J. J. Carvalho, M. A. Walter, Y. Baermann-Stapel, M. G. Weller, U. Panne, J. A. Schenk and R. J. Schneider, *In Vivo*, 2012, 26, 63-69.

196. H. Lin and K. S. Suslick, *J. Am. Chem. Soc.*, 2010, 132, 15519-15521.

197. P. Anh Le-Tuan, D. L. Sedlak and F. M. Doyle, *Appl. Catal. B*, 2012, 126, 258-264.

198. F. M. M. Morel, A. M. L. Kraepiel and M. Amyot, *Annu. Rev. Ecol. Syst.*, 1998, 29, 543-566.

199. D. W. Boening, *Chemosphere*, 2000, 40, 1335-1351.

200. R. von Burg and M. R. Greenwood, in *Metals and Their Compounds in the Enironment*, ed. E. Merian, VCH, Weinheim, 1991, pp. 1045-1088.

201. L. D. Hylander, *Water Air Soil Poll.*, 2001, 125, 331-344.

202. W. F. Fitzgerald, C. H. Lamborg and C. R. Hammerschmidt, *Chem. Rev.*, 2007, 107, 641-662.

203. T. W. Clarkson, L. Magos and G. J. Myers, *New Engl. J. Med.*, 2003, 349, 1731-1737.

204. WHO, in *Guidelines for drinking-water quality*, Geneve, 3rd edn., 2004, vol. 1, p. 188.

205. W. R. Hatch and W. L. Ott, *Anal. Chem.*, 1968, 40, 2085-2089.

206. H. Hintelmann, R. Falter, G. Ilgen and R. D. Evans, *Fresenius J. Anal. Chem.*, 1997, 358, 363-370.

207. H. N. Kim, W. X. Ren, J. S. Kim and J. Yoon, *Chem. Soc. Rev.*, 2012, 41, 3210-3244.

208. X. F. Guo, X. H. Qian and L. H. Jia, *J. Am. Chem. Soc.*, 2004, 126, 2272-2273.

209. A. B. Descalzo, R. Martinez-Manez, R. Radeglia, K. Rurack and J. Soto, *J. Am. Chem. Soc.*, 2003, 125, 3418-3419.

210. J. F. Callan, A. P. de Silva and D. C. Magri, *Tetrahedron*, 2005, 61, 8551-8588.

211. B. Valeur and I. Leray, *Coord. Chem. Rev.*, 2000, 205, 3-40.

212. C. Bargossi, M. C. Fiorini, M. Montalti, L. Prodi and N. Zaccheroni, *Coord. Chem. Rev.*, 2000, 208, 17-32.

213. Y.-F. Li, Y.-F. Wei, Y. Tan, X.-F. Kong, K. Zhou, Z.-M. Wu and Y.-J. Liu, *Anal. Sci.*, 2014, 30, 257-262.

214. Q. Duong Tuan and J. S. Kim, *Chem. Rev.*, 2010, 110, 6280-6301.

215. C. Sanchez, B. Lebeau, F. Chaput and J. P. Boilot, *Adv. Mater.*, 2003, 15, 1969-1994.

216. R. Martinez-Manez, F. Sancenon, M. Biyikal, M. Hecht and K. Rurack, *J. Mater. Chem.*, 2011, 21, 12588-12604.

217. F. Hoffmann, M. Cornelius, J. Morell and M. Froeba, *Angew. Chem. Int. Ed.*, 2006, 45, 3216-3251.

218. K. Rurack, J. L. Bricks, G. Reck, R. Radeglia and U. Resch-Genger, *J. Phys. Chem. A*, 2000, 104, 3087-3109.

219. K. Rurack, M. Kollmannsberger, U. Resch-Genger and J. Daub, *J. Am. Chem. Soc.*, 2000, 122, 968-969.

220. Z. Tao, B. B. Toms, J. Goodisman and T. Asefa, *Chem. Res. Toxicol.*, 2009, 22, 1869-1880.

221. H. Goesmann and C. Feldmann, *Angew. Chem. Int. Ed.*, 2010, 49, 1362-1395.

222. U. Resch-Genger, M. Grabolle, S. Cavaliere-Jaricot, R. Nitschke and T. Nann, *Nat. Methods*, 2008, 5, 763-775.

223. W. Stöber and A. Fink, *J. Colloid Interface Sci.*, 1968, 26, 62-69.

224. Y. N. Xia, B. Gates, Y. D. Yin and Y. Lu, *Adv. Mater.*, 2000, 12, 693-713.

225. L. M. Rossi, L. F. Shi, F. H. Quina and Z. Rosenzweig, *Langmuir*, 2005, 21, 4277-4280.

226. F. J. Arriagada and K. Osseoasare, *J. Colloid Interface Sci.*, 1995, 170, 8-17.

227. R. J. P. Corriu and D. Leclercq, *Angew. Chem. Int. Ed.*, 1996, 35, 1420-1436.

228. G. H. Bogush and C. F. Zukoski, *J. Colloid Interface Sci.*, 1991, 142, 19-34.

229. A. Vanblaaderen and A. Vrij, *Langmuir*, 1992, 8, 2921-2931.

230. H. Giesche, *J. Eur. Ceram. Soc.*, 1994, 14, 205-214.

231. K. D. Hartlen, A. P. T. Athanasopoulos and V. Kitaev, *Langmuir*, 2008, 24, 1714-1720.

232. A. Burns, H. Ow and U. Wiesner, *Chem. Soc. Rev.*, 2006, 35, 1028-1042.

233. M. Montalti, E. Rampazzo, N. Zaccheroni and L. Prodi, *New J. Chem.*, 2013, 37, 28-34.

234. C. Eggeling, A. Volkmer and C. A. M. Seidel, *ChemPhysChem*, 2005, 6, 791-804.

235. D. Avnir, D. Levy and R. Reisfeld, *J. Phys. Chem.*, 1984, 88, 5956-5959.

236. A. Vanblaaderen and A. Vrij, *J. Colloid Interface Sci.*, 1993, 156, 1-18.

237. R. Nyffenegger, C. Quellet and J. Ricka, *J. Colloid Interface Sci.*, 1993, 159, 150-157.

238. N. A. M. Verhaegh and A. Vanblaaderen, *Langmuir*, 1994, 10, 1427-1438.

239. X. X. He, K. M. Wang, W. H. Tan, J. Li, X. H. Yang, S. S. Huang, D. Li and D. Xiao, *J. Nanosci. Nanotechnol.*, 2002, 2, 317-320.

240. S. Santra, P. Zhang, K. M. Wang, R. Tapec and W. H. Tan, *Anal. Chem.*, 2001, 73, 4988-4993.

241. X. J. Zhao, R. P. Bagwe and W. H. Tan, *Adv. Mater.*, 2004, 16, 173-176.

242. M. L. Ferrer, F. del Monte and D. Levy, *Langmuir*, 2003, 19, 2782-2786.

243. M. L. Ferrer and F. del Monte, *Langmuir*, 2003, 19, 650-653.

244. F. P. Schmidtchen and M. Berger, *Chem. Rev.*, 1997, 97, 1609-1646.

245. P. D. Beer and P. A. Gale, *Angew. Chem. Int. Ed.*, 2001, 40, 486-516.

246. D. A. S. Razo, L. Pallavidino, E. Garrone, F. Geobaldo, E. Descrovi, A. Chiodoni and F. Giorgis, *J. Nanopart. Res.*, 2008, 10, 1225-1229.

247. C. Chen, Y. Li and S. Liu, *J. Electroanal. Chem.*, 2009, 632, 14-19.

248. L. C. J. Thomassen, A. Aerts, V. Rabolli, D. Lison, L. Gonzalez, M. Kirsch-Volders, D. Napierska, P. H. Hoet, C. E. A. Kirschhock and J. A. Martens, *Langmuir*, 2010, 26, 328-335.

249. S. Shibata, T. Taniguchi, T. Yano and M. Yamane, *J. Sol-Gel Sci. Technol.*, 1997, 10, 263-268.

250. H. Zhou, E. M. Sabio, T. K. Townsend, T. Fan, D. Zhang and F. E. Osterloh, *Chem. Mater.*, 2010, 22, 3362-3368.

251. T. Yokoi, Y. Sakamoto, O. Terasaki, Y. Kubota, T. Okubo and T. Tatsumi, *J. Am. Chem. Soc.*, 2006, 128, 13664-13665.

252. T. M. Davis, M. A. Snyder, J. E. Krohn and M. Tsapatsis, *Chem. Mater.*, 2006, 18, 5814-5816.

253. V. Mailaender and K. Landfester, *Biomacromolecules*, 2009, 10, 2379-2400.

254. L. Shang, K. Nienhaus and G. U. Nienhaus, *J. Nanobiotechnol.* , 2014, 12.

255. T. McKee and J. R. McKee, *Biochemistry: An Introduction*, McGraw-Hill Companies Inc, New York, 2nd edn., 1999.

256. L. Shang, K. Nienhaus, X. Jiang, L. Yang, K. Landfester, V. Mailaender, T. Simmet and G. U. Nienhaus, *Beilstein J. Nanotechnol.*, 2014, 5, 2388-2397.

257. G. Oberdorster, E. Oberdorster and J. Oberdorster, *Environ. Health Persp.*, 2005, 113, 823-839.

258. N. Phuong-Diem, N. Dung Thi Xuan, S. J. Son and J. Min, *J. Nanosci. Nanotechnol.*, 2014, 14, 8719-8723.

259. X. J. Zhao, R. Tapec-Dytioco and W. H. Tan, *J. Am. Chem. Soc.*, 2003, 125, 11474-11475.

260. J. Yao, M. Yang and Y. Duan, *Chem. Rev.*, 2014, 114, 6130-6178.

261. R. Weissleder, *Nat. Biotechnol.*, 2001, 19, 316-317.

262. A. Gomez-Hens and M. P. Aguilar-Caballos, *Trend. Anal. Chem.*, 2004, 23, 127-136.

263. M. A. Snyder, J. A. Lee, T. M. Davis, L. E. Scriven and M. Tsapatsis, *Langmuir*, 2007, 23, 9924-9928.

264. N. Atchison, W. Fan, D. D. Brewer, M. A. Arunagirinathan, B. J. Hering, S. Kumar, K. K. Papas, E. Kokkoli and M. Tsapatsis, *Angew. Chem. Int. Ed.*, 2011, 50, 1617-1621.

265. K. Borchers, A. Weber, H. Brunner and G. E. M. Tovar, *Anal. Bioanal. Chem.*, 2005, 383, 738-746.

266. H. Ju, X. Zhang and J. Wang, in *Nanobiosensing: Principles, Development and Application*, eds. H. Ju and X. Zhang, 2011, pp. 305-332.

267. R. Kumar, I. Roy, T. Y. Hulchanskyy, L. N. Goswami, A. C. Bonoiu, E. J. Bergey, K. M. Tramposch, A. Maitra and P. N. Prasad, *ACS Nano*, 2008, 2, 449-456.

268. H. Ow, D. R. Larson, M. Srivastava, B. A. Baird, W. W. Webb and U. Wiesner, *Nano Lett.*, 2005, 5, 113-117.

269. R. Shenhar and V. M. Rotello, *Acc. Chem. Res.*, 2003, 36, 549-561.

270. M. J. W. Ludden, D. N. Reinhoudt and J. Huskens, *Chem. Soc. Rev.*, 2006, 35, 1122-1134.

271. E. Rampazzo, E. Brasola, S. Marcuz, F. Mancin, P. Tecilla and U. Tonellato, *J. Mater. Chem.*, 2005, 15, 2687-2696.

272. M. Crego-Calama and D. N. Reinhoudt, *Adv. Mater.*, 2001, 13, 1171-1174.

273. P. Calero, E. Aznar, J. M. Lloris, M. D. Marcos, R. Martinez-Manez, J. V. Ros-Lis, J. Soto and F. Sancenon, *Chem. Commun.*, 2008, 14, 1668-1670.

274. L. Basabe-Desmonts, J. Beld, R. S. Zimmerman, J. Hernando, P. Mela, M. F. Garcia-Parajo, N. F. van Hulst, A. van den Berg, D. N. Reinhoudt and M. Crego-Calama, *J. Am. Chem. Soc.*, 2004, 126, 7293-7299.

275. P. Calero, M. Hecht, R. Martinez-Manez, F. Sancenon, J. Soto, J. L. Vivancos and K. Rurack, *Chem. Commun.*, 2011, 47, 10599-10601.

276. K. Rurack, *Spectrochim. Acta Part A*, 2001, 57, 2161.

277. U. Resch and K. Rurack, *Steady-state and time-resolved fluorometry of fluorescent pollutants and heavy metal complexes*, Spie - Int Soc Optical Engineering, Bellingham, 1997.

278. I. 15472, Int. Org. f. Standardization, Geneva, Switzerland, 2010.

279. I. 19318, Int. Org. f. Standardization, Geneva, Switzerland, 2004.

280. G. B. a. D. Briggs, *High Resolution XPS of Organic Polymers*, John Wiley & Sons, Chichester, UK, 1st edn., 1992.

281. B. M. Weidgans, C. Krause, I. Klimant and O. S. Wolfbeis, *Analyst*, 2004, 129, 645-650.

282. S. M. Saleh, R. Mueller, H. S. Mader, A. Duerkop and O. S. Wolfbeis, *Anal. Bioanal. Chem.*, 2010, 398, 1615-1623.

283. J. Y. Liu, H. S. Yeung, W. Xu, X. Y. Li and D. K. P. Ng, *Org. Lett.*, 2008, 10, 5421-5424.

284. R. Ziessel, L. Bonardi, P. Retailleau and G. Ulrich, *J. Org. Chem.*, 2006, 71, 3093-3102.

285. A. Coskun and E. U. Akkaya, *J. Am. Chem. Soc.*, 2005, 127, 10464-10465.

286. N. Malatesti, R. Hudson, K. Smith, H. Savoie, K. Rix, K. Welham and R. W. Boyle, *Photochem. Photobiol.*, 2006, 82, 746-749.

List of compounds

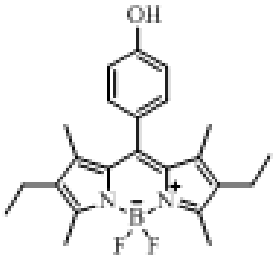

5

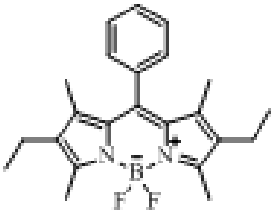

6

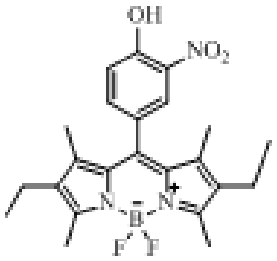

21a

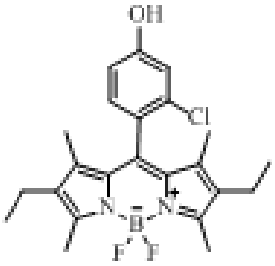

21b

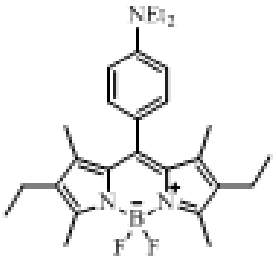

21c

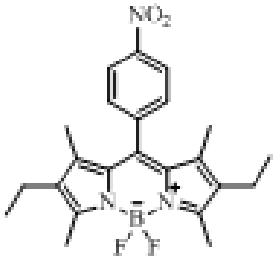

21d

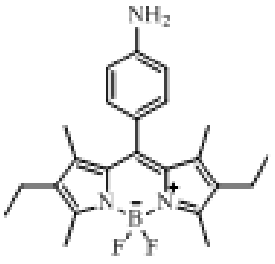

21e

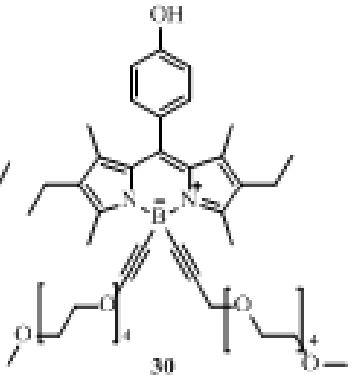

30

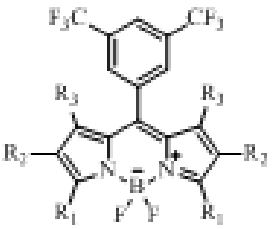

36 R_1=Cl, R_2= R_3=H
37 R_1= R_3=Me, R_2=Et
38 R_1= R_3=Me, R_2=H

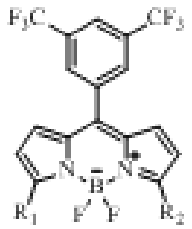

36A$_1$ R_1 = Cl, R_2 = $NH(CH_2)_3Si(OEt)_3$
36B$_1$ R_1 = Cl, R_2 = $NH(CH_2)_4CH_3$
36C$_1$ R_1 = Cl, R_2 = NEt_2
36D$_1$ R_1 = Cl, R_2 = NH^iPr_2
36A$_2$ R_1= R_2= $NH(CH_2)_3Si(OEt)_3$
36B$_2$ R_1 = R_2 = $NH(CH_2)_4CH_3$
36C$_2$ R_1 = R_2 = NEt_2
36D$_2$ R_1 = R_2 = NH^iPr_2

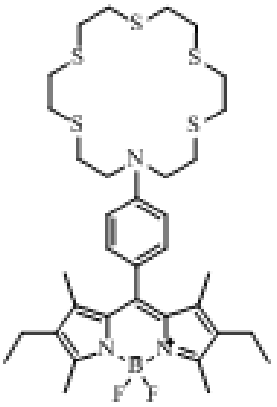

47

33

List of additional compounds

Additional compounds were synthesized and characterized but finally not applied for particulate or thin-film based platforms.

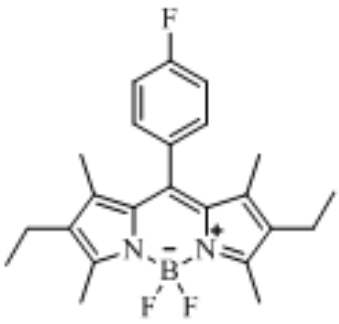

48

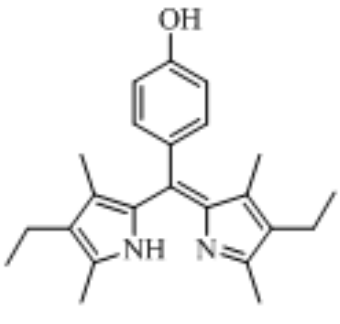

49

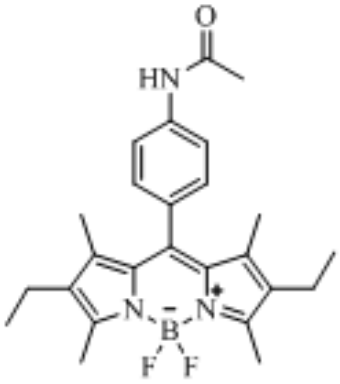

50

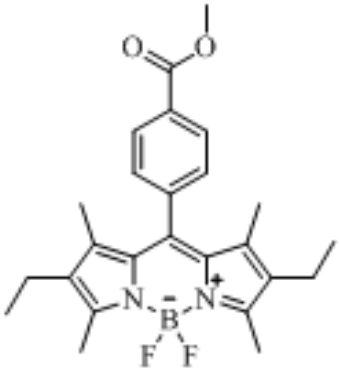

51

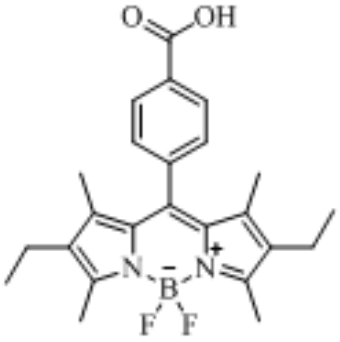

52

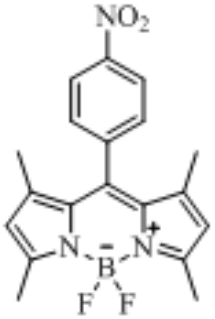

53

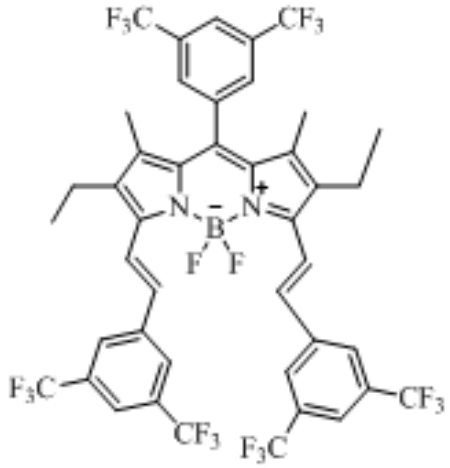

54

Danksagung

Ich möchte mich an erster Stelle bei meinem wissenschaftlichen Betreuer Herrn Dr. Knut Rurack und meinem Doktorvater Herrn Dr. Michael G. Weller herzlichst bedanken. Sie haben mir die Möglichkeit und ihr Vertrauen gegeben, dieses außerordentlich interessante und facettenreiche Forschungsthema zu bearbeiten. Durch ihr Engagement und ihre Diskussionsbereitschaft konnte ich unsere Forschungsergebnisse auf zahlreichen Konferenzen präsentieren und von internationalen Kooperationen profitieren.

Allen, auch ehemaligen, Mitarbeitern des Fachbereichs 1.9, besonders aber Delia Gröninger, Karin Keil, Dominik Sarma, Tobias Fischer, Dr. Mustafa Biyikal, Dr. Wei Wan, Shengchao Zhu, Dr. Pichandi Ashokkumar, Dr. Estela Climent, Dr. Jeremy Bell und Dr. Ana B. Descalzo gebührt mein aufrichtiger Dank für die angenehme Arbeitsatmosphäre und die stetige Unterstützung.

Einen besonderen Dank möchte ich für Dr. David Siegel aussprechen, für seine Art, die Dinge zu sehen und die Gespräche über den Arbeitsalltag hinaus.

Ich danke auch Dr. Paul Kuhlich, Dr. Stefan Merkel, Dr. Astrid Walter, Dr. Julia Grandke und Dr. Heike Pecher für das Interesse an meiner Arbeit. Für ihren Einsatz möchte ich auch meinen Praktikanten Anna van Eijk, Sarah-Luise Abrahm und Bastian Fritz danken.

Ein Dankeschön an Shireen Weise für die HR-MS Aufnahmen. Danke auch an Herrn Kraus und Frau Dr. Emmerling für das Messen und Auswerten der Kristallstrukturen. Herrn Altenburg danke ich für die Messungen der NMR-Proben.

Bedanken möchte ich mich bei den Mitarbeitern der analytischen Abteilung des Instituts für Chemie der HU Berlin für die Anfertigung zahlreicher Spektren und Analysen. Herrn Prof. Dr. Mügge und Frau Thiesies danke ich für die NMR-Analysen, Frau Dr. Zehl und Frau Kätel für die Elementaranalysen, insbesondere Herrn Dr. Leistner für die Aufnahmen der Massenspektren und die Unterstützung darüber hinaus. Ich danke Herrn Dr. Selve von der TU Berlin für die zahlreichen TEM-Aufnahmen und Frau Feldmann danke ich für die Aufnahmen mittels ESEM.

Mein ganz besonderer und tiefer Dank gilt meinen Eltern und Großeltern, Familie Czesnat und Planitzer, und auch den lieben Menschen, die mich über diese Zeit im Leben begleitet haben. Ich bin aus tiefstem Herzen dankbar für Eure uneingeschränkte Unterstützung, eure Liebe und das Vertrauen für diesen, meinen Weg.

"Some periods of our growth are so confusing that we don't even recognize that growth is happening. We may feel hostile or angry or weepy and hysterical, or we may feel depressed. It would never occur to us, unless we stumbled on a book or a person who explained to us, that we were in fact in the process of change, of actually becoming larger, spiritually, than we were before. Whenever we grow, we tend to feel it, as a young seed must feel the weight and inertia of the earth as it seeks to break out of its shell on its way to becoming a plant. Often the feeling is anything but pleasant. But what is most unpleasant is the not knowing what is happening[...]Those long periods when something inside ourselves seems to be waiting, holding its breath, unsure about what the next step should be, eventually become the periods we wait for, for it is in those periods that we realize that we are being prepared for the next phase of our life and that, in all probability, a new level of the personality is about to be revealed."

-Alice Walker, Living By the Word, 1989

Declaration of authorship / Selbstständigkeitserklärung

I hereby declare that this thesis is my own work and effort. All utilized sources, aids and appliances are declared in the text. Contributions of others are referenced appropriately.

Hiermit versichere ich, die vorliegende Dissertation selbstständig erarbeitet und verfasst zu haben. Alle verwendeten Quellen und Hilfsmittel werden im Text genannt. Fremdbeiträge sind eindeutig als solche gekennzeichnet.

Berlin, 23.04.2015, _____

Mandy Hecht